Mixed-Cation Zeolites with Minimum Lithium and Silver for Air Separation

by

Franklin E. Epiepang

A dissertation submitted in partial fulfillment
of the requirements for the degree of
Doctor of Philosophy
(Chemical Engineering)
in The University of Michigan
2018

Doctoral Committee:

Professor Ralph T. Yang, Chair
Professor Erdogan Gulari
Professor Jwo Pan
Assistant Professor Fei Wen

Franklin E. Epiepang

epiepang@umich.edu

ORCID iD: 0000-0002-9354-313X

Dedication

To my beloved and departed sister, Evelyne Ebane Epiepang.

Acknowledgement

There is a long list of people I would like to acknowledge for their priceless contributions throughout my time in graduate school. My advisor, my mentor, and a father figure, professor Ralph T. Yang, thank you for constantly challenging me and for all the guidance and encouragements you offered me. You provided me with the environment to excel as a researcher and above all, held me up, stood by me, and supported me (emotionally and financially) as I recovered from the most difficult time of my life (the loss of my sister) so far. I am forever in your debt.

I would also like to thank the members of my committee, Dr. Erdogan Gulari, Dr. Fei Wen, and Dr. Jwo Pan for their guidance and to Dr. Lola Eniola-Adefeso for all her motivational words throughout my graduate studies. To Dr. Michael Gyamerah of PVAMU, thank you for your perspective on the importance of higher education.

To all the members of the Yang research group, past and present, Dr. Lifeng Wang, Dr. Ming Hao, Dr. Chengyang Yin, Dr. Peifu Cheng, Dr. Xiong Yang, Dong Zhang, John-Timothy Anyanwu, and Yiren Wang, I say thank you for the interesting discussions and the constant willingness to assist.

A special acknowledgement to the staff of the Chemical Engineering department for all the assistance and support you provided through the years. You all make the department what it is. Thank you also to the staff of the Michigan Center for Materials Characterization and Materials Science and Engineering Department for the provision of training and sample characterization equipment.

With the stress that comes from conducting research and the expectations of impactful results, I want to thank all the friends I made through this journey. You provided me many outlets to unwind and refocus.

I am beyond grateful to my family for their patience, support, encouragements and words of wisdom. You all have each played such an important role in this journey. Though we lost one along the way, she is smiling down and willing each of us to become the best versions of ourselves.

Lastly, all thanks to The Almighty without whom, none of this would have been possible.

Table of Contents

List of Figures

List of Tables

Abstract

Air separation is a key process in today's industry and is achieved by various methods including but not limited to the energy intensive cryogenic distillation of liquefied air and pressure swing adsorption process. The cryogenic process is preferable for high-volume production of Oxygen and Nitrogen from atmospheric air while the pressure swing adsorption process is more applicable for low-to-medium volume production. In this dissertation, we focused mainly on air separation by adsorption which is based on the unique adsorption property of zeolites with high N_2/O_2 selectivities. An introductory chapter is presented here-in that gives an in-depth picture of various air separation processes and technologies. The second chapter evaluates carbon dioxide, water vapor, and methane on Li-LSX (where LSX denotes low-silica X-zeolite with Si/Al = 1.0) as a superior adsorbent for air separation at low pressure. Prior to feeding ambient air into the air separation unit, it must be prepurified by the removal of trace impurities such as carbon dioxide, water vapor, and light hydrocarbons (such as methane) to their tolerable limits of 1.0 ppm, 0.1 ppm, and to a few ppb, respectively. Characteristic adsorption isotherms to very low partial pressures (to a few ppm at 1 atm) were measured for Li-LSX and compared with the conventional synthetic 13X zeolite as well as two ion-exchanged zeolites in K-LSX and Ca-LSX. As anticipated, the superior adsorption properties of Li-LSX for air prepurification are demonstrated in this chapter.

Though Li-LSX has been the sorbent of choice since its invention for air separation by pressure swing adsorption and vacuum swing adsorption, the demand for lithium has steeply risen

due to its application in lithium ion-batteries for energy storage as well as the fact that its reserves are dwindling, thereby driving up its cost, we set out in the third chapter to develop new zeolites in which lithium is substantially reduced and replaced by a low cost alkali-earth metal cation, in this case, Ca^{2+}. To accomplish this ground-breaking task, we reduced/minimized lithium in Li-LSX by replacing the 70% Li^+ in Li-LSX that are bonded to the inaccessible sites which are normally used for adsorption. Thus, mixed-cation LiCa-LSX containing minimum lithium were prepared by exchanging small fractions of Li^+ into Ca-LSX, followed by dehydration under mild conditions to avoid equilibration/migration of the lithium cations. Upon comparing the N_2/O_2 adsorption isotherms and heats of adsorption of the LiCa-LSX sample to that of the pure-cation Li-LSX and Ca-LSX, there were strong evidence that significant amounts of the Li cations indeed remained on the exposed sites (SIII). Results after comparing the mixed-cation samples the pure-cation samples based on their performance for oxygen production by pressure swing adsorption via a model simulation showed that the LiCa-LSX samples yielded significantly higher O_2 product productivities at the same product purity and recovery than their pure-cation precursor, Ca-LSX and only 25% less the Li-LSX.

Chapter 4 involves the desulfurization of natural gas using nitrogen-doped carbon. Comparisons of adsorption isotherms for hydrogen sulfide and methane showed that the nitrogen-doped carbon sample (7 wt% N_2) adsorbs hydrogen sulfide 5 times more and adsorbs methane 1.3 times less than commercial Calgon BPL 12x30 activated carbon respectively. The regeneration energy required for the synthesized nitrogen-doped carbon sample was very low as cyclic adsorption-desorption isotherms revealed complete hydrogen sulfide desorption in about 8 minutes on nitrogen-doped carbon at 333 K. In chapter 5, more mixed-cations, LiSr-LSX, AgCa-LSX and AgSr-LSX containing minimum lithium and silver were prepared by exchanging small fractions

of Li^+ into Sr-LSX and Ag^+ into Sr-LSX and Ca-LSX respectively. Strong evidences were provided that significant fractions of the exchanged Li^+ and Ag^+ remained in SIII and SII* respectively after comparisons of the N_2/O_2 adsorption isotherms and isosteric heats of adsorption of the mixed-cation and pure-cation samples. Furthermore, the mixed-cation LiSr-LSX, AgCa-LSX and AgSr-LSX samples were compared against the pure Li-LSX sample based on their O_2 productivity performance via a PSA simulation model. Chapter 6 covers the study of Sr-LSX zeolite and its possibility of completely replacing Li-LSX for air separation in adsorption processes. The O_2 productivity performance results from this study were quite promising and are discussed in detail along with treatment conditions for adsorption capacity optimization.

Chapter 1

Introduction

1.1 Air Separation

Air separation is the separation of ambient air into its primary components, mainly oxygen and nitrogen, and in some cases, argon and rare inert gases such as krypton, xenon, and neon. This is achieved by flowing atmospheric air through a set of equipment and devices which separates them at various stages depending on the applied technology. However, prior to feeding the ambient air into the separation unit, it must be prepurified. Prepurification involves the removal of trace impurities such as CO_2, H_2O vapor and light hydrocarbons (CH_4, C_2-hydrocarbons) to their tolerable limits of 1.0 ppm, 0.1 ppm, and a few ppb respectively. Since atmospheric air contains ~400 ppm carbon dioxide, up to ~3% water vapor, and a few ppm of hydrocarbons, failure to remove these impurities to their tolerable limits leads to not just to operating issues but also to serious safety hazards.

1.2 Air Separation Technologies

Most air separation systems employ two basic technologies namely cryogenic and non-cryogenic (membrane, pressure swing adsorption (PSA), and vacuum pressure swing adsorption (VPSA)) air separation processes. The choice of application depends on various factors such as

demand and purity of the products. Today, majority of the nitrogen and oxygen - which are respectively the second and third most human-made chemicals - produced comes from the cryogenic air separation process as shown in Figure 1.1.

1.2.1 Cryogenic Air Separation

The first cryogenic air separation columns for the recovery of oxygen and nitrogen were created by Carl Von Linde in 1902 and 1904 respectively while the first air separation plant using the double column rectification process was created in 1910 which allowed the simultaneous production of pure oxygen and nitrogen [1]. Cryogenic air separation still serves as one of the most viable processes for the mass (high-volume) production of pure nitrogen, oxygen, and argon as opposed to the non-cryogenic processes. The cryogenic air separation is a high energy consumption process which is in part due to the very tight integration of heat exchangers and separation columns to obtain excellent efficiency while all the refrigeration energy is provided by the compression of air at the inlet of the unit. Another drawback of the cryogenic process is that is requires a high capital cost [2].

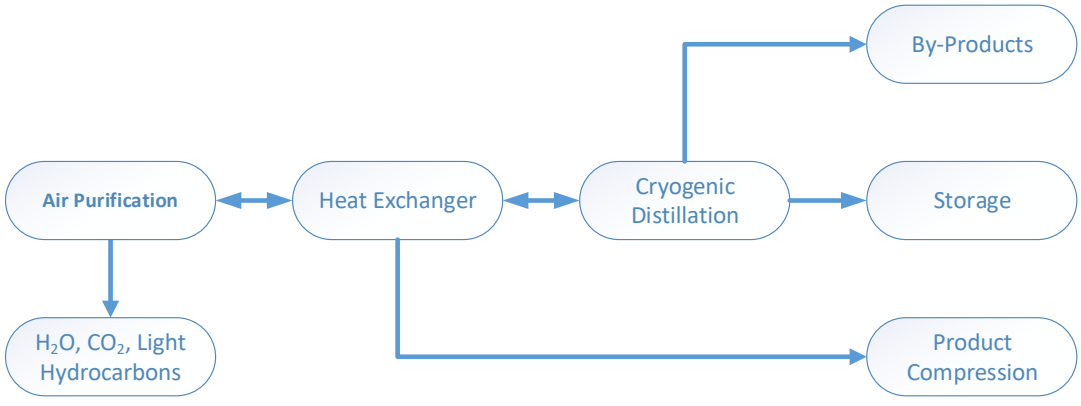

Figure 1.1 Schematics of a cryogenic air separation process.

1.2.2 Membrane Separation

Membrane separation is one of many non-cryogenic separation processes. It isolates nitrogen from ambient air by selective permeation across a membrane wall. The membrane is a bundle of selective permeable hollow fibers that allows fast gases such as oxygen, carbon dioxide and water vapor to permeate the membrane wall much faster as opposed to the slow nitrogen gas. The permeate – one of two streams in the membrane separation process – contains O_2, CO_2 and water vapor while the other stream known as the product, contains the high-pressure nitrogen as shown in Figure 1.2. Unlike the cryogenic air separation process, the membrane process is a low capital cost process with a very flexible production output capability. The production output can be improved by changing a few operating conditions. For example, by decreasing the nitrogen flow rate, the nitrogen purity is increased. Of all the air separation processes, it requires the least repair and maintenance costs. The downside of the membrane separation process however is that its produced nitrogen purity is below par for processes that demands a 1 ppb purity [2].

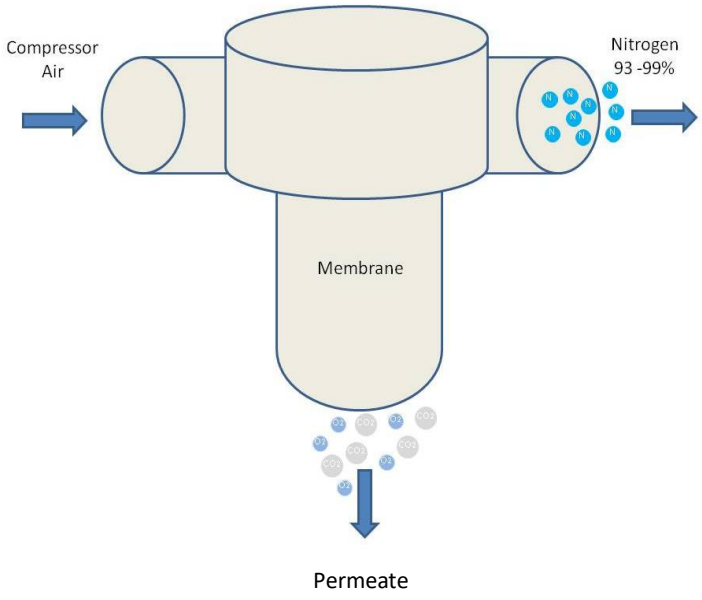

Figure 1.2 Membrane air separation [2].

1.2.3 Pressure Swing Adsorption

One of the most popular non-cryogenic air separation process is pressure swing adsorption (PSA). PSA is a widely used regeneration technology used for the separation of gases from a feed stream of mixed gases. Unlike the cryogenic process that operates at liquid nitrogen temperature, PSA systems operates at near-atmospheric temperatures. It only requires a low-to-moderate capital cost and has a cost-effective nitrogen production of relative high purities. However, equipment maintenance is high, and its operation is quite noisy. PSA processes are strictly based on the knowledge that under high pressure, gases tend to adsorb to solid surfaces. This means that at higher pressures, more gases are adsorbed to the surfaces of the adsorption material; and as the pressure is decreased, the gases are desorbed. It is also worth mentioning that different gases more or less adsorbed strongly to different surfaces based on the choice of sorbents.

Figure 1.3 shows a basic schematic of a two-bed PSA system. The use of the two beds in PSA processes is simply to address the continuous production of the target gas. The operation of the pressure swing adsorption is straight-forward. For example, to separate a feed mixture of methane (CH_4) and carbon dioxide (CO_2), the pressurized feed is passed through one of the adsorption beds containing a sorbent that attracts that has a high affinity with CH_4 than it does CO_2. Part or all of the CH_4 will adsorb on the bed while the exit gas will be enriched in CO_2. Once the bed becomes saturated, the feed is switched to the second bed as CO_2 production continues while the first bed is regenerated by reducing the pressure of the bed and hence releasing the adsorbed CH_4. The performance of the PSA separation process is based on the choice of sorbent and three parameters: a) product purity, b) product recovery, c) adsorbent productivity. Product purity is a volume-averaged quantity, as the effluent concentration and flow rate from a PSA process, without the use of surge or mixing tanks, vary with time [3]. Product recovery measures

the amount of component that is contained in the product stream divided by the amount of the same component in the feed mixture processes per unit amount of the sorbent per unit time [3]. Adsorbent productivity is measured by the amount of product or feed mixture processed per unit amount of sorbent per unit time [3]. It must be noted that for a given separation, the product purity is predetermined, the energy requirement is usually proportional to the recovery, and the size of the sorbent bed is inversely proportional to the sorbent productivity.

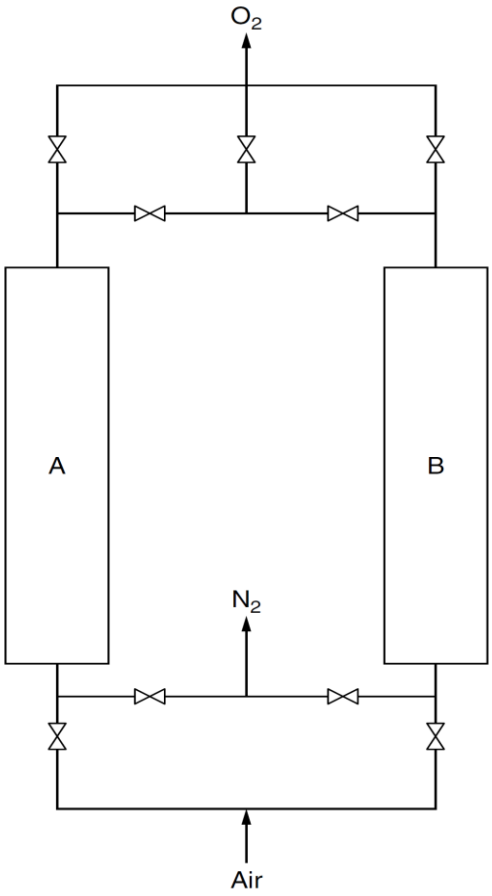

Figure 1.3 The Skarstrom PSA cycle for air separation [3].

1.3 Adsorbents

At the heart of all PSA and VPSA systems is the sorbent which can either be activated alumina, activated carbon, silica gel or zeolites. In this work, we focused solely on zeolitic

materials in pure and mixed-cation forms. Zeolites are 3-dimensional, crystalline, microporous aluminosilicate materials with well-defined inter-connecting channels that leads to structures with large surface areas. The silicon (neutrally-charged) and the aluminum (negatively-charged) forms a tetrahedral through the shared oxygen atom. The negatively-charged aluminum creates negative areas within the aluminosilicate framework that are countered by loading a cation (Na^+, Ca^{2+}, K^+, etc.…) in the cage-like cavities to balance the overall charge in the material. They exist naturally while most used in commercial applications are synthetically produced. Since the crystal structure of a zeolite is partially determined by the ring size, altering the silicon-to-aluminum (Si/Al) ratio can cause a huge impact on the pore size of the resulting material.

1.3.1 Zeolites

The general formula for zeolites is $M_{e2/n}O \cdot Al_2O_3 \cdot xSiO_2 \cdot yH_2O$ where M_e is any alkali or alkaline earth atom, n is the valence of or charge on the atom, x is the number of silicon tetrahedron varying from 2 -10, and y is the number of water molecules varying from 2 – 7 [4]. For example, Zeolite A has the following formula: $Na_{12} \cdot (Al_{12}Si_{12}O_{48}) \cdot 27H_2O$. This means that the charge on the aluminosilicate ($Al_{12}Si_{12}O_{48}$) is 12+ and are balanced by the 12+ sodium charges to give chemically neutral material. The ions in the cages can be removed or exchanged without damaging the aluminosilicate framework and hence, one of the most important characteristic of zeolites as it simply means that they can be tailored for various applications including but not limited to ion-exchange agents (water softening), catalysis (petroleum cracking), and molecular filters (gas separation).

1.3.2 Ion Exchange

In air separation applications for example, the alkali or alkaline earth metals in the zeolites can be ion-exchanged to create a material with altered pore sizes capable of filtering gas mixtures as they flow through. Ion exchange is simply a chemical reaction in which ions are reversibly transferred between an insoluble solid and an aqueous solution. A generic ion exchange reaction equation can be written as follows:

$$M^+X^- + N^+Y^- \quad \rightarrow \quad N^+X^- + M^+Y^- \tag{1}$$

Where M^+X^- is the ion exchanger that ionizes to yield the N^+ and Y^- ions when placed in an N^+Y^- salt solution.

Ion exchange was a major part in the work communicated here-in. All the studied pure and mixed zeolites in this work were prepared via ion exchange at varying extents. Some of the used pure samples include 13X, Na-LSX, Li-LSX, Ca-LSX and Sr-LSX while the mixed-cation zeolites include LiCa-LSX, LiSr-LSX, AgCa-LSX and AgSr-LSX. Ca-LSX and Sr-LSX were prepared via ion exchanging Na-LSX which along with Li-LSX, were supplied by Luoyang Jianlong.

1.4 Lithium Forecast

In general, the ceramics and glass industries still dominate lithium consumption compared to the battery industry. The use of lithium in the latter industries is due to the fact that it lowers the melting points of both materials, and thereby making them more malleable. However, it is expected that by 2025, battery production will consume 70% of global lithium supplies [5]. The increase in demand from an economic standpoint means a hike in prices as reflected in Figure 1.4.

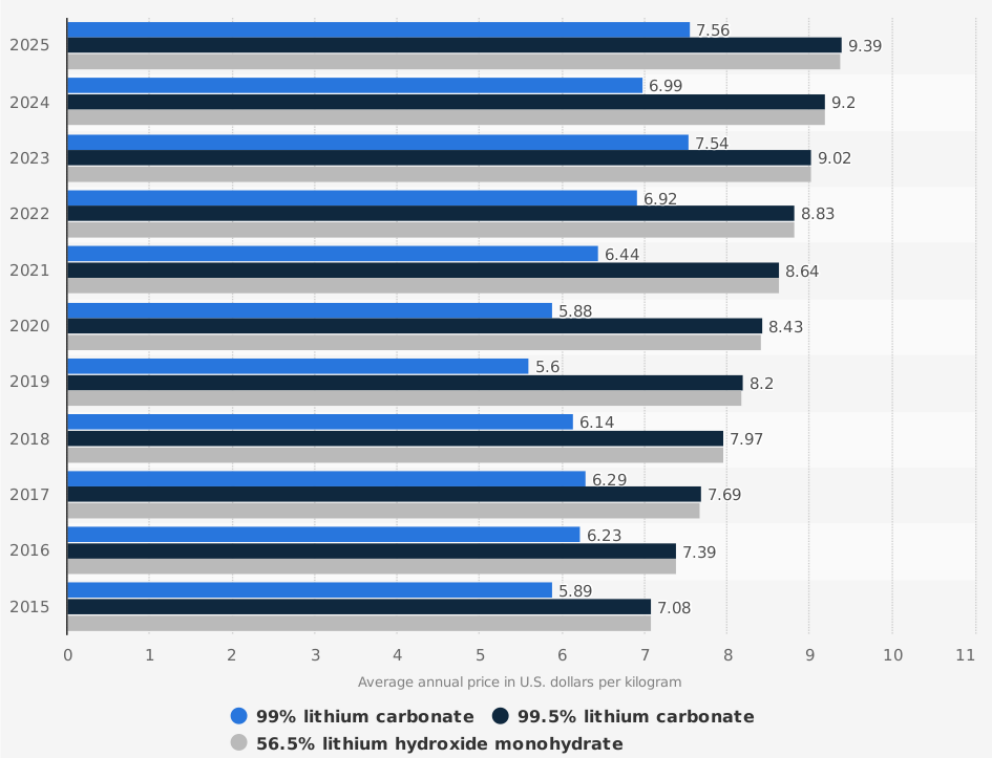

Figure 1.4 Forecast of annual price averages for lithium chemicals worldwide from 2015 to 2025 (in US dollars per kilogram) [5].

1.5 Research Objective

With Li-LSX still being the best adsorbent (porous solids with preferably high surface areas per unit mass) used in adsorption processes for air separation, the rise in lithium price due to its high demand for lithium-ion batteries [6-7], calls for the development of new and better sorbents not just to accommodate the overall operating cost of such processes but also to manage the overall higher demand of this precious metal in all its applications. This was the main objective behind the creation of the mixed-cation samples listed above.

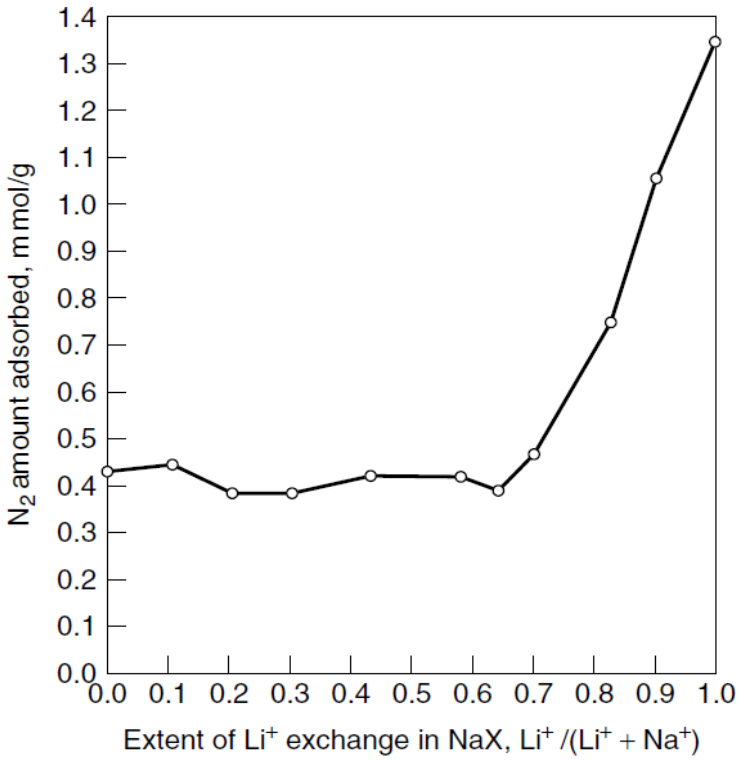

Figure 1.5 Dependence of nitrogen adsorption at 296 K and 101 kPa on fractional Na^+ exchange by Li^+ in LSX [3].

Figure 1.5 shows the dependence of nitrogen adsorption at 296 K and 1 atm on fractional Na^+ exchange by Li^+ in LSX. It is clearly seen that at below ~70 % Li^+ exchange, the N_2 adsorption capacity remained unchanged while between 70 – 100 % Li^+ exchange, N_2 capacity increased almost linearly. This phenomenon can be explained by cation site occupancy.

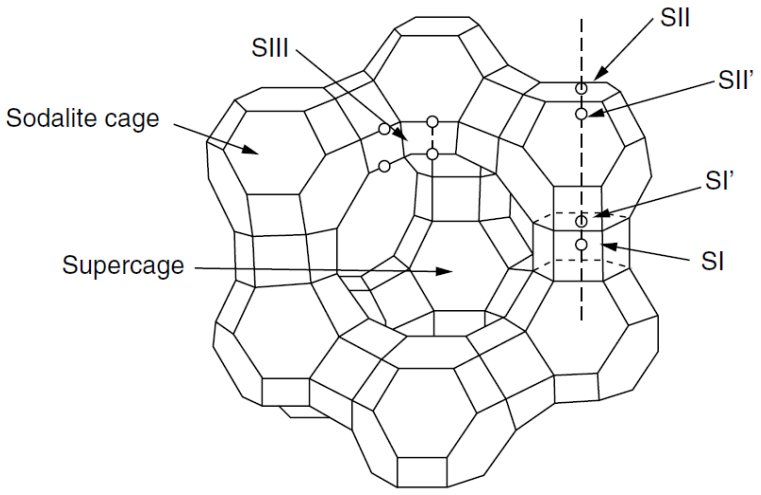

Figure 1.6 Unit cell of faujasite (Type-X and -Y) zeolites, including cation sites [3].

As will be further explained in subsequent chapters, cations in SI and SII' (Sites I and II') inside the six-ring and beta cages of the zeolite structure in Figure 1.6 are the sites inaccessible to the sorbate while SII and SIII are responsible for sorbate interaction. This means that in the pure Li-LSX zeolite, only about 1/3 of the exchanged Li^+ participate in sorbate-sorbent interactions hence wasting 2/3 of the exchanged Lithium. To eliminate the waste of the lithium in the lower Li-LSX sites, we developed a new approach that completely differs from the orthodox synthesis methods to produce mixed-cation zeolites. The new synthesis method addresses the cost implications for future exponential lithium demands by minimizing the lithium content within the mixed-cation samples while maintaining their higher capacities and PSA performance.

References

[1] History and Technological Progress: Cryogenic Air Separation.

[2] A. Jaya, Air Separation Units (Engineering Design Guideline), 2013.

[3] R. T. Yang, Adsorbents: Fundamentals and Applications, New Jersey: John Wiley & Sons, Inc., 2003.

[4] S. Kumar, S. Jain, History, Introduction, and Kinetics of Ion Exchange Materials. Journal of Chemistry, 2013.

[5] J. Hykawy, T CHudnovsky, LITHIUM DEMAND, SUPPLY AND PRICE FORECASTS – Who do we throw out of the boat? Mines and Money Asia, 2017.

[6] An increasingly precious metal; clean energy, The Economist, 418 (2016) 63-70.

[7] P. Barrera, Lithium Trends 2017: EV Plans Fuels Supply Concerns, 2017.

Chapter 2

Low-Pressure Performance Evaluation of CO_2, H_2O and CH_4 on Li-LSX as a Superior Adsorbent for Air Prepurification

Abstract

High-volume production of oxygen and nitrogen from atmospheric air is accomplished by cryogenic distillation. Prior to feeding to the air separation unit, the ambient air must be pre-purified by the removal of trace impurities such as CO_2, H_2O vapor, and light hydrocarbons (e.g., CH_4) to their tolerable limits of 1.0 ppm, 0.1ppm, and to a few parts per billion, respectively. In this study, the adsorption characteristics of a synthetic zeolite, Li-LSX (where LSX denotes low-silica type-X zeolite where Si/Al = 1), for the removal of trace amounts of CO_2, CH_4, and H_2O vapor impurities were analyzed and compared with the conventional synthetic 13X zeolite that has been used for air prepurification as well as the ion-exchanged K-LSX and Ca-LSX zeolites. Isotherms to very low partial pressures (to a few ppm of 1 atm) were measured. The Tòth, Langmuir-Freundlich (L-F), and the Dubinin-Astakhov (D-A) isotherm models were used to correlate the low-pressure experimental data and the Tòth model was found to be the better fit especially in the low-pressure range. The superior adsorption properties of Li-LSX for air prepurification are demonstrated in this work.

2.1 Introduction

The first industrial cryogenic air distillation plant for the production of oxygen was launched over a century ago. Today the majority of the nitrogen and oxygen are produced by cryogenic air distillation and they account for, respectively, the second and third human-made chemicals. This process still serves as one of the most viable processes for mass production of pure oxygen, nitrogen and argon. The demand for such high-purity air separation products ranges from and not limited to several sectors including the food processing, medical, semiconductor, oil refining, metals production, chemicals, and gasification industries.

Oxygen and nitrogen are produced from atmospheric air by two methods depending on the volume of production. For high-volume production, cryogenic distillation of liquefied air is used, while for low to medium volume production, adsorption via pressure swing adsorption (PSA) is used [1]. For cryogenic distillation, however, it is essential to remove trace impurities such as carbon dioxide (~ 400 ppm), water vapor (up to ~ 3%), and light hydrocarbons (CH_4 and C_2 hydrocarbons, ranging around a few ppm) from the air stream to tolerable limits before it is fed into the cryogenic distillation system. The freezing points of CO_2 and water vapor are well above the cryogenic temperature of liquefied air, so failure to remove them from the air in its crude form will risk the possibility of occluding the distillation column internals. The light hydrocarbons (particularly the C_2 hydrocarbons) have low solubilities in liquid oxygen, failure to remove them would risk their possible accumulation in the reboiler of the distillation column, leading to an explosion hazard. Thus, failure to remove these impurities will lead to not just operating issues but also safety hazards. The tolerable limits for CO_2 and H_2O in the feed to an air separation unit (ASU) are 1.0 ppm and 0.1 ppm, respectively, while the limit for light hydrocarbons is around a few ppb (parts per billion).

Adsorptive processes are ideally suited for air prepurification because these aforementioned limits can be achieved via fixed-bed adsorption. Both pressure-swing adsorption (PSA) and temperature swing adsorption (TSA) processes have been applied for air prepurification [2]. However, with the PSA process' ability to process higher product throughput coupled with lower capital and energy costs, it is often preferable to the TSA depending on the sorbent that is used [2]. Although both processes use adsorptive materials with strong affinity to the trace impurities, the TSA typically uses activated alumina and 13X (Na-X) as its sorbent for the removal of water and other impurities respectively while the PSA process generally employs activated alumina to remove all impurities [3]. Each of these adsorptive methods employs a bed of sorbent which is exposed to the feed air for a certain time period to adsorb the impurities. After the feed air is cut off from the sorbent bed, a degas step or a purge gas is fed through to strip the adsorbed contaminants and in turn, regenerates the bed. Prepurification units are generally regenerated using high temperature nitrogen at low pressure in the case of the TSA while in the PSA, the bed is regenerated at ambient temperature and low pressure [4].

A number of adsorbents have been used for air prepurification. The most widely used sorbents have been activated alumina, silica gel and a variety of synthetic zeolite molecular sieves, such as 13X. The choice of PSA vs. TSA also depends on the sorbent that is used. Activated alumina and silica gel adsorb CO_2 and water vapor less strongly compared to zeolites, and are easier to regenerate (i.e., PSA is sufficient), while regeneration of zeolites requires elevated temperatures (i.e., requiring TSA). Layered beds have also been used for PSA processes where the weaker sorbents (alumina or silica gel) are placed in front of the zeolite layer, so CO_2 and water vapor are kept within the front layer.

Besides synthetic zeolites, studies on naturally occurring zeolites such as clinoptilolites [5] and ion-exchanged clinoptilolites [2] for gas separation and air prepurification both showed promising properties for such applications as well. There is also a promising potential with chabazites - another naturally occurring zeolite [6-10] for air purification. Mixed metal (Ag/Zn) oxides have also been suggested in space shuttle air regeneration systems [11].

Although the measurement of adsorption isotherms at very low pressures (to a few ppm levels of atmospheric pressure) are crucially important for application to air prepurification, such measurements are scarce in literature. As mentioned, among the most widely used sorbent is 13X zeolite. Zeolite 13X has been extensively studied not only for air prepurification from ASUs, but also for methane purification from natural gas, as well as for carbon sequestration from flue gas [12-15]. In this work, we are focused on Li-LSX as a superior sorbent for the removal of trace impurities from the air fed into cryogenic distillation systems in air separation processes. The low-pressure adsorption results will be compared with the conventional synthetic 13X zeolite as well as non-conventional sorbents such as the ion-exchanged K-LSX and Ca-LSX. In our earlier studies on sorbents for air prepurification [2, 4], five different sorbents (including activated alumina and 13X) were evaluated and compared for adsorption of CO_2, water vapor and light hydrocarbons. For the hydrocarbons, CH_4, C_2H_4 and C_2H_6 were studied. It was concluded that the relative strengths of adsorption of the five sorbents for these light hydrocarbons follow the same trend, i.e., the best sorbents for CH_4 were also the best sorbents for C_2H_4 and C_2H_6, as expected. Thus, in this study, only CH_4 was studied as the light hydrocarbon.

2.2 Experimental Section

2.2.1 Equilibrium Isotherms

The adsorption equilibrium of pure CO_2 CH_4, and H_2O vapor was measured with a Micromeritics ASAP 2020 Sorptometer (which is based on volumetric technique) on synthetic 13X and Li-LSX zeolites and ion-exchanged samples of K-LSX and Ca-LSX.

2.2.2 Zeolites - sorbents used

The 13X and Li-LSX zeolites, available as 13X-APG and JLOX-100 respectively, were supplied by Luoyang Jianlong Micro-Nano New Materials Co., Ltd., China, in binderless or powder form. The 13X was Na-X zeolite with a Si/Al ratio of 1.2. In order to obtain the potassium and calcium forms of LSX, Li-LSX was ion-exchanged with 1.0 M solution of potassium chloride and calcium chloride, respectively, at 363 K and with stirring overnight. This exchange process was repeated 5 times and after filtration, the obtained solid was thoroughly washed with deionized water and dried in an oven at 383 K for 24 hours. Although we aimed at achieving complete ion-exchange, X-ray photoelectron spectroscopy (XPS) results indicated that well over 95% exchange was obtained in the exchanged samples. (It is noted that XPS is a surface analysis technique. However, because of the uniformity of the zeolite structure, XPS provides a reasonable estimate for the extent of exchange.)

2.2.3 Sample Pretreatment and Isotherm Measurements

The degas/dehydration conditions were as follows: 648 K for Li-LSX, 648 K for 13X, and 623 K for K-LSX and Ca-LSX. The samples were treated in-situ the Micromeritics ASAP 2020 overnight to desorb all adsorbed gases and dehydrate the samples until a final pressure of 25 μmHg before each analysis.

The measurements were carried out at the following temperatures: 298 K, 323 K, and 343 K for all sorbents. The analyses gases were supplied by Cryogenic Gases with their respective purities and grades as follows: CO_2 (99.995%, Bone Dry), CH_4, (99.97%, UHP grade)

The H_2O vapor source was prepared as in [2]. A custom-built H_2O vapor source for the Micromeritics ASAP 2020 instrument was assembled using a 150 cm^3 quartz tube containing 50 cm^3 of deionized water. The water was first boiled for 10 minutes to remove dissolved gases and further degassed in-situ the vapor inlet port of the Micromeritics until the 1000 mmHg transducer read between 40 – 45 mmHg.

2.3 Results and Discussion

2.3.1 Carbon Dioxide Isotherms

Figures 2.1 – 2.3 show CO_2 experimental adsorption isotherms on various sorbents and temperatures (298 K, 323 K, and 343 K). Using the volumetric technique, it was able to measure the equilibrium amounts adsorbed at CO_2 pressures as low as 0.5 ppm of 1 atm. A comparison of all sorbents studied, Li-LSX shows the highest CO_2 adsorption capacities at all temperatures, particularly at the important temperature, 298 K (Figure 2.1).

Carbon dioxide is a trace gas that exists in atmospheric air at concentrations currently at ~ 400 ppm, and with ASUs requiring a CO_2 tolerable limit of below 1.0 ppm, prepurification of the feed air has become a mainstay in these processes. From Figure 2.1, it is seen that an appreciable amount adsorbed of CO_2 of 0.003 mmol/g at 0.5 ppm of 1 atm pressure coupled with its high overall capacity makes Li-LSX a superior sorbent for air prepurification. K-LSX also exhibited interesting adsorption characteristics at low pressures. It may be noted that the CO_2 capacities (e.g.,

by 13X) reported here agree with earlier works and are higher than those reported for its pelletized form which contains approximately 15% of clay or inert binders [16-20].

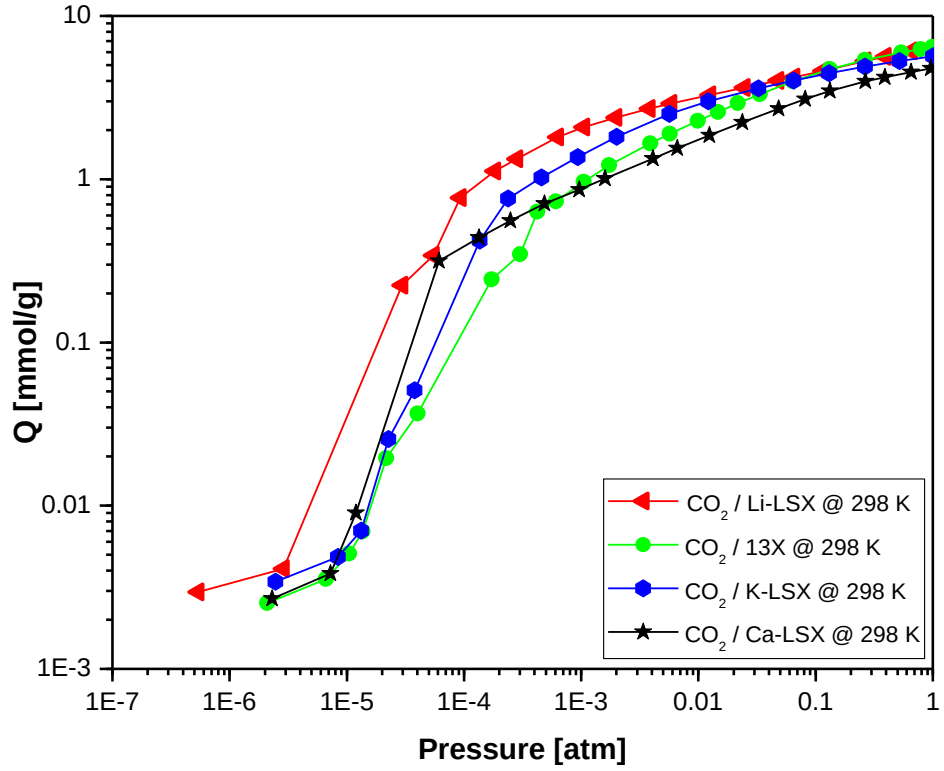

Figure 2.1 Experimental adsorption Isotherms of CO_2 at 298 K and 101 kPa on representative adsorbents.

Also, literature review of previous work on the studies on CO_2 uptakes on binderless or pure zeolites shows lower adsorption amounts than the results presented here and might presumably be due to differences in elemental compositions, i.e., higher Si/Al ratios hence lower numbers of cations per unit cell of faujasite [21-22].

It is interesting to note that there were distinct "steps" (i.e., steep rises) in the CO_2 isotherms, particularly at 298 K (which is below the critical temperature of CO_2, 304 K). The "step" was caused by micropore filling and in fact, it is most useful for determining the pore size distribution of microporous materials [23].

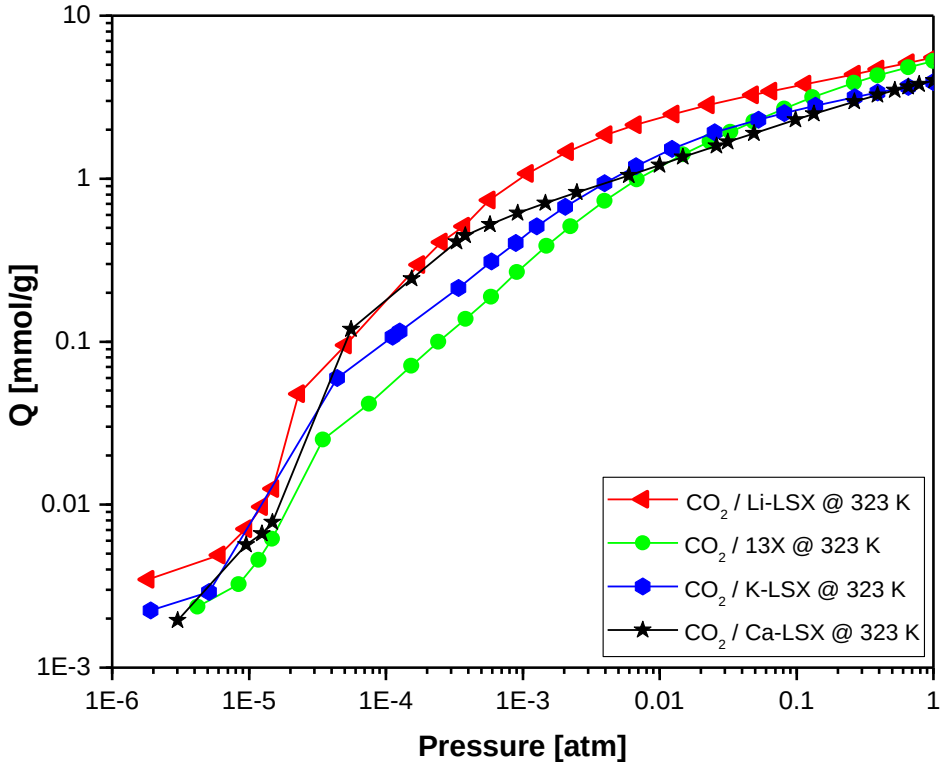

Figure 2.2 Experimental adsorption Isotherms of CO_2 at 323 K and 101 kPa on representative adsorbents.

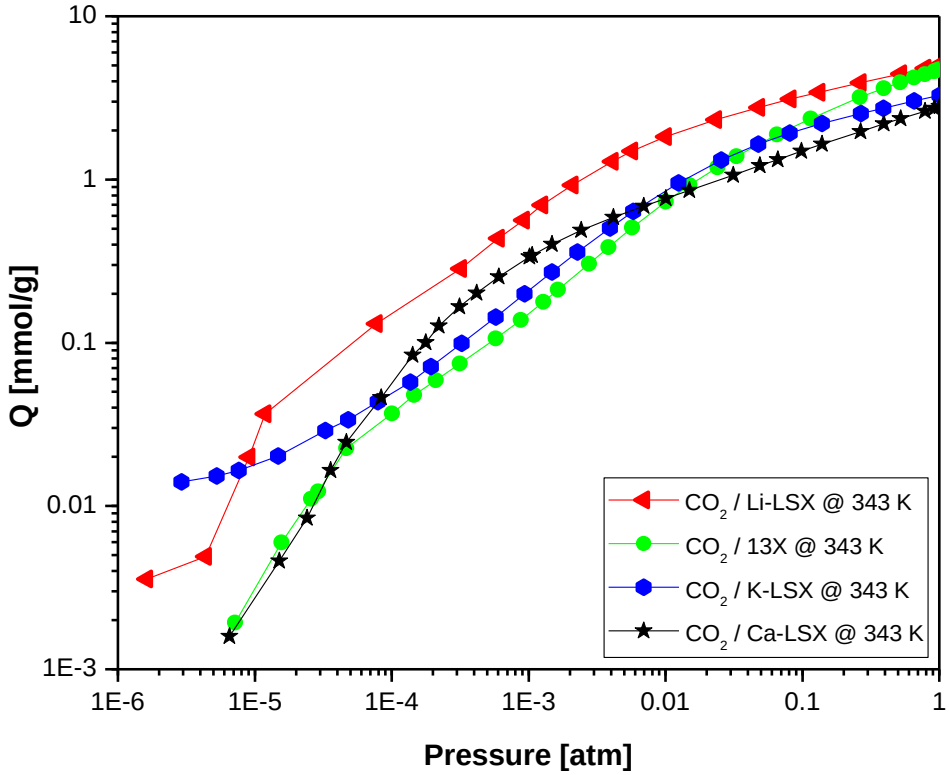

Figure 2.3 Experimental adsorption Isotherms of CO_2 at 343 K and 101 kPa on representative adsorbents.

By equating the free energy change upon adsorption from gas phase to the average interaction energy of the adsorbing molecules, the "step" in the isotherm can be translated into a pore size distribution. Thus, the mathematical solution relating the relative pressure of the adsorbing gas to the pore size was first given by Horvath and Kawazoe [24], referred to as Horvath-Kawazoe model or HK model. It was derived for slit-shaped pores. This model was later corrected by Rege and Yang [25] and extended to cylindrical pores by Saito and Foley [26], and spherical pores by Cheng and Yang [27]. These models have been used based on N_2 isotherms at 77 K. The results shown in Figure 2.1 show that it is also possible to use CO_2 as the adsorbing gas for determination of pore size distribution. Since the kinetic diameter of CO_2 (0.33 nm) is smaller than N_2 (0.364 nm), using CO_2 could probe micropores of smaller sizes.

2.3.2 Hydrocarbon (CH_4)

Reactions between hydrocarbons (trace contaminants in air) and oxygen (O_2) in the ASUs can occur when they accumulate in O_2 above the lower flammability levels (LFL). These usually occur in one of two ways: 1) they dissolve in the oxygen or 2) as an enriched phase such as acetylene or liquid propane droplets [28-29]. Based on the reactive nature of these two gases, air pre-purification units are expected to eliminate most trace amounts of hydrocarbons from the feed air of the separation units.

As mentioned, the adsorption capacities for CH_4, C_2H_4 and C_2H_6 by five sorbents (including activated alumina and commercial 13X zeolite) have been compared in an earlier study by Rege and Yang [2]. The results showed that the relative capacities of these sorbents are consistent with the three hydrocarbons. Thus, only CH_4 was used in this work.

Figures 2.4 – 2.6 show experimental adsorption isotherms of CH_4 at 298 K, 323 K, and 343 K. Comparison of different sorbents showed that Li-LSX performed best at the low-pressure range

as expected showing significant adsorption capacities as low as about 20 ppm, making it a better candidate to meet the hydrocarbon requirements.

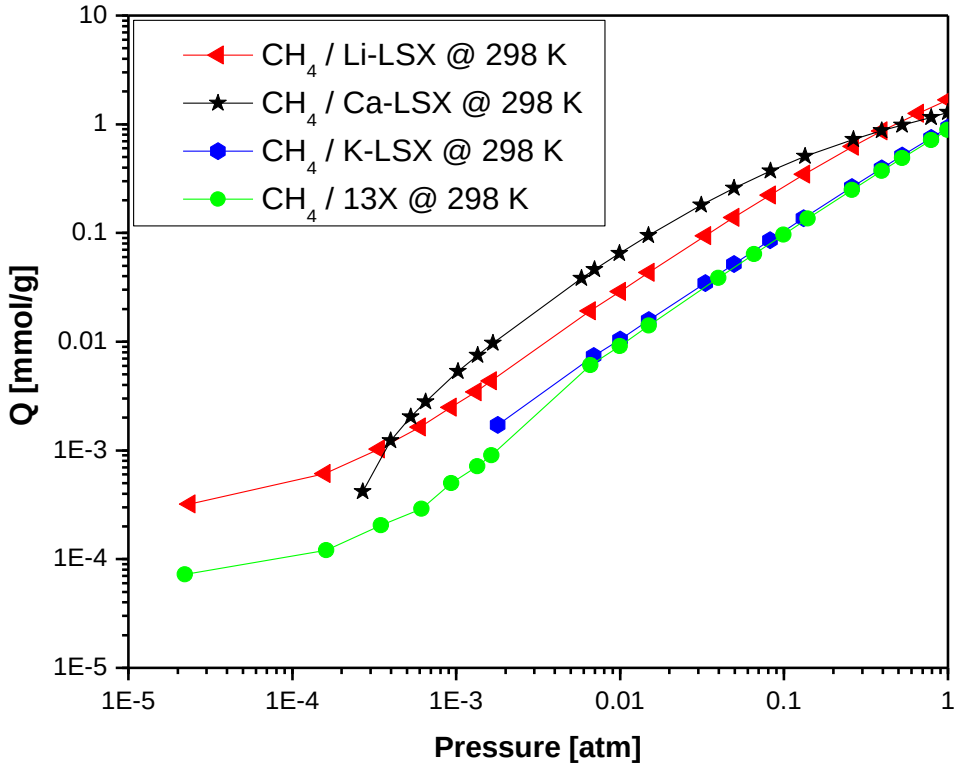

Figure 2.4 Experimental adsorption Isotherms of CH_4 at 298 K and 101 kPa on representative adsorbents.

Li-LSX showed higher capacities at pressure below ~300 ppm of 1 atm at 298 K. At higher pressures, i.e., between 300 ppm and 1 atm pressures, Ca-LSX showed the highest adsorption capacity due to stronger interaction between methane and Ca^{2+} cations than that with Li^{+} ions, as will be shown below. A similar trend is observed for comparisons of sorbents at higher temperatures (323 K and 343 K).

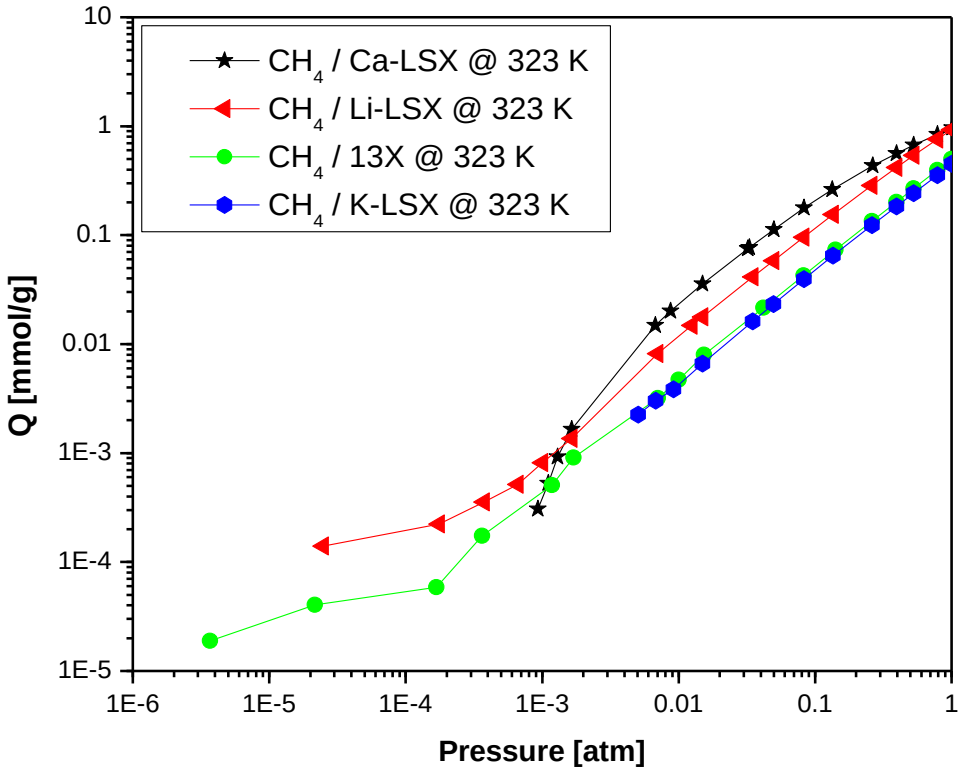

Figure 2.5 Experimental adsorption Isotherms of CH_4 at 323 K and 101 kPa on representative adsorbents.

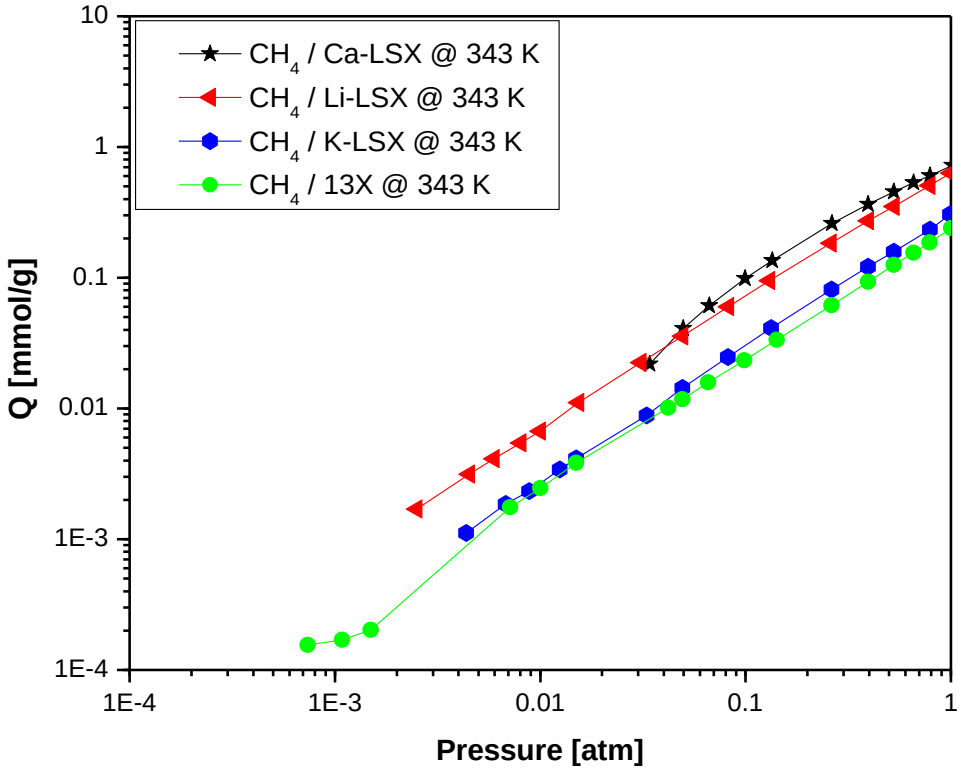

Figure 2.6 Experimental adsorption Isotherms of CH_4 at 343 K and 101 kPa on representative adsorbents.

2.3.3 *H_2O Vapor*

Typical air pre-purification units require a 0.1 ppm tolerable limit of water vapor – which is a major fouling contaminant in the ASUs - content in the air feed.

The experimental H_2O vapor adsorption data on Li-LSX and 13X zeolites at 298 K are presented in Figure 2.7. Both sorbents show similar capacities around partial pressures of 100 ppm while Li-LSX showed higher capacities above 0.003 atm. Based on the required specifications of H_2O vapor in ASUs, it would have been ideal studying their adsorption isotherms below the 0.1 ppm level, but the unstable nature and inaccuracies observed during the measurements especially at the extremely low pressure range, prompted experimentation at pressures around the 100 ppm range.

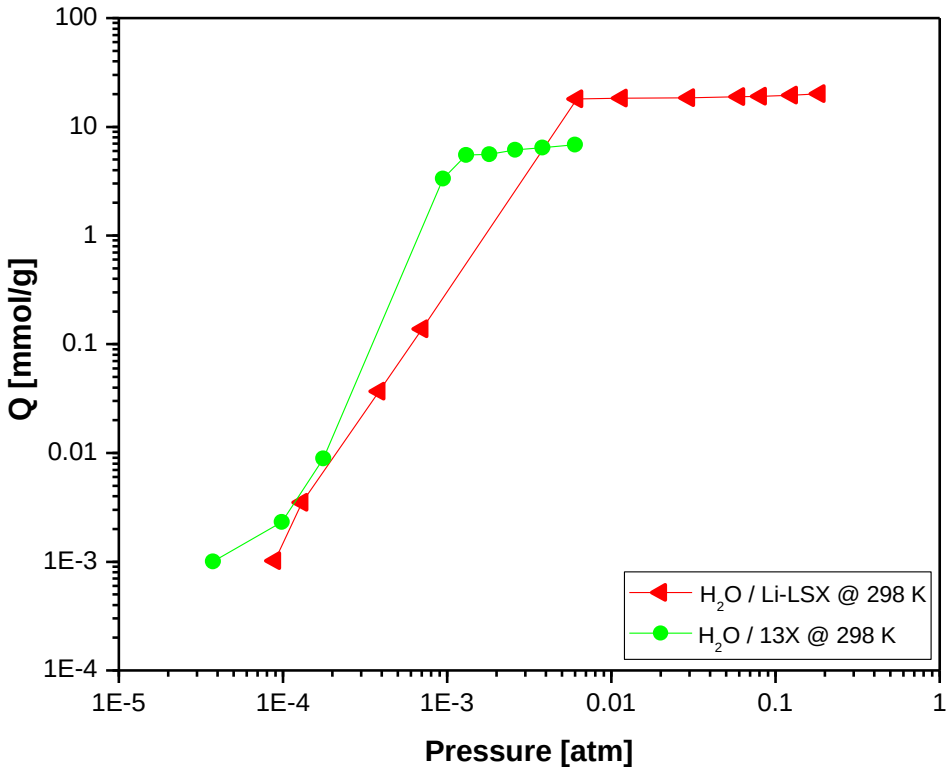

Figure 2.7 Experimental adsorption Isotherms of H_2O at 298 K and 101 kPa on representative adsorbents.

The difficulty of measuring water vapor isotherms was partly due to the slow rate of evaporation of the water from the reservoir at ambient temperature while heating the reservoir was to be avoided due to errors caused by condensation in the system. The obtained experimental data would have also been extrapolated to the low-pressure range but because of the nonlinearity of the experimental data, it would have only generated unreliable results. From the results shown in Figure 2.7, it is concluded that the capacities for water vapor at the very low-pressure range are similar for both zeolites.

In general, the adsorption capacities for zeolites usually increase with decreasing cation diameter and an increase in cationic charge. This would be seen in the theoretical determination of adsorbate-adsorbent interaction potential as Ca-LSX (Ca^{2+}, zeolite with highest charge in this study) and Li-LSX (smallest ionic radius, 0.68 Å [23]) both presented the highest total potentials. The number of exposed cations within the faujasite zeolite structure also affects the adsorption capacity of sorbents as zeolites with lower Si/Al ratios (Si/Al_{LiLSX} = 1.0 and Si/Al_{13X} = 1.25) contain more cations and more exposed cations. It should also be noted that sorbates with larger quadrupole moments (CO_2 = -4.3 x 10^{-26} esu; CH_4 = 0; [23]) and permanent dipoles (CO_2 = CH_4 = 0; [23]) increase the total interaction energy as will be seen in section 3.5.

2.3.4 Pure Component Isotherms

Adsorption equilibrium isotherms of CO_2, CH_4, and H_2O vapor on the studied samples presented in Figures 2.1 – 2.7 were fitted with the Langmuir-Freundlich (L-F), Tóth, and the Dubinin-Astakhov (D-A) isotherm models. However, only the non-fitted equilibrium isotherms at the studied temperatures are presented here for the CO_2 and CH_4 sorbates while the H_2O vapor isotherms for Li-LSX and 13X zeolites at 298 K is best fitted with the D-A model. All others could be found in Appendix A.

$$Q = \frac{Q^*_{sat} K C^n}{1 + K C^n} \qquad \text{Langmuir-Freundlich (L-F) Model} \qquad (2.1)$$

$$Q = \frac{aP}{(d + P^k)^{\frac{1}{k}}} \qquad \text{Tóth Model} \qquad (2.2)$$

$$n = n_o \exp\left[-\left(C \ln \frac{P_s}{P}\right)^m\right] \qquad \text{Dubinin-Astakhov (D-A) Model} \qquad (2.3)$$

Where C = RT/βE, E is the characteristic energy of adsorption of a standard vapor, Q and n are amounts adsorbed, P is pressure and the constants are fitting constants from experimental data.

It is experimentally possible to control pressure and measure the adsorbed amount, but exceedingly difficult to fix the adsorbed amount and measure the equilibrium pressure. Therefore, a fitting equation is required to interpolate the measured values.

However, the interpolation of adsorption data turns out to be very sensitive to the fitting method chosen, and small deviations from the true value can cause significant errors in thermodynamic calculations [30-31].

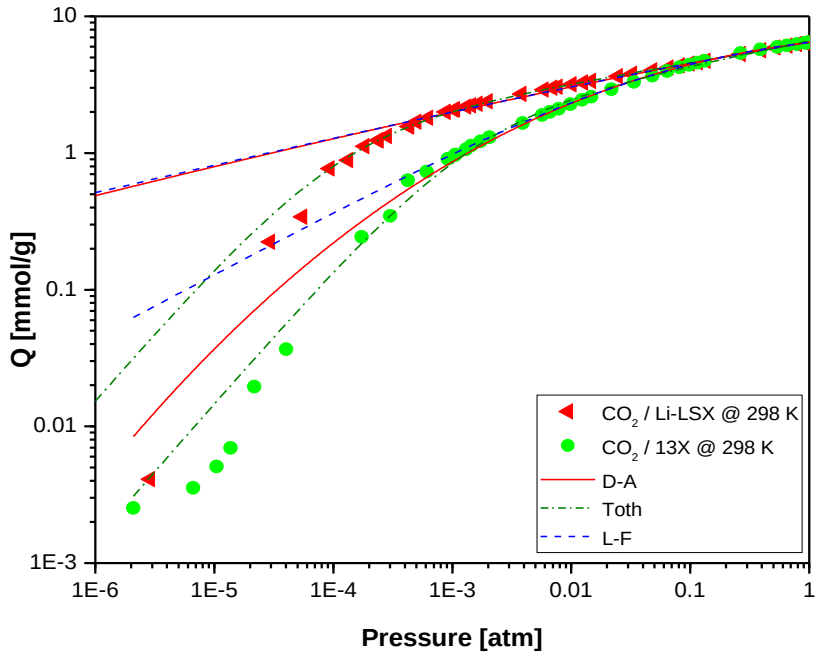

Figure 2.8 Dubinin-Astakhov, Tóth, and Langmuir-Freundlich model fits to adsorption data of CO_2 on Li-LSX and 13X at 298 K and 101 kPa.

Figure 2.8 shows all studied model fits on adsorption isotherms for Li-LSX and 13X zeolites while Table 2.1 summarizes fitting parameters to experimental adsorption data at 298 K respectively. Model fitting results for all isotherms are shown in Figures S2.1 to S2.18, in Appendix A.

Table 2.1 Representative values of model parameters fit to experimental adsorption data at 298 K.

	Tòth			**Dubinin-Astakhov**			**Langmuir-Freundlich**		
	a [mmol/g]	d [atm^k]	k	n_o [mmol/g]	C	m	Q_{sat} [mmol/g]	K [atm^{-n}]	n
CO_2 / Li-LSX	5.50	0.000415	0.85	10.40	0.14	1.26	22.43	0.41	0.21
CO_2 / 13X	5.46	0.004	0.82	7.67	0.12	2.55	8.45	3.23	0.46
CO_2 / K-LSX	5.01	0.002	0.87	8.89	1.75	0.73	8.90	1.75	0.27
CO_2 / Ca-LSX	3.96	0.002	0.80	5.90	0.13	2.33	6.67	2.56	0.43
CH_4 / Li-LSX	3.13	1.26	0.83	7.35	0.31	1.78	4.80	0.53	0.95
CH_4 / 13X	7.84	8.94	0.89	20.42	0.65	1.19	9.80	0.10	0.99
CH_4 / K-LSX	3.14	5.35	0.53	23.94	0.69	1.14	13.78	0.07	0.98
CH_4 / Ca-LSX	1.13	0.18	0.75	2.60	0.21	2.09	2.61	0.95	0.70
H_2O / Li-LSX	18.14	0.003	1.1	19.30	0.10	66.36	17.74	366.70	136.80
H_2O / 13X	1.87	0.001	0.001	6.66	0.09	22.36	6.58	2.06	2.72

2.3.5 Heats of Adsorption

It is crucially important to have strong sorbate-sorbent interaction energy for adsorption at very low pressures, as in air prepurification. The sorbate-sorbent interaction energy is approximately equal to the experimental heat of adsorption, while they differ by only 3RT/2 which is negligible at near ambient temperature [23].

For adsorption of gas molecules on zeolites, the main interaction energies are between the gas molecule and the metal cations on the surface, while its interaction energies with the oxide

atoms on the surface are considerably weaker than that with the cations. Thus, to understand adsorption at low pressures, we may focus our attention on the interactions with the cation sites. First, an understanding of the cation sites in the faujasite zeolite structure is needed.

The structure and cation sites for faujasite are shown in Figure 2.11. There are 5 different cation sites on faujasite [23]. Site I (SI) is inside the double six-ring and SII' is inside the beta-cage, both are inaccessible to the sorbate molecule. Only site II (SII) and site III (SIII) are accessible to the sorbate. However, the electric fields around the "exposed" cations (as in SII) are partially shielded by the surrounding oxygen atoms. This shielding significantly lowers the interactions between the sorbate molecule and the SII cation. Such shielding also depends on the size of the cation. The small Li cation can sit crystallographically very low in the face of the single 6-ring (SR6, at SII site), allowing the electric field to be nearly completely shielded by the surrounding framework oxygen. Thus, the sorbate-sorbent interaction energy is mainly contributed by the Li cation sitting on site III or SIII. For the larger cations such as K and Ca, the shielding can be substantially weaker for SII cations.

The cation sites for all zeolites studied in this work have been determined, as shown in Table 2.3, although for K and Ca forms, only Type X zeolites rather than LSX were studied.

For obtaining a basic understanding of the experimental results, the sorbate-sorbent interaction energies for the gas-sorbent pairs were estimated. The estimation may be performed by calculating the potential energies between each gas molecule and a free or isolated cation, e.g., Li^+, Na^+, etc.

The total sorbate-sorbent potential (ϕ_T) for physical adsorption [23] is given as follows:

$$\phi_T = \phi_D + \phi_R + \phi_{Ind} + \phi_{F\mu} + \phi_{\dot{F}Q} \quad (2.4)$$

Where

$$\phi_D = -\frac{A}{r^6} \quad (2.5)$$

$$\phi_R = \frac{B}{r^{12}} \quad (2.6)$$

$$A = \frac{6mc^2\alpha_i\alpha_j}{(\alpha_i/\chi_i)+(\alpha_j/\chi_j)} \quad (2.7)$$

$$B = \frac{Ar_0^6}{2} \quad (2.8)$$

$$\phi_{Ind} = -\frac{\alpha q^2}{2r^4(4\pi\epsilon_0)^2} \quad (2.9)$$

$$\phi_{F\mu} = -\frac{q\mu\cos\theta}{r^2(4\pi\epsilon_0)} \quad (2.10)$$

$$\phi_{\dot{F}Q} = -\frac{Qq(3\cos^2-1)}{4r^3(4\pi\epsilon_0)} \quad (2.11)$$

The five terms in Equation 2.4 represent, respectively, dispersion energy, repulsion energy, induction energy (i.e., interaction between electric field of the cation and induced dipole of sorbate), interaction between the field (F) and a permanent dipole (μ), and interaction between field gradient and a quadrupole (Q).

Equations 4 - 11 as well as parameters found in references [23, 32-33] were used to determine the potentials in Table 2.2. Table 2.2 also gives the quadrupole moment (Q), dipole moment (μ), as well as the polarizability (α), of different sorbates. The results showed that the interaction energies for all three gases (CO_2, CH_4 and water vapor) and the energies followed the order: $Ca^{2+} > Li^+ > Na^+ > K^+$

Table 2.2 Theoretical Adsorbate – Adsorbent Interaction Potentials of studied gas/sorbent pairs.

Gas/Sample	φ_D [kJ/mol]	φ_R [kJ/mol]	φ_{Ind} [kJ/mol]	$\varphi_{F\mu}$ [kJ/mol]	$\varphi_{\dot{F}Q}$ [kJ/mol]	φ_T [kJ/mol]
CO_2 / Li-LSX	-1.52	0.76	-62.23	--	-49.17	**-112.16**
CO_2 / 13X	-26.33	13.16	-38.92	--	-34.80	**-86.88**
CO_2 / K-LSX	-8.54	4.27	-23.26	--	-23.65	**-51.17**
CO_2 / Ca-LSX	-10.55	5.28	-151.02	--	-68.02	**-224.32**
CH_4 / Li-LSX	-0.70	0.35	-40.66	--	--	**-41.01**
CH_4 / 13X	-2.34	1.17	-26.55	--	--	**-27.72**
CH_4 / K-LSX	-4.59	2.29	-16.55	--	--	**-18.84**
CH_4 / Ca-LSX	-5.30	2.65	-103.29	--	--	**-105.94**
H_2O / Li-LSX	-2.28	1.14	-62.33	-1.04E-4	--	**-63.47**
H_2O / 13X	-6.40	3.20	-36.31	-7.96E-5	--	**-39.51**
H_2O / K-LSX	-10.22	5.11	-20.27	-5.95E-5	--	**-25.38**
H_2O / Ca-LSX	-13.97	6.99	-140.29	-1.57E-4	--	**-147.27**

The effect of introducing different types of cations into the zeolite's framework can be seen from the difference in potential between CO_2 and CH_4 on the samples. The presence of these cations generates electrostatic fields that interact strongly with molecules such as CO_2 with higher quadrupole moments. By so doing, increased selectivity between the sorbates (CO_2 and CH_4) is observed and as seen in literature [16, 23, 33].

The isosteric heats of adsorption of the gas-sorbent systems were estimated by the Clausius-Clapeyron relation [34]. It is noted that the calculations were very sensitive to errors in the equilibrium pressure meaning interpolation can sometimes introduce significant uncertainties into the calculated isosteric heat determined by using measured adsorption isotherms at different

temperatures. The Tòth model fit along with the Clausius-Clapeyron relation were used to determine the isosteric heats of adsorption of CO_2 and CH_4 presented in Figures 2.9 and 2.10.

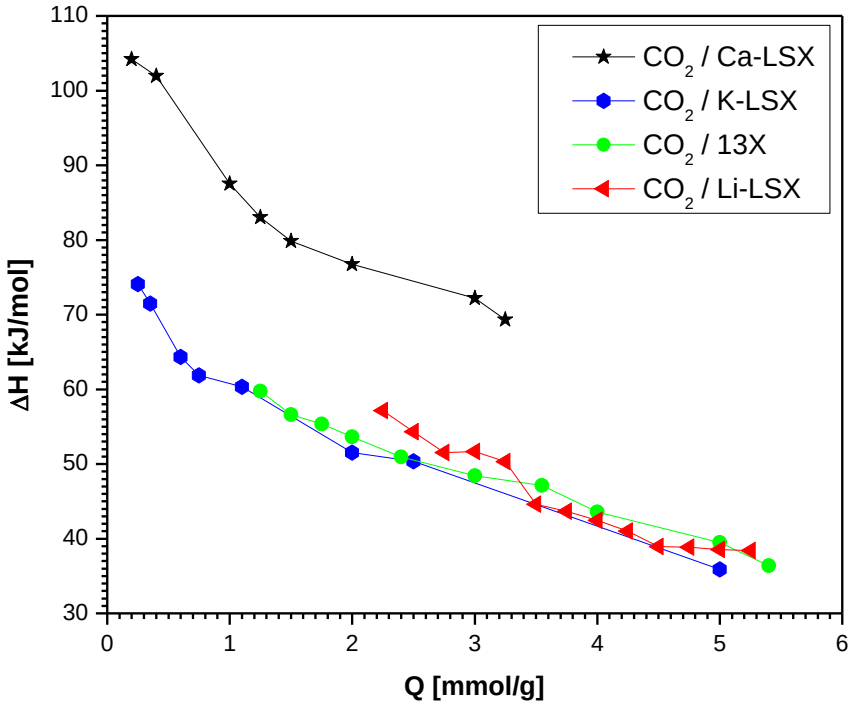

Figure 2.9 CO_2 Isosteric heats of adsorption on representative adsorbents.

The experimental heats of adsorption may now be compared with the theoretical calculations of the interaction energies, by comparing Table 2.2 and Figures 2.9 and 2.10. The calculations were performed assuming the cations were free or isolated cations, not bonded to oxygen atoms. In fact, each SII cation is bonded to 6 oxygen atoms on the 6-ring and is nearly completely shielded. Cations sitting on SIII sites are less shielded and hence have stronger interactions with the sorbate molecules. Thus, the calculated energies based on free cations may be regarded as the upper bound for the interaction energies. The cation sites for faujasite (type X zeolite) are illustrated in Figure 2.11.

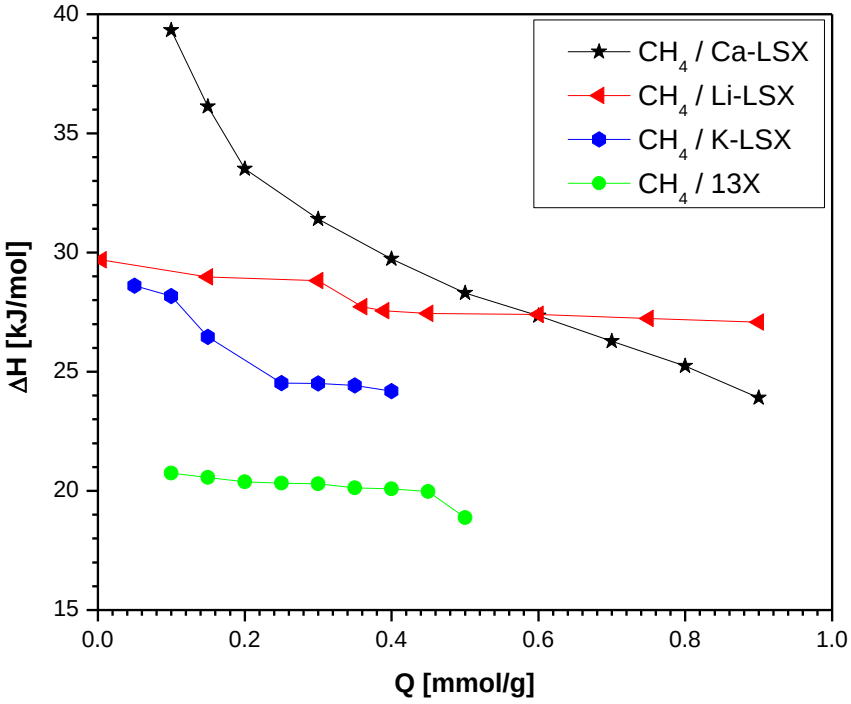

Figure 2.10 CH_4 Isosteric heats of adsorption on representative adsorbents.

As mentioned, the calculated energies followed the order: $Ca^{2+} > Li^{+} > Na^{+} > K^{+}$. The experimental heats of adsorption are all lower than the calculated energies. Figure 2.9 shows that for CO_2, this order was indeed followed, although the differences among the alkali cations were not as significant as the theoretical values.

The comparison between theory and experiment for CH_4 adsorption is interesting. Here again, adsorption on the Ca-form was the strongest, followed by Li-form, in agreement with calculations. However, adsorption was clearly stronger on K-LSX compared to that on 13X (or Na-X) (Figure 2.10). In Figure 2.10, the loading of CH_4 was much lower than that of CO_2 (Figure 2.9). Two factors may be attributed to the stronger adsorption on the K-form than the Na-form. At such low loading of CH_4, site III (SIII) cations are the major sites for adsorption. Table 2.3 shows that there are many more K cations on Site III (in K-X) than the Na cations on Site III for Na-X

(38 vs. 7.9 per unit cell). For K-LSX, there are even more K cations on SIII (than K-X). There are abundant cations on Site II in both K-X and Na-X (Table 2.3), and SII is also exposed. Here, there is less electron shielding on the K cation (than Na cation), leading to stronger interactions on K-X. These two factors could explain the higher heats of adsorption of CH_4 on the K-form than the Na-form.

Table 2.3 Cation site occupancies in dehydrated X zeolites (maximum = 96 monovalent cations per unit cell for Si/Al = 1).

Zeolite	Al/Unit Cell	Sites				
		I	I'	II	II'	III
Li-LSX[a]	95.8	--	27.2	33.9	--	32.4
Li-LSX[b]	96	--	33	34	--	29
Na-X (13X)[c]	81	3.8	32.3	30.8	--	7.9
K-X[d]	87	9	13	26	--	38
Ca-X[e]	86	7.5	17.3	17.3	9.0	--

a. Hutson and Yang, 2000
b. Feuerstein et al., 1998
c. Mortier, 1982
d. Hseu, 1972
e. Mortier et al., 1972

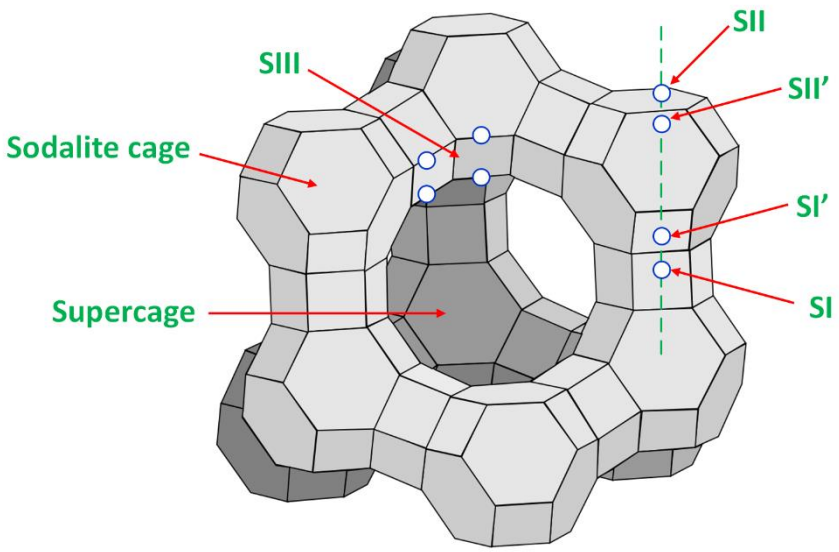

Figure 2.11 Unit cell of faujasite-type (X and Y) zeolites, including cation sites.

It is noted that Na-LSX (with Si/Al = 1) was not included in this work. Table 2.3 shows that for 13X (i.e., Na-X), there are only 7.9 Na cations on the open site, SIII, compared with 32 Li cations on SIII sites of the Li-LSX. Na-LSX should have a similarly high number of cations on SIII as Li-LSX. In addition, the theoretical sorbate-cation interaction energy with Na^+ is only slightly less that that with Li^+. Thus, Na-LSX is also a promising sorbent for air prepurification.

2.3.6 Rates of Adsorption

The rate of adsorption (ROA) data is not only needed for the determination of the fixed bed adsorption performance [23] but also aids to better understand the sorbent's surface and pore structures. Assuming pore diffusion is the rate limiting step in zeolites and carbons, the inverse diffusion time constant (D/R^2) has been commonly used for expressing the uptake rate of sorbates on the sorbents.

The diffusion equation is given by:

$$\frac{\partial u}{\partial r} = D\frac{\partial^2 u}{\partial r^2} \tag{2.12}$$

where u = Cr, D is the pore diffusivity, R is the radius of the particle, while C is the concentration at radial distance, r.

The short time approximation for $M_t/M_\infty < 0.3$ is given by Equation 2.13 after solving Equation 2.12 for a step change in the surface concentration at r = R. Here, t is time and M_t and M_∞ are the total sorbate amounts adsorbed at time t and at equilibrium, respectively [35-36].

$$\frac{M_t}{M_\infty} = \frac{4}{\sqrt{\pi}} \left(\frac{Dt}{R^2}\right)^{\frac{1}{2}} \tag{2.13}$$

Figures 2.12 and 2.13 shows uptake rates (amount adsorbed vs. time by a step change in the gas-phase concentration) obtained from Micromeritics Sorptometer while Table 2.4 gives a summary of calculated D/R^2 for pure component adsorbates on the studied sorbents at 298 K. The diffusion time constant is an important parameter in the design of adsorbers and it has been shown that a high D/R^2 yields sharp breakthroughs, as opposed to low D/R^2 which leads to dispersed breakthroughs [1, 37] which in turn, defines the capacity of the sorbent.

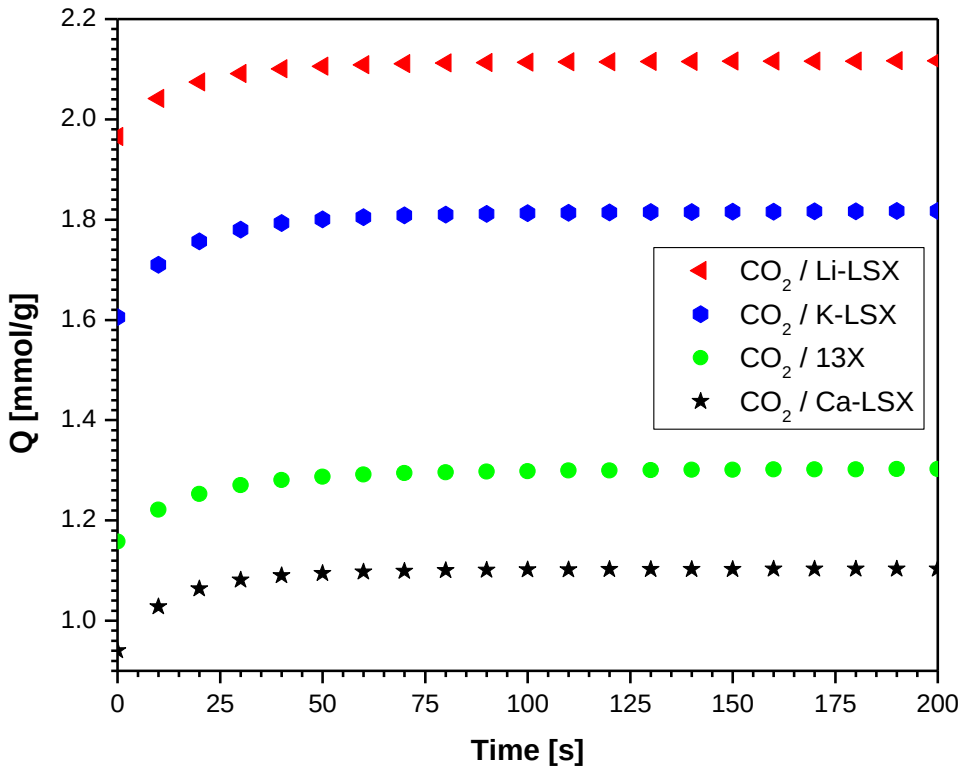

Figure 2.12 Experimental rates of adsorption (ROA) of CO_2 on Li-LSX, 13 X, K-LSX, and Ca-LSX zeolites.

It can be seen from Table 2.4 that the CO_2 uptake rates follows the following trend: (Li-LSX > K-LSX > 13X > Ca-LSX) which are in accordance with diffusion of CO_2 in type X zeolites [38]. On the other hand, CH_4 diffusion time constants were as follows: Ca-LSX > Li-LSX > K-LSX > 13X. It is also seen that the rate of adsorption of both sorbates on Li-LSX are significantly higher than those of 13X which is still the most widely used sorbent in TSA. The uptake rates are high for applications in air prepurification.

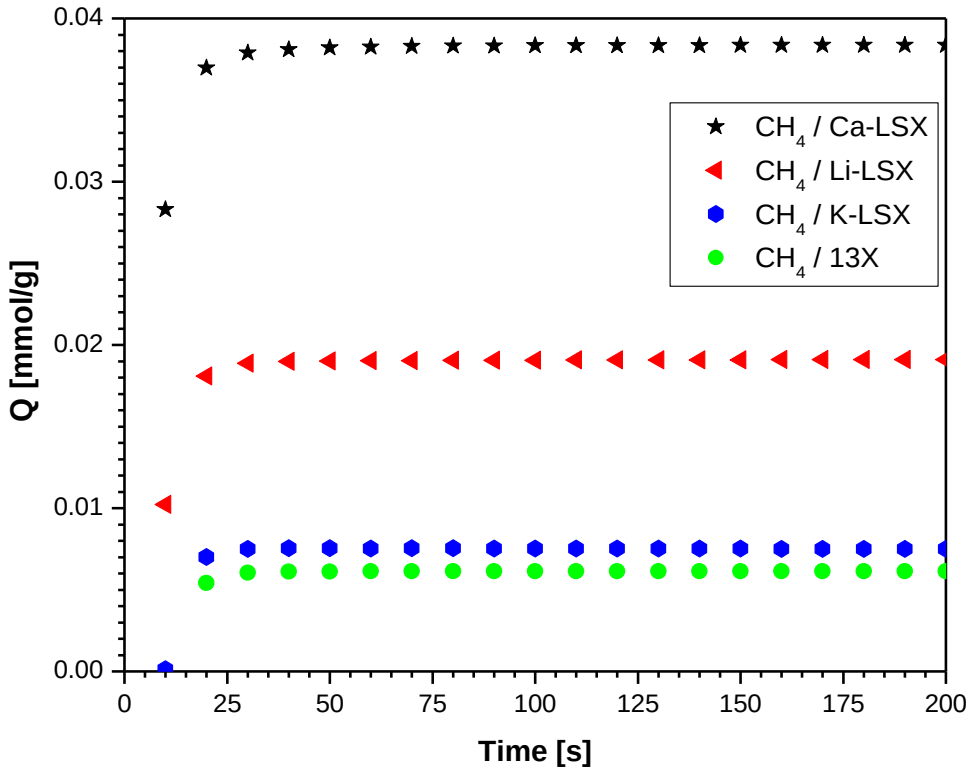

Figure 2.13 Experimental rates of adsorption (ROA) of CH_4 on Li-LSX, 13 X, K-LSX, and Ca-LSX zeolites.

Table 2.4 Inverse Diffusion Time Constants (D/R^2) for sorbates on Various Sorbents at 298 K.

	D/R^2 (1×10^{-2} s^{-1})			
	JLOX-100	**13X-APG**	**K-LSX**	**Ca-LSX**
CO_2	3.00	2.91	2.93	2.19
CH_4	4.42	2.67	3.65	5.30

2.4 Conclusion

Low pressure adsorption analysis for CO_2, CH_4, and H_2O vapor were studied at 298 K, 323 K, and 343 K on synthetic zeolites 13X and Li-LSX (both from Luoyang Jianlong Micro-Nano New Materials Co., Ltd., binderless or powder forms) as well as ion-exchanged K-LSX and Ca-LSX. The experimental data were fitted with the Langmuir-Freundlich, Tòth, and the Dubinin-Astakhov models and it was observed that the Tòth model comparatively fitted the data best in a wider range.

It is shown that the capacity and uptake rates of CO_2 and CH_4 on Li-LSX in the low-pressure range were higher than that of the widely used sorbent (13X) for air prepurification applications. This can further be interpreted that a bed of Li-LSX similar to that of 13X would significantly increase the air processing capacity, reduce the sorbent's regeneration time, and better performance for air prepurification applications. The experimental results can be satisfactorily understood based on simple theoretical calculations of interaction potential energies assuming sorbate-sorbent interactions with free cations and information on cation sites.

2.5 References

[1] R. T. Yang, Gas Separation by Adsorption Processes. London: Imperial College Press. 1997.

[2] S. U. Rege, R. T. Yang, M. A. Buzanowski, Sorbents for Air Prepurification in Air Separation. Chem. Eng. Sci. 55 (2000) 4827-4838.

[3] W. Schmidt, K. Kovak, W. Licht, S. Feldman, Managing Trace Contaminants in Cryogenic Air Separation, AIChE Spring Meeting, 2000.

[4] S. U. Rege, R. T. Yang, K. Qian, M. A. Buzanowski, Air-Prepurification by Pressure Swing Adsorption Using Single/Layered Beds. Chem. Eng. Sci. 56 (2001) 2745-2759.

[5] M. W. Ackley, R. F. Giese, R. T. Yang, Clinoptilolite: Untapped potential for kinetic gas separations. Zeolites. 12 (1992) 780-788.

[6] C. G. Coe, T. R. Gaffney, Process for the purification of bulk gases using chabazite adsorbents. US Patent 4,943,304 1990.

[7] C. G. Coe, D. A. Roberts, Process for the purification of permanent gases using chabazite adsorbents. US Patent 4,732,584 1988.

[8] L. Czepirski, E. K. Czepirska, G. Cacciola, Adsorption equilibria and kinetics of water vapour on modified chabazite. Adsorption Science and Technology. 14 (1996) 83-88.

[9] J. L. Stakebake, J. Fritz, Characterization of natural chabazite and SA synthetic zeolites. Part II: Adsorption properties and porosity. J. Colloid Interf. Sci. 100 (1984) 33-40.

[10] F. H. Tezel, G. Aplonatos, Chromatographic study of adsorption for N_2, CO and CH_4 in molecular sieve zeolites. Gas Separation & Purification. 7 (1993) 11-17.

[11] C. H. Chang, G. T. Stonesifer, R. J. Cusick, J. M. Hart, Comparison of metal oxide adsorbents for regenerative carbon dioxide and water vapor removal for advanced portable life support systems. Space Station and Advanced EVA: SAE Special Publications. 872 (1991) 1-10.

[12] Engelhard Corporation. Purification Technologies Brochure, 2001.

[13] C. A. Grande, R. Blom, Cryogenic Adsorption of Methane and Carbon Dioxide on Zeolites 4A and 13X. Energy Fuels. 28 (2014) 6688-6693, DOI: 10.1021/ef501814x.

[14] T. He, Q. Li, Y. Ju, Adsorption and Desorption Experimental Study of Carbon Dioxide/Methane Mixture Gas on 13X-type Molecular Sieves. Journal of Chem. Eng. Japan, 46 (2013) 811-820.

[15] D. Ko, R. Siriwardane, L. T. Biegler, Optimization of Pressure Swing Adsorption Process Using Zeolite 13X for CO_2 Sequestration. Ind. Eng. Chem. Res. 42 (2003) 339-348.

[16] S. Cavenati, C. A. Grande, A. E. Rodrigues, Adsorption Equilibrium of Methane, Carbon Dioxide, and Nitrogen on Zeolite 13X at High Pressures. J. Chem. Eng. Data. 49 (2004) 1095−1101.

[17] J. S. Lee, J. H. Kim, J. T. Kim, J. K. Suh, J. M. Lee, C. H. Lee, Adsorption Equilibria of CO_2 on Zeolite 13X and Zeolite X/Activated Carbon Composite. J. Chem. Eng. Data. 47 (2002) 1237−1242.

[18] K. F. Loughlin, M. A. Hasanain, H. B. Abdul-Rehman, Quaternary, Ternary, Binary and Pure Component Sorption on Zeolites. 2. Light Alkanes on Linde 5A and 13X Zeolites at Moderate to High Pressures. Ind. Eng. Chem. Res. 29 (1990) 1535−1549.

[19] D. Saha, Z. Bao, F. Jia, S. Deng, Adsorption of CO_2, CH_4, N_2O, and N_2 on MOF-5, MOF-177, and Zeolite 5A, Environ. Sci. Technol. 44 (2010) 1820-1826, DOI: 10.1021/es9032309.

[20] Y. Wang, M. D. LeVan, Adsorption Equilibrium of Carbon Dioxide and Water Vapor on Zeolites 5A and13X and Silica Gel: Pure Components. J. Chem. Eng. Data. 54 (2009) 2839−2844.

[21] J. A. C. Silva, K. Schumann, A. E. Rodrigues, Sorption and Kinetics of CO_2 and CH_4 in binderless beads of 13X zeolite. Microp. Mesop. Mater. 158 (2012) 219–228.

[22] R. V. Siriwardane, M. S. Shen, E. P. Fisher, J. A. Poston, Adsorption of CO_2 on molecular sieves and activated carbon. Energy and Fuels. 15 (2001) 279–284.

[23] R. T. Yang, Adsorbents: Fundamentals and Applications, Wiley: Hoboken, NJ. (2003) 8-371.

[24] G. Horvath, K. Kawazoe, Method for the calculation of effective pore size distribution in molecular sieve carbon. Journal of Chemical Engineering of Japan. 16 (1983) 470–475.

[25] S. U. Rege, R. T. Yang, Corrected Horvath-Kawazoe equations for pore-size distribution. AICHE Journal 46 (2000) 734-750.

[26] A. Saito, H. C. Foley, Curvature and parametric sensitivity in models for adsorption in micropores. AIChE Journal 37 (1991) 429-436.

[27] L. S. Cheng, R. T. Yang, Improved Horvath-Kawazoe equations including spherical pore models for calculating micropore size distribution. Chem. Eng. Sci. 49 (1994) 2599–2609.

[28] R. M. Hardeveld, M. J. Groeneveld, J. Y. Lehman, D. C. Bull, Investigation of an Air Separation Unit Explosion, Journal of Loss Prevention in the Process Industries. 14 (2001) 167-180.

[29] C. McKinley, F. Himmelberger, Oxygen Plant Safety Principals, Chemical Engineering Progress. 53 (1957) 112-121.

[30] F. O. Mertens, Determination of absolute adsorption in highly ordered porous media, Surf. Sci. 603 (2009) 1979-1984.

[31] J. Purewal, D. Liu, A. Sudik, M. Veenstra, J. Yang, S. Maurer, U. Müller, D. J. Siegel, Improved hydrogen storage and thermal conductivity in high-density MOF-5 composites, J. Phys. Chem. 116 (2012) 20199-20212.

[32] D. R. Lide, CRC Handbook of Chemistry and Physics, Internet Version ed., 2005.

[33] S. Sircar, Separation of Methane and Carbon Dioxide Gas Mixtures by Pressure Swing Adsorption. Sep. Sci. Technol. 23 (1988) 519-529.

[34] K. E. Maly, E. Gagnon, J. D. Wuest, Engineering molecular crystals with abnormally weak cohesion, Chem. Commun. 47 (2011) 5163-5165.

[35] H. S. Carslaw, J. C. Jaeger, Conduction of Heat in Solids, Second ed., Oxford Clarendon Press, Oxford University Press. Oxford, UK. 1959.

[36] Z. Zhao, X. Cui, J. Ma, R. Li, Adsorption of Carbon Dioxide on Alkali-Modified Zeolite 13X Adsorbents. Int. J. of Greenhouse Gas Control. 1 (2007) 355-359. DOI: 10.1016/S1750-5836(07)00072-2.

[37] N. R. Stuckert, R. T. Yang, CO_2 Capture from the Atmosphere and Simultaneous Concentration using Zeolites and Amine-Grafted SBA-15. Environ. Sci. Technol. 45 (2011) 10257-10264, DOI: 10.1021/es202647a.

[38] R. T. Maurer, Apparent surface diffusion effects for carbon dioxide/air and carbon dioxide/nitrogen mixtures with pelleted zeolite beds. In Adsorption and Ion Exchange with Synthetic Zeolites. American Chemical Society. 135 (1980) 73-104, **DOI:** 10.1021/bk-1980-0135.ch004.

Chapter 3

Mixed-Cation LiCa-LSX Zeolite with Minimum Lithium for Air Separation

Abstract

The aim of this work was to reduce/minimize Li in Li-LSX by replacing the 70% Li^+ cations in Li-LSX that are bonded to the interior or inaccessible sites which are not used for adsorption. Thus, mixed-cation LiCa-LSX containing minimum lithium were prepared by exchanging small fractions of Li^+ into Ca-LSX, followed by dehydration under mild conditions to avoid migration/equilibration of Li^+ cations. Comparisons of adsorption isotherms of N_2/O_2 and heats of adsorption for the LiCa-LSX samples with that for pure-cation Li-LSX and Ca-LSX provided strong evidence that significant amounts of these Li^+ cations indeed remained on the exposed sites (SIII). The mixed-cation LiCa-LSX samples were compared against the pure-cation Ca-LSX and Li-LSX based on their performance for oxygen production by PSA, via model simulation. The results showed that the mixed-cation LiCa-LSX samples yielded significantly higher O_2 product productivities at the same product purity and recovery than their pure-cation precursor (Ca-LSX).

3.1 Introduction

The demand for oxygen and nitrogen spans over a wide range of industries including oil refining, medical, metal production, food processing, and chemicals to name a few. Cryogenic distillation of liquefied air and pressure swing adsorption (PSA) are the two major technologies for high and low-to-medium volume productions, respectively [1].

Air separation by adsorption is based on the unique adsorption property of zeolites which have high N_2/O_2 selectivities due to the interactions between the electric field gradient of the zeolitic cation and the quadrupole moment of N_2 [2]. Commercial PSA oxygen production began in 1972. A major breakthrough occurred in 1989 with the invention of Li-LSX (i.e., low silica type-X, Si/Al = 1) zeolite by Chao [3]. In the preparation of Li-LSX, the as-synthesized Na-LSX is ion-exchanged by Li cations via conventional means. It was found that below approximately 70% Li exchange, the N_2 capacity was unchanged, while it increased nearly linearly upon further increase in Li exchange from 70% to 100%. This phenomenon has been explained by the occupancy of different cation sites; the N_2 (and O_2) molecules can interact only with cations occupying the exposed sites. The cation sites for faujasite are shown in Figure 3.1. For Li-X, only sites III (SIII) are accessible to N_2 (and O_2); Li^+ on SII is not "accessible" due to electron shielding effects by the surrounding framework oxygen and the small size of the Li ion.

The site occupancies have been characterized [4-6] and are shown in Table 3.1. It is noted that, after ion exchange, zeolites need to be thermally dehydrated prior to isotherm measurements (and during manufacturing), typically at above 673 K for 4 or more hours. Under such treatment, cations migrate or diffuse to their equilibrium positions or sites. For zeolites containing mixed cations, it has long been observed that the lighter cations tend to migrate to the lower numbered

sites (SI, SI', SII", SII). For example, in mixed CeNaCa-X zeolite, Na and Ca are at lower-numbered sites while

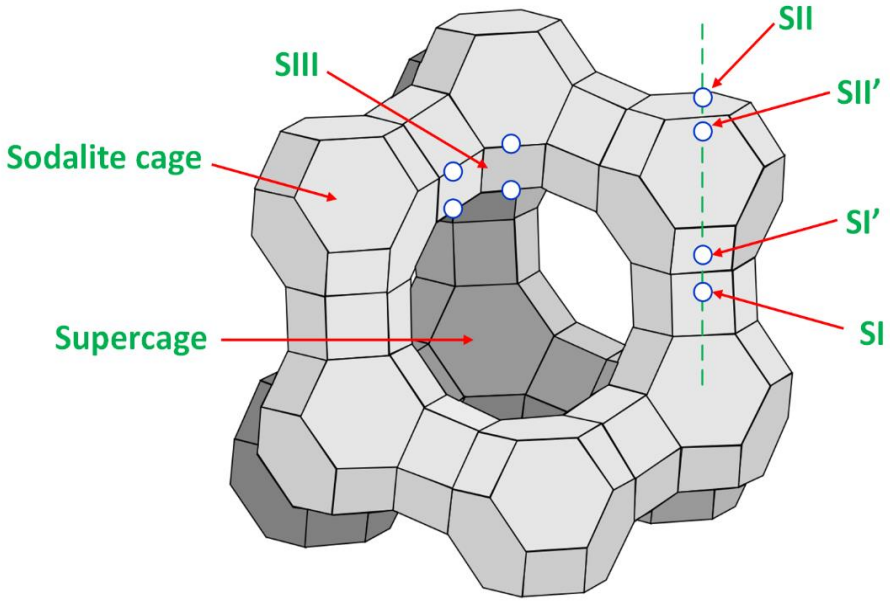

Figure 3.1 Unit cell of faujasite-type (X and Y) zeolites, including cation sites.

Ce(III) cations are located at outer sites, and in mixed NaSr-X zeolite, Na^{+} is at SI while Sr^{2+} is at SII [7]. This ordering is also seen in the mixed LiNa-LSX system discussed above.

As mentioned, since its invention Li-LSX has been the sorbent of choice for air separation by PSA or Vacuum Swing Adsorption (VSA). A wide variety of other zeolites have also been considered, particularly the LSX zeolites containing alkali-earth metal cations. These cations are divalent and hence they form strong electrostatic interactions with N_2 molecules (as well as O_2). Thus, intense interests were attracted to the mixed-cation LSX zeolites containing Li and an alkali-earth metal. [8-13] Coe et al. [8-11] studied various binary exchanged X-zeolites containing varying lithium-calcium and lithium-strontium mixtures all of which provided enhanced nitrogen sorption capacities over those of the pure samples. Sircar et al. [12], also showed a binary ion-

exchanged Type-X zeolite of calcium and strontium. Their invention was especially useful in the adsorption of N_2 from an air stream at superambient pressure to produce an O_2-rich product stream. Furthermore, Chao et al. [13] presented mixed ion-exchanged zeolites of type-A and type-X with lithium (30% - 90%) and alkaline earth metals (10% - 70%) such as Ca^{2+} and Sr^{2+}, with high N_2 adsorption capacity. It is important to note that these mixed cation zeolites required over 70 mol% Li^+ (and < 30 mol% alkali-earth cation). Typically, 90% Li^+ was required. Moreover, it was necessary to ion exchange Li^+ first, followed by exchange for the alkali earth cations. Of particular interest was the Ca-LSX zeolite [14] due to its high N_2 capacities over that of Li-LSX. Thus, for mixed-cation LiCa-LSX, it was specifically stated that fully exchanged Li-LSX was prepared first, followed by Ca^{2+} exchange [8, 10, 13]. In all cases, well over 70% Li^+ was needed to see the effect of Li^+.

Table 3.1 Cation site occupancies in dehydrated X zeolites (maximum = 96 monovalent cations per unit cell for Si/Al = 1).

Zeolite	**Al/unit cell**	**Sites**				
		I	**I'**	**II**	**II'**	**III**
Li-LSX [24]	95.8	--	27.2	33.9	--	32.4
Li-LSX [25]	96	--	33	34	--	29
Na-X (13X) [26]	81	3.8	32.3	30.8	--	7.9
K-X [27]	87	9	13	26	--	38
Ca-X [28]	86	7.5	17.3	17.3	9.0	--

The demand for lithium has been rising steeply due to the application of lithium ion batteries for energy storage and due to its limited reserves worldwide. As a result, the price of lithium has been surging since 2016 while the reserve is dwindling. Therefore, the motivation for this work is to develop zeolites for air separation in which lithium is substantially reduced or

replaced by a low-cost and abundant alkali-earth metal cation, such as Ca^{2+}. Using LiCa-LSX as an example, our strategy is to first exchange as-synthesized Na-LSX to fully-exchanged Ca-LSX, followed by exchange of a small fraction of Ca^{2+} by Li^{+}. During the ion exchange process (in an aqueous solution such as $LiCl_2$) and prior to any heat treatment, it is reasonable to assume that these Li^{+} cations are located on SIII because they are the most accessible ion exchange sites and are hence exchanged first. Equally important, in this work the dehydration step is performed at the lowest possible temperature in a relatively short time to avoid diffusion and equilibration of Li^{+} ions to lower-number or interior sites.

In this work, we focused on four synthetic zeolites: two pure-cation zeolites (Ca-LSX and Li-LSX) and two mixed-cation zeolites (2.5%LiCa- and 4.2%LiCa-LSX, both in mol%) for the PSA/VSA system. The mixed cation samples will be represented as follows henceforth: 2.5% LiCa-LSX and 4.2% LiCa-LSX = $Li_{2.5}Ca_{46.75}$-LSX and $Li_{4.2}Ca_{45.9}$-LSX respectively. These zeolites will be compared for their PSA/VSA separation performance using a proven PSA model.

3.2 Experimental Section

3.2.1 Materials

The analysis gases obtained from Cryogenic Gases included: helium (99.995%, prepurified), nitrogen (99.998%, prepurified), and oxygen (99.6%, extra dry).

Luoyang Jianlong micro-Nano New materials Co., Ltd., China, supplied the Na-LSX zeolite (powder form) with a Na exchange extent of 99.5% (Na/(Na + K) and a Si/Al ratio of 1.005. Calcium dihydrate 99% and lithium chloride 99% were both obtained from Sigma Aldrich.

3.2.2 Preparation of Ca-LSX zeolite

Na-LSX zeolite was used as the starting sorbent for the ion-exchange procedure which could be readily exchanged with most cations. To obtain pure Ca-LSX zeolite, Na-LSX was ion-exchanged with a 1.0 M solution of calcium chloride (with ~3 equivalent excess of Ca^{2+} to Na^{+}) at ambient conditions and stirred for a minimum of 6 hrs. The solution was decanted and a 3X $CaCl_2$ solution was added, and the ion-exchange procedure was repeated 6 times. The sample was vacuum filtered after the final ion-exchange, washed with copious amounts of deionized water, and air dried at 298 K for 24 hrs. One of the main differences between this study and other published literature [8, 14] is the fact that here-in, Li ions are introduced into Ca-LSX as opposed to Ca cations being incorporated into Li-LSX zeolite.

3.2.3 Preparation of LiCa-LSX

A pre-determined equivalent amount of Li^{+} enough to exchange the desired target Ca^{2+} in the Ca-LSX zeolite (assuming hypothetically that all Li^{+} would undergo exchange) was used to prepare the mixed cation samples. This was achieved by using a 0.1 M LiCl solution exchanged with 1.5 g of Ca-LSX with Li^{+} equivalent = 0.15 and 0.3. The mixture was stirred for 1 hr at 298 K followed by vacuum filtration without washing and dried in an oven for 24 hrs at 298 K. It should be noted that, due to the preference of LSX for Ca^{2+} over Li^{+}, the actual Li^{+} exchange was substantially less than the amount of Li^{+} in the liquid phase, as determined by ICP results.

3.2.4 Sample pretreatment and isotherm measurements

All pure gas adsorption equilibrium analysis on the studied pure and mixed ion-exchanged samples were carried out with a Micromeritics ASAP 2020 Sorptometer which uses the volumetric measurement technique. Prior to analysis, all samples were degassed/dehydrated in-situ the Micromeritics to remove all adsorbed moisture and/or adsorbed gasses.

The pretreatment conditions varied per sample and were as follows: 8 hrs at 648 K and 623 K for Li-LSX and Ca-LSX respectively. 1 hr at 623 K for $Li_{2.5}Ca_{46.75}$-LSX and $Li_{4.2}Ca_{45.9}$-LSX while the ramp rate for all dehydration conditions was 283 K/min. The 1 hr at 623 K pretreatment condition allows most of the theoretically determined Li^+ to remain on site III while not allowing adequate time for all Li^+ cations to diffuse to the lower-numbered sites (SI and SII). The temperature of 623 K was determined to be the lowest temperature that was adequate for full dehydration of Li-LSX [15]. In the work of Hutson et al., residual water amounts and N_2 isotherms were measured on Li-LSX after dehydration at various temperatures up to 723 K, and full dehydration was seen after dehydration at 623 K [15]. All studied samples were pretreated under vacuum: 30 μmHg for the pure samples and 60 μmHg (due to the short pretreatment time) for the mixed samples.

3.2.5 Sample Characterization

The samples were compositionally characterized using an ICP-OES (Inductively Coupled Plasma – Optical Emission Spectrometer) system at Galbraith Laboratories Inc. in Knoxville, Tennessee. ICP is an analytical technique that quantifies the elemental composition of samples in various states (e.g. powders, liquids, suspensions, etc.). Powders are usually digested by an acid (highly concentrated HNO_3, HCl, or H_2SO_4) or a combination of acids with the resulting solution then nebulized into the core of the instrument's inductively coupled argon plasma at elevated temperatures. The high temperature vaporizes, ionizes and thermally excites the analyte species in the solution which are then detected and quantified by the OES by measuring (in % or ppm concentration) the element's characteristic wavelength from the intensity of the emitted radiation.

3.3 Results and Discussion

3.3.1 Analytical sample characterization

As mentioned above, the mixed ion-exchanged samples were compositionally analyzed and quantified for Li and Ca content using an Inductively Coupled Plasma – Optical Emission Spectroscopy (ICP-OES) system. The extent of the Li^+ exchange obtained from the mixed ion-exchanged samples by ICP were 2.5%Li and 4.2%Li (mole percent and on a dry basis) represented as $Li_{2.5}Ca_{46.75}$-LSX and $Li_{4.2}Ca_{45.9}$-LSX respectively. The results of the analyzed LSX sample are presented in Table 3.2.

Table 3.2 Composition of various represented sorbents.

Zeolite	**Mole Ratio**			
	Si/Al	Li/Al	Ca/Al	Na/Al
Na-LSX	1.005	--	--	0.995
Ca-LSX	1.005	--	0.991	--
$Li_{2.5}Ca_{46.75}$-LSX	1.005	0.025	0.467	--
$Li_{4.2}Ca_{45.9}$-LSX	1.005	0.042	0.459	--

3.3.2 Nitrogen adsorption isotherms

As stated earlier, the volumetric technique was used to measure the equilibrium N_2 adsorbed amounts to pressures of 1 atm. N_2 experimental adsorption isotherms on the studied sorbents at temperatures 298 K, 323 K and 343 K after *in vacuo* dehydration are shown in Figures 3.2 - 3.4 respectively.

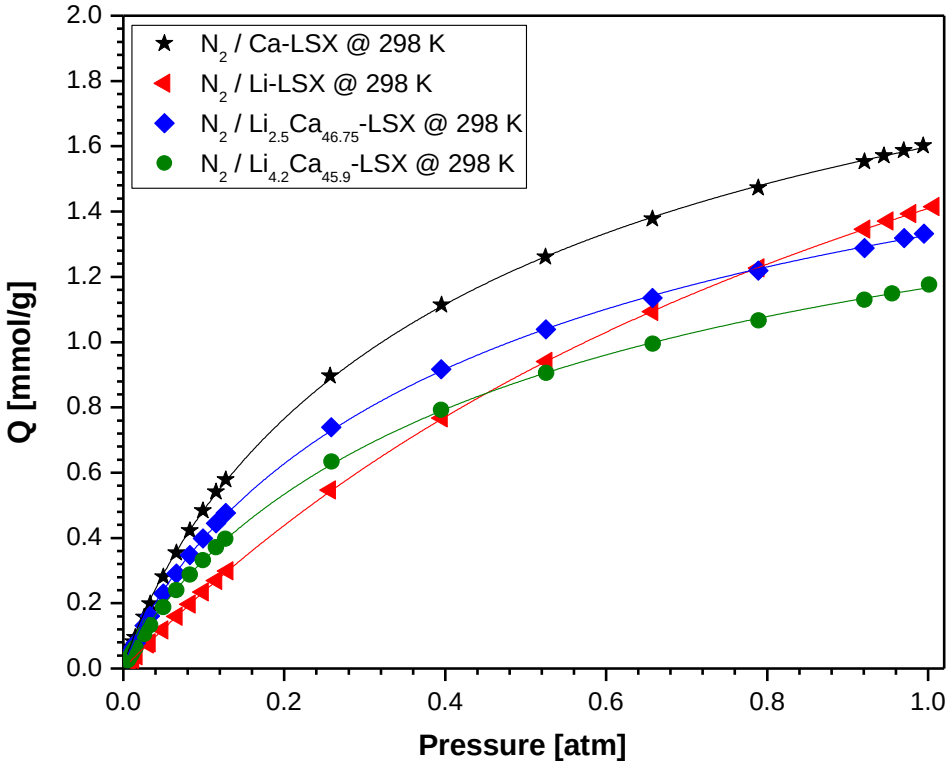

Figure 3.2 Experimental adsorption isotherms of N_2 at 298 K and 101 kPa on representative sorbents.

Upon inspection, Ca-LSX shows the highest N_2 adsorption capacity followed by $Li_{2.5}Ca_{46.75}$-LSX and $Li_{4.2}Ca_{45.9}$-LSX at ambient conditions respectively. The pure Ca-LSX sample shows a high capacity for N_2 at 298 K in comparison with other published data [2, 8]. Figure 3.2 (N_2 isotherms at 298 K and 101 kPa) also reveals that the introduction of such low Li amounts changes the adsorptive properties (low pressure knee of the pure zeolite) of the mixed cation zeolite. The sorbents' high N_2 capacities are attractive properties for air separation by PSA.

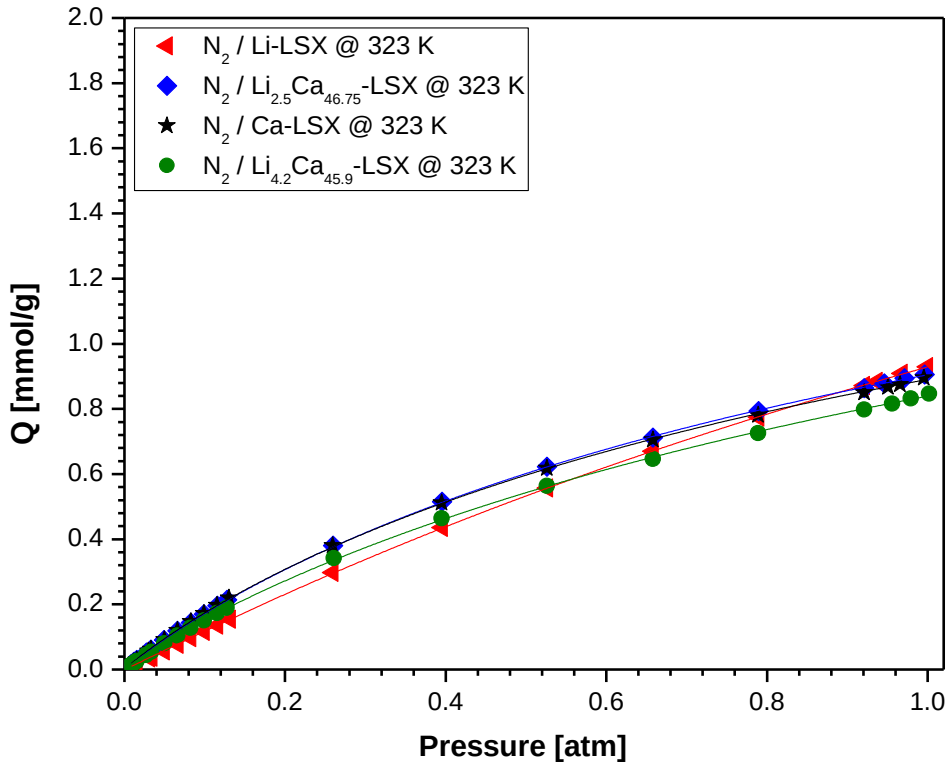

Figure 3.3 Experimental adsorption isotherms of N_2 at 323 K and 101 kPa on representative sorbents.

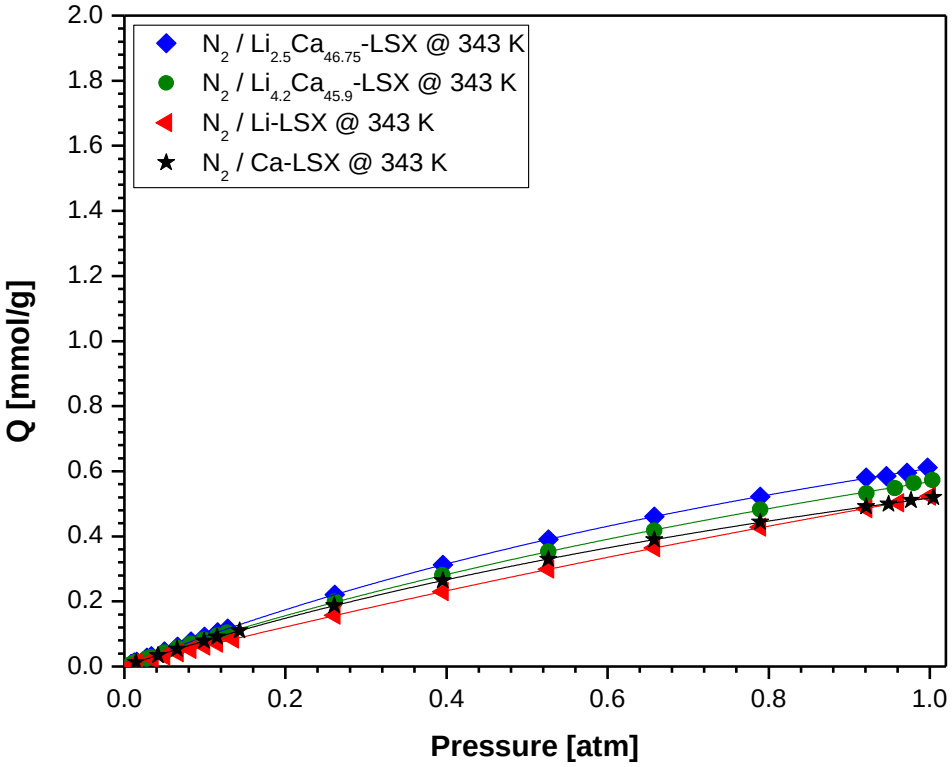

Figure 3.4 Experimental adsorption isotherms of N_2 at 343 K and 101 kPa on representative sorbents.

3.3.3 Oxygen adsorption isotherms

Figures 3.5 – 3.7 show O_2 experimental adsorption isotherms on the studied sorbents at 298 K, 323 K, and 343 K respectively. A comparison of the different sorbents shows that Ca-LSX adsorbed significantly more oxygen than Li-LSX (slightly above 60%), and the mixed cation LSX fell in between.

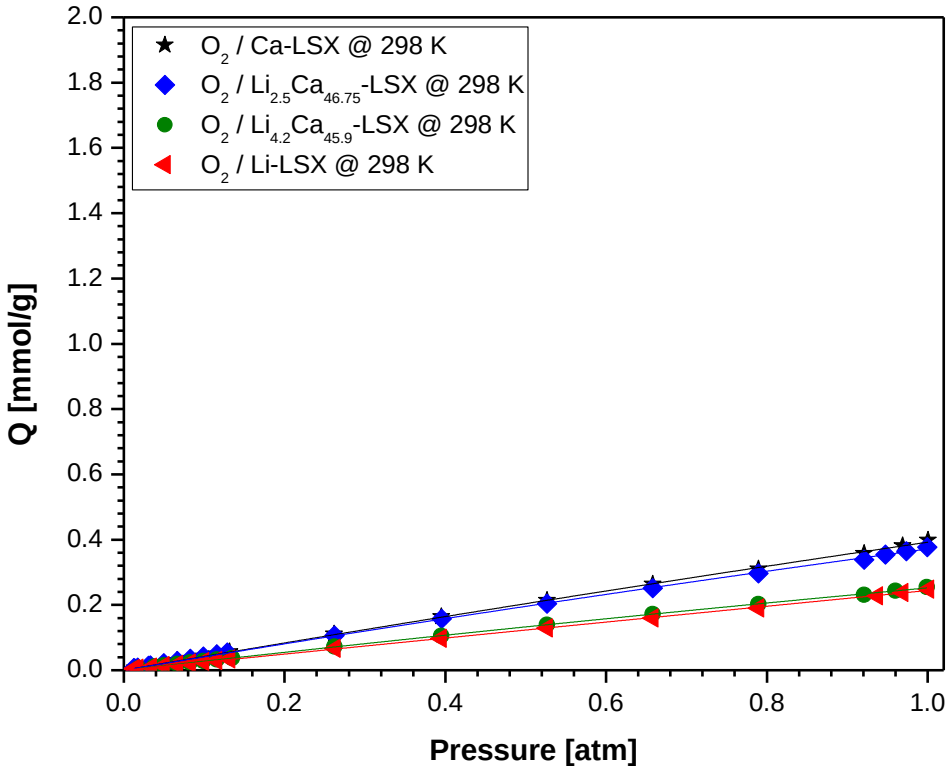

Figure 3.5 Experimental adsorption isotherms of O_2 at 298 K and 101 kPa on representative sorbents.

This result is expected because Ca^{2+} has higher polarizability than Li^+ and the van der Waals interactions were the main interactions for adsorption of O_2 which has a very low quadrupole moment. The lower O_2 capacities for the mixed cation LSX are favorable for PSA separation. This result also indicates the presence of some Li^+ cations on SIII in the mixed-cation samples.

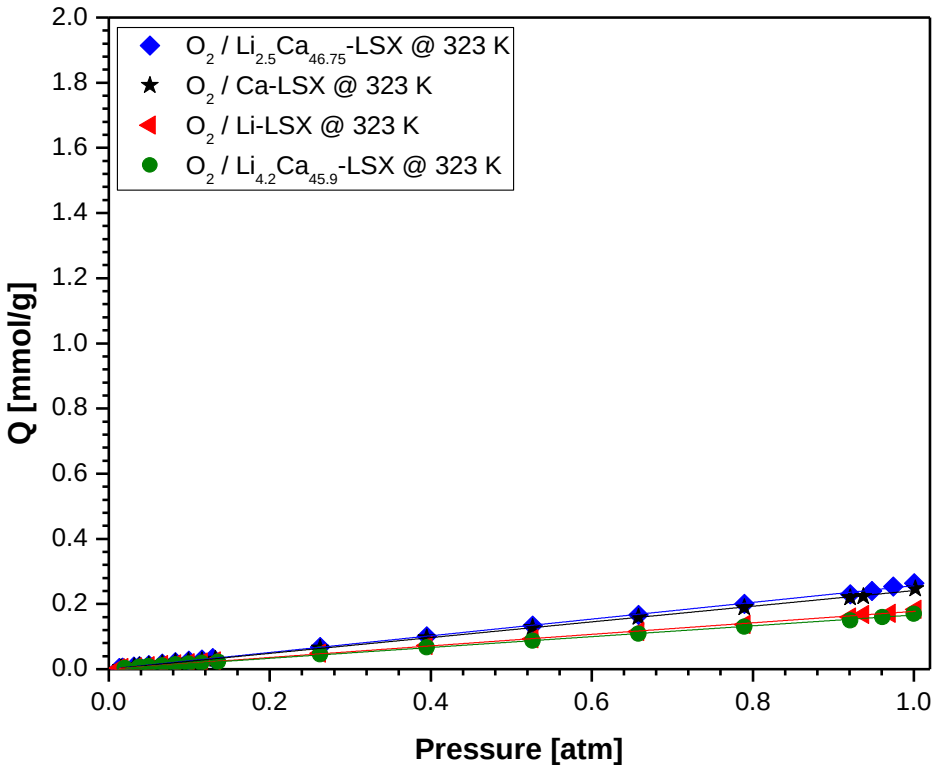

Figure 3.6 Experimental adsorption isotherms of O_2 at 323 K and 101 kPa on representative sorbents.

It should be noted that the differences in adsorption capacities of both gases on the studied sorbents are due to the magnitude of interactions between the Ca^{2+}, Li^{+} and the sorbates which in turn are due to the location of the cations within the zeolite's framework. Figure 3.1 shows the 5 different cation sites in the faujasite-type (X and Y) zeolites. It should be noted that only sites II and III (SII and SIII) are accessible to the sorbate while SI (inside the double ring) and SII' (within the beta cage) are inaccessible to the sorbate molecule. As mentioned, the electric field around the cations in the exposed sites are however, partially shielded (cation size dependent) by the surrounding oxygen atoms thereby significantly lowering the interactions between the sorbate molecule and the SII cations.

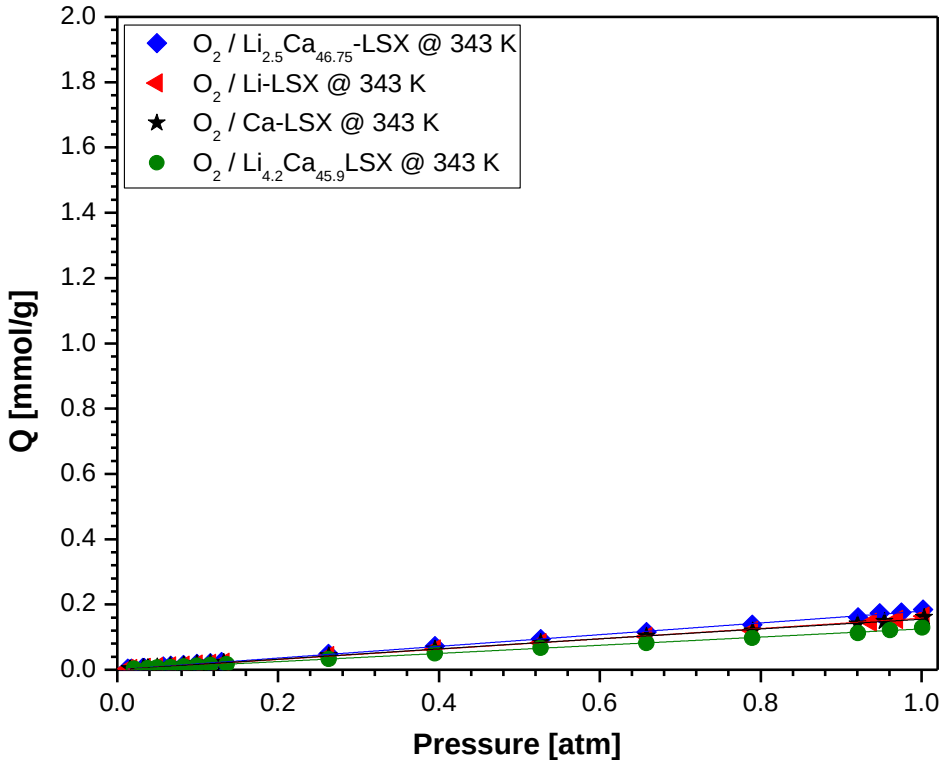

Figure 3.7 Experimental adsorption isotherms of O_2 at 343 K and 101 kPa on representative sorbents.

For example, the small Li cation can sit crystallographically very low within the face of the single 6-ring (SII), allowing the electric field to be nearly completely shielded by the six surrounding framework oxygen atoms thereby allowing the sorbate-sorbent energy to be entirely contributed by the Li cation sitting on SIII [2]. For a larger cation like Ca, its shielding can be substantially weaker due to its size.

3.3.4 Pure component isotherms

The equilibrium adsorption isotherms of N_2 and O_2 on the various sorbents in this study were fitted with the Langmuir-Freundlich (L-F) isotherm model. Figures 3.2 – 3.7 show just a few of the experimentally obtained isotherms. All others could be found in the supplementary material.

The temperature dependence of the isotherms allowed calculation for the isosteric heats of adsorption, as to be discussed further below.

$$Q = \frac{Q^*_{sat} K C^n}{1 + K C^n} \tag{3.1}$$

where Q is the adsorbed amount with the rest being fitting constants from experimental data. A fitting model is usually required to interpolate the measured values. Also, the interpolation of the said data is quite sensitive to the choice of the fitting model and minute deviations from the true value can cause significant errors in thermodynamic calculations [16, 19].

3.3.5 Heats of adsorption

At near ambient temperature, there is a negligible (3RT/2) difference between the sorbate-sorbent interaction energy and the experimental heats of adsorption [2]. For a basic understanding of the experimental results, the sorbate-sorbent interaction energies for the gas-sorbent pairs could be estimated by calculating the potential energies between the gas molecule and a free or isolated cation such as Ca^{2+}, Li^{+}, etc. A breakdown of the theoretical total sorbate-sorbent potential (ϕ_T) for physical adsorption is shown in our previous work [20]. It is worth noting that for the adsorption of gas molecules on zeolites, the main interaction energies are between the gas molecules and the metal cations on its surface. Though interaction energies between the gas molecules and the oxide atoms on the surface also exists, they are significantly weaker than those formed with the cations.

Here-in, the isosteric heats of adsorption of the gas-sorbent pairings were estimated by the application of the Clausius-Clapeyron relation [17, 18, 21] as shown below:

$$\ln\left(\frac{P_1}{P_2}\right) = \frac{\Delta H_{vap}}{R}\left(\frac{1}{T_2} - \frac{1}{T_1}\right) \tag{3.2}$$

where ΔH_{vap} is the heat of adsorption, R is the gas constant (8.3145 J/mol K), while P_1 and P_2 are the corresponding pressures at temperatures T_1 and T_2. Such calculations are very sensitive to errors in the equilibrium pressure. This means that interpolations can sometimes introduce significant uncertainties into the calculated isosteric heat determined by using fitted experimental data.

Figures 3.8 and 3.9 shows the isosteric heats of adsorption for N_2 and O_2 on various representative sorbents at different coverages. The N_2 experimental heats of adsorption followed the order: Ca-LSX > $Li_{2.5}Ca_{46.75}$-LSX > $Li_{4.2}Ca_{45.9}$-LSX > Li-LSX > Na-LSX.

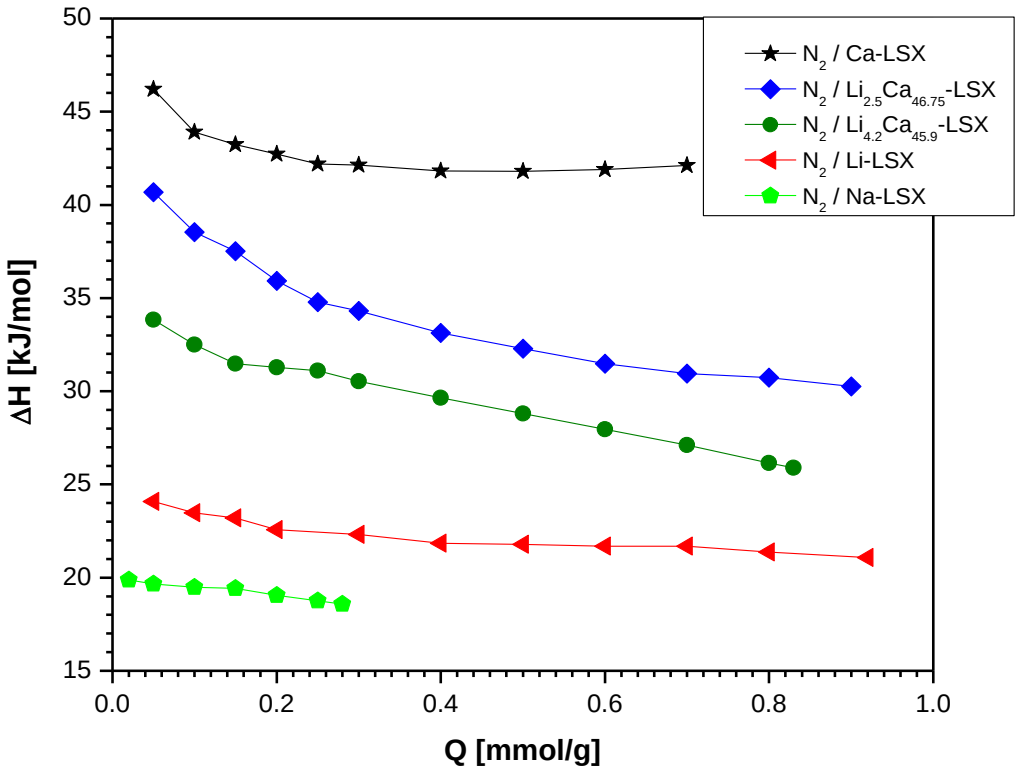

Figure 3.8 N_2 Heats of Adsorption on various sorbents.

The interaction energies for N_2 are mainly from the electrostatic energies. The interactions of N_2 with Ca^{2+} are significantly stronger than that with Li^+. This is caused mainly by the higher

electric charge of Ca^{2+} that doubles the charge of Li^{+}, while the ionic radii are similar (0.69 Å for Li^{+} and 1.0 Å for Ca^{2+}).

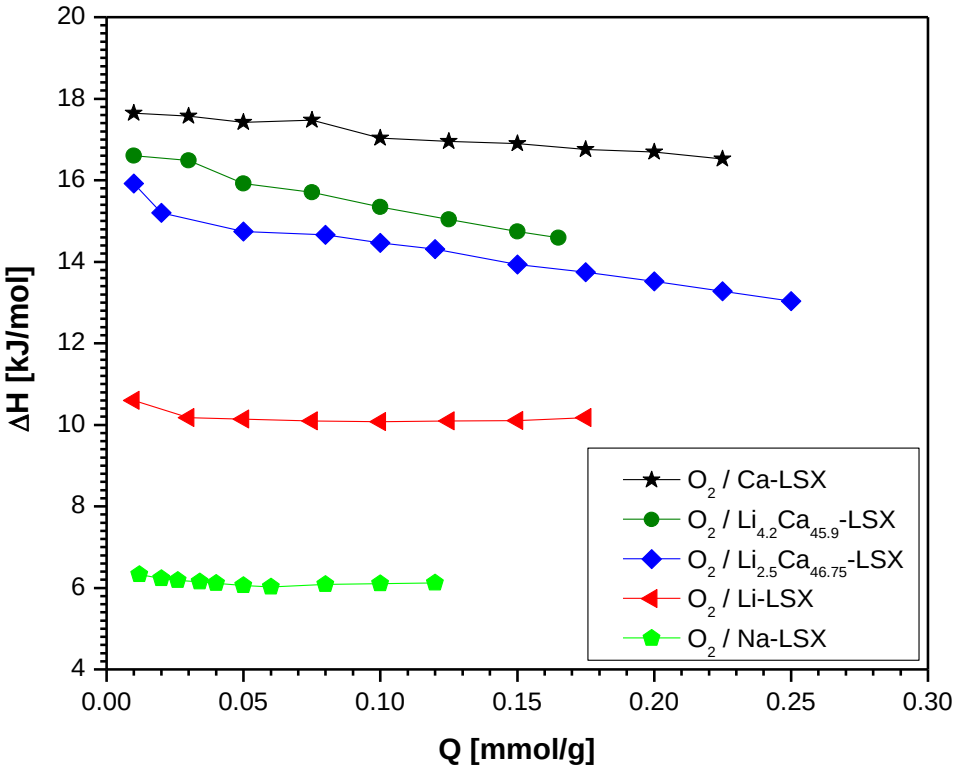

Figure 3.9 O_2 Heats of Adsorption on various sorbents.

An almost similar trend is observed for the O_2 experimental heats of adsorption Ca-LSX > $Li_{4.2}Ca_{45.9}$-LSX > $Li_{2.5}Ca_{46.75}$-LSX > Li-LSX > Na-LSX. As discussed in the foregoing, this trend was caused by the fact that Ca^{2+} has a higher polarizability than Li^{+} and the van der Waals interactions were the main interactions for adsorption of O_2.

3.3.6 Cation Site Location

Table 3.1 shows the occupancy of cations in dehydrated X-type zeolites with pure cations. Several other studies have been employed to determine Li^{+} in the extra framework of types X, Y, and A zeolites [6, 22, 23] using solid state NMR and neutron diffraction methods. The Li cations

were found to be evenly distributed with 32 cations each in SI' (energetically preferred over SI for monovalent cations), SII, and SIII for the Li-LSX (Si/Al = 1) zeolite as opposed to 22 cations in SIII for the X-zeolite. Single Crystal XRD, Powder XRD, and Powder XRD & Neutron Diffraction have all been used to determine the location of Ca ions mostly in Ca-X zeolites. It was found that for a fully dehydrated Ca^{2+}-exchanged FAU-type zeolite, the calcium cations were distributed among sites SI, SI' and SII [24-36].

No Li^+ and Ca^{2+} location and site distribution studies were carried out in this study for the mixed-cation samples. Knowing that the SI and SI' sites are sterically inaccessible to the sorbate gases (N_2 and O_2), it is therefore expected that only the Ca cations in SII and Li^+ in SIII are accessible to the sorbates.

For N_2 adsorption, as expected, the heats of adsorption followed the order: Ca^{2+} (42 kJ/mol) > Li^+ (22 kJ/mol) > Na^+ (20 kJ/mol). It is most interesting that the ΔH values for the mixed LiCa-LSX samples fell between that of pure Ca-LSX and Li-LSX. This result was a strong indication that the N_2 molecules were interacting with both exposed Ca and exposed Li cations. Furthermore, the intermediacy of the ΔH value (between Ca^{2+} and Li^+) indicates that some N_2 molecules were interacting with (or shared by) both Ca^{2+} and Li^+ in possibly a bridged configuration.

Further work has been done in our laboratory on the relationship between SIII occupancy of Li^+ in mixed-cation LiNa-LSX zeolite and the heats of adsorption of N_2. It is shown that the N_2 heats of adsorption can indeed be used as an indicator of the presence of the lithium ions in SIII for mixed-cation zeolites (to be published).

3.3.7 PSA (or VPSA) cycle description

A standard, commercially used, five-step PSA (or vacuum pressure swing adsorption, VPSA) cycle similar to that described by Hutson et al. [37] was used in this study. The cycle configuration is shown in Figure 3.10 and the five steps are as follows: (step I) Pressurization with feed (air); (step II) High-pressure feed; (step III) Co-current depressurization; (step IV) Countercurrent blowdown; (step V) Low-pressure purge with the product. This standard PSA cycle and even more complicated cycles can be accomplished in a two-bed or four-bed systems with interconnections [38].

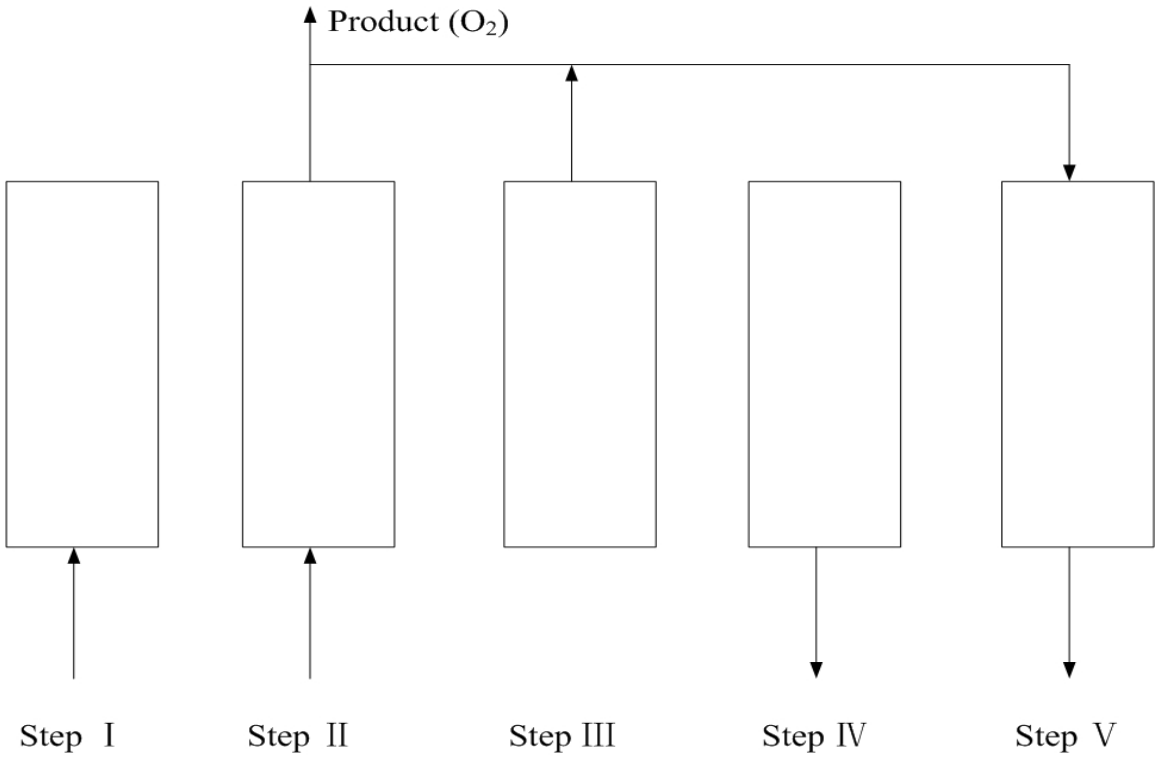

Figure 3.10 PSA cycle configuration.

Each of the above steps ran for a duration of 30 seconds, thus the time required for the complete cycle was 2.5 mins. The model assumed only two components (i.e. O_2 and N_2). Since Ar (Argon) and O_2 both have similar adsorption capacities on LSX zeolites, the oxygen component was assumed to be 22% (21% O_2 and 1% Ar) for the simulation. The product of each cycle was comprised of a volumetric mixture of the output stream from the feed step and the co-current depressurization step. A portion of this product stream was used to purge another bed countercurrently in step V.

The performance of PSA for oxygen production is judged by three inter-related results: O_2 product purity, O_2 product recovery, and O_2 product throughput. When two of these are fixed, the other is also set provided the PSA operating conditions are optimized. To compare the performance of the sorbents developed in this work, the product throughputs of the sorbent were studied under several different cycle conditions.

Similarly, to facilitate a fair comparison of each sorbent's performance, the cycle conditions were optimized such that the product purity and product recovery obtained were the same for all sorbents in each simulation run. The product purity, product recovery, and product throughput in this study are defined as follows:

$$\text{Product Purity} = \frac{\text{Amount of } O_2 \text{ from Steps II and III}}{\text{Amount of } N_2 \text{ and } O_2 \text{ from Steps II and III}} \tag{3.3}$$

$$\text{Product Recovery} = \frac{(O_2 \text{ from Steps II and III}) - (O_2 \text{ from Step VI})}{(O_2 \text{ fed in Steps I and II})} \tag{3.4}$$

$$\text{Product Throughput} = \frac{\text{Amount of } O_2 \text{ produced per hour } (t/h)}{\text{Amount of sorbent used in the bed } (t)} \tag{3.5}$$

The mathematical model and the numerical method used for the PSA simulations have been explained in detail in an earlier work by Rege et al. [39]. Hence, only the basic assumptions

are listed here. The model used assumes the flow of a gaseous mixture of two components in a fixed bed packed with spherical adsorbent particles. The bed was considered to be adiabatic and the diffusional resistance is assumed to be negligible since the diffusion of O_2 and N_2 in the sorbents is relatively fast considering the long cycle time. Thus, local equilibrium existed between the gas and the solid phase for each gas component. Axial dispersion for mass and heat transfer was accounted for but dispersion in the radial direction is taken to be negligible. Axial pressure drop was neglected, and ideal gas law was assumed to hold since pressures involved were near atmospheric. Also, the gas was assumed to have constant viscosity and heat capacity.

The pure component equilibrium amounts adsorbed on the respective adsorbents were fit using the well-known Langmuir-Freundlich isotherm with temperature-dependent constants. The equilibrium loading under mixture conditions were then predicted by the extended Langmuir-Freundlich equation in the simulation model:

$$q_k^* = \frac{q_{m_k} b_k p_k^{n_k}}{1+\sum_{j=1}^{m} b_k p_k^{n_k}} \quad k = 1,2 \tag{3.6}$$

The Langmuir-Freundlich parameters were assumed to be as follows:

$$q_m = k_1 e^{(k_2/T)} \quad and \quad b = k_3 e^{(k_4/T)}$$

The Extended Langmuir model is one of the simplest and most practical models for the prediction of binary gas adsorption behavior from pure component isotherms [40]. Using the extended Langmuir-Freundlich model for binary mixtures, similar to the use of the extended Langmuir model, is also a simple yet reasonably good way of fitting binary experimental data, as shown by Mulgundmath et al. [41].

Table 3.3 Temperature-Dependent parameters of Langmuir-Freundlich Isotherm of N_2 and O_2.

Sorbent	Sorbate	k_1 [mmol/g]	k_2 [K]	k_3 [atm^{-1}]	k_4 [K]	n	ΔH [kJ/mol]
Li-LSX	O_2	0.4798	636.6	0.00948	500	1.08168	9.17
Li-LSX	N_2	1.84559	139.68	2.19×10^{-4}	2484.2	1.033	21.79
Ca-LSX	O_2	0.01448	1385.97	0.12788	207.35	1.152	12
Ca-LSX	N_2	0.2623	646.75	6.88×10^{-6}	3785.11	0.931	43.39
$Li_{2.5}Ca_{46.75}$-LSX	O_2	1.89933	145.55	6.20294×10^{-4}	1609.13	1.021	15.63
$Li_{2.5}Ca_{46.75}$-LSX	N_2	1.31846	104.23	1.9726×10^{-5}	3489.63	0.958	31.47
$Li_{4.2}Ca_{45.9}$-LSX	O_2	2.20255	179.35	4.02105×10^{-4}	1525.38	0.992	15.09
$Li_{4.2}Ca_{45.9}$-LSX	N_2	0.98863	149.34	4.67445×10^{-5}	3243.35	0.999	28.72

The values of the Langmuir-Freundlich equation fitting constants and the heats of adsorption are shown in Table 3.3 while Table 3.4 shows the PSA bed characteristics and the operating conditions used.

Table 3.4 Adsorption Bed Characteristics and Operating Conditions for PSA Simulations.

Bed length	2.5 m
Diameter of sorbent	1.0 m
Bed external porosity	0.4
Bed density	720 kg/m^3
Heat capacity of gases	28.72 J/mol/K
Heat capacity of sorbent	1.17 kJ/kg/K
Ambient temperature	298 K
Feed gas temperature	298 K
Feed gas composition	78% N_2, 22% O_2
Axial dispersion coefficient (D_{ax})	5×10^{-5} m^2/s
Effective heat conductive	0.2 w/m/K

3.3.8 VPSA simulation results

The pressure ratio (ratio of the feed pressure P_H to the desorption pressure P_L) is an important operating parameter for PSA systems. In this study, the feed pressure of 120 kPa and 150 kPa with different pressure ratios were investigated and the same pressure ratios were employed for comparison of the studied sorbents.

A summary of the simulation conditions and separation results for the studied materials is given in Table S3.1 (Appendix B). The feed and purge velocities were optimized so as to obtain the same product purity (near 95%) and recovery (near 52%) for all sorbents. Thus, the VPSA performance was judged by the O_2 productivities. Figures 3.11 and 3.12, which are both extracted from Table S3.1, shows the effect of pressure ratio on productivity for all four sorbents.

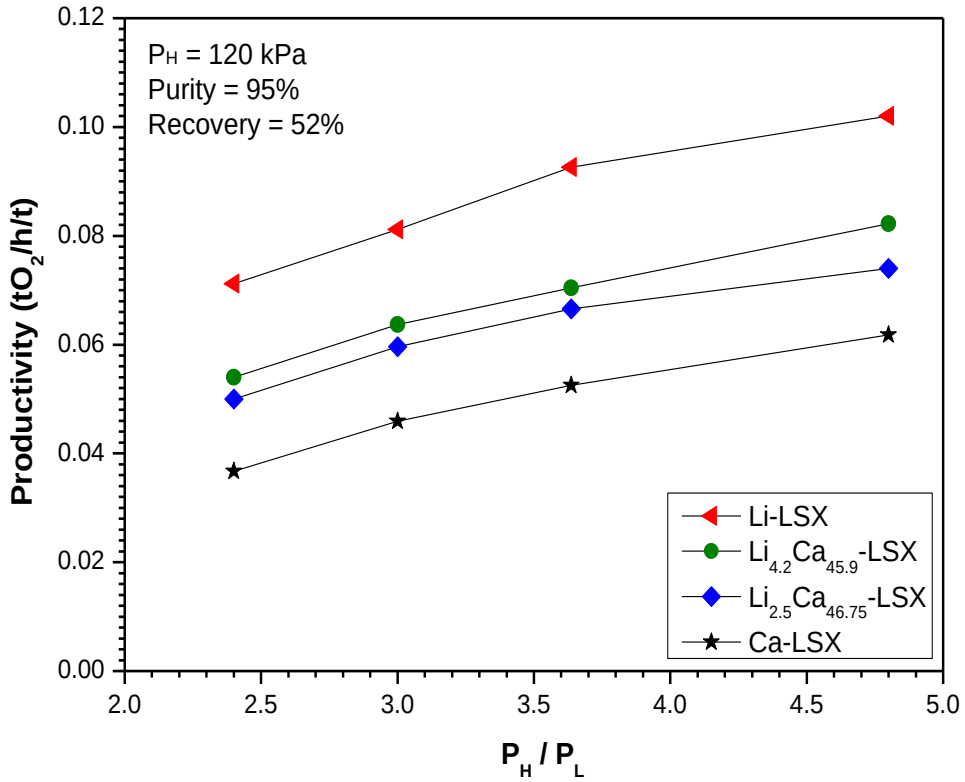

Figure 3.11 Comparison of O_2 Productivity at 120 kPa pressure.

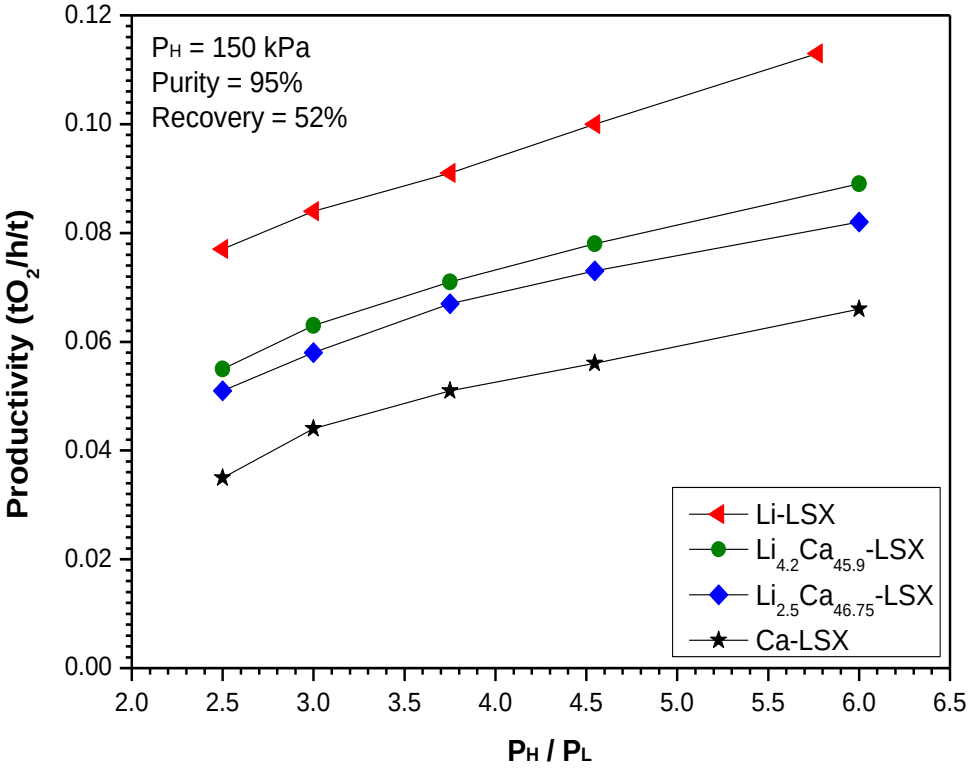

Figure 3.12 Comparison of O_2 Productivity at 150 kPa pressure.

As can be seen from Figures 3.11 and 3.12, the higher the pressure ratio, the higher the productivity. It also shows that the O_2 productivity follows the following trend: (Li-LSX > $Li_{4.2}Ca_{45.9}$-LSX > $Li_{2.5}Ca_{46.75}$-LSX > Ca-LSX). The above result also justifies that Li-LSX is better than Ca-LSX for O_2 production and this is because the Ca-LSX zeolite has a higher heat of adsorption, higher O_2 capacity, and a lower N_2 working capacity. Upon comparison, the trend (Ca-LSX > $Li_{2.5}Ca_{46.75}$-LSX > $Li_{4.2}Ca_{45.9}$-LSX > Li-LSX) for the N_2 heats of adsorption for the four sorbents appears to be the reverse of the O_2 productivity above. Since adsorption is an exothermic process, the temperature in the bed will increase in the high-pressure feed step thereby affecting the O_2 separation results. It can be seen from the isotherms that the adsorption amount of N_2 on Ca-LSX is higher than that of the Li-LSX at 298 K. However, when the temperature is higher than 323 K, the adsorption amount of N_2 on Ca-LSX is lower compared to Li-LSX. Hence, the working capacity decreases sharply with increasing temperature for N_2 adsorption on Ca-LSX. A higher N_2 adsorption capacity could be achieved by employing a higher feed velocity at the same product purity and recovery. It is seen in Table S3.1 that Li-LSX has the highest feed velocity at the same simulation pressure.

The adsorption capacity of O_2 also has an important effect on PSA performance. When the Li^+ is exchanged into the Ca-LSX zeolite, the oxygen adsorption capacity decreased in comparison with Ca-LSX. The decrease is beneficial because the lower the oxygen adsorption capacity, the better the PSA separation performance. In order to quantitatively study the effects of N_2 heats of adsorption and O_2 adsorption capacity on the separation results, the Ca-LSX zeolite was employed to simulate air separation by using, hypothetically, the N_2 heats of adsorption and O_2 isotherm of $Li_{4.2}Ca_{45.9}$-LSX, respectively. For simplicity purposes, Ca-LSX@1 and Ca-LSX@2 will be used

to denote the sorbent pairings of Ca-LSX with $Li_{4.2}Ca_{45.9}$-LSX N_2 heats of adsorption and Ca-LSX with $Li_{4.2}Ca_{45.9}$-LSX O_2 isotherm, respectively.

All other simulation conditions were maintained except the high-pressure feed which was set at 120 kPa. The feed and purge velocities were also optimized so as to obtain the same product purity and recovery for both sorbents. Table 3.5 shows the simulation results while Figure 3.13 shows the separation results in comparison with the Ca-LSX and $Li_{4.2}Ca_{45.9}$-LSX sorbents.

Table 3.5 Effects of N_2 heats of adsorption and O_2 adsorption capacity on PSA performance.

Sorbent	P_H [kPa]	P_{CD} [kPa]	P_L [kPa]	U_H [m/s]	U_L [m/s]	O_2 Product purity [%]	O_2 Product purity [%]	Product productivity [tO_2/h/t]
	120	75	20	1.21	3.05	94.744	52.289	0.084
	120	80	25	1.13	2.27	94.995	51.903	0.0759
Ca-LSX@1	120	80	33	0.99	1.59	95.238	52.146	0.0659
(See Text)	120	85	40	0.92	1.21	95.307	51.992	0.0584
	120	90	50	0.802	0.85	94.971	51.821	0.0484
	120	75	20	1.04	2.8	94.959	52.426	0.0749
	120	80	25	0.99	2.1	95.225	52.718	0.0684
Ca-LSX@2	120	80	33	0.87	1.45	95.255	52.464	0.0578
(See Text)	120	85	40	0.835	1.13	95.316	52.293	0.0519
	120	90	50	0.765	0.83	95.118	51.955	0.044

As can be seen from the result, the sorbent $Li_{4.2}Ca_{45.9}$-LSX has a higher O_2 productivity. Also, CaLSX@1 has a higher productivity than CaLSX@2. When the pressure ratio is 3, the O_2 productivity for sorbents CaLSX@1 and CaLSX@2 are 0.0584 tO_2/h/t and 0.0519 tO_2/h/t respectively which are 27% and 13% higher than that of pure Ca-LSX. The result also shows that the decrease in the N_2 heat of adsorption on Li^+-exchanged Ca-LSX has more contribution than

the decrease in O_2 adsorption capacity to enhance O_2 productivity. As can be seen from Table 3.2, the N_2 heats of adsorption on Ca-LSX is 43.39 kJ/mol, which is much higher than that of $Li_{4.2}Ca_{45.9}$-LSX (28.72 kJ/mol). The detrimental effect of the heat of adsorption on the PSA performance is well illustrated by Lee et al. [42] in their development of heat-exchange PSA. Where significant improvement was shown in the PSA performance by using a two-bed PSA system in a shell-and-tube configuration that allowed heat transfer between the two beds. The effects of heats of adsorption/desorption are further complicated by their effects on the mass transfer rates [43] which can be significant in rapid or kinetically controlled PSA.

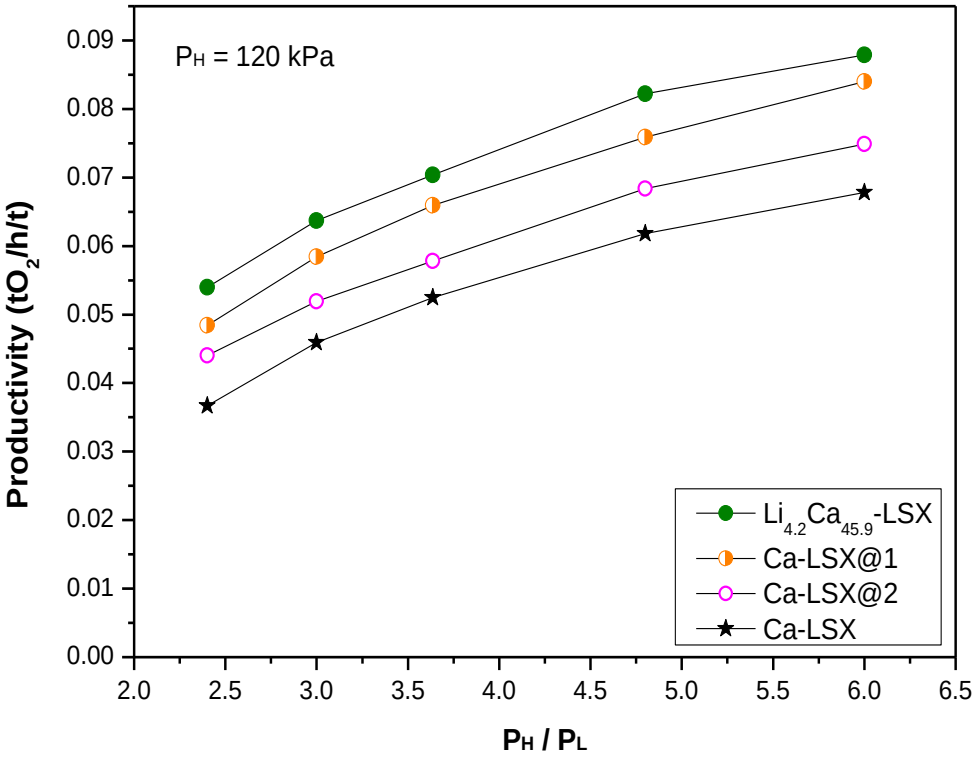

Figure 3.13. Effect of N_2 heats of adsorption and O_2 isotherm on O_2 productivity.

In the PSA system under consideration, as mentioned above, mass transfer resistance was neglected due to the relatively long cycle time.

In commercial operation of VPSA, the operating high and low pressures are normally set as 150 kPa and 50 kPa respectively for the production of O_2 via VPSA. With a pressure ratio of 3, it can be seen from Table S3.1 that when the feed pressure is 150 kPa, the O_2 productivity obtained using $Li_{4.2}Ca_{45.9}$-LSX is 0.0637 tO_2/h/t-sorbent compared to the throughput of 0.046 tO_2/h/t-sorbent and 0.084 tO_2/h/t-sorbent using Ca-LSX and Li-LSX respectively. The corresponding O_2 product purity and recovery were approximately 95% and 52%. This shows that using the $Li_{4.2}Ca_{45.9}$-LSX sample enhanced O_2 productivity by 43% more than Ca-LSX, and only 25% lower than the productivity of Li-LSX. This is to say, in order to achieve the same O_2 productivity from using the $Li_{4.2}Ca_{45.9}$-LSX sorbent, one only has to increase the bed size by 1.32 times (or 32%). A similar trend was observed when the feed pressure was set at 120 kPa. The use of the mixed-cation LiCa-LSX results in savings of 70% lithium. Knowing that most of the fixed investments in VPSA O_2 production industry lies in the cost of the sorbent, these results present the possibility of considerable savings in capital and operating costs, especially with the steep rise in price (driven by the demand for rechargeable batteries) of lithium. On the other hand, increasing the bed size factor would require larger vessels and larger compressors/vacuum blowers which should also be considered.

It should be noted that zeolitic sorbents used in industrial PSA/VSA processes are in the form of pellets that are formed with a clay binder, and the pelletized products need to be calcined in air at a high temperature. For example, in the improved sorbent (with high diffusion rates) of Ackley et al. [44], the Li-LSX crystals were mixed with a clay binder to form pelletized beads and the beads needed to be calcined in dry air at up to 866 K for 3 hours. Thus, for practical application of the LiCa-LSX zeolite, a modification of the sample preparation steps is required. Pelletization of Ca-LSX with a binder followed by high temperature calcination will be performed first, which

is to be followed by the Li^+ ion exchange and mild calcination steps as described above. Ion exchange of zeolites in their pelletized form is practiced in laboratories [45] and, in fact, occurs in industrial wastewater treatment such as radioactive waste treatment [46].

3.4 Conclusion

Mixed-cation LiCa-LSX with less than 5% Li were prepared by sequential exchange (with Li exchange as the last step) followed by mild and short-time dehydration. Comparisons of adsorption isotherms of N_2 and O_2 and heats of adsorption data for the LiCa-LSX samples with that for pure-cation Li-LSX and Ca-LSX provided strong evidence that significant fractions of these Li^+ cations remained on the exposed exchange sites (SIII), thereby participating in adsorption of N_2 and O_2.

The mixed-cation LiCa-LSX samples were compared against the pure-cation Ca-LSX and Li-LSX based on their performance for oxygen production by PSA, via PSA model simulation. The simulation results show that the $Li_{4.2}Ca_{45.9}$-LSX sorbent with only a few Li cations exchanged into the pure Ca-LSX sample, could lead to significant improvements in the PSA production of O_2. This new exchange method shows a significant advantage over earlier research where more than 70% Li cations were exchanged with pure Na-LSX [3, 8, 10, 13].

3.5 References

[1] R. T. Yang, Gas Separation by Adsorption Processes. London: Imperial College Press, (1997).

[2] R. T. Yang, Adsorbents: Fundamentals and Applications. New Jersey: John Wiley & Sons, Inc. (2003).

[3] C. C. Chao, Process for Separating Nitrogen from Mixtures Thereof with Less Polar Substances. US Patent. 4,859,217 (1989).

[4] Hutson ND, Yang RT. Structural effects on the adsorption of atmospheric gases in mixed Li,Ag–X-Zeolite. AIChE Journal. 46 (2000) 2305-2317.

[5] M. Feuerstein, G. Engelhardt, P. L. McDaniel, J. E. MacDougall, T. R. Gaffney, Solid-state nuclear magnetic resonance investigation of cation siting in LiNaLSX zeolites. Microporous Mesoporous Mater. 26 (1998) 27-35.

[6] M. Feuerstein, R. F. Lobo, Characterization of Li Cation in Zeolite LiX by Solid-State NMR Spectroscopy and Neutron Diffraction. Chem. Mater. 10 (1998) 2197-2204.

[7] D. H. Olson, H. S. Sherry, An X-Ray Study of Strontium-Sodium Ion Exchange in Linde X. An Example of a Two-Phase Zeolite System. J. Phys. Chem. 72 (1968) 4095-4104.

[8] C. G. Coe, J. F. Kirner, R. Pierantozzi, T. R. White, Nitrogen Adsorption with a Ca and/or Sr Exchanged Zeolite. US Patent. 5,152,813 (1992).

[9] C. G. Coe, J. F. Kirner, R. Pierantozzi, T. R. White, Nitrogen Adsorption with a Divalent Cation Exchanged Zeolite. US Patent. 5,258,058 (1993).

[10] C. G. Coe, J. F. Kirner, R. Pierantozzi, T. R. White, Divalent Cation Exchanged Lithium X-Zeolite for Nitrogen Adsorption. US Patent. 5,417,957 (1995).

[11] C. G. Coe, J. F. Kirner, R. Pierantozzi, T. R. White, Zinc Cation Exchanged Lithium X-Zeolite for Nitrogen Adsorption. US Patent. 5,419,891 (1995).

[12] S. Sircar, R. R. Conrad, W. J. Ambs, Binary Ion Exchanged Type-X Zeolite Adsorbent. US Patent. 4,557,736 (1985).

[13] C. C. Chao, J. D. Sherman, J. T. Mullhaupt, C. M. Bolinger, Mixed Ion-Exchanged Zeolites and Processes for the use Thereof in Gas Separations. US Patent. 5,174,979 (1992).

[14] S. Sircar, W. E. Waldron, Oxygen Production by Adsorption. US Patent. 0108494A1 (2002).

[15] N. D. Hutson, S. C. Zajic, R. T. Yang, Influence of residual water on the adsorption of atmospheric gases in Li-X zeolite: experiment and simulation. Ind. Eng. Chem. Res. 39 (2000) 1775-1780.

[16] F. O. Mertens, Determination of absolute adsorption in highly ordered porous media. Surf. Sci. 603 (2009) 1979-1984.

[17] B. Mu, K. S. Walton, Adsorption equilibrium of methane and carbon dioxide on porous metal-organic framework Zn-BTB. Adsorption. 17 (2011) 777-782.

[18] B. Mu, P. M. Schoenecker, K. S. Walton, Gas adsorption Study on Mesoporous Metal-Organic Framework UMCM-1. J. Phys. Chem. 114 (2010) 6464-6471.

[19] J. Purewal, D. Liu, A. Sudik, M. Veenstra, J. Yang, S. Maurer, U. Müller, D. J. Siegel, Improved hydrogen storage and thermal conductivity in high-density MOF-5 composites. J. Phys. Chem. C116 (2012) 20199-20212.

[20] F. E. Epiepang, J. Li, Y. Liu, R. T. Yang, Low-pressure performance evaluation of CO_2, H_2O, and CH_4 on Li-LSX as a superior adsorbent for air prepurification. Chem. Eng. Sci. 147 (2016) 100-108.

[21] K. E. Maly, E. Gagnon, J. D. Wuest, Engineering molecular crystals with abnormally weak cohesion. Chem. Commun. 47 (2011) 5163-5165.

[22] M. Feuerstein, G. Engelhardt, P. L. McDaniel, J. E. MacDougall, T. R. Gaffney, Solid-state nuclear magnetic resonance investigation of cation siting in LiNaLSX zeolites. Microporous Mesoporous Mater. 26 (1998) 27-35.

[23] H. Herden, W. D. Einicke, R. Schollner, W. J. Mortier, L. R. Gellens, J. B. Uytterhoeven, Location of Li-ions in Synthetic Zeolites X and Y. *Zeolites*. 2 (1982) 131-134.

[24] J. M Bennett, J. V. Smith, Positions of Cations and Molecules in Zeolites with the Faujasite-Type Framework I. Dehydrated Ca-Exchanged Faujasite. Mat. Res. Bull. 3 (1968) 633-642.

[25] H. S. Sherry, The Ion-Exchange Properties of Zeolites. I. Univalent Ion Exchange in Synthetic Faujasite. J. Phys. Chem. 70 (1968) 1158-1168.

[26] G. Vitale, L. M. Bull, R. E. Morris, A. K. Cheetham, B. H. Toby, C. G. Coe, J. E. MacDougall, Combined neutron and X-ray Powder Diffraction Study of Zeolite Ca LSX and a ^{2}H NMR Study of Its Complex with Benzene. J. Phys. Chem. 99 (1995) 16087-16092.

[27] J. J. Pluth, J. V. Smith, Positions of Cations and Molecules in Zeolites with the Faujasite-Type Framework VII. Dehydrated Ca-Exchanged X. Mat. Res. Bull. 7 (1972) 1311-1322.

[28] J. J. Pluth, J. V. Smith, Positions of Cations and Molecules in Zeolites with the Faujasite-Type Framework VIII. Dehydrated Ca-Exchanged X. Mat. Res. Bull. 8 (1973) 459-468.

[29] M. L. Costenoble, W. J. Mortier, J. B. Uytterhoeven, Location of Cations in Synthetic Zeolites-X and -Y Part 5. – The cation Distribution in Ca-Y, Ca-X and La-Y in the Ultimate Stages of Dehydration. J. Chem. Soc. 74 (1978) 466-476.

[30] M. L. Costenoble, W. J. Mortier, J. B. Uytterhoeven, Location of Cations in Synthetic Zeolites-X and -Y Part 6. – The cation Distribution in Ca-Y, Ca-X and La-Y in the Ultimate Stages of Dehydration. J. Chem. Soc. 74 (1978) 477-483.

[31] Y. I. Smolin, Y. F. Shepelev, A. A. Anderson, Atomic Scale mechanism of CaX Zeolite Dehydration. Acta Cryst. B45 (1989) 124-128.

[32] S. B. Jang, M. S. Jeong, Y. Kim, Crystal Structures of the Ethylene and Acetylene Sorption Complexes of Fully Ca^{2+}-Exchanged Zeolite X. J. Phys. Chem. B. 101 (1997) 3091-3096.

[33] Y. H. Yeom, A. N. Kim, Y. Kim, Crystal Structure of a Benzene Sorption Complex of Dehydrated Fully Ca^{2+}-Exchanged Zeolite X., J. Phys. Chem. 102 (1998) 6071-6077.

[34] S. B. Jang, M. S. Jeong, Y. Kim, S.H. Song, K. Seff, Crystal Structure of an Ammonia Sorption Complex of Dehydrated Fully Ca^{2+}-Exchanged Zeolite X., Micropor. Mesopor. Mater. 28 (1999) 173-183.

[35] E. Y. Choi, Y. Kim, K. Seff, Crystal Structure of a Mesitylene Sorption Complex of Dehydrated Fully Ca^{2+}- Exchanged Zeolite X. Sorbed Mesitylene Appears to be Significantly Nonplanar. J. Phys. Chem. 106 (2002) 5827-5832.

[36] G. H. Jeong, Y. Kim, H. Seff, Crystal Structure of a Mesitylene Sorption Complex of Dehydrated Fully Ca^{2+}- Exchanged Zeolite X. $|Ca_{46}(CH_3NH_2)16|[Si_{100}Al_{92}O_{384}]$-FAU. Langmuir. 20 (2004) 9354-9359.

[37] N. D. Hutson, S. U. Rege, R. T. Yang, Mixed Cation Zeolites: Li_xAg_y-X as a Superior Adsorbent for Air Separation. AIChE Journal. 45 (1999) 724-734.

[38] Y. H. Kim, J. J. Kim, C. H. Lee, Adsorptive cyclic purification process for CO_2 mixtures captured from coal power plants, AIChE Journal. 63 (2017) 1051-1063.

[39] S. U. Rege, R. T. Yang, Limits for air separation by adsorption with LiX zeolite. Ind. Eng. Chem. Res. 36 (1997) 5358-5365.

[40] D. A. Kennedy, M. Mujcin, E. Trudeau, F. H. Tezel, Pure and Binary Adsorption Equilibria of Methane and Nitrogen on Activated Carbons, Desiccants, and Zeolites at Different Pressures. J. Chem. Eng. Data 61 (2016) 3163-3176.

[41] V. P. Mulgundmath, F. H. Tezel, F. Hou, T. C. Golden, Binary Adsorption Behavior of Methane and Nitrogen gases. J. Porous Mater. 19 (2012) 455-464.

[42] J. J. Lee, M. K. Kim, D. G. Lee, H. W. Ahn, M. J. Kim, C. H. Lee, Heat-exchange pressure swing adsorption process for hydrogen separation. AIChE Journal 54 (2008) 2054-2064.

[43] Y. Wang, M. D. LeVan, Master curves for mass transfer in bidisperse adsorbents for pressure-swing and volume-swing frequency response methods. AIChE Journal 57 (2011) 2054-2069.

[44] M. W. Ackley, P. A. Barrett, N. A. Stephenson, E. S. Kikkinides, High Rate Compositions. US Patent. 0340612A1 (2013).

[45] P. A. S. Moura, D. P. Bezerra, E. Vilarrasa-Garcia, M. Bastos-Neto, D. C. S. Azevedo. Adsorption Equilibria of CO_2 and CH_4 in Cation-Exchanged Zeolites 13X, Adsorption. 22 (2016) 71-80.

[46] D. W. Breck, Zeolite Molecular Sieves: Structure, Chemistry, and Use. Malabar, FL: RE Krieger, (1984) 529-588.

Chapter 4

Desulfurization of Natural Gas Using Nitrogen Doped Carbon

Abstract

This work is aimed at expanding on the adsorption process for the removal of H_2S from natural gas with Nitrogen Doped Carbon as the sorbent. The nitrogen doped carbon sample was prepared via the chemical vapor deposition with Na-Y zeolite as the hard template and acetonitrile as the carbon and nitrogen source. Surface area characterization showed a BET of 1375 m^2/g while XPS analysis indicated a 7 wt% nitrogen content. Comparisons of adsorption isotherms for H_2S and CH_4 showed that the NDC sample adsorbs H_2S 5 times more and adsorbs CH_4 1.3 times less than commercial BPL 12x30 activated carbon respectively. The regeneration energy required for the synthesized NDC sample was very low as cyclic adsorption-desorption isotherms revealed complete H_2S desorption in about 8 minutes on NDC at 333 K.

4.1 Introduction

Desulfurization is the removal and processing of sulfur and sulfur compounds from sour gas (acid gas) containing systems and it is a very important part in the natural gas and shale gas processing industries [1]. Raw natural gas contains different levels of Hydrogen Sulfide (H_2S) ranging from a few ppm up to 5%. For it to be considered "pipeline grade", its H_2S content has to be decreased to below 1 ppm although the US allowable limit is usually 4 ppm or 0.25 grain per 100 standard cubic foot (scf) [2]. The removal of these acidic gases is extremely important in the oil and natural gas production operations, natural gas processing, liquefied natural gas (LNG) transport, crude oil refining, and transportation.

H_2S is an odorous pollutant and it is commonly regarded as toxic. In addition to its health effects, it is a corrosive gas, exerting adverse effects in many industrial processes. One of the many reasons why desulfurization is important is that H_2S can be very destructive to process equipment and be very harmful to an organization's ability to market high quality products. Once the acidic gases are removed and the hydrocarbon stream is processed, the handling is vastly improved, and the product's value is increased. The current dominant commercial technology is plagued with numerous adverse effects (some of which will be discussed subsequently), so any positive results from this work will not only further the plight for a sustainable environment, but also bridge the existing gab in literature regarding the adsorption of H_2S on Nitrogen-Doped carbon (NDC).

4.2 Background

There are numerous existing gas sweetening technologies available and the choice of preference depends on several factors. Some of the major factors include; the nature and number of contaminants in the feed gas, the amount of every contaminants present in feed gas and the

targeted removal capacity, amount of hydrocarbon in the gas, pipeline specification, capital and operating cost, amount of gas to be processed, desired selectivity, and conditions at which the feed gas is available for processing. These factors are extremely important because each technology has its advantages and limitations vis-à-vis the others.

The conventional desulfurization process is accomplished by the solvent extraction (gas-liquid adsorption/stripping processes) using aqueous solutions of alkanoamines (weak organic bases) such as Monoethanolamine (MEA), Diethanolamine (DEA), and Methyldiethanolamine (MDEA) [3-5]. The liquid adsorption process is technologically viable but has numerous disadvantages which includes high energy requirements for solvent regeneration, solvent loss, and corrosion of equipment [5]. Another technology for gas purification to surface during the last couple of decades is the membrane technology. As every technology, this approach also has its advantages (higher energy efficiency, ease of process scale-up, great operational flexibility, and environmental safety) and disadvantages (possible methane (CH_4) losses and high costs) [6].

The main reason for the continued use of the scrubbing technology has been its relatively low cost. One of its other strength is that it can also be used to remove acid gases from liquid hydrocarbons such as Liquefied Petroleum Gas (LPG) [7]. This technology just as any has quite a few weaknesses including the need for a high energy requirement for its solvent regeneration, equipment corrosion, and the ever-present solvent loss issue since all of the solvents cannot be recycled back to the absorber column, meaning the disposal of the solvents causes environmental hazards. Knowing that the gas/liquid absorption/stripping process is slow (slow gas-liquid reaction), this significantly introduces the domino effect by limiting the rate of the process throughput as a result.

The adsorption process is ideally suited for natural gas sweetening and its primary requirement for an economic adsorption separation process is an adsorbent with sufficient selectivity, capacity and service life. Selectivity is generally possible mainly with microporous adsorbents such as pelleted zeolites or carbon molecular sieves. Since adsorption is a surface phenomenon, an adsorbent should have a high surface area to volume ratio. The main advantage of physical adsorption methods is its low energy requirement for the regeneration of the sorbent material with short periods associated with the change in pressure. The widely used adsorption processes includes the metal oxide (metal organic frameworks) and molecular sieves (zeolites, activated carbon) [7]. Commercial adsorbents that show ultraporosity have been used for the selective separation of gases, and included activated carbons, charcoal, activated clays, silica gel, activated alumina, and crystalline aluminosilicate zeolites [7]. This process is quite simple to operate, its molecular sieve beds can withstand mechanical degradation, and the possibility of simultaneous dehydration of gases and acid removal are just a few of its many advantages. Once saturation of the adsorbent is attained, regeneration is conducted by either applying heat or by lowering the pressure.

Gas purification by adsorption is mostly carried out either by Temperature Swing Adsorption (TSA) or Pressure Swing Adsorption (PSA). In TSA, desorption is achieved by increasing the temperature of the adsorption bed by applying heat to the fixed bed or more commonly by purging with a hot purge gas. At higher temperatures, the adsorption equilibrium constant is reduced so that even quite strongly adsorbed species can be removed with a comparatively small purge gas volume [7]. The main limitation of the TSA process is the adsorption cycle time required to cool down the bed. Other obstacles are the high energy requirements and large heat loss. The major advantages of the PSA system are low capital and

maintenance costs, high purity product, rapid shutdown and start-up characteristics, lack of corrosions problems, absence of heat requirement and pipe insulation and comparative straight forward operation. In contrast however, the PSA requires high pressure and vacuum pressure that contribute to high operating cost.

The increased demand for natural gas in recent years has brought along the development of highly efficient and environmentally friendly methods for acidic gas removal with lower economic costs. The development of re-generable solid sorbents with high selectivities and high adsorption capacities for acidic gases is a potential alternative for natural gas purification because such materials are environmentally benign and easier to handle (solid). Most importantly, these materials could be regenerated under mild conditions and are thus more energy efficient [8]. Recent review of literature show that most of the solid sorbents studied for natural gas purification had at least one major issue that prevent their industrial application. For example, the two most widely studied solid sorbents are Activated Carbon which presents the problem of low selectivity toward acidic gases and zeolites showing a strong water inhibition effect [9-12].

With the emergence of shale gas, adsorption technology could be the preferred process for natural gas sweetening especially for small to mid-sized production wells thereby replacing the solvent extraction process. Carbon-based sorbents have been evaluated for the removal of hydrogen sulfide due to the need to control odorous/acidic gases generated in sewer systems, wastewater treatment, and natural gas plants, at ambient conditions [13-15]. Those result showed that the surface area and pore volume are not the only factors contributing to H_2S adsorption, and that surface chemistry played a significant role in the uptake of H_2S. Mikhalovsky and Zaitsev [16] showed that H_2S adsorption from an inert atmosphere on activated carbons resulted in the

formation of elemental sulfur, thereby suggesting that the adsorption of hydrogen sulfide on carbon surface may be dissociative.

The widespread interest in developing high-surface-area solid sorbents has been mainly due to their exceptionally high surface areas, which allow binding to occur at a large number of highly dispersed active sites within the framework [8]. Silica and ordered mesoporous silica are ideal solid supports for the active functions because of their large surface areas and/or well-defined pore structures. More importantly, the hydroxyl groups on their surfaces are important for many surface phenomena, such as gas adsorption, surface modification, wetting, and so on [17-20]. Yang et al. [8] first reported the adsorption of CO_2 and H_2S (along with CH_4 for comparison) on amine-surface modified silica xerogels and MCM-48. Their results showed that both materials are excellent sorbents for selective removal of CO_2 and H_2S from natural gas.

We are here-in focused on expanding on the adsorption process for the removal of H_2S from natural gas using NDC as the sorbent. This interest was driven by the fact that there is very little work (literature) that details the adsorption of H_2S on NDC on a wider temperature range. Hence, any positive results from this work would make a significant contribution to the natural gas purification process especially if it is economically tailored. We have so far synthesized (via chemical vapor deposition, CVD) a few NDC samples at various experimental conditions (temperature, ramp rate, hold times, etc.) to study the effect of not just the sample's surface chemistry but also performed X-ray Photoelectron Spectroscopy (XPS) core scans to determine the various types of Nitrogen doped on the carbon framework. N_2 adsorption analysis at Liquid Nitrogen temperature (77 K) were carried out to further characterize (Brunauer-Emmett-Teller, BET surface area, pore volume and distribution, rates of adsorption, etc…) each sample. We observed some interesting and positive preliminary results (some of which were expected) from

the H_2S and CH_4 adsorption isotherms on the sorbents (NDC and Calgon BPL 12x30 Activated Carbon) studied so far.

4.3 Description of Research

The main objectives of this research proposal were as follows: i) to synthesize a reliable, economical, and low temperature regenerable sorbent (NDC) for the desulfurization of natural gas; ii) to determine the adsorption capacity (mass of pollutant adsorbed per mass of adsorbent) of carbon(s) of interest; iii) to determine the sorbent's (NDC) H_2S/CH_4 selectivity; iv) and further investigate whether the injection of ammonia increases the H_2S adsorption capacity. Results obtained from this work will not only be compared with those of other commercial sorbents for H_2S adsorption but also doubles to bridge the existing gap in literature regarding the adsorption of H_2S on NDC. Knowing that the amine technology is highly suitable for larger production sites, the adsorption process, with NDC as its sorbent of choice, is envisioned to be perfectly suitable for the emerging shale gas industry with small to mid-sized (< 20 Mcf/day) production wells.

Sorbents such as activated carbons (shows low H_2S/CH_4 selectivity), while zeolites and alkalized alumina (strongly adsorbs water vapor) are amongst some of the popular commercial sorbents being used in current adsorption processes [8]. Metal oxide-based sorbents have also been shown to reduce sulfur concentration from several thousand ppm to sub ppm levels [21-25]. However, metal oxide adsorbents for removal of H_2S are used at high temperatures (573–973 K) and suffer from poor H_2S adsorption selectivities in the presence of other species such as CO, CO_2, and water vapor [21-25], whereas our NDC sample works best at the preferred lower temperatures and pressures.

4.4 General Plan of Work:

The proposed work plan is structured as follows: i) preparation of sorbent(s); ii) sample characterization; iii) adsorption and breakthrough experiments; iv) preliminary results and discussion; v) and future work.

4.4.1 Sorbent Preparation

There are three popular methods for the introduction of carbon into the zeolite micropores. These include: (A) Polymer carbonization which consists of the introduction or organic monomers, followed by polymerization and carbonization, (B) the Chemical Vapor Deposition (CVD) method using small organic molecules as carbon/nitrogen sources and, (C) the Two-Step method which consists of the polymer carbonization followed by further CVD [26]. Here-in, we employed the CVD method with Acetonitrile (CH_3CN) as our carbon and nitrogen source.

A 2 g sample of NaY zeolite (2.40 Si/Al molar ratio, Strem Chemicals) was degassed in an oven for 12 h at 423 K to remove all moisture and other atmospheric gases. The dried sample was then placed in a vertical quartz tube and heated to 1,023 K under a He (or N_2) flow. When the temperature reached 1,023 K (ramp rate of 279 K/min), the He flow is switched to Acetonitrile (CH_3CN) (saturated in a He flow rate of 100 cm^3/min) to pass through the NaY zeolite for 4 h. After the Chemical Vapor Deposition (CVD) treatment, the composite is further heated at 1,173 K for 2 h under a flow of He.

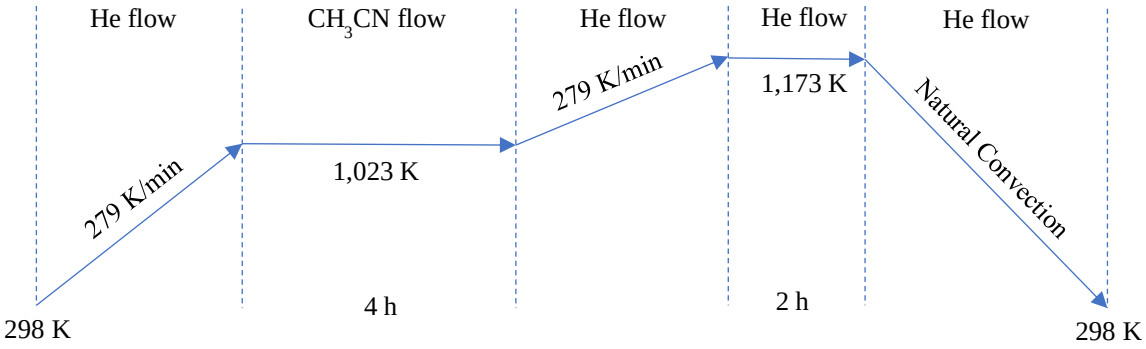

Figure 4.1 Schematic of synthesis procedure of NaY-zeolite templated carbon composite using CH_3CN as carbon and nitrogen precursor.

The obtained NaY/Carbon composite was treated in a 48% hydrofluoric acid (HF) solution for 24 h (removal of silica) and subsequently refluxed by a concentrated HCl solution for 4 h (removal of alumina) to dissolve the NaY template. The resulting microporous carbon was collected by filtration, washed with deionized water and dried in an oven (393 K) for 24 h [27].

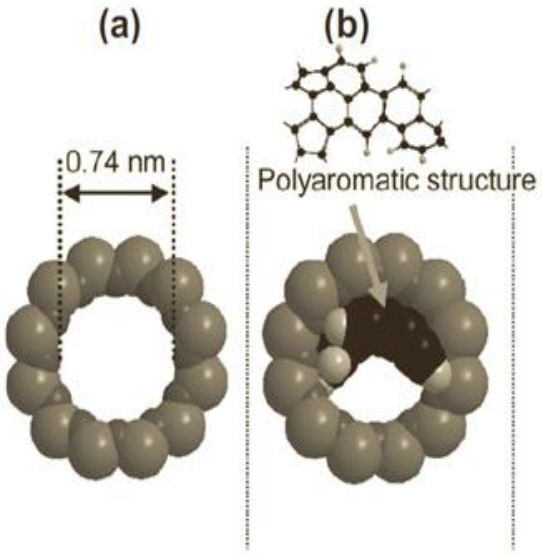

Figure 4.2. The pore entrance structure of NaY zeolite **(a)** before and **(b)** after carbon deposition. **(b)** a Polyaromatic structure showing a fragment of the

4.4.2 Sample Characterization

The Brunauer-Emmett-Teller (BET) surface area and pore size distribution of the samples was measured by physical adsorption of N_2 at 77 K using a Micromeritics ASAP 2020. Whereas Powder X-ray Diffraction (XRD) patterns were obtained from a Rigaku Miniflex diffractiometer at 40 kV and 100 mA for Cu Kα (λ = 0.1543 nm) radiation, with a step size of 0.02 degrees (slow scan) in 2θ. X-ray Photoelectron Spectroscopy was recorded using Kratos Axis Ultra XPS Spectrometer. The rates of adsorption (ROA) of H_2S and CH_4 on the adsorbents were determined using the D/R^2 equation (Diffusion in a sphere).

4.4.3 *Experimental Setup*

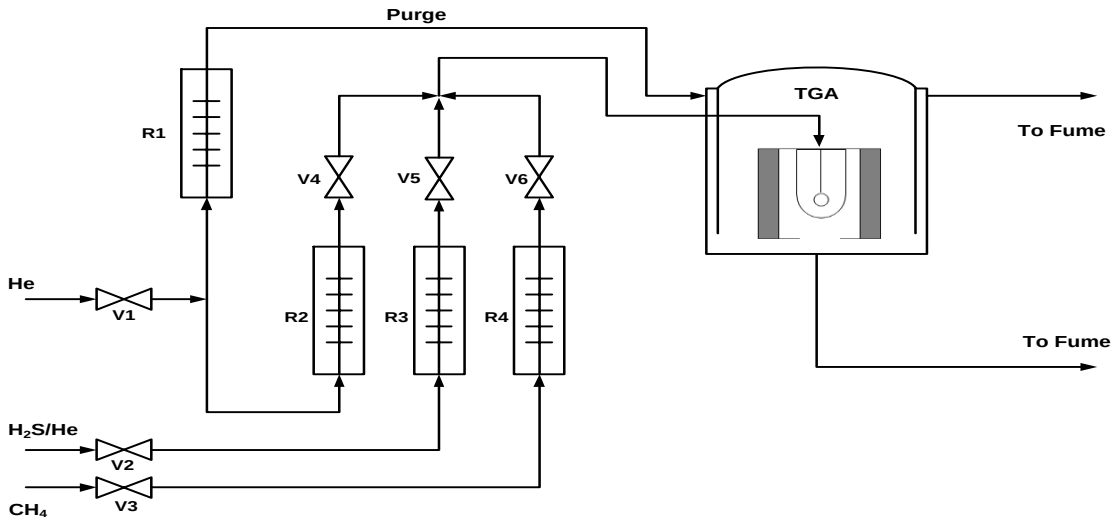

Figure 4.3. Experimental setup of H_2S adsorption/desorption. [R = Rotameter; V = Valve; TGA = Thermogravimetric Analyzer].

Figure 4.3 shows the fixed bed reactor system used for the H_2S adsorption studies. Single-component H_2S adsorption isotherms were measured using a standard gravimetric (Shimadzu TGA-50 automatic recording microbalance) approach at various temperatures (298 and 323 K) while desorption was carried out at 333 K. Thorough calibrations of the gas composition changes

were employed to accurately account for differences in buoyancy. Ultrahigh purity He (UHP, 99.999%) was used as the carrier gas pretreated in 3A zeolite to remove all traces of moisture. The H_2S/He mixture (100 ppm H_2S, balance He) was also passed through a 3A zeolite. The desired H_2S concentrations were obtained by additional dilution of the H_2S/He mixture with Helium at a flow rate of 100 cm^3/min. The desired concentrations were fed through a quartz reactor (holding the NDC sample) positioned vertically in the center of the heating chamber of the TGA.

The samples (NDC and activated carbon) were each pretreated at 573 K in helium flow for 2 h before each experimental run (to remove all moisture and atmospheric gases). Once the temperature of the sample was at the specified temperature (e.g. 298 K via natural convection), the feed gas is switched from the helium to the sample gas mixture with the desired H_2S concentrations. There was a 20-minute wait time after each equilibrium concentration point.

4.5 Results and Discussion

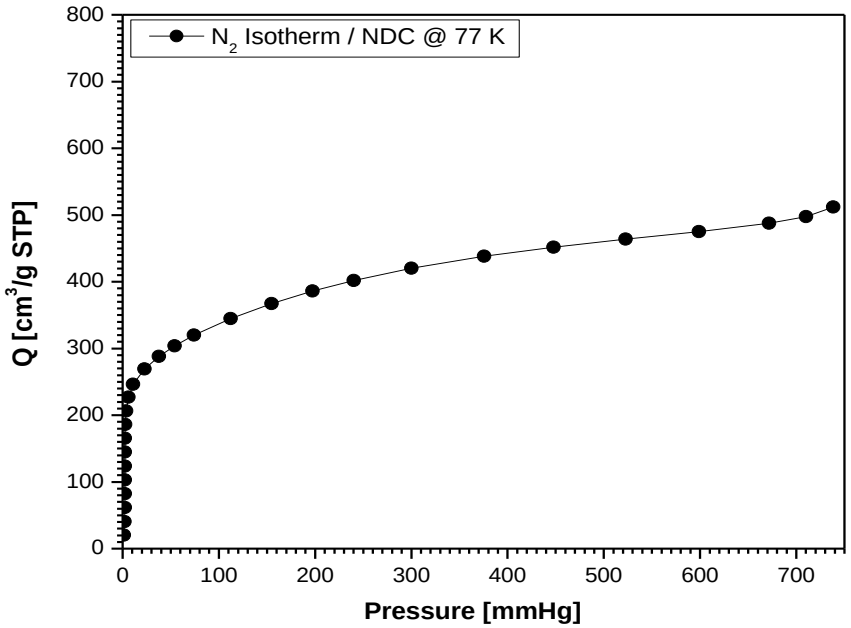

Figure 4.4 Nitrogen Isotherm on Nitrogen-Doped Carbon @ 77K.

To characterize the surface area and porosity of the Nitrogen-doped carbon, N_2 adsorption at 77 K was employed. Figure 4.4 shows the isotherm of NDC which exhibits a sharp rise in the low relative pressure ($P/Po < 0.1$) and a gradual rise in the high relative pressure, which indicates the presence of microporosity and some mesopores (due to incomplete infiltration of acetonitrile into the NaY zeolite's channel). The BET surface areas were determined to be 1375 m^2/g and 1050 m^2/g for NDC and AC respectively whereas the pore volumes for both adsorbents were found to be 1.43 cm^3/g and 0.8 cm^3/g respectively. The increased surface area of NDC correlates the prediction that the NaY zeolite is an excellent carbon template for NDC synthesis.

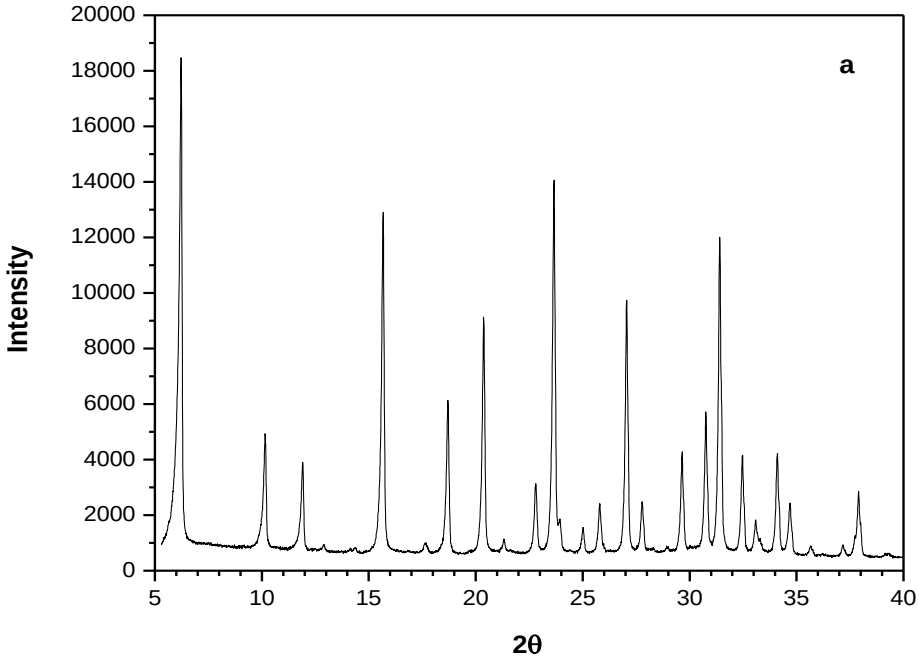

The X-ray diffraction patterns shown in Figure 4.5 represent typical peaks for the zeolite template (NaY) and NDC. The spectrum in Figure 4.5a (NaY zeolite) depicts that of a FAU

structure while Figure 4.5b (NDC) shows a peak at 2θ = 6.3, an indication of the replication of the microstructure of the NaY zeolite.

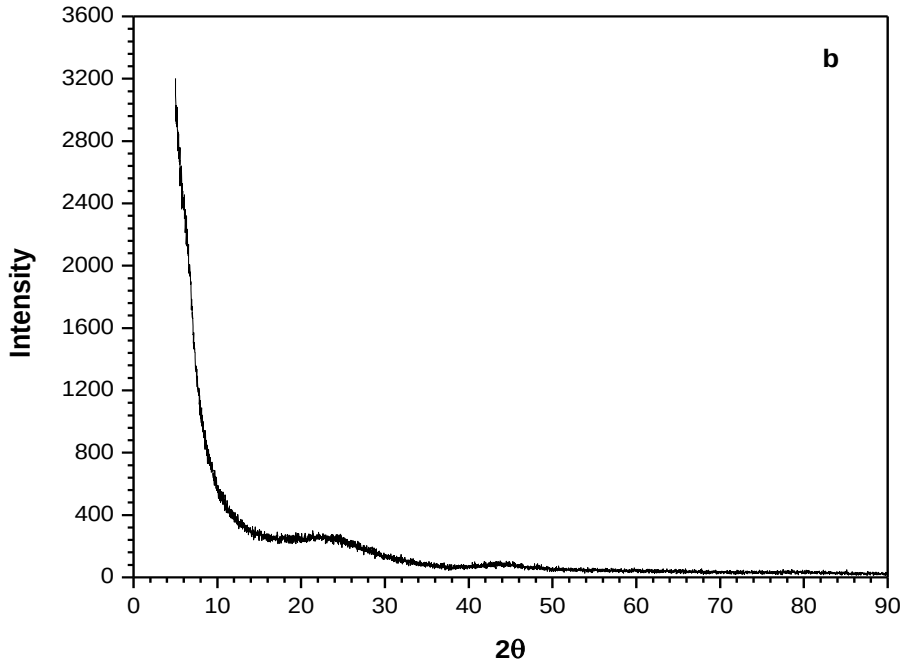

Figure 4.5. X-ray diffraction (XRD) patterns: (**a**) NaY Zeolite (**b**) Nitrogen-Doped carbon.

The success of NaY zeolite hard template Nitrogen doping was confirmed by the use of an X-ray Photoelectron Spectrometer (XPS) which showed 7 wt% nitrogen-content. The three sharp peaks in Figure 4.6 indicate the presence of C (88%), N (7%), and O (5%) elements. This again proves that the use of acetonitrile as a precursor for both carbon and Nitrogen in the NDC synthesis was plausible.

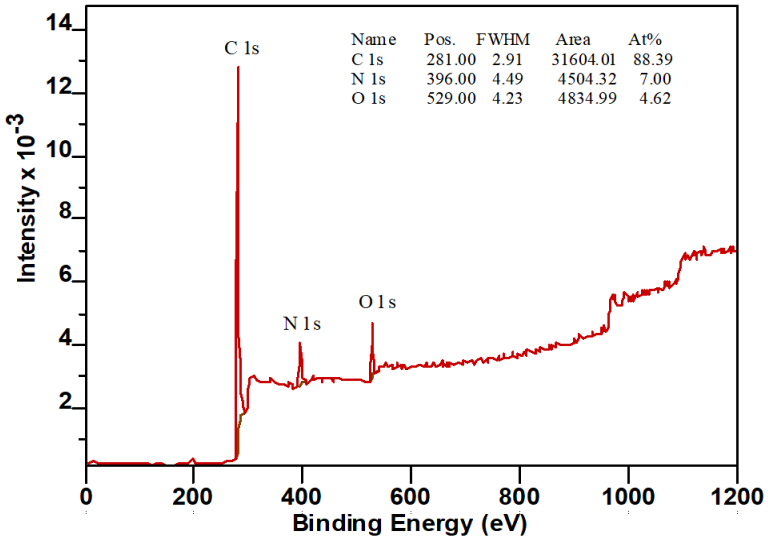

Figure 4.6 X-ray Photoelectron Spectrum (XPS) of NDC sample.

These results are in conjunction with earlier studies on the use of acetonitrile for NDC synthesis [29-31]. It can also be confirmed that nitrogen doped through this approach are mostly in the pyridine-like nitrogen based on their binding energy.

4.5.1 H_2S adsorption isotherms

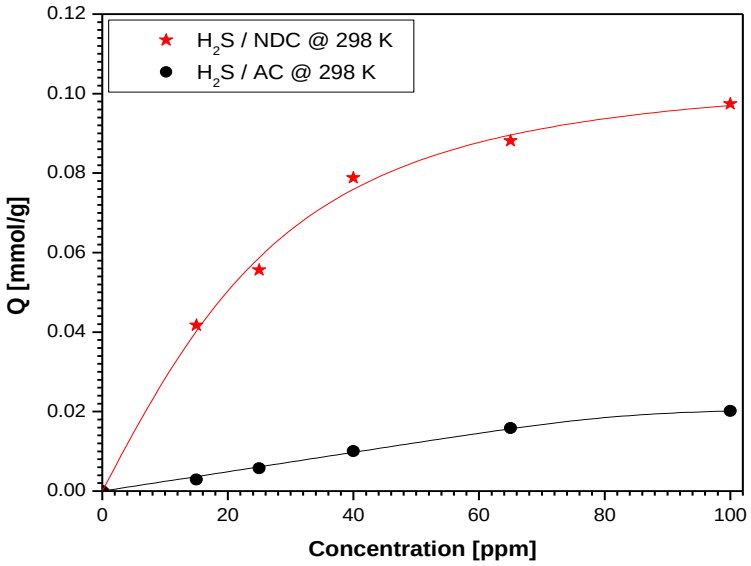

Figure 4.7a. H_2S adsorption isotherms of NDC and BPL 12x30 activated carbon at 298 K and 101 kPa.

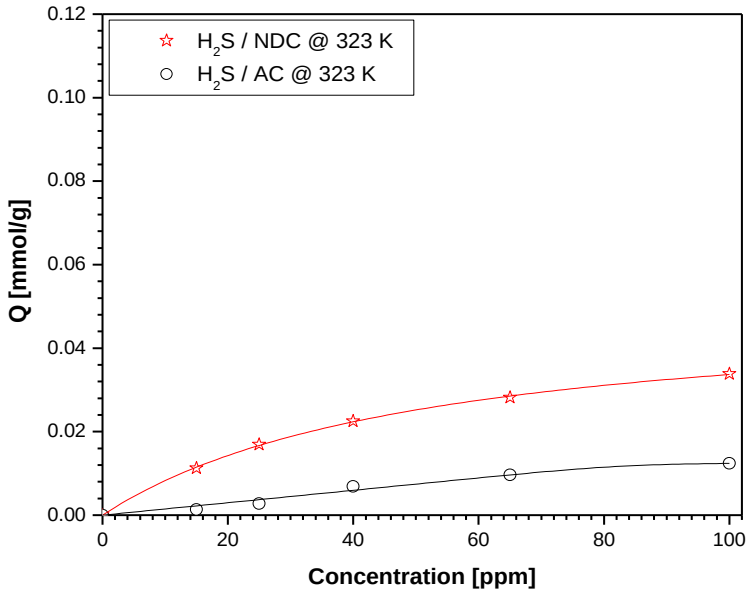

Figure 4.7b. H_2S adsorption isotherms of NDC and BPL 12x30 activated carbon at 323 K and 101 kPa.

Figures 4.7a and 4.7b shows equilibrium isotherms of H_2S on NDC and activated carbon (AC) at 298 K and 323 K respectively. The solid lines show the data fitted with the Tóth model isotherm shown in Equation 4.1

$$Q = \frac{aP}{(d+P^k)^{\frac{1}{k}}} \tag{4.1}$$

The NDC sample adsorbs H_2S almost 5 times more than the commercial BPL 12x30 activated carbon at 298 K and about 2.5 times higher at 323 K. These results only reinforce our theory that NDC is an excellent H_2S sorbent vis-à-vis the AC.

4.5.2 *CH_4 adsorption isotherms*

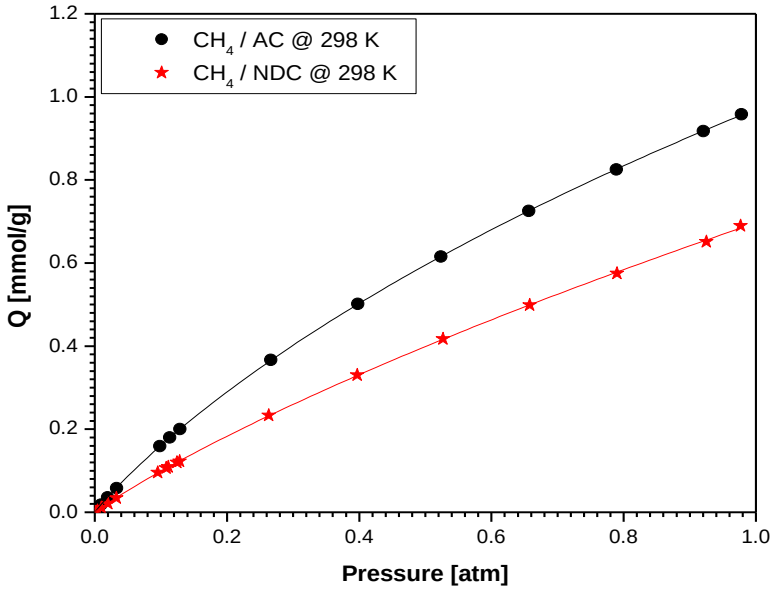

Figure 4.8a. CH_4 adsorption isotherms on NDC and BPL 12x30 activated carbon at 298 K and 101 kPa.

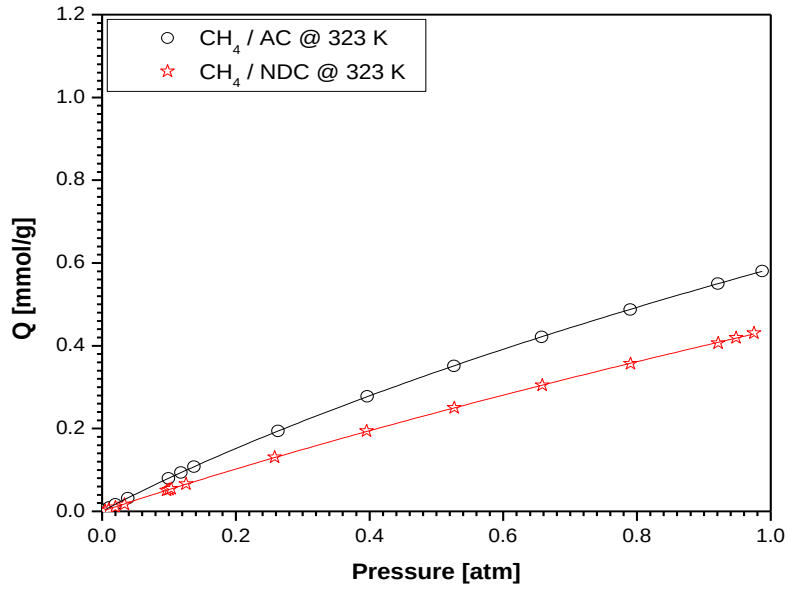

Figure 4.8b. CH_4 adsorption isotherms on NDC and BPL 12x30 activated carbon at 323 K and 101 kPa.

Figures 4.8a and 4.8b shows equilibrium isotherms of CH_4 on NDC and AC at 298 K and 323 K respectively. The Toth Model isotherm given above was used to fit the experimental data and represented with the solid lines. The AC sample adsorbs CH_4 almost 1.3 times more than the NDC at 298 K and about 1.2 times higher at 323 K. We still do not understand why AC adsorbs methane more than NDC. However, it is known that the higher the atomic polarizability of an atom, the greater its adsorption of organics. Since carbon has a higher atomic polarizability (11.67 a.u) [32] than nitrogen (7.26 a.u) [32], this might explain why it adsorbs more CH_4 than the nitrogen in the NDC sample.

4.5.3 Isosteric heats of adsorption

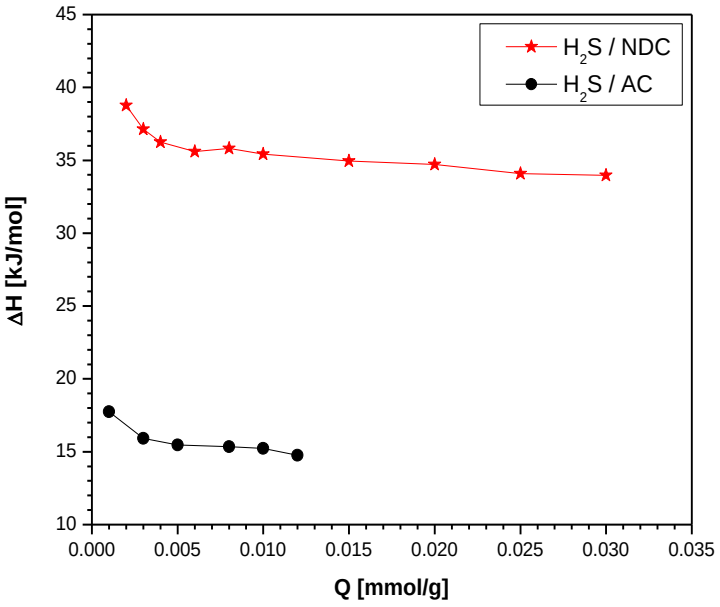

Figure 4.9 Isosteric heats of adsorption vs H_2S Coverage obtained for NDC and AC

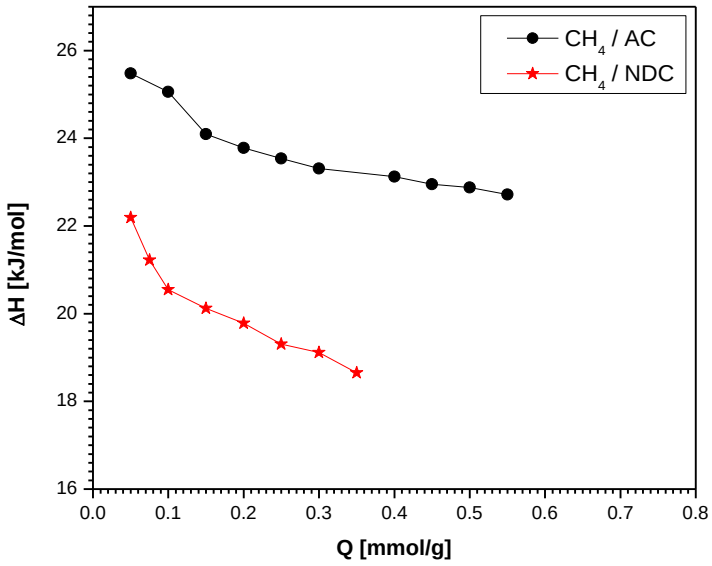

Figure 4.10 Isosteric heat of adsorption vs CH_4 Coverage obtained for NDC and AC

Adsorption isotherm data for both adsorbates were used in conjunction with the Clausius-Clapeyron equation (shown below) to determine the heats of adsorption.

$$\frac{d(\ln P)}{d(1/T)} = -\frac{\Delta H}{R} \tag{4.2}$$

As expected, the adsorption energy of H_2S on NDC was greater than that of AC (Figure 4.9). Also, the adsorption energy of CH_4 on AC was greater than that of NDC as shown in Figure 4.10. It should be noted that isosteric heats of adsorption is an important point to consider knowing that the sorbent's regenerability will strongly depend on its interaction with the sorbate. This implies low adsorption energies would provide easier regeneration but lower adsorption capacities. On the contrary, high adsorption capacities are achieved when high energy adsorption processes are concerned, but with poor sorbent regeneration values. Finding the window of heat of adsorption that simultaneously optimizes both adsorption capacity and regenerability will be a goal for future work.

4.5.4 Adsorption cycle isotherms

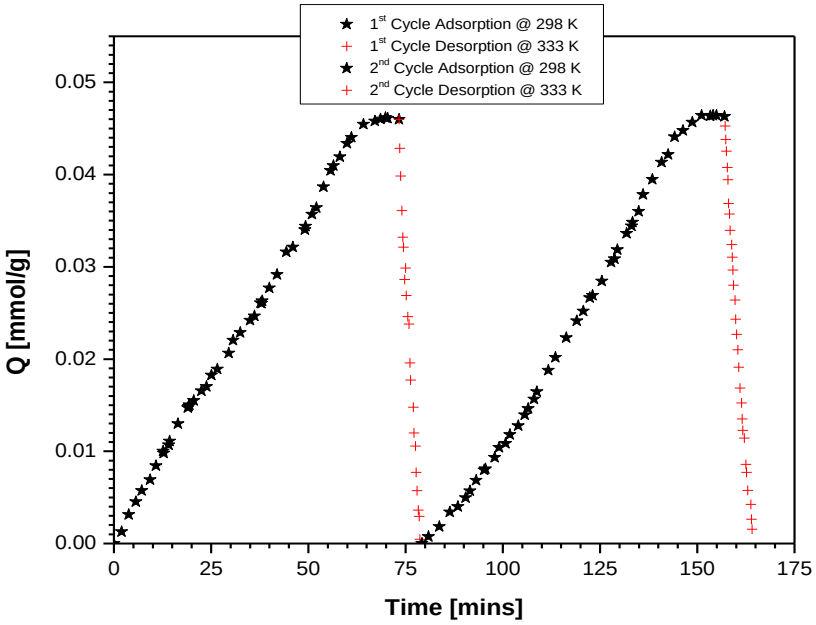

Figure 4.11 Cyclic H_2S adsorption (298 K) - desorption (333 K) on N-Doped Carbon

Adsorption cycle experiments were conducted to investigate the regeneration temperature of the NDC sample. The results presented in Figure 4.11 shows that the NDC sample can be fully regenerated at 333 K in helium flow making it a highly desirable material for natural gas desulfurization.

These TGA results show that the adsorption-desorption reactions of H_2S are thermally reversible. The regenerated sample also shows an adsorption performance similar to that of the fresh sample even after five regeneration cycles. It was also observed that H_2S completely desorbed in about 8 minutes at the desorption temperature of 333 K.

4.6 Conclusion

The nitrogen-doped carbon was prepared via the CVD process with NaY zeolite as the hard template and CH_3CN (34.1 wt% nitrogen) as both the carbon and nitrogen sources. The CVD synthesis scheme led to the successful doping of 7 wt% nitrogen on the carbon structure. Characterization of the NDC sample also confirmed that the starting hard template was an ideal choice based on the resulting high pore volume and BET surface area of the final sample, meaning more active sites for adsorption. The preliminary results from this work also justified our initial theory that nitrogen-doped carbon is a comparatively better natural gas desulfurization sorbent than the commercially used activated carbon as the H_2S amount adsorbed on NDC was found to be significantly higher than that of activated carbon. This work also showed NDC's low methane adsorption thereby reinforcing its adsorption selectivity to acidic gases (primarily due to the chemical interactions between the basic groups and the acidic gases) from natural gas streams. It can also be added that the success of the sorbent is dependent on the successful doping of nitrogen on to the material's carbon matrix and that it can be completely regenerated at temperatures as low as 333 K.

4.7 Future Work

The preliminary results presented in this work are quite satisfactory but there is still much to be done to completely bridge the existing literature gap on H_2S adsorption on NDC. The next phase includes but not limited to i) the chemical vapor deposition of other nitrogen-containing compounds; ii) further increasing the nitrogen-content by post ammonia treatment; iii) as well as performing fixed bed breakthrough experiments.

4.7.1 CVD of other Nitrogen-containing compounds

Our results on CVD of CH_3CN on microporous zeolite (NaY) showed that acetonitrile (works efficiently as both carbon and nitrogen precursors) is an effective precursor for N doping. As expected, our NDC exhibited a high H_2S capacity and a high H_2S/CH_4 selectivity. Our group's results [33] also indicated that by adjusting the concentration of CH_3CN vapor and CVD temperature, we can further increase the N content and control the N type in the final N-doped carbon. This will allow us to prepare the desired basic nitrogen functional groups for enhanced H_2S adsorption.

Similarly, other N-containing compounds including but not limited to acrylonitrilen[34], melamine [35], amino acid L-lysine [36], will also be used as precursors for N-substituted carbons. These different doping precursors will allow us to prepare N-substituted carbon sorbents with different N contents and N types. We will employ the templating approach to enhance the surface area of N-doped carbon and as shown in previous studies [37-38], porous plain carbons templated from zeolite or silica have high surface areas (1000–3800 m^2/g). There is no doubt that this will also be the case for synthesis of N-doped templated carbon using these hard templates.

4.7.2 Post ammonia treatment to further increase N-content

Starting from the carbon sorbents with the highest surface areas and highest N-dopings obtained via the template approach [37-38], we will exploit the amination approach for N-doping of Jansen & Bekkum [39] by using the vapor of NH_3 and/or HCN. Our templated carbon has shown the highest hydrogen storage capacity at room temperature due to its large amount of adsorption sites, which can also be modified as H_2S adsorption sites. Its highly porous textures are favorable for gas treatment and adsorption. It is known that ammonia decomposes at high temperatures to form radicals, such as NH_2, NH and H [39] which reacts with the carbon surface to form functional

groups, such as –NH_2–, –CN, pyridinic, pyrrolic, and quaternary nitrogen. Because of the much smaller size of NH_3 molecule and its radicals relative to the pore sizes of our templated carbon, they can penetrate or infiltrate easily into the pores. The templated carbon will be subjected to ammonia at temperatures between 473–693 K. Since at the relatively low reaction temperatures, the pore structure of templated carbon will be well preserved. The low amination temperature will allow us to form imide-, amide-, and lactam-type surface species on the carbon sorbent. These groups will increase the interactions with H_2S molecules but not decrease the uptake rates significantly.

An alternative route is to react the high-surface-area carbon with NH_3 (and/or HCN) between 873 K and 1,173 K. By controlling the temperature and other synthesis conditions, we can obtain amine groups and nitrile and/or pyridine-like nitrogen on the carbons as well as higher nitrogen contents.

4.7.3 Fixed bed breakthrough experiments

The best sorbents (i.e. with the highest H_2S capacities, H_2S/CH_4 selectivities and with high rates of uptake) will be subjected to fixed bed breakthrough analysis using controlled H_2S/CH_4 mixtures to mimic natural gas streams environments. We will study the effects of initial concentration, flow rate, and bed height on the breakthrough curves using H_2S (ppm level) and H_2S/CH_4 mixtures. These studies will not only give us a better idea of the sorbents adsorption capacities but also tell us if they can desulfurize natural gas lines to or below the required H_2S limit (4 ppm, US).

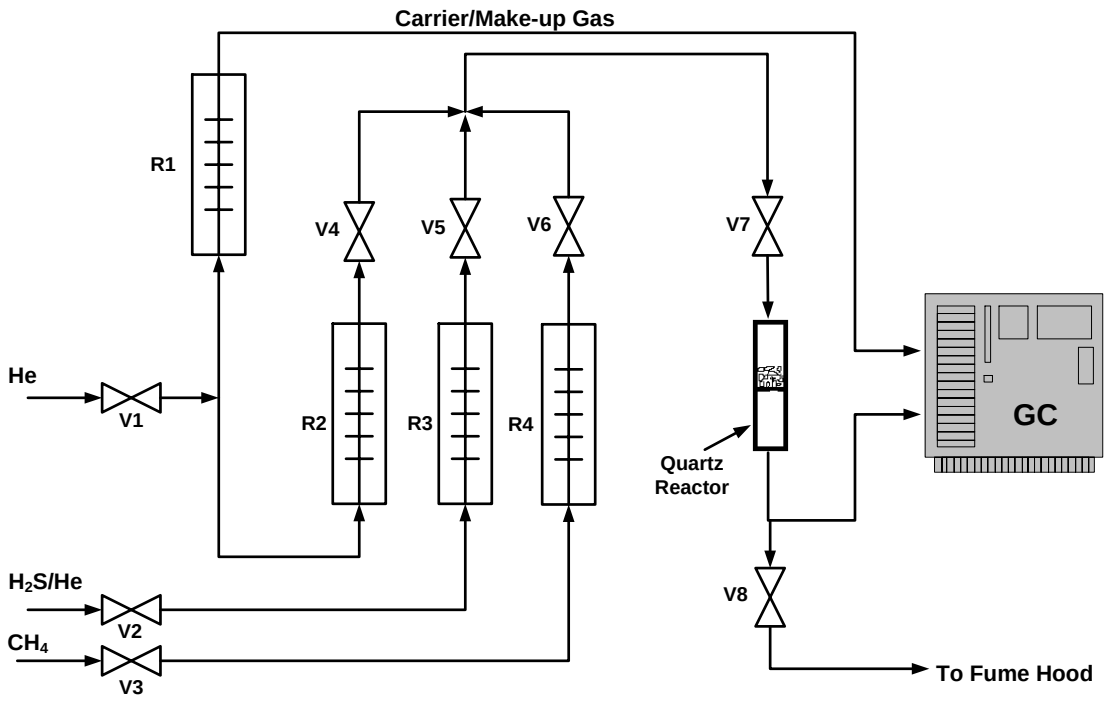

Figure 4.12 Fixed bed breakthrough experimental setup using controlled H_2S/CH_4 mixtures. [R = Rotameter; V = Valve; GC = Gas Chromatograph with FID/FPD

4.8 References

[1] D. L. George, E. C. Bowles, Shale Gas Measurement and Associated Issues, 238 (2011)

[2] H. W. Haring, Industrial Gas Processing. Weinheim: Wiley-VCH, (2008) 217–238.

[3] M. L. Posey, K. G. Tapperson, G. T. Rochelle, A simple model for prediction of acid gas solubilities in alkanolamines. Gas Separation & Purification, 10 (1996) 181–186.

[4] F. Pani, A. Gaunand, D. Richon, R. Cadours, C. Bouallou, Absorption of H_2S by an aqueous methyldiethanolamine solution at 296 and 343 K. Journal of Chemical & Engineering Data, 42 (1997) 865–870.

[5] A. L. Kohl, R. Nielsen, Gas Purification. Houston: Gulf Publishing Company, (1997) 40–186.

[6] B. D. Bhide, A. Voskericyan, S. A. Stern, Hybrid Processes for the Removal of Acid Gases from Natural Gas. J. Membr. Sci. 140 (1998) 27-49.

[7] B. Shimekit, H. Mukhtar, Natural Gas Purification Technologies – Major Advances for CO_2 Separation and Future Directions, Chap 9, 13-14.

[8] H. Y. Huang, R. T. Yang, Amine-Grafted MCM-48 and Silica Xerogel as Superior Sorbents for Acidic Gas Removal from Natural Gas. Ind. Eng. Chem. Res 42 (2003) 2427-2433.

[9] E. S. Kikkinides, V. I. Sikavitsas, R. T. Yang, Natural gas desulfurization by adsorption: Feasibility and multiplicity of cyclic steady states. Industrial & Engineering Chemistry Research. 34 (1995) 255–262.

[10] E. S. Kikkinides, R. T. Yang, S. H. Cho, Concentration and Recovery of Carbon Dioxide from Flue Gas by Pressure Swing Adsorption. *Ind. Eng. Chem. Res*. 32 (1993) 2714-2720.

[11] Y. D. Chen, J. A. Ritter, R. T. Yang, Nonideal Adsorption from Multicomponent Gas Mixtures at Elevated Pressures on a 5A Molecular Sieve. *Chem. Eng. Sci*. 45 (1990) 2877-2894.

[12] K. T. Chue, J. N. Kim, Y. J. Yoo, S. H. Cho, R. T. Yang, Comparison of Activated Carbon and Zeolite 13X for CO_2 Recovery from Flue Gas by Pressure Swing Adsorption. *Ind. Eng. Chem. Res.* 34 (1995) 591-598.

[13] T. J. Bandosz, On the adsorption/oxidation of hydrogen sulfide on activated carbons at ambient temperatures. J Colloid Interface Sci. 246 (2002) 1–20.

[14] T. J. Bandosz, Effect of pore structure and surface chemistry of virgin activated carbons on removal of hydrogen sulfide. Carbon 37 (1999) 483–491.

[15] T. J. Bandosz, S. Askew, W. R. Kelly, A. Bagreev, F. Adib, A. Turk, Biofiltering action on hydrogen sulfide by unmodified activated carbon in sewage treatment plants. Water Sci Technol. 42 (2000) 399–401.

[16] S. V. Mikhalovsky, Y. P. Zaitsev, Catalytic properties of activated carbons. I. Gas-phase oxidation of hydrogen sulfide. Carbon 35 (1997) 1367–1374.

[17] A. Jentys, K. Kleestorfer, H. Vinek, Concentration of Surface Hydroxyl Groups on MCM-41. Microporous Mesoporous Mater. 27 (1999) 321-328.

[18] H. Landmesser, H. Kosslick, W. Storek, R. Fricke, Interior Surface Hydroxyl Groups in Ordered Mesoporous Silicates. Solid State Ionics 101 (1997) 271-277.

[19] T. Takei, K. Kato, A. Meguro, M. Chikazawa, Infrared Spectra of Geminal and Novel Triple Hydroxyl Groups on Silica Surface. Colloids Surf. A 150 (1999) 77-84.

[20] X. S. Zhao, G. Q. Lu, A. K. Whittaker, G. J. Millar, H. Y. Zhu, Comprehensive Study of Surface Chemistry of MCM-41Using 29Si CP/MAS NMR, FTIR, Pyridine-TPD, and TGA. J. Phys.Chem. 101 (1997) 6525-6531.

[21] H. Yang, R. Sothen, D. R. Cahela, B. R. Tatarchuk, Ind. Eng. Chem. Res. 47 (2008) 10064–10070.

[22] R. B. Slimane, J. Abbasian, Adv. Environ. Res. 4 (2000) 147–162.

[23] S. S. Tamhankar, M. Bagajewicz, G. R. Gavalas, P. K. Sharma, M. Flytzani-Stephanopoulos, Ind. Eng. Chem. Process Des. Dev. 25 (1986) 429–437.

[24] E. Sasaoka, S. Hirano, S. Kasaoka, Y. Sakata, Energy Fuels 8 (1994) 1100–1105.

[25] C. Pham-Huu, C. Crouzet, C. Estournes, M. J. Ledoux, J. Chem. Soc., Faraday Trans. 94 (1998) 443–450.

[26] R. T. Yang, Gas Separation by Adsorption Processes. London: Imperial College Press, (1997) 201–236.

[27] Z. Ma, T. Kyotani, Z. Liu, O. Terasaki, A. Tomita, Very High Surface Area Microporous Carbon with a Three-Dimensional Nano-Array Structure: Synthesis and Its Molecular Structure, Chem. Mater. 13 (2001) 4413-4415.

[28] H. Nishihara, T. Kyotani, Novel Carbon Adsorbents, Zeolite-Templated Carbon – Its Unique Characteristics and Applications, (2012) 295-322.

[29] Z. Yang, Y. Xia, R. Mokaya, Aligned N-Doped Carbon Nanotube Bundles Prepared via CVD Using Zeolite Substrates, Chem. Mater. 17 (2005) 4502-4508.

[30] M. He, S. Zhou, J. Zhang, Z. Liu, C. Robinson, CVD growth of N-doped carbon nanotubes on Silicon substrate and its mechanism, J. Phys. Chem. 109 (2005) 9275-9279.

[31] Q. Yang, W. Xu, A. Tomita, T. Kyotani, Double Coaxial Structure and Dual Physicochemical Properties of Carbon Nanotubes Composed of Stacked Nitrogen-Doped and Undoped Multiwalls, Chem. Mater. 17 (2005) 2940-2945.

[32] P. Schwerdtfeger, Table of experimental and calculated static dipole polarizabilities for the electronic ground states of the neutral elements (in atomic units), 2014.

[33] L. F. Wang, R. T. Yang, Significantly Increased CO_2 Adsorption Performance of Nanostructured Templated Carbon by Tuning Surface Area and Nitrogen Doping, J. Phys. Chem. 116 (2012) 1099-1106.

[34] A. H. Lu, A. Kiefer, W. Schmidt, and F. Schuth, Synthesis of Polyacrylonitrile-Based Ordered Mesoporous Carbon with Tunable Pore Structures, Chem. Mater. 16 (2004) 100-103.

[35] D. Hulicova, J. Yamashita, Y. Soneda, H. Hatori, and M. Kodama, Supercapacitors Prepared from Melamine-Based Carbon, Chem. Mater. 17 (2005) 1241–1247.

[36] G. P. Hao, W. C. Li, D. Qian, A. H. Lu, Rapid Synthesis of Nitrogen-doped Porous Carbon Monolith for CO_2 Capture, Adv. Mater. 22 (2010) 853-857.

[37] J. Lachawiec, R. T. Yang, Isotope Tracer Study of Hydrogen Spillover on Carbon-Based Adsorbents for Hydrogen Storage, Langmuir 24 (2008) 6159–6165.

[38] L. F. Wang, F. H. Yang, R. T. Yang, Hydrogen Storage Properties of B- and N-doped Microporous Carbon, AIChE Journal 55 (2009) 1823-1833.

[39] R. J. J. Janssen, H. van Bekkum, Amination and ammoxidation of activated carbons, Carbon 32 (1994) 1507-1516.

Chapter 5

Air Separation Sorbents: Mixed-Cation Zeolites with Minimum Lithium and Silver

Abstract

Mixed-cation LiSr-LSX, AgCa-LSX and AgSr-LSX containing minimum lithium and silver were prepared by exchanging small fractions of Li^+ into Sr-LSX and Ag^+ into Sr-LSX and Ca-LSX. To avoid diffusion of the Li^+ into the inaccessible sites, the LiSr-LSX sample was exposed to a specifically derived dehydration condition. Similarly, the mixed-silver cation samples were treated to the selected condition post-ion-exchange to allow the Ag^+ to migrate into SII*. Strong evidences were provided that significant fractions of the exchanged Li^+ and Ag^+ remained in SIII and SII* respectively after comparisons of the N_2/O_2 adsorption isotherms and isosteric heats of adsorption of the mixed-cation and pure-cation samples. Furthermore, the mixed-cation LiSr-LSX, AgCa-LSX and AgSr-LSX samples were compared against the pure Li-LSX sample based on their O_2 productivity performance via a PSA simulation model.

5.1 Introduction

In each gas' purest form, the components of air have numerous applications in research and in the industry. Ambient air is constituted by ~78.1% Nitrogen, ~21% Oxygen, ~0.9% Argon and all its trace constituents (Helium, Neon, Krypton and Xenon) amount to less than 1%. There is also small fractions of Water Vapor and Carbon Dioxide in ambient air, but these are usually removed during the pre-purification phase of the air separation process.

Air separation processes employ two basic technologies in principle: cryogenic and noncryogenic (membrane, pressure swing adsorption and vacuum pressure swing adsorption) process. The choice of technology applied hinges on the demand and quality (purity) of the final products. For large scale and high purity oxygen and nitrogen production, cryogenic air separation processes has been the technology of choice though quite energy intensive and requires a high capital cost. The adsorptive processes and specifically, the PSA system operates at near-atmospheric temperatures and are suited for low-to-medium scale production of O_2 and N_2 at relatively high purities [1]. Adsorptive processes have become more efficient and as such, more effective adsorbents are being developed to make them competitive.

A major breakthrough in the development of adsorbents occurred in 1989 with the invention of the Li-LSX zeolite by Chen Chao [2]. It was found after conventionally ion-exchanging Na-LSX by Li^+ that below approximately 70% lithium exchange, the N_2 capacity of Li-LSX remained unchanged as shown in Figure 5.1. However, between 70 to 100% lithium exchange, the N_2 capacity increased linearly [3]. Different cations crystallographically sit in different cation sites [4-6] as seen in Table 5.1 and has been used to explain the above phenomenon. Basically, sorbates (N_2 or O_2 in this case) can only interact and adsorb to cations in the exposed sites and for the case of Li-X, only site III (SIII) as shown in Figure 5.2 are accessible

to the sorbates while lithium cations in the lower sites (SI and SII) are inaccessible to N_2 or O_2. This is due to the electron shielding effect of oxygen in the surrounding framework and the small size of the lithium ion.

Table 5.1 Cation site occupancies in dehydrated X zeolites (maximum = 96 monovalent cations per unit cell for Si/Al = 1).

Zeolite	Al / Unit Cell	Sites				
		I	I'	II	II'	III
Li-LSX [4]	95.8		27.2	33.9		32.4
Li-LSX [5]	96		33	34		29
Na-X (13X) [29]	81	3.8	32.3	30.8		7.9
K-X [30]	87	9	13	26		38
Ca-X [31]	86	7.5	17.3	17.3	9.0	

Pure and mixed-cation Zeolites are required to be thermally treated prior to isotherm measurements not just to get rid of adsorbed atmospheric gases but also to allow the exchanged cations to diffuse to their preferred equilibrium sites. The treatment conditions can vary with different sorbents between 623 to 723 K and a minimum of four hours for pure samples. Hutson et. al. [7] for example, showed that heating Ag-X to 723 K allowed the silver cations to migrate from the conventional site SII location to a novel and more sorbate accessible SII* site. In the case of mixed-cation zeolites such as CeNaCa-X, LiNa-LSX, and NaSr-X zeolites, it has been observed that the smaller or lighter cations tend to diffuse to the lower numbered sites i.e. SI, SI', SII" and SII. For the mixed-cation examples above, Na^+, Ca^{2+} will migrate to the lower sites while Ce^{3+} and Sr^{2+} are at the outer sites [8].

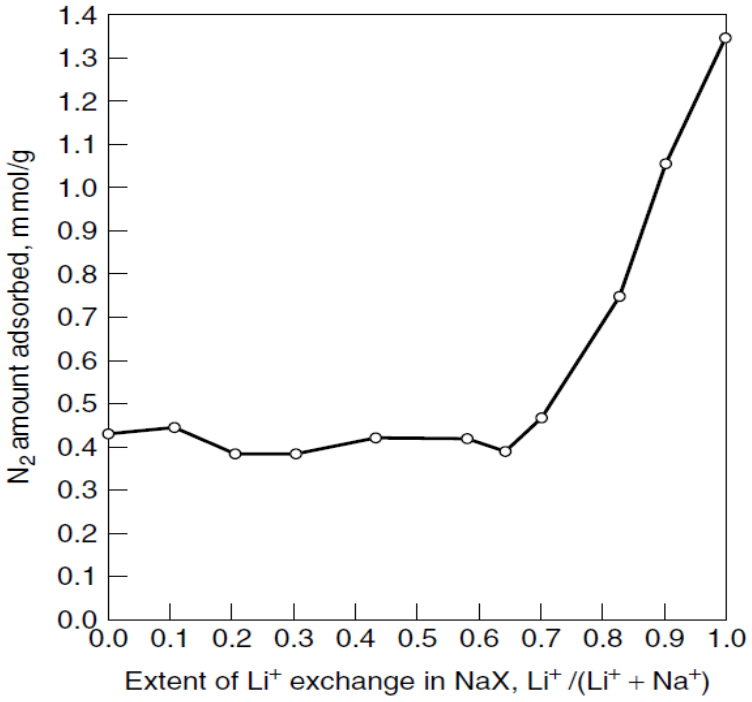

Figure 5.1 Dependence of nitrogen adsorption at 296 K and 101 kPa on fractional Na^+ exchange by Li^+ in LSX.

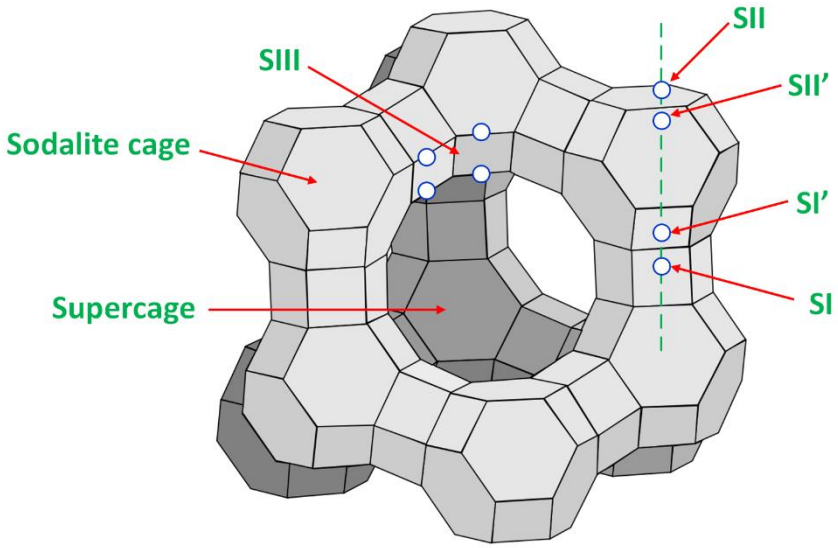

Figure 5.2 Unit cell of faujasite-type (X and Y) zeolites, including cation sites.

Li-LSX, since its invention, is has been the preferred sorbent for air separation in PSA or vacuum pressure swing adsorption processes (VPSA). Mixed-cation LSX zeolites containing alkali-earth metal cations have exhaustively been investigated as potential alternatives over the last few decades [9-14]. Since alkali-earth metal cations are divalent, they form strong electrostatic interactions with the sorbates of interest (N_2 and O_2). Besides the alkali-earth metal cations, silver has also shown to strongly affect the adsorptive properties of zeolites [15-16] as was seen in the synthesis of mixed LiAg-LSX. Hutson et al. [17], showed that by merely adding small amounts of silver coupled with specific treatment conditions results in a sample with enhanced adsorptive characteristics for air separation. However, the most studied binary exchanged X-zeolites has been lithium-calcium and lithium-strontium mixtures. Coe et al. [9-12], Sircar et al. [13], and Chao et al. [14], all conducted impactful studies on the above samples containing varying degrees of the binary mixtures. The results all showed increased N_2 adsorption capacities, but the mixed-cation zeolites required over 70 mol% lithium cations to see the lithium effect.

Until a few years ago, the main source of lithium demand came from the glass-ceramics industry as an added agent to enhance the mechanical strength . However, with the high demand of lithium for lithium-ion batteries (energy storage) and its dwindling reserves worldwide, the price of lithium has seen a steady rise and is projected to maintain the trend for the foreseeable future. It is hence imperative to develop efficient zeolites for air separation with significantly lower lithium content or completely replace it with abundant and low-cost alkali-earth metal cations such as Sr^{2+} or Ca^{2+}. In the binary mixtures developed and studied by Coe et al., Sircar et al., and Chao et al., Li-LSX was first prepared then followed by the alkali-earth metal cation exchange. As mentioned earlier, well over 70% lithium cation was needed to see the effect of lithium. The ion-exchange strategy in this work for the preparation of LiSr-LSX for example was designed to limit

the amount of lithium cations that sits in the lower-numbered sites (SI, SI' SII' and SII). The procedure employed here was to exchange the as-synthesized Na-LSX to a fully-exchanged Sr-LSX, followed by exchanging a small fraction of the Sr^{2+} by Li^{+} in an aqueous phase [18]. As opposed to pretreating the mixed-cation sample for a minimum of four hours as required for zeolites, the ion-exchanged LiSr-LSX was dehydrated at the lowest possible temperature and at a relatively short time to allow the Li^{+} to stay in site III (SIII) and hence, avoid migration and equilibration of the Li^{+} to the lower-numbered sites.

Ten synthetic zeolites in total were studied in this work that include four pure samples (Ca-LSX, Li-LSX, Sr-LSX and Ag-LSX) and six mixed-cation samples ($Ag_{2.0}Ca_{47.0}$-LSX, $Ag_{3.0}Ca_{46.5}$-LSX, $Ag_{2.0}Sr_{47.0}$-LSX, $Ag_{3.0}Sr_{46.5}$-LSX, $Li_{2.74}Sr_{46.63}$-LSX, $Li_{3.13}Sr_{46.44}$-LSX) where for example, $Ag_{2.0}Ca_{47.0}$-LSX represents 2.0 mol% Ag and 47.0 mol% Ca. The N_2/O_2 capacities of these zeolites will be compared along with their PSA/VPSA separation performance via a PSA simulation model.

5.2 Experimental Section

5.2.1 Materials

All analysis gases: Helium (99.995%, prepurified), Nitrogen (99.998%, prepurified), and Oxygen (99.6%, extra dry) were obtained from Cryogenic Gases. The as-synthesized Na-LSX (powder form) was supplied by Luoyang Jianlong Micro-Nano New Materials Co., Ltd., China. The Na-LSX sample had a Na exchange extent of 99.5% (Na/(Na + K)) and a Si/Al ratio of 1.005. Calcium Dihydrate 99% and Lithium Chloride 99% were obtained from Sigma Aldrich while Strontium Nitrate Anhydrous (ACS) and Silver Nitrate 99.9% were obtained from Fisher Chemical and Strem Chemicals respectively.

5.2.2 Preparation of Ca-LSX Zeolite

Ca-LSX was obtained by ion-exchanging Na-LSX with a 1.0 M solution of calcium chloride ($CaCl_2$) at ambient conditions and stirred for a minimum of 6 h. The solution contained ~3 equivalent excess of Ca^{2+} to Na^+ and was decanted after each ion-exchange and repeated six times. After the final exchange, the sample was vacuum filtered, washed with copious amounts of deionized water and air dried at 298 K for 24 h.

5.2.3 Preparation of Sr-LSX Zeolite

A 1.0 M Strontium Nitrate, $Sr(NO_3)_2$ solution with a 3.8-fold equivalent excess was used to prepare Sr-LSX by ion-exchanging with Na-LSX at mild temperature conditions. The $Sr(NO_3)_2$ solution was adjusted to a pH of 7 using $Sr(OH)_2$ which helps to prevent hydrolysis and the collapsing of the zeolite crystal structure during the ion-exchange process. A total of six ion-exchanges were carried out and the solution was decanted after each exchange procedure and refilled with a fresh strontium nitrate solution. After the final exchange, the sample was vacuum filtered, washed with copious amounts of deionized water and air dried at 298 K for 24 h.

5.2.4 Preparation of Ag-LSX Zeolite

The pure Ag-LSX zeolite sample was prepared after two consecutive ion-exchanges using a 1.0 M Silver Nitrate ($AgNO_3$) solution containing 2.4-folds equivalent excess required for a 100 % exchange. The $AgNO_3$ ion-exchange solution was heated to a mild boil and immediately allowed to cool and decanted. After the second exchange, the solution was vacuum filtered, washed with copious amounts of DI water, and dried at atmospheric conditions in a dark environment however. The final product was then stored in a dark area until prior to isotherm measurements.

5.2.5 Preparation of Mixed-Cation LiSr-LSX Zeolite

A similar procedure as that used by Epiepang et al. [18] was applied here for the preparation of LiSr-LSX. A predetermined equivalent amount of Li^+ enough to exchange a desired target Sr^{2+} in the pure Sr-LSX zeolite - with the hypothetical assumption that all the Li^+ would undergo ion-exchange - was used to prepare the mixed-cation LiSr-LSX. To do so, a 0.1 M Lithium Chloride (LiCl), with Li^+ equivalents of 0.15 and 0.3 solution were used to exchange with 1.5 g of Sr-LSX. The mixtures were stirred for 1 h at 298 K followed by vacuum filtration without washing and dried in an oven at atmospheric conditions for 24 h. Since the Li^+ is significantly smaller than Ca^{2+}, it is worth noting that the actual amount of Li^+ exchanged was significantly less than the targeted estimate in the aqueous phase.

5.2.6 Preparation of Mixed-Cation AgCa-LSX and AgSr-LSX Zeolites

The AgCa-LSX and AgSr-LSX were prepared by ion-exchanging the pure Ca-LSX and Sr-LSX zeolites with a 0.025 M solution of $AgNO_3$. The silver nitrate solution contained a cation content with an equivalent to the targeted amounts. The silver solution was heated to mild boil while stirring for 2 h mainly because the silver cation quickly and easily exchanges [19]. After allowing the resulting mixture to cool and settle, it was vacuum filtered and washed with copious amounts of DI water. The mixed-cation zeolites were eventually dried at atmospheric conditions and stored in a dark area until being dehydrated in vacuo prior to isotherm measurements and sample characterizations.

5.2.7 Sample Characterization

The compositional characteristics of the prepared samples were done by inductively coupled plasma – optical emission (ICP-OES) system at the University of Science and Technology - School of Energy and Environment Engineering in Beijing, China. The mixed-cation samples

were specifically analyzed for Li and Ag content and results of these analyses are given in Table 5.2. The samples will be identified henceforth with respect to the number of charge-compensating cations present in the zeolite's unit cell. The six mixed-cation zeolite samples studied are as follows: $Li_{2.74}Sr_{46.63}$-LSX, $Li_{3.13}Sr_{46.44}$-LSX, $Ag_{2.0}Ca_{47.0}$-LSX, $Ag_{3.0}Ca_{46.5}$-LSX, $Ag_{2.0}Sr_{47.0}$-LSX, and $Ag_{3.0}Sr_{46.5}$-LSX. For example, the sample $Li_{2.74}Sr_{46.63}$-LSX refers to low-silica X-type zeolite containing on average, 2.74 Li^+ and 46.63 Sr^{2+} per unit cell.

5.2.8 Sample Dehydration and Isotherm Measurements

Micromeritics ASAP 2020 sorptometer which uses a volumetric measurement technique was used to carry out all pure gas adsorption equilibrium analyses on the studied samples. Prior to isotherm measurements, *in vacuo* sample dehydration was done as expected for the removal of all adsorbed atmospheric gases and moisture.

The dehydration conditions varied per studied sample and were chosen for reasons to be explained next in the results and discussion section. The pretreatment conditions were as follows: 6 h at 623 K for Ca-LSX, Li-LSX, and Sr-LSX; 5 h at 723 K for Ag-LSX, $Ag_{2.0}Ca_{47.0}$-LSX, $Ag_{3.0}Ca_{46.5}$-LSX, $Ag_{2.0}Sr_{47.0}$-LSX, and $Ag_{3.0}Sr_{46.5}$-LSX; and 1 h at 623 K for $Li_{2.74}Sr_{46.63}$-LSX and $Li_{3.13}Sr_{46.44}$-LSX. The ramp rate for all pretreatment conditions was 283 K/min under vacuum of 30 μmHg for the samples dehydrated for a minimum of 5 h and 60 μmHg for samples dehydrated for 1 h. It has been shown [20] that Li-LSX fully dehydrates at 623 K hence the same conditions were applied to Ca-LSX and Sr-LSX. The 1 h 623 K condition was chosen for the LiSr-LSX samples allowed most of the exchanged Li^+ to remain in SIII and avoid diffusion to the lower-numbered or inaccessible sites. Hutson et al. [7], showed that pretreating Ag-LSX at 723 K allowed Ag^+ to migrate into a new site called SII* which in combination with the silver in SIII, improved the overall N_2 adsorption capacity of the sample. It was observed that dehydrating the Ag-LSX

zeolite at 723 K displayed a deep yellow color while the mixed-cation AgSr-LSX and AgCa-LSX samples turned into a dark grey upon treatment at the stated conditions above. The changes in color are related to an autoreductive (reduction of the transition metal ion and the oxidation of H_2O or lattice O_2) process that involves oxygen [21].

5.3 Results and Discussion

5.3.1 Analytical Sample Characterization

Table 5.2 Elemental Composition of Sorbents

	Mole Ratio					
Zeolite	Si/Al	Li/Al	Ca/Al	Ag/Al	Sr/Al	Na/Al
Na-LSX	1.005	--	--	--	--	0.995
Ca-LSX	1.005	--	0.991	--	--	--
Sr-LSX	1.005	--	--	--	0.995	--
$Ag_{2.0}Ca_{47.0}$-LSX	1.005	--	--	0.02	0.47	--
$Ag_{3.0}Ca_{46.5}$-LSX	1.005	--	--	0.03	0.465	--
$Ag_{2.0}Sr_{47.0}$-LSX	1.005	--	--	0.02	0.47	--
$Ag_{3.0}Sr_{46.5}$-LSX	1.005	--	--	0.03	0.465	--
$Li_{2.74}Sr_{46.63}$-LSX	1.005	0.0274	--	--	0.4663	--
$Li_{3.13}Sr_{46.44}$-LSX	1.005	0.0313	--	--	0.4644	--

The results obtained from ICP-OES are reported in Table 5.2 and are given on a mole percent and on a dry basis. The six mixed-cation zeolite samples $Li_{2.74}Sr_{46.63}$-LSX, $Li_{3.13}Sr_{46.44}$-LSX, $Ag_{2.0}Ca_{47.0}$-LSX, $Ag_{3.0}Ca_{46.5}$-LSX, $Ag_{2.0}Sr_{47.0}$-LSX, and $Ag_{3.0}Sr_{46.5}$-LSX were analyzed for the Li^+ and Ag^+ contents respectively and will henceforth be referred to as stated above unless otherwise stated.

5.3.2 Nitrogen Adsorption Isotherms

Micromeritics ASAP 2020 uses the volumetric technique for the measurements of adsorption capacities at pressures up to 101 kPa. Prior to the equilibrium adsorption measurements, all samples were dehydrated *in vacuo* at their specific pretreating conditions. Pure N_2 gas adsorption isotherms were measured at three temperatures – 298, 323 and 343 K as shown in Figures 5.3 – 5.5 respectively. Comparison of the isotherms in Figure 5.3 (N_2 adsorption at 298 K and 101 kPa) shows that the exchange of very small amounts of Ag^+ and Li^+ with the pure Ca-LSX and Sr-LSX samples, improves their N_2 adsorption capacities. The higher N_2 capacities of the mixed-cation samples (outperforming their pure precursors) makes them very attractive materials for air separation via PSA or VPSA. The boost in the N_2 adsorption capacities for the mixed-cation (Silver-alkali earth metal cations) is a result of the combination of the Ag^+ in SII* and SIII whereas the capacity boost for the LiSr-LSX samples is solely based on the presence of some Li^+ in SIII.

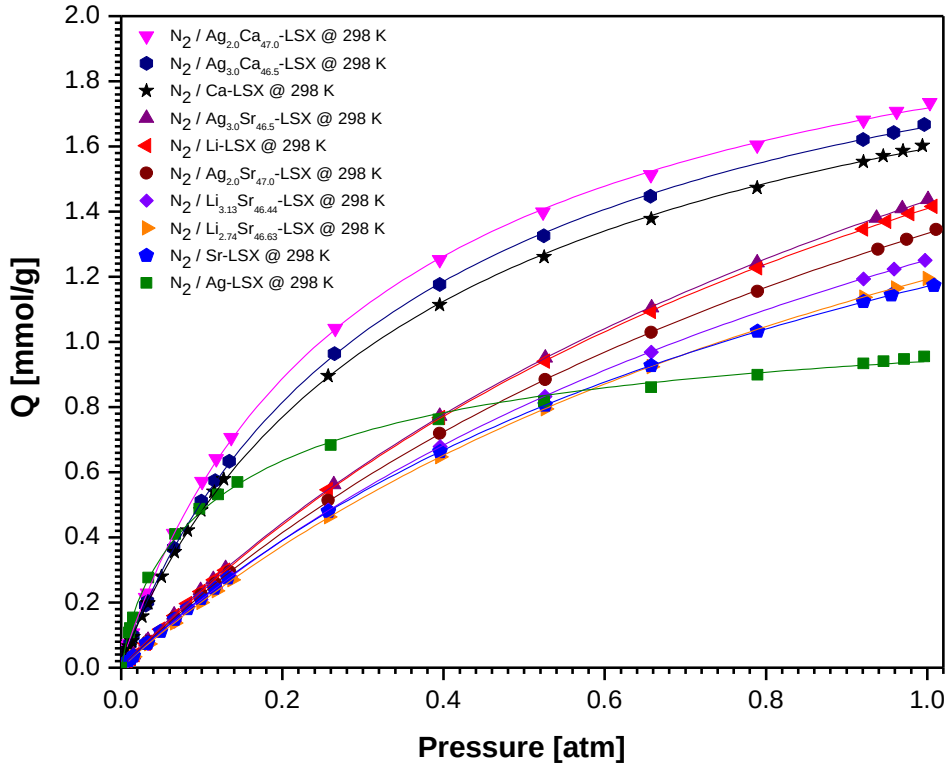

Figure 5.3 N_2 adsorption isotherms measured at 298 K and 101 kPa on representative sorbents.

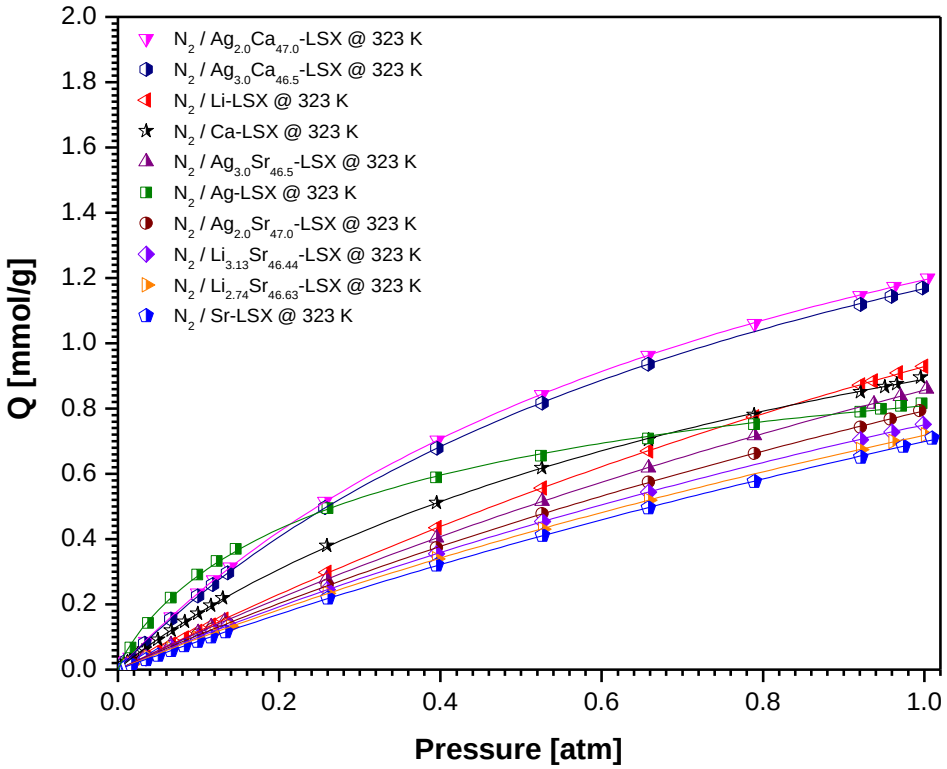

Figure 5.4 N_2 adsorption isotherms measured at 323 K and 101 kPa on representative sorbents.

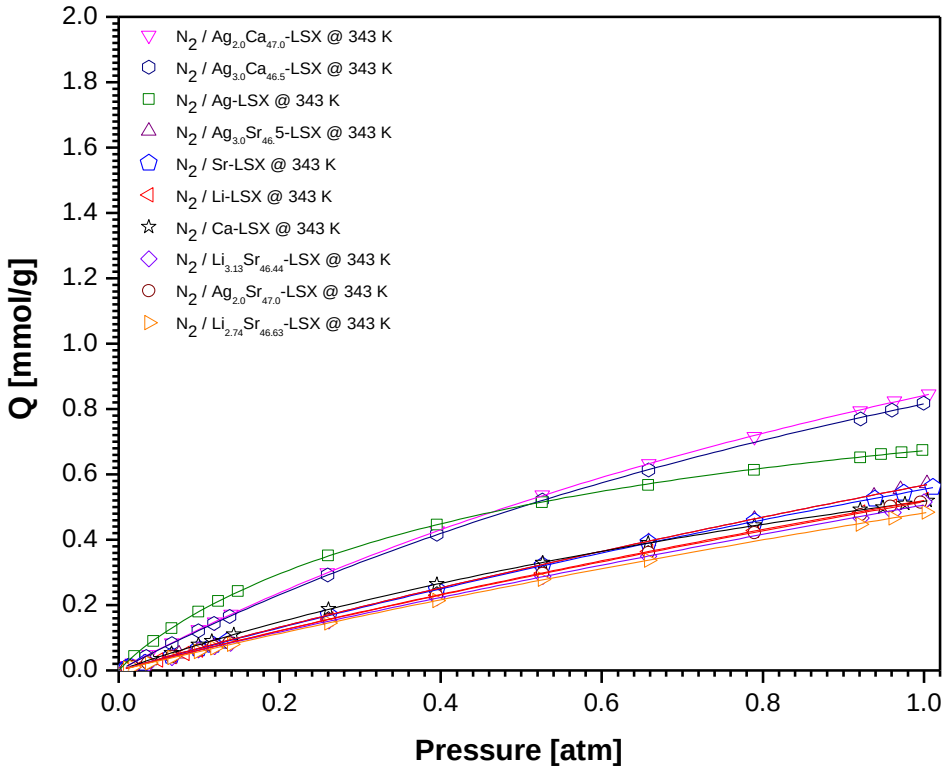

Figure 5.5 N_2 adsorption isotherms measured at 343 K and 101 kPa on representative sorbents.

5.3.3 Oxygen Adsorption Isotherms

O_2 experimental adsorption isotherms are presented in Figures 5.6 – 5.8. These show combined isotherms at 298, 323 and 343 K respectively. Upon inspection of the O_2 adsorption isotherms, it can be seen that Ca-LSX with Ca^{2+} having a higher polarizability than Sr^{2+}, Li^+ and Ag^+, adsorbed significantly more oxygen than all the studied sorbents. The lower the O_2 capacities, the more favorable they are for PSA air separation. This thereby makes the mixed-cation samples quite interesting materials for the PSA system. These results also indicates the presence of Li^+ in SIII and Ag^+ in SII* and SIII in the respective mixed-cation samples.

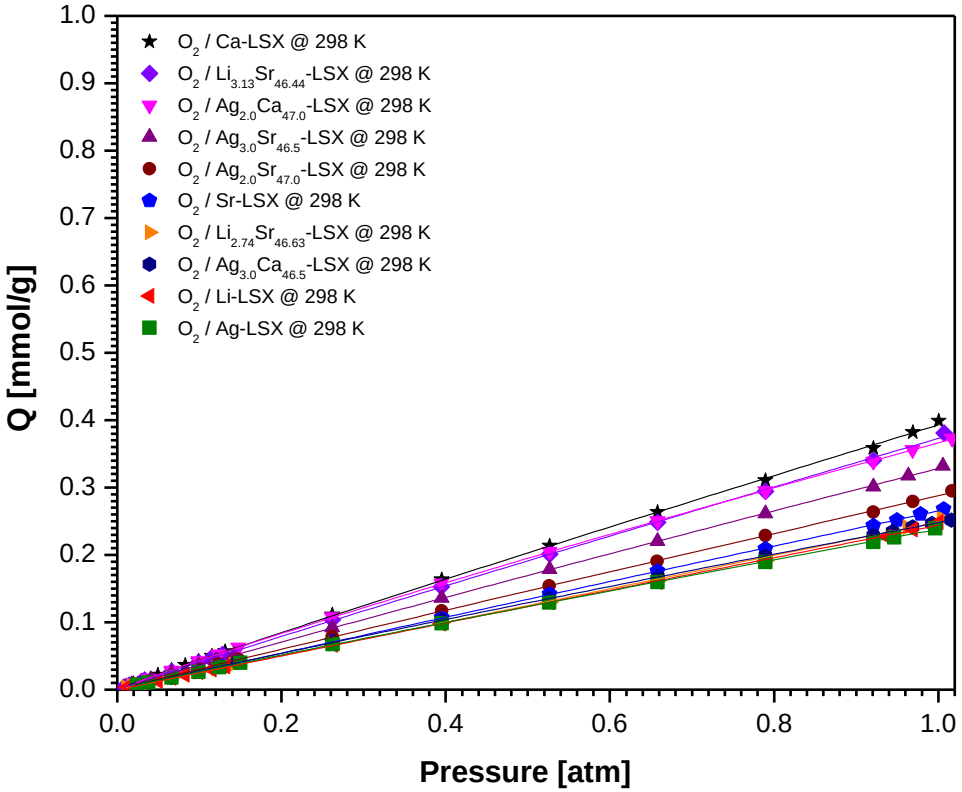

Figure 5.6 O_2 adsorption isotherms measured at 298 K and 101 kPa on representative sorbents.

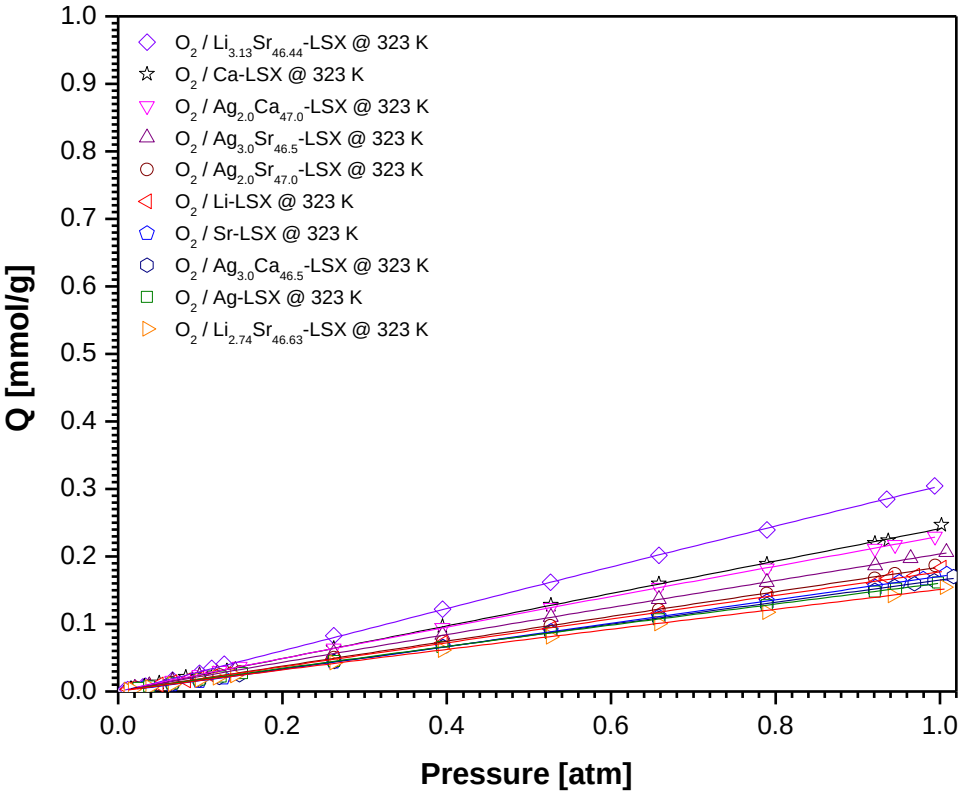

Figure 5.7 O_2 adsorption isotherms measured at 323 K and 101 kPa on representative sorbents.

The location of these cations in the zeolite's framework is key to the observed results for both gases simply because interactions between the cations and the sorbate strictly dictates the magnitude of the adsorbed capacities. Although cations in SII (as well as SIII) participate in adsorption, smaller cations such as Li^+, witnesses partial shielding which is as a result of the electric field around the cation from the surrounding oxygen. The shielding, which is cation size dependent, significantly lowers interactions between the SII cations and the sorbate molecules. Cations such as calcium and strontium have significantly less shielding due to their size and hence contacts more sorbate molecules.

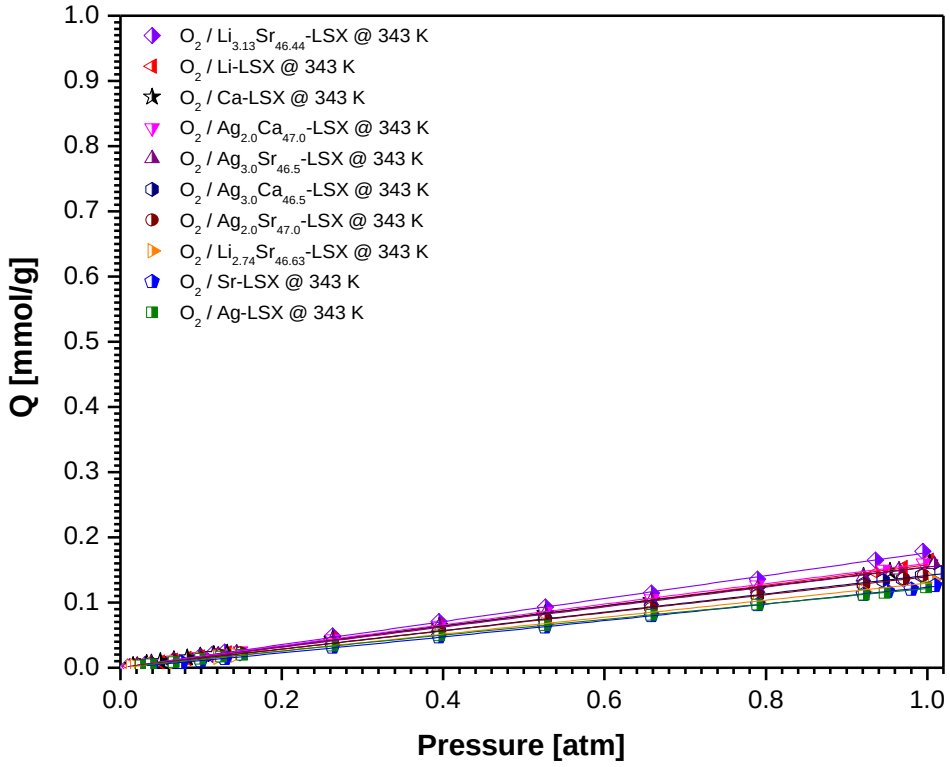

Figure 5.8 O_2 adsorption isotherms measured at 343 K and 101 kPa on representative sorbents.

5.3.4 Pure Isotherm Fitting Model

The Freundlich-Langmuir (F-L) isotherm model shown in Equation (5.1) was used as the base model to fit all experimental equilibrium adsorption data for both sorbates. A good fitting model is quite important for the derivation of the heats of adsorption [22-23]. Due to the sensitivity of the fitting models, failure to apply the best choice can significantly affect thermodynamic calculations. The fitted data can be found in the supplementary material.

$$Q = \frac{Q^*_{sat} K C^n}{1 + K C^n} \tag{5.1}$$

Where Q is the equilibrium amount adsorbed, Q^*_{sat} is the adsorption capacity of the system, K is the affinity constant for adsorption, C is the equilibrium aqueous phase concentration while n is the index of heterogeneity.

5.3.5 Heats of adsorption

$$\ln\left(\frac{P_1}{P_2}\right) = \frac{\Delta H_{vap}}{R}\left(\frac{1}{T_2} - \frac{1}{T_1}\right) \tag{5.2}$$

Where ΔH_{vap} is the heat of adsorption, with R being the gas constant (8.3145 J/mol.K), P_1 and P_2 are the corresponding pressures at temperatures T_1 and T_2. The Clausius -Clapeyron relation [24-26] shown in Equation (5.2) above is commonly used (and was the tool of choice here as well) for the estimation of the isosteric heats of adsorption of the studied gas-sorbent pairings. Another great tool for the estimation of physical adsorption is the Theoretical Total Sorbate-Sorbent Potential (ϕ_T) [27]. It should however be noted that the sorbate-sorbent potential calculation estimates only for a gas molecule and a free isolated cation.

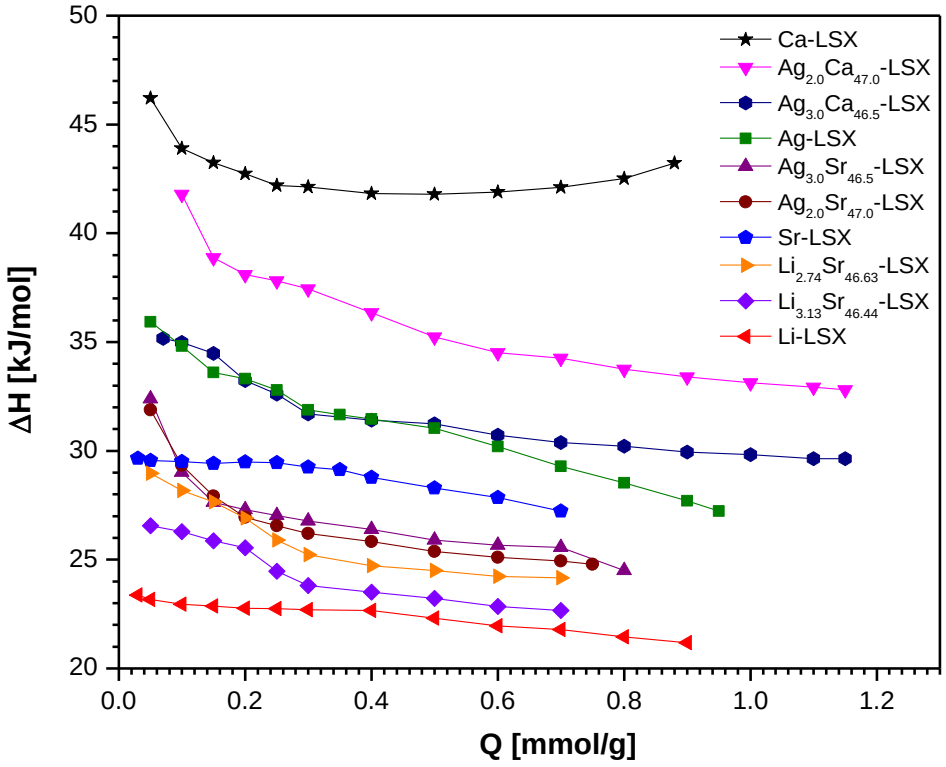

Figure 5.9 N_2 heats of adsorption on representative sorbents.

The N_2 and O_2 isosteric heats of adsorption on various sorbents are shown in Figures 5.9 and 5.10 respectively. Ca-LSX as expected, has significantly stronger interactions with N_2 as opposed to the other cations as it shows the highest heats of adsorption in the following order: Ca-LSX > $Ag_{2.0}Ca_{47.0}$-LSX > $Ag_{3.0}Ca_{46.5}$-LSX > Ag-LSX > $Ag_{3.0}Sr_{46.5}$-LSX > $Ag_{2.0}Sr_{47.0}$-LSX > Sr-LSX > $Li_{2.74}Sr_{46.63}$-LSX > $Li_{3.13}Sr_{46.44}$-LSX > Li-LSX. This clearly shows that the incorporation (ion-exchange) of Ag^+ and Li^+ in the pure precursors lowers the heats of adsorption which makes it an attractive property for air separation by PSA. Another important observation is that all the heats of adsorption of the mixed-cation samples are between their respective pure precursors which is an indication that the sorbate molecules were interacting with both exposed cations in the mixed-cation zeolites.

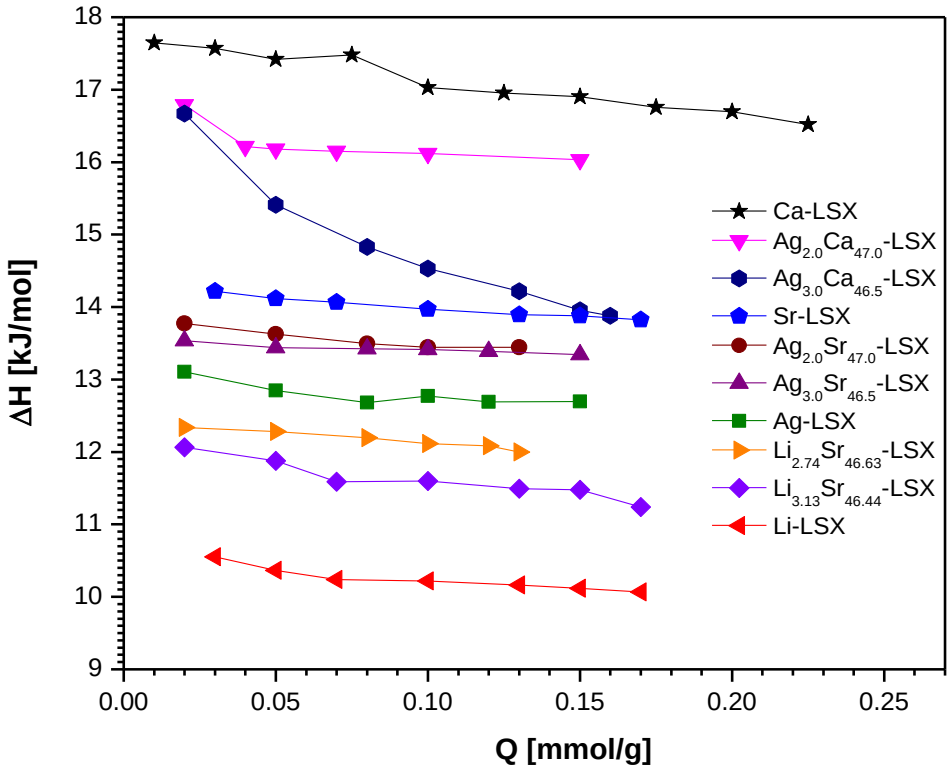

Figure 5.10 O_2 heats of adsorption on representative sorbents.

For the O_2 heats of adsorption, van der Waals interactions were the main cause for adsorption. Ca^{2+} and Sr^{2+} both have higher polarizabilities than the other cations hence their stronger adsorption energies. The trend observed for O_2 is almost identical to that of N_2 besides the switch of position between Sr-LSX and Ag-LSX zeolites.

5.3.6 Cation Site Location

Solid State NMR and Neutron Diffraction methods have been used to determine the lithium cations in the extraframework of type A, X and Y zeolites [5-6]. It was found that the 96 Li^+ available in Li-LSX were evenly distributed across SI', SII and SIII with 32 cations in each site as opposed to 22 cations in SIII for the X type zeolite. Table 5.1 for example, shows the occupancy

of cations in dehydrated X Type zeolites with pure cations. Yang et al. [28] showed the relationship between SIII Li^+ occupancy in mixed-cation LiNa-LSX zeolite and the heats of adsorption of N_2. It clearly shows that N_2 heats of adsorption can indeed be used to indicate the presence of Li ions in SIII for mixed-cation zeolites. Other analytic and characterization techniques such as Single Crystal XRD, Powder XRD, and Powder XRD & Neutron Diffraction have long been used to locate calcium ions in Ca-X zeolites. Results from these methods showed that a fully dehydrated calcium-exchanged faujasite-type sample had Ca^{2+} distributed among sites SI, SI' and SII [32-43].

The characterization of strontium exchanged faujasite (Sr-X) has only been done by X-ray diffraction methods (Single Crystal, Powder and Anomalous XRD) [44-46]. The strontium cations are mostly distributed between SI, SI' and SII. In comparison with other cations, SI in Sr-X occupies more cations. SII is also relatively populated due to its electrostatic repulsion minimum [47]. It must be noted that the more dehydrated the sample, the more cations migrate to SI because it offers an octahedral interaction using six neighboring oxygen atoms.

Powder, Single Crystal, Anomalous Powder XRD and Powder Neutron Diffraction are all techniques that have been used to determine cation distribution in Ag-X, Ag-Y, Ag-LSX and silver-containing mixed-cation zeolites [4,7,48]. Silver among the few cations that basically occupy almost all sites in the zeolite except SIII and like potassium cations, do not respect the rule stating that SI and SI' can not be simultaneously occupied in the same hexagonal prism. As mentioned earlier, Figure 5.11 shows the position of extraframework sites and of great interest is the novel SII* when the sample is pretreated at 723 K.

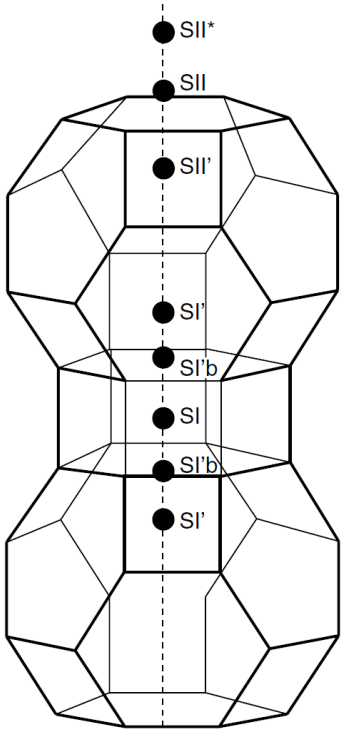

Figure 5.11 Extraframework sites for Ag+ in the faujasite structure.

It should be noted that no site distribution studies were carried out for the samples in this work. It is however expected that only the SII and SII* Ag cations and Ca^{2+} and Sr^{2+} in the AgCa-, AgSr-LSX mixed-cation samples interact with the sorbates. Likewise, the SIII Li^{+} and the SII Sr^{2+} in the LiSr-LSX mixed-cation zeolites are accessible to the sorbates.

5.3.7 PSA (VPSA) Simulation

Figure 5.12 shows a standard and commercially used five-step PSA or VPSA cycle similar to that described by Epiepang et al. [18] Step I of the five-step cycle is the Feed (air) Pressurization step, Step II is the High-pressure Feed, Step III is the Co-current Depressurization step, while Steps IV and V are the Countercurrent Blowdown and the Low Pressure Purge.

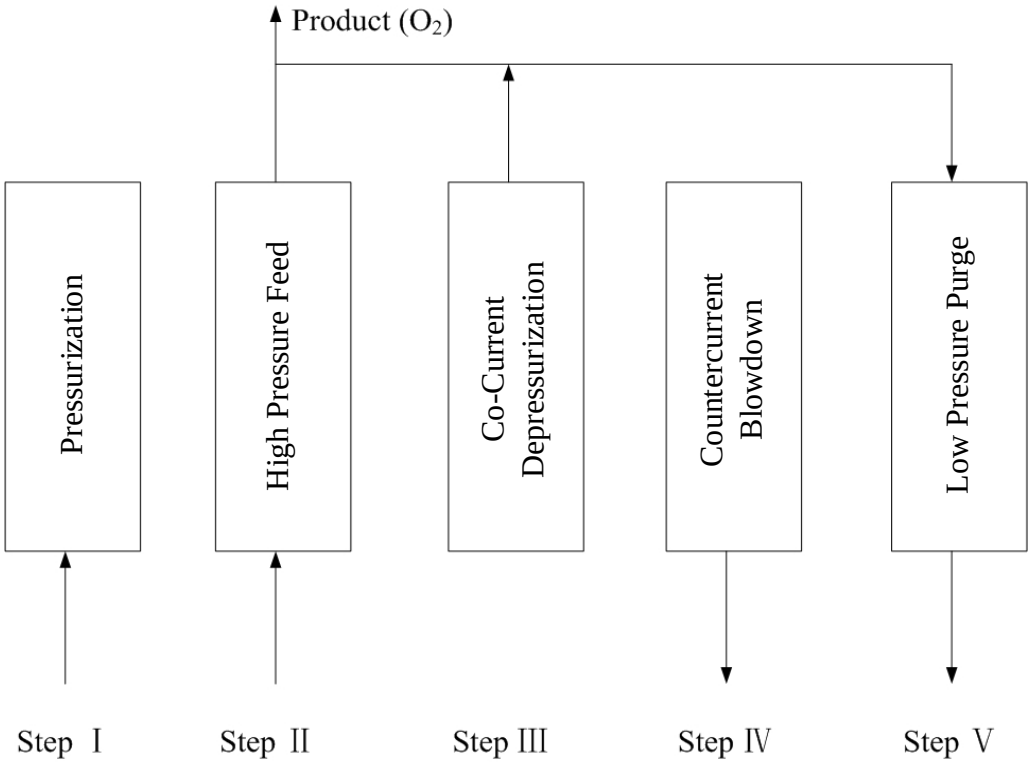

Figure 5.12 PSA cycle configuration.

The completion time for the entire cycle was set at 2.5 minutes with each step running for an equal duration of 30 seconds. Since Argon (Ar) and O_2 have similar adsorption capacities on LSX zeolites, the O_2 component was approximated to be 22% (i.e. 21% O_2 and 1% Ar) hence, only O_2 and N_2 were assumed as the basic component of the simulation model. Figure 5.12 also shows that the product of each cycle comprised of a volumetric mixture of the output stream from the feed and co-current depressurization steps. In addition, a fraction of the product stream was used as a countercurrent purge for the bed in Step V.

PSA systems are specifically judged on three inter-related results which sums up its performance for oxygen production. The three results defined in Equations 5.3 – 5.5 are i) O_2

product purity, ii) O_2 product recovery, and iii) O_2 product throughput respectively. In principle, fixing two of the inter-related results sets the third provided the PSA conditions are optimized.

$$\text{Product Purity} = \frac{\text{Amount of } O_2 \text{ from Steps II and III}}{\text{Amount of } N_2 \text{ and } O_2 \text{ from Steps II and III}} \tag{5.3}$$

$$\text{Product Recovery} = \frac{(O_2 \text{ from Steps II and III}) - (O_2 \text{ from Step VI})}{(O_2 \text{ fed in Steps I and II})} \tag{5.4}$$

$$\text{Product Throughput} = \frac{\text{Amount of } O_2 \text{ produced per hour } (^{t}/_{h})}{\text{Amount of sorbent used in the bed (t)}} \tag{5.5}$$

The product throughputs of the sorbents developed in this work were studied under various cycle conditions in order to compare their performances. It must be noted that for a fair performance comparison, cycle conditions were optimized such that two of the inter-related results, in this case, the obtained product purity and product recovery were held the same in every simulation run.

A detailed explanation of both the numerical methods and mathematical model used for this PSA simulation model was presented by Rege et al. [49] The major assumptions made for this model include a two-component gas mixture flowing through a fixed adiabatic bed packed with spherical adsorbent particle; the diffusional resistance was assumed to be negligible since diffusion of the sorbates is relatively fast considering the long cycle time; the axial dispersion of heat and mass transfer was accounted for but dispersion in the radial direction was assumed negligible as well; local equilibrium existed between the gas and solid phases for each gas component; the gas was assumed to have constant viscosity and heat capacity while the axial pressure drop was neglected and the ideal gas law was assumed because the pressures involved were at atmospheric conditions.

Tables 5.3 and 5.4 shows the Langmuir-Freundlich fitting constants including the sample's heats of adsorption and the PSA bed characteristics and the applied operating conditions

respectively. The constants shown in Table 5.3 were obtained using the Langmuir-Freundlich isotherm with temperature dependence on the experimental pure component equilibrium isotherms. Under mixture conditions, the equilibrium loadings were predicted by the Extended Langmuir-Freundlich (Equation 5.6) in the simulation model while the Langmuir-Freundlich parameters assumed are given in Equation 5.7. The Langmuir-type model is simple yet a reasonably good way of fitting binary experimental data, as shown by Mulgundmath et al. [50].

$$q_k^* = \frac{q_{m_k} b_k p_k^{n_k}}{1+\sum_{j=1}^{m} b_k p_k^{n_k}} \quad k = 1,2 \tag{5.6}$$

$$q_m = k_1 e^{(k_2/T)} \quad and \quad b = k_3 e^{(k_4/T)} \tag{5.7}$$

5.3.8 Simulation Results

The feed pressures, PH, of 120 and 150 kPa with various pressure ratios (PH/PL with PL being the desorption pressure) were investigated. It must also be noted that the same pressure ratios were employed for the comparison of the studied adsorbents and a summary of the simulation conditions and separation results are given in Table 5.5. Here-in, the feed and purge velocities were optimized to achieve the same product purity and recovery near 95% and 52% for all sorbents respectively.

Table 5.3 Temperature-Dependent parameters for Langmuir-Freundlich Isotherm of N_2 and O_2

Sorbent	Sorbate	k_1 (mmol/g)	k_2 (K)	k_3 (atm^{-1})	k_4 (K)	n	ΔH (kcal/mol)
$Ag_{2.0}Ca_{47.0}$-LSX	O_2	2.28007	78.83	2.01E-04	1952.57806	0.99607	3.858
$Ag_{2.0}Ca_{47.0}$-LSX	N_2	1.63201	98.0495	1.29E-05	3690.92116	0.97852	8.431
$Ag_{3.0}Ca_{46.5}$-LSX	O_2	4.21151	117.80771	5.36E-04	1292.48613	0.9859	3.459
$Ag_{3.0}Ca_{46.5}$-LSX	N_2	1.84434	62.1356	2.13E-05	3501.69557	0.97608	7.447
$Ag_{3.0}Sr_{46.5}$-LSX	O_2	0.52991	1492.8597	0.00165	275.35234	0.96207	3.203
$Ag_{3.0}Sr_{46.5}$-LSX	N_2	2.1373	871.5279	0.00221	836.21744	0.80513	6.287
$Ag_{2.0}Sr_{47.0}$-LSX	O_2	0.88625	1602.17714	0.00117	74.03769	0.98061	3.227
$Ag_{2.0}Sr_{47.0}$-LSX	N_2	7.70095	1106.65628	1.06E-04	1113.96336	0.9045	6.206
$Li_{3.13}Sr_{46.44}$-LSX	O_2	1.56223	2.735	0.00106	1697.27728	1.09953	2.759
$Li_{3.13}Sr_{46.44}$-LSX	N_2	1.38733	214.4702	8.83E-05	2708.9239	0.99472	5.734
$Li_{2.74}Sr_{46.63}$-LSX	O_2	0.89403	703.1392	0.00119	927.37	1.00103	2.900
$Li_{2.74}Sr_{46.63}$-LSX	N_2	1.7834	1040.3929	6.82E-04	1039.2506	0.9765	6.074

Figures 5.13 and 5.14, which shows the effects of pressure ratio on O_2 productivity for the various sorbents, are extracts from Tables S5.3 through S5.8 in the supplementary Information while Table 5.4 shows the PSA bed characteristics and operating conditions used. Interpretation of the results show the same O_2 product purity and recovery of almost 95% and 52% respectively while the O_2 productivity increases with increasing pressure ratio. Li-LSX show the best VPSA performance, outperforming $Ag_{3.0}Ca_{46.5}$-LSX which had the highest N_2 adsorption capacity.

Table 5.4 Adsorption Bed Characteristics and Operating Conditions for PSA Simulations.

Bed length	2.5 m
Diameter of sorbent	1.0 m
Bed external porosity	0.4
Bed density	720 kg/m^3
Heat capacity of gases	28.72 J/mol/K
Heat capacity of sorbent	1.17 kJ/kg/K
Ambient temperature	298 K
Feed gas temperature	298 K
Feed gas composition	78% N_2, 22% O_2
Axial dispersion coefficient (D_{ax})	5×10^{-5} m^2/s
Effective heat conductive	0.2 w/m/K

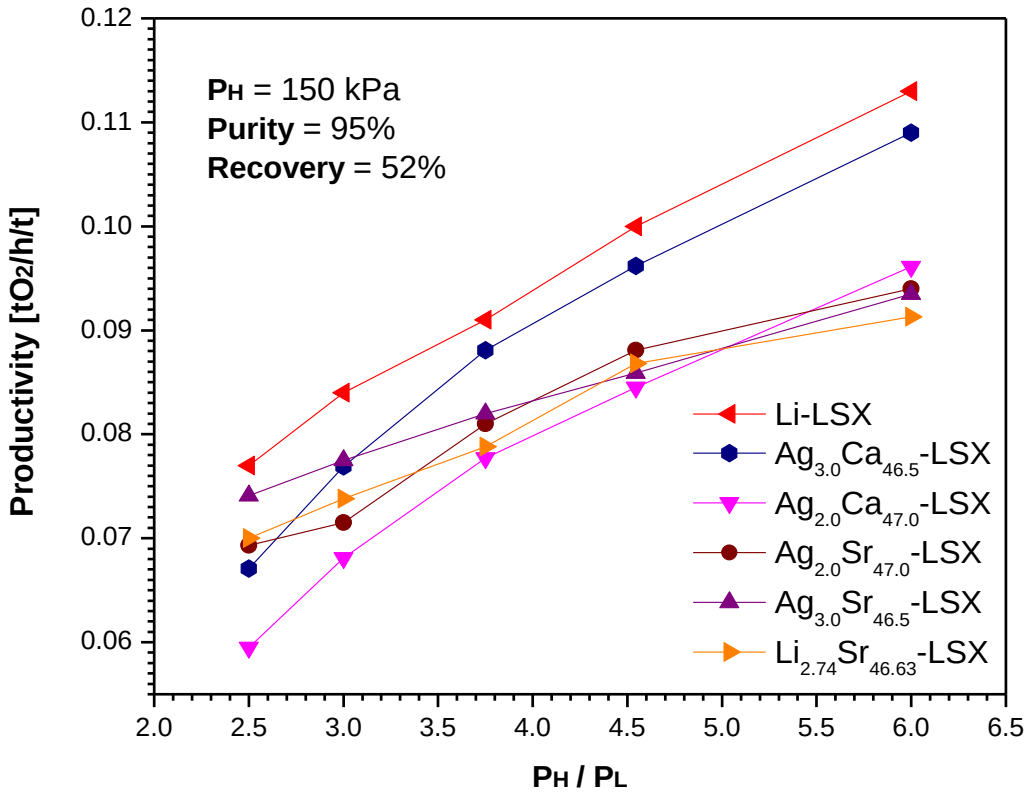

Figure 5.13 Comparison of O_2 productivity at 150 kPa pressure.

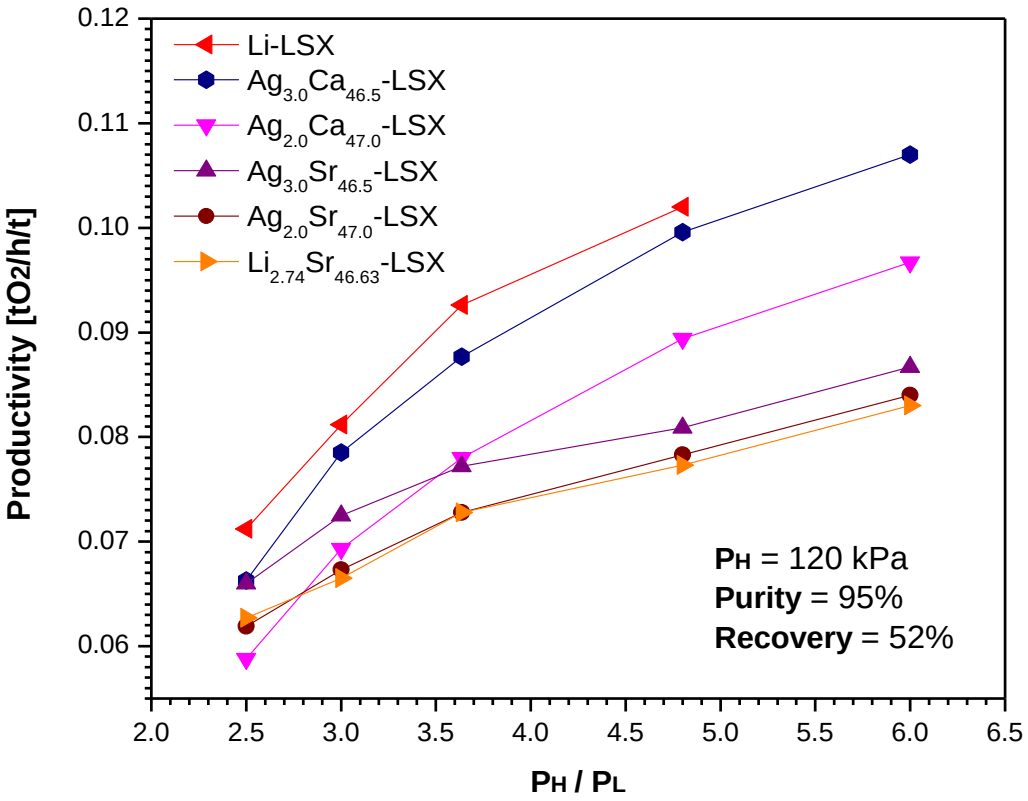

Figure 5.14 Comparison of O_2 productivity at 120 kPa pressure.

The N_2 adsorption isotherm of Li-LSX is quite linear which favors PSA-VPSA air separation due to its large working capacity. As mentioned earlier, $Ag_{3.0}Ca_{46.5}$-LSX has a higher N_2 capacity the Li-LSX at 298 K. However, $Ag_{3.0}Ca_{46.5}$-LSX has a far higher O_2 capacity and heats of adsorption, both of which are detrimental to PSA/VPSA performance. The detrimental effect of the heat of adsorption on the PSA performance is well illustrated by Lee et al. [51] in their development of heat-exchange PSA. Recall that the adsorption capacity of O_2 has an important effect on the PSA performance because the lower the O_2 capacity, the better the PSA separation capacity. The advantage of Li-LSX over $Ag_{3.0}Ca_{46.5}$-LSX becomes more visible at low pressures ratios as seen in Figures 5.13 and 5.14. At adsorption pressure of 150 kPa and pressure ratio of 3, the O_2 productivities of Li-LSX and $Ag_{3.0}Ca_{46.5}$-LSX are 0.084 and 0.0769 $tO_2/h/t$ while at pressure ratio of 6, the O_2 productivities are 0.113 and 0.109 $tO_2/h/t$ respectively.

In the current commercial operations of VPSA O_2 generators, the adsorption pressures are not higher than 150 kPa, while the desorption pressures are not lower than 50 kPa (i.e., using blowers). Under these conditions, Li-LSX is the best sorbent. However, with the strictly surging cost of lithium, this work shows that $Ag_{3.0}Ca_{46.5}$-LSX (along with some of the other mentioned mixed-cation samples) may be desirable alternatives due to the abundance of calcium and strontium and the minimal silver and lithium used in their development.

5.4 Conclusion

The mixed-cation samples developed in this work with less than 4% Li+ and Ag+ shows a significant advantage over previous published literature where almost 70% Li cations were exchanged with pure Na-LSX [2,9,11,14]. Both the Li and Ag cations were exchanged as the last step followed by a mild and short-time dehydration for the LiSr-LSX samples and a 5 h, 723 K dehydration temperature for the AgCa-, AgSr-LSX samples. Comparisons of the experimental O_2 and N_2 adsorption isotherms and isosteric heats of adsorption of the mixed-cation samples against that of the pure samples provided strong evidence of significant amounts of the exchanged Li^+ residing in SIII and Ag^+ in SII*.

Additionally, the mixed-cations were compared against the pure-cation Li-LSX based on their O_2 productivity performance by PSA simulation model. The simulated results show that with only a few Li^+ and Ag^+ exchanged into the pure Sr-LSX and Ca-LSX samples could lead to significant advancement in the production of O_2 via PSA.

5.5 References

[1] R. T. Yang, Gas Separation by Adsorption Processes. London: Imperial College Press, (1997).

[2] C. C. Chao, Process for Separating Nitrogen from Mixtures Thereof with Less Polar Substances. US Patent. 4,859,217 (1989).

[3] R. T. Yang, Adsorbents: Fundamentals and Applications. New Jersey: John Wiley & Sons, Inc. (2003).

[4] N. D. Hutson, R. T. Yang, Structural effects on the adsorption of atmospheric gases in mixed Li,Ag–X-Zeolite. AIChE Journal. 46 (2000) 2305-2317.

[5] M. Feuerstein, G. Engelhardt, P. L. McDaniel, J. E. MacDougall, T. R. Gaffney, Solid-state nuclear magnetic resonance investigation of cation siting in LiNaLSX zeolites. Microporous Mesoporous Mater. 26 (1998) 27-35.

[6] M. Feuerstein, R. F. Lobo, Characterization of Li Cation in Zeolite LiX by Solid-State NMR Spectroscopy and Neutron Diffraction. Chem. Mater. 10 (1998) 2197-2204.

[7] N. D. Hutson, B. A. Reisner, R. T. Yang, B. H. Toby, Silver Ion-Exchanged Zeolites Y, X, and Low Silica X: Observations of Thermally Induced Cation/Cluster Migration and the Resulting Effects on the Equilibrium Adsorption of Nitrogen. Chem. Mater. 12 (2000) 3020-3031.

[8] D. H. Olson, H. S. Sherry, An X-Ray Study of Strontium-Sodium Ion Exchange in Linde X. An Example of a Two-Phase Zeolite System. J. Phys. Chem. 72 (1968) 4095-4104.

[9] C. G. Coe, J. F. Kirner, R. Pierantozzi, T. R. White, Nitrogen Adsorption with a Ca and/or Sr Exchanged Zeolite. US Patent. 5,152,813 (1992).

[10] C. G. Coe, J. F. Kirner, R. Pierantozzi, T. R. White, Nitrogen Adsorption with a Divalent Cation Exchanged Zeolite. US Patent. 5,258,058 (1993).

[11] C. G. Coe, J. F. Kirner, R. Pierantozzi, T. R. White, Divalent Cation Exchanged Lithium X-Zeolite for Nitrogen Adsorption. US Patent. 5,417,957 (1995).

[12] C. G. Coe, J. F. Kirner, R. Pierantozzi, T. R. White, Zinc Cation Exchanged Lithium X-Zeolite for Nitrogen Adsorption. US Patent. 5,419,891 (1995).

[13] S. Sircar, R. R. Conrad, W. J. Ambs, Binary Ion Exchanged Type-X Zeolite Adsorbent. US Patent. 4,557,736 (1985).

[14] C. C. Chao, J. D. Sherman, J. T. Mullhaupt, C. M. Bolinger, Mixed Ion-Exchanged Zeolites and Processes for the use Thereof in Gas Separations. US Patent. 5,174,979 (1992).

[15] H. W. Habgood, Adsorptive and Gas Chromatographic Properties of Various Cationic Forms of Zeolite X. Canadian Journal of Chemistry. 42 (1964) 2340-2350.

[16] Y. Y. Huang, Adsorption in AgX and AgY zeolites by carbon monoxide and other simple molecules. Journal of Catalysis. 32 (1974) 482-491.

[17] N. D. Hutson, R. T. Yang, Structural Effects on Adsorption of Atmospheric Gases in Mixed Li,Ag-X-Zeolite, AIChE Journal. 46 (2000) 2305-2317.

[18] F. E. Epiepang, X. Yang, J. Li, Y. Liu, R. T. Yang, Mixed-Cation LiCa-LSX Zeolite with Minimum Lithium for Air Separation, AIChE Journal. 64 (2017) 406-415.

[19] D. W. Breck, Zeolite Molecular Sieves: Structure, Chemistry, and Use. Malabar, FL: RE Krieger, (1984) 529-588.

[20] N. D. Hutson, S. C. Zajic, R. T. Yang, Influence of residual water on the adsorption of atmospheric gases in Li-X zeolite: experiment and simulation. Ind. Eng. Chem. Res. 39 (2000) 1775-1780.

[21] P. A. Jacobs, J. B. Uytterhoeven, H. K. Beyer, Some Unusual Properties of Activated and Reduced AgNaA Zeolites. J. Chem. Soc. Faraday Trans. 75 (1979) 56-64.

[22] F. O. Mertens, Determination of absolute adsorption in highly ordered porous media. Surf. Sci. 603 (2009) 1979-1984.

[23] J. Purewal, D. Liu, A. Sudik, M. Veenstra, J. Yang, S. Maurer, U. Müller, D. J. Siegel, Improved hydrogen storage and thermal conductivity in high-density MOF-5 composites. J. Phys. Chem. C116 (2012) 20199-20212.

[24] B. Mu, K. S. Walton, Adsorption equilibrium of methane and carbon dioxide on porous metal-organic framework Zn-BTB. Adsorption. 17 (2011) 777-782.

[25] B. Mu, P. M. Schoenecker, K. S. Walton, Gas adsorption Study on Mesoporous Metal-Organic Framework UMCM-1. J. Phys. Chem. 114 (2010) 6464-6471.

[26] Maly KE, Gagnon E, Wuest JD. Engineering molecular crystals with abnormally weak cohesion. Chem. Commun. 2011;47:5163-5165.

[27] F. E. Epiepang, J. Li, Y. Liu, R. T. Yang, Low-pressure performance evaluation of CO_2, H_2O, and CH_4 on Li-LSX as a superior adsorbent for air prepurification. Chem. Eng. Sci. 147 (2016) 100-108.

[28] X. Yang, F. E. Epiepang, Y. Liu, R. T. Yang, Heats of adsorption on mixed-cation LiNa-LSX: Estimating SIII site occupancy by Li. Chem. Eng. Sci. 178 (2018) 194-198.

[29] H. Herden, W. D. Einicke, R. Schollner, W. J. Mortier, L. R. Gellens, J. B. Uytterhoeven, Location of Li-ions in Synthetic Zeolites X and Y. *Zeolites*. 2 (1982) 131-134.

[30] T. Hseu, PhD. Thesis, University of Washington, Seattle, WA. (1972).

[31] W. J. Mortier, H. J. Bosmans, J. B. Uytterhoeven, Location of univalent cations in synthetic zeolites of the Y and X type with varying silicon to aluminum ratio. II. Dehydrated potassium exchanged forms. J. Phys. Chem. 76 (1972) 650-656, DOI: 10.1021/j100649a008.

[32] J. M. Bennett, J. V. Smith, Positions of Cations and Molecules in Zeolites with the Faujasite-Type Framework I. Dehydrated Ca-Exchanged Faujasite. Mat. Res. Bull. 3 (1968) 633-642.

[33] H. S. Sherry, The Ion-Exchange Properties of Zeolites. I. Univalent Ion Exchange in Synthetic Faujasite. J. Phys. Chem. 70 (1968) 1158-1168.

[34] G. Vitale, L. M. Bull, R. E. Morris, A. K. Cheetham, B. H. Toby, C. G. Coe, J. E. MacDougall, Combined neutron and X-ray Powder Diffraction Study of Zeolite Ca LSX and a ^{2}H NMR Study of Its Complex with Benzene. J. Phys. Chem. 99 (1995) 16087-16092.

[35] J. J. Pluth, J. V. Smith, Positions of Cations and Molecules in Zeolites with the Faujasite-Type Framework VII. Dehydrated Ca-Exchanged X. Mat. Res. Bull. 7 (1972) 1311-1322.

[36] J. J. Pluth, J. V. Smith, Positions of Cations and Molecules in Zeolites with the Faujasite-Type Framework VIII. Dehydrated Ca-Exchanged X. Mat. Res. Bull. 8 (1973) 459-468.

[37] M. L. Costenoble, W. J. Mortier, J. B. Uytterhoeven, Location of Cations in Synthetic Zeolites-X and -Y Part 5. – The cation Distribution in Ca-Y, Ca-X and La-Y in the Ultimate Stages of Dehydration. J. Chem. Soc. 74 (1978) 466-476.

[38] M. L. Costenoble, W. J. Mortier, J. B. Uytterhoeven, Location of Cations in Synthetic Zeolites-X and -Y Part 6. – The cation Distribution in Ca-Y, Ca-X and La-Y in the Ultimate Stages of Dehydration. J. Chem. Soc. 74 (1978) 477-483.

[39] Y. I. Smolin, Y. F. Shepelev, A. A. Anderson, Atomic Scale mechanism of CaX Zeolite Dehydration. Acta Cryst. B45 (1989) 124-128.

[40] S. B. Jang, M. S. Jeong, Y. Kim, Crystal Structures of the Ethylene and Acetylene Sorption Complexes of Fully Ca^{2+}-Exchanged Zeolite X. J. Phys. Chem. B. 101 (1997) 3091-3096.

[41] Y. H. Yeom, A. N. Kim, Y. Kim, Crystal Structure of a Benzene Sorption Complex of Dehydrated Fully Ca^{2+}-Exchanged Zeolite X., J. Phys. Chem. 102 (1998) 6071-6077.

[42] S. B. Jang, M. S. Jeong, Y. Kim, S.H. Song, K. Seff, Crystal Structure of an Ammonia Sorption Complex of Dehydrated Fully Ca^{2+}-Exchanged Zeolite X., Micropor. Mesopor. Mater. 28 (1999) 173-183.

[43] E. Y. Choi, Y. Kim, K. Seff, Crystal Structure of a Mesitylene Sorption Complex of Dehydrated Fully Ca^{2+}- Exchanged Zeolite X. Sorbed Mesitylene Appears to be Significantly Nonplanar. J. Phys. Chem. 106 (2002) 5827-5832.

[44] D. H. Olson, H. S. Sherry, An X-Ray Study of Strontium-Sodium Ion Exchange in Linde X. An Example of a Two-Phase Zeolite System. J. Phys. Chem. 72 (1968) 4095-4104.

[45] C. Pichon, H. Palancher, J. Lynch, J. L. Hodeau, J. F. Berar, Cationic distribution of Ca2+ and Sr2+ cations in hydrated and dehydrated zeolite SrX, CaX and CaSrX. An in situ anomalous X-ray diffraction study. Studies in Surface Science and Catalysis. 158 (2005) 789-796.

[46] H. Palancher, C. Pichon, B. Rebours, J. L. Hodeau, J. Lynch, J. F. Berar, S. Prevot, G. Conan, C. Bouchard, A cell for in situ dynamic X-ray diffraction studies: application to the dehydration of zeolite SrX. J. Appl. Cryst. 38 (2005) 370-373.

[47] T. Frising, P. Leflaive, Extraframework cation distributions in X and Y faujasite zeolites: A review. Micro. and Meso. Mat. 114 (2008) 27-63.

[48] N. D. Hutson, S. U. Rege, R. T. Yang, Mixed Cation Zeolites: Li_xAg_y-X as a Superior Adsorbent for Air Separation. AIChE Journal. 45 (1999) 724-734.

[49] S. U. Rege, R. T. Yang, Limits for air separation by adsorption with LiX zeolite. Ind. Eng. Chem. Res. 36 (1997) 5358-5365.

[50] Mulgundmath VP, Tezel FH, Hou F, Golden TC. Binary Adsorption Behavior of Methane and Nitrogen gases. J. Porous Mater. 2012;19:455-464.

[51] Lee, J.-J., Kim, M.-K., Lee, D.-G., Ahn, H-W., Kim, M.-J., and Lee, C.-H., Heat-exchange pressure swing adsorption process for hydrogen separation. AIChE Journal 2008;54:2054-2064.

Chapter 6

Sr-LSX Zeolite for Air Separation

Significance

Due to the surging demand of lithium for lithium-ion batteries, the price of lithium has seen a steep rise and is projected to maintain the trend for the foreseeable future. With Li-LSX being the sorbent of choice in pressure swing adsorption systems for air separation, it is imperative to develop efficient adsorbents with significantly lower lithium content (mixed-cations zeolites) or completely replace it with abundant and low-cost alkali-earth metal cations such as Sr^{2+}. This article presents promising results for pure Sr-LSX zeolite for O_2 productivity performance via PSA and the possibility of completely replacing Li-LSX with Sr-LSX.

6.1 Introduction

Air separation is key to the successful operation of numerous engineering and manufacturing industries. It is the separation of ambient air (composed of ~78.1% Nitrogen, ~21% Oxygen, ~0.9% Argon and less than 1% of its trace constituents (Helium, Neon, Krypton and Xenon)), into the pure forms of the Oxygen, Nitrogen and in some cases, Argon. The application of these pure components ranges from the medical field to the mass production of steel, the manufacture of semiconductors and microchips to the petroleum and chemicals industries, just to name a few.

The separation of ambient air into its pure components is accomplished by cryogenic and non-cryogenic processes in principle. The energy intensive cryogenic process, which is suitable for high volume and high purity (>99.5%) nitrogen, oxygen and argon production, separates air through liquefaction by cooling and selectively distilling its constituents at their various boiling points. The cooling (energy intensive) requirement of the cryogenic process drives its high capital cost. On the other hand, various technologies fall under the non-cryogenic process including the membrane, pressure swing adsorption (PSA) and the vacuum pressure swing adsorption (VPSA) processes. The PSA for example, is preferred for low-to-medium scale production of O_2 and N_2 at relatively high purities [1] (>94%) and operates at near atmospheric temperatures. The success of the adsorptive processes lies in the effectiveness of the sorbents used and the continuous development of more effective sorbents over the years have made this technology quite competitive.

This work is aimed towards the optimization and development of sorbents for the adsorptive processes and more specifically the PSA (VPSA) system. Chao's 1989 [2] invention of the Li-LSX zeolite was the breakthrough in sorbent development. Though Li-LSX has been the

preferred sorbent for air separation in PSA systems, there has been exhaustive investigations for the development of potentially better alternatives over the years [3-8]. These includes pure (single-cation) and binary mixtures (mixed-cation zeolites). For example, pure Ca-LSX was investigated and although it comparatively showed higher N_2 adsorption capacities than Li-LSX, its simulated O_2 productivity performance fell short (68%) to that of Li-LSX [9]. Coe et al. [3-6] investigated other pure zeolites such Zn-LSX, Li-LSX, and Ca-LSX; Although most of the mixed-cation zeolites investigated have centered around alkali-earth metal cations, some transition metals have also been studied as in the case of silver. Chao et al., [8] investigated Sr-A, Li-A, Ca-A; Yang et al. [10] studied Li-A and Ag-X; Sircar et al. [11] investigated pure Ca-X and Ca-LSX; while Hutson et al. [12] studied Ag-Y, Ag-X and Ag-LSX. There has also been extensive study of mixed-cation zeolites for air separation and amongst them are LiSr-LSX, [3] LiZn-LSX, [6] LiCa-LSX, [3,9] LiSr-A, [7] NaCe-X, [13] as well as LiAg-LSX [14-16] with silver proving to strongly affect the adsorptive properties of zeolites [17-18]. Another interesting invention, Li-ZSM-2, by Weigel et al. [19], was the development of a selective adsorptive method for separating nitrogen from oxygen using a crystalline metallosilicate having a ZSM-2 structure with a Si-Al ratio of 1.6 and a lithium cation exchange of at least 50%. These are all impactful contributions to the field but most of the Li-alkali-earth metal cation binary mixtures required >70% Li^+ to see the effect of lithium on the increased N_2 adsorption capacities.

Lithium has been the preferred sorbent in adsorptive processes but the last few years have seen the demand of lithium for Li-ion battery (energy storage) drive up the price of Lithium Carbonate. With the increasing demand and higher lithium cost, adsorptive processes such as PSA and VPSA would find it difficult to compete even at the low-to-medium scale O_2 production level and let alone the cryogenic process. In this work, we aim to address this issue with the alkali-earth

metal cation Sr-LSX in combination with a specific treatment scheme that optimizes its N_2 adsorptive properties. Its O_2 productivity performance in connection with its N_2/O_2 capacities are compared vis-à-vis Li-LSX via PSA simulation and adsorption isotherms respectively.

6.2 Methods

6.2.1 Materials

Powder Li-LSX (Si/Al = 1.0) and the precursor as-synthesized Na-LSX (extent of exchange of 99.5, Si/Al = 1.005) were obtained from Luoyang Jianlong Micro-Nano New Materials Co., Ltd., China. Strontium Nitrate Anhydrous (ACS) was purchased from Fisher Chemical while Helium (99.995%, prepurified), Nitrogen (99.998%, prepurified), and Oxygen (99.6%, extra dry) were all obtained from Cryogenic Gases.

6.2.2 Preparation of Sr-LSX Zeolite

A few grams of Na-LSX was used to prepare Sr-LSX by ion-exchanging in a 1.0 M Strontium Nitrate, $Sr(NO_3)_2$ solution with a 3.8-fold equivalent excess at mild temperature conditions and stirring. To prevent hydrolysis and hence the collapse of the zeolite structure during the ion exchange procedure, the $Sr(NO_3)_2$ solution was adjusted to a pH of 7 using $Sr(OH)_2$. Six total ion-exchanges were carried out and the solution was decanted after each exchange step and refilled with a fresh $Sr(NO_3)_2$ solution. After the final exchange, the sample was vacuum filtered, washed with copious amounts of deionized water and air dried for 24 h at 298 K.

6.2.3 Sample characterization, dehydration, and isotherm measurements

The Li-LSX zeolite sample was dehydrated at 623 K for 5 h and will be referred henceforth as Li-LSX. The above conditions had shown that Li-LSX fully dehydrates at 623 K [20]. Similarly, the Sr-LSX sample (Sr/Al = 0.995) was pre-treated for 5 h at five different temperatures namely 623, 648, 673, 698, and 723 K. The five Sr-LSX samples are labeled as follows: Sr-LSX-623, Sr-

LSX-648, Sr-LSX-673, Sr-LSX-698, and Sr-LSX-723. The ramp rate for all pretreatment conditions was 10K/min under a vacuum of 30 μmHg.

The pure gas adsorption equilibrium analyses were measured using the Micromeritics ASAP 2020 sorptometer which employs the volumetric technique. All samples were dehydrated in vacuo prior to isotherm measurements.

6.3 Results and Discussions

6.3.1 Nitrogen and Oxygen adsorption isotherms.

Pure sorbate (N_2 and O_2) adsorption isotherms were measured at three different temperatures – 298, 323, and 343 K and to pressures up to 101 kPa. However, only isotherms measured at 298 K on both sorbates for all samples are shown here and all others can be found in Figures S6.1 and S6.2 in the supplementary material in appendix E. Figure 6.1 shows the equilibrium isotherms at 298 K for the various samples. Close inspection of the N_2 results in Figure 6.1 show that the Sr-LSX-673 and Sr-LSX-648 have better N_2 capacities than pure Li-LSX treated at 623 K followed by Sr-LSX-698, Sr-LSX-723 and Sr-LSX-623. It can also be concluded that 673 K is the optimal pre-treatment temperature for the pure Sr-LSX sample as further increasing the dehydration temperature to 723 K saw a decline in N_2 capacity. The increases observed in the N_2 capacities of Sr-LSX-673 and Sr-LSX-648 are favorable characteristics for air separation via PSA (VPSA).

Figure 6.1 also shows O_2 experimental adsorption isotherms at the same three temperatures mentioned above. As expected, the strontium sample pre-treated at various temperatures all measure higher O_2 capacities than the Li-LSX zeolite and should be attributed to the higher polarizability of Sr^{2+} over Li^{+}. Partial shielding of the Li cations by the electric field from the surrounding framework oxygen also limits interactions between SII cations and sorbate molecules

resulting in lower O_2 capacities. In other words, larger cations like Sr^{2+} experiences less shielding effect and hence, interacts more and easily with the sorbates. It is noted that cationic locations in the framework of the zeolite plays a vital role in determining the magnitude of the adsorbed capacities of both sorbates.

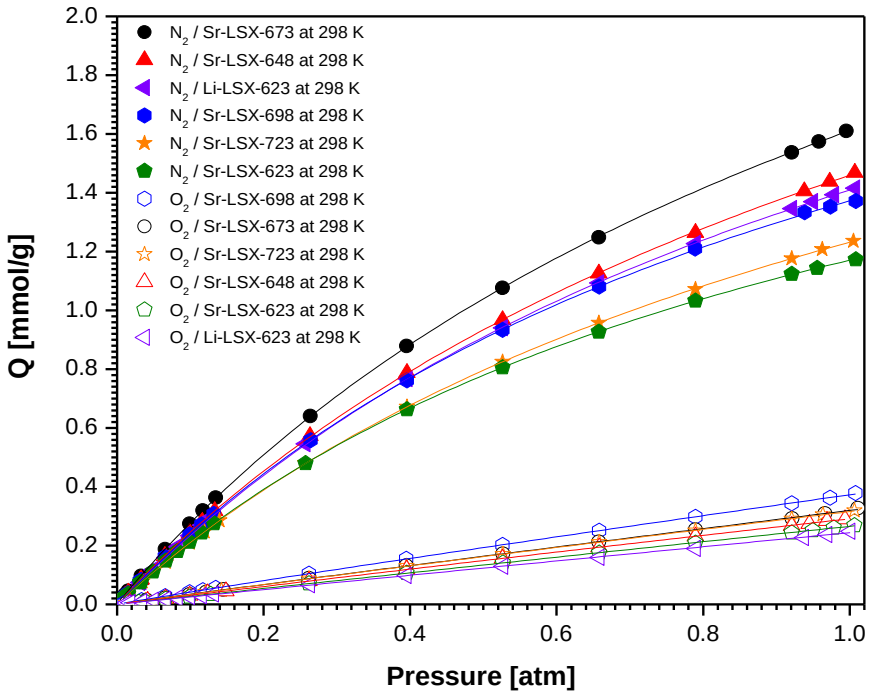

Figure 6.1 Combined N_2 and O_2 adsorption isotherms at 323 K and 101 kPa on sorbents dehydrated at various temperatures.

6.3.2 Dehydration temperature effects and cation site analysis

To evaluate the dehydration effects on the Sr-LSX zeolite, the sample was exposed to five sets of dehydration temperatures ranging between 623 and 723 K while holding the pre-treatment time constant (5 h in this case). The base case, extracted from the 298 K isotherms, is shown in Figure 6.2 which is the capacity (mmol/g) vs dehydration temperature (K). It can clearly be seen here that, maximum N_2 capacity and hence, an optimal treatment temperature is at 673 K. A similar

trend was observed with the obviously lower O_2 capacity curve. There is a considerable increase in N_2 capacity between 673 K and the commonly used 623 K dehydration temperature. The observed increase cannot be attributed solely to water loss during dehydration because even the most tenaciously held water would be lost at 623 K. The increase is rather due to the migration of the Sr cations in response to the treatment temperature.

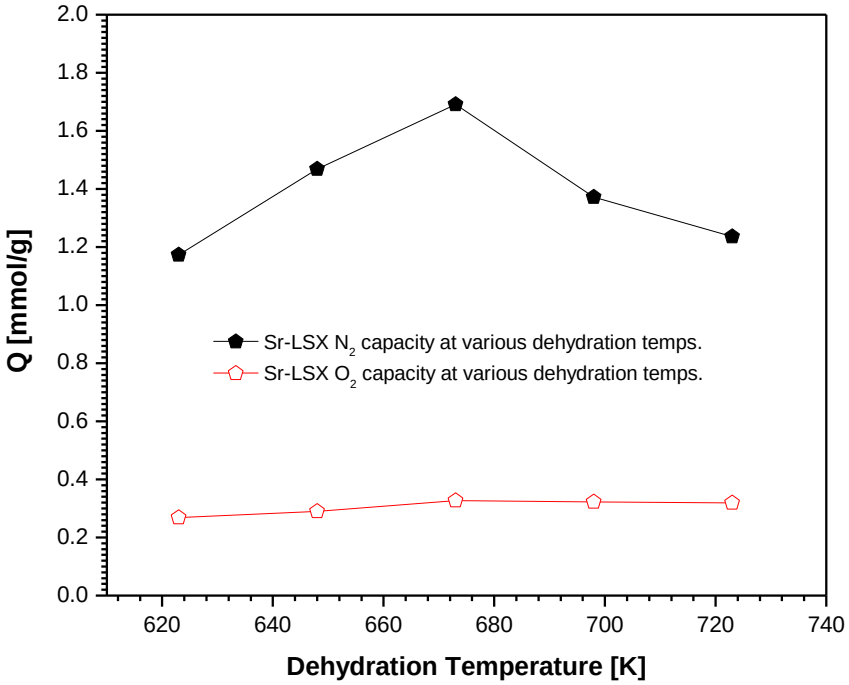

Figure 6.2 N_2 and O_2 adsorption capacity (at 1 atm and 298K) on Sr-LSX at various dehydration temperatures.

A review of past studies showed that the strontium cations (as with all cations) migrate and redistribute themselves across sites SI, SI' and SII based on the dehydration conditions.[21] It was also noticed that the extent of cationic exchange as well as the level of vacuum during sample dehydration both affect the cation site distribution [21].

The characterization of the structure of strontium exchanged FAU have only been studied by X-ray diffraction (Powder XRD, Single Crystral XRD, and Anomalous XRD) methods [21-

24]. These studies were carried out on Sr-Y, Sr-X and Sr-LSX. In most cases, SII which in these samples is the most exposed to the sorbates, is always relatively populated due to the fact that it offers an electrostatic repulsion minimum. SI' on the other hand, seems always less occupied which might in fact be as a result of a high repulsion which exists between SI and SI'. Figure S6.1 shows the powder XRD patterns for the studied sorbents and it was concluded that the temperature at which the X-ray diffraction measurement is carried out does not have any or much influence on the cation distribution considering they were properly dehydrated prior to the measurements. No site distribution analysis were carried out in this work for the studied samples taking into consideration the breadth of analysis in literature.

6.3.3 Pure isotherm fitting model and heats of adsorption

Equation 6.1, which represents the Freundlich-Langmuir (F-L) isotherm model was used to fit all equilibrium adsorption isotherms for both sorbates as seen in Figure 6.1.

$$Q = \frac{Q^*_{sat} K C^n}{1 + K C^n} \tag{6.1}$$

$$\ln\left(\frac{P_1}{P_2}\right) = \frac{\Delta H_{vap}}{R}\left(\frac{1}{T_2} - \frac{1}{T_1}\right) \tag{6.2}$$

Where Q is the equilibrium amount adsorbed, Q^*_{sat} is the adsorption capacity of the system, C is the equilibrium aqueous phase concentration, n is the index of heterogeneity, K is the affinity constant of adsorption, ΔH_{vap} is the isosteric heats of adsorption, R is the gas constant (8.3145 J/mol.K), while P_1 and P_2 are the corresponding pressures at temperatures T_1 and T_2. The heats of adsorption for the studied gas-sorbate pairings were determined using the L-F fitted isotherms and the Clausius-Clapeyron equation (Equation 6.2).

Figure 6.3 shows the N_2 and O_2 heats of adsorption on the studied sorbents. The observed trend for both sorbates which seems a mirror reflection of the equilibrium adsorption isotherms, is almost identical from high to low: Sr-LSX-673 > Sr-LSx-648 > Sr-LSX-698 > Sr-LSX-723 > Sr-

LSX-623 > Li-LSX-623. A theoretical total sorbate-sorbent potential calculation [25] would show a similar though it only estimates for a single gas molecule and a free isolated cation. The higher heats of adsorption of the Sr-LSX samples are simply due to their higher polarizabilities in relation to Li-LSX i.e. polarizability of Sr^{2+} > Li^{+}.

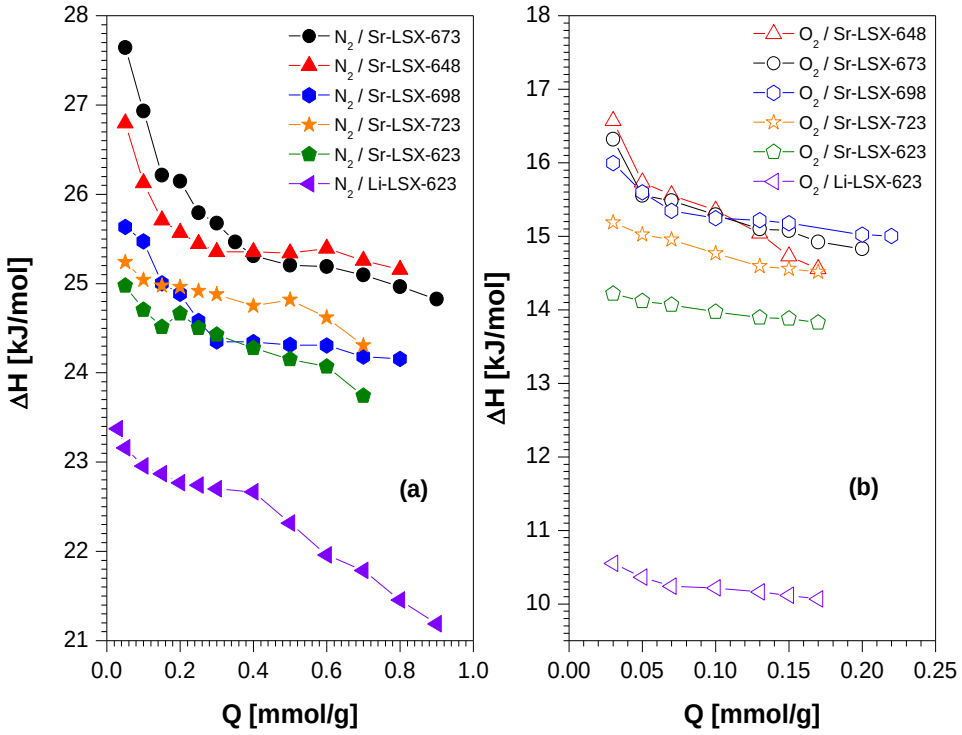

Figure 6.3 Isosteric heats of adsorption on sorbents dehydrated at various temperatures. **(a)** N_2 and **(b)** O_2.

6.3.4 PSA simulation and results

A comprehensive analysis for sorbent selection for PSA/VSA separation has been given recently by Marine and Webley [26], which includes caveats as well as factors that are favorable and unfavorable for PSA/VSA performance. In this work, the sorbents were assessed and compared by model simulation using a commercial five-step PSA cycle that had a cycle time set at 2.5 minutes (30 seconds per step). For clarification purposes, the schematics of the five-step

cycle is given in Figure S6.4 and as described by Epiepang et al. [27], Step I is the Feed (air) Pressurization step, Step II is the High-pressure Feed, Step III is the Co-current Depressurization step, while Steps IV and V are the Countercurrent Blowdown and the Low Pressure Purge. The basic components employed in this simulation were N_2 (78%) and O_2 (22% i.e. 21% O_2 and 1% Ar).

The O_2 product purity, O_2 product recovery and O_2 product throughput, given in Equations 6.3 – 6.5, are the three inter-related results with which the PSA performance is evaluated. Fixing any two of the above results sets the third in principle.

$$\text{Product Purity} = \frac{\text{Amount of } O_2 \text{ from Steps II and III}}{\text{Amount of } N_2 \text{ and } O_2 \text{ from Steps II and III}} \tag{6.3}$$

$$\text{Product Recovery} = \frac{(O_2 \text{ from Steps II and III}) - (O_2 \text{ from Step VI})}{(O_2 \text{ fed in Steps I and II})} \tag{6.4}$$

$$\text{Product Throughput} = \frac{\text{Amount of } O_2 \text{ produced per hour } (^{t}/_{h})}{\text{Amount of sorbent used in the bed (t)}} \tag{6.5}$$

Rege et al. [28], presented a detailed explanation of the numerical and mathematical methods used for this simulation. Assumptions made for this model include a two-component gas mixture flowing through a fixed adiabatic bed packed with spherical adsorbent particle; the axial dispersion of heat and mass transfer was accounted for but dispersion in the radial direction was assumed negligible as well; the diffusional resistance was assumed to be negligible since diffusion of the sorbates is relatively fast considering the long cycle time; the gas was assumed to have constant viscosity and heat capacity; local equilibrium existed between the gas and solid phases for each gas component while the axial pressure drop was neglected and the ideal gas law was assumed because the pressures involved were at atmospheric conditions. Also, the throughputs of the sorbents were studied under various cycle conditions to compare their performances.

Table S6.1 shows the PSA bed characteristics and the applied operating conditions while Table S6.2 gives the L-F isotherm with temperature dependent fitting constants including the heats of adsorption. The Extended L-F model given in Equation 6.6 was used to predict equilibrium loadings under mixture conditions while Equation 6.7 gives the L-F parameters.

$$q_k^* = \frac{q_{m_k} b_k p_k^{n_k}}{1+\sum_{j=1}^{m} b_k p_k^{n_k}} \quad k = 1,2 \tag{6.6}$$

$$q_m = k_1 e^{(k_2/T)} \quad and \quad b = k_3 e^{(k_4/T)} \tag{6.7}$$

Mulgundmath et al. [29], also showed that the Langmuir-type, though simple, is a reasonable method for fitting binary mixtures.

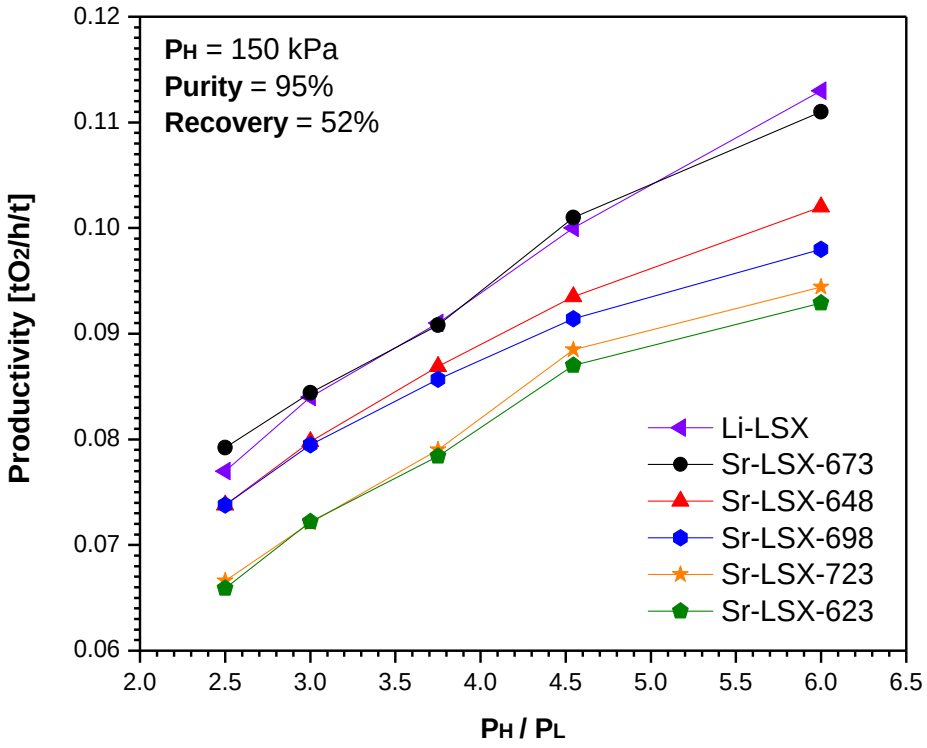

Figure 6.4 Comparison of O_2 productivity at 150 kPa pressure.

The simulation results shown in Figure 6.4 were achieved at a feed pressure of 150 kPa at various pressure ratios. The same pressure ratios, PH/PL (where PH and PL are the feed pressure

and desorption pressure respectively) were maintained for a fair comparison of the different sorbents. The feed and purge velocities for all sorbents were optimized to obtain the same O_2 product purity and recovery at approximately 95% and 52% respectively. Tables S6.3 through S6.8 which summarizes the simulation conditions, were used to extract the results shown in Figures S6.4 and S6.5 (comparison of O_2 productivity at P_H = 120 kPa pressure on various sorbents).

The results show that the O_2 productivity increases with increasing P_H/P_L (Figure 6.4) as well as O_2 product purity and recovery of ~95% and ~52% respectively. With the conclusion that 673 K was the optimal dehydration temperature, the sample Sr-LSX-673 had an almost identical VPSA performance at Li-LSX which is an excellent development satisfying the primary objective of this work.

At 298 K, and as with the other temperatures, it can be seen that the isotherms of the studied sorbents are similar in the sense that they are all almost linear. This linearity is highly favorable for the PSA (VPSA) separation systems due to their large working capacities. It should also be recalled that Sr-LSX-673 had an almost 13.5% higher N_2 adsorption capacity than Li-LSX-623 but forfeits that positive with its higher O_2 capacity relative to Li-LSX-623. Higher O_2 capacities and heats of adsorption are two key variables that are detrimental to PSA (VPSA) performance. To further investigate the similarities between Li-LSX-623 and Sr-LSX-673, one can see that at adsorption pressure of 150 kPa and P_H/P_L = 3.0, the O_2 productivities of both samples are 0.084 and 0.0844 respectively. At the same feed pressure and P_H/P_L = 6.0, the productivities are 0.113 and 0.111 respectively which makes Sr-LSX-673 a viable replacement for Li-LSX in adsorptive (specifically, PSA) processes. The extra energy requirement which comes from dehydrating the sorbents at 673 K instead of its usual 623 K is an option that is compensated by the Sr-LSX-673 sample's PSA performance.

The P_H and P_L of 150 kPa and 50 kPa are respectively the range within with current commercial VPSA O_2 generators operate and it had seen Li-LSX as its sorbent of choice. However, with the results uncovered in this work and the present and projected rise in lithium demand and cost, the abundant alkali-earth metal cation, strontium-exchanged faujasite appears to be a promising alternative.

6.4 Conclusion

The investigation into the effect of dehydration temperature on Sr-LSX led to the conclusion that 5 h and 673 K are the optimal treatment conditions for Sr-LSX zeolites. Comparison of the N_2 adsorption isotherms at 298 K show highly linear isotherms which are attractive characteristics for PSA systems. By comparison, the Sr-LSX-673 not only show an almost 13.5% higher N_2 adsorption capacity than Li-LSX-623, but also matches the O_2 productivity performance from the simulated PSA model. With the projected increasing demand and cost of Lithium, the abundant strontium-exchanged LSX zeolite is a promising replacement for Li-LSX.

6.5 References

[1] R. T. Yang, Gas Separation by Adsorption Processes. London: Imperial College Press, 1997.

[2] C. C. Chao, Process for Separating Nitrogen from Mixtures Thereof with Less Polar Substances. US Patent. (1989) 4,859,217.

[3] C. G. Coe,J. F. Kirner, R. Pierantozzi, T. R. White, Nitrogen Adsorption with a Ca and/or Sr Exchanged Zeolite. US Patent. (1992) 5,152,813.

[4] C. G. Coe, J. F. Kirner, R. Pierantozzi, T. R. White, Nitrogen Adsorption with a Divalent Cation Exchanged Zeolite. US Patent. (1993) 5,258,058.

[5] C. G. Coe, J. F. Kirner, R. Pierantozzi, T. R. White, Divalent Cation Exchanged Lithium X-Zeolite for Nitrogen Adsorption. US Patent. (1995) 5,417,957.

[6] C. G. Coe, J. F. Kirner, R. Pierantozzi, T. R. White, Zinc Cation Exchanged Lithium X-Zeolite for Nitrogen Adsorption. US Patent. (1995) 5,419,891.

[7] S. Sircar, R. R. Conrad, W. J. Ambs, Binary Ion Exchanged Type-X Zeolite Adsorbent. US Patent. (1985) 4,557,736.

[8] C. C. Chao, J. D. Sherman, J. T. Mullhaupt, C. M. Bolinger, Mixed Ion-Exchanged Zeolites and Processes for the use Thereof in Gas Separations. US Patent. (1992) 5,174,979.

[9] F. E. Epiepang, X. Yang, J. Li, Y. Liu, R. T. Yang, Mixed-Cation LiCa-LSX Zeolite with Minimum Lithium for Air Separation, AIChE Journal, 64 (2017) 406-415.

[10] R. T. Yang, Y. D. Chen, J. D. Peck, N. Chen, Zeolites Containing Mixed Cations for Air Separation by Weak Chemisorption-Assisted Adsorption, Ind. Eng. Chem. Res. 35 (1996) 3093-3099.

[11] S. Sircar, W. E. Waldron, Oxygen Production by Adsorption. US Patent. (2002) 0108494A1.

[12] N. D. Hutson, B. A. Reisner, R. T. Yang, B. H. Toby, Silver Ion-Exchanged Zeolites Y, X, and Low Silica X: Observations of Thermally Induced Cation/Cluster Migration and the Resulting Effects on the Equilibrium Adsorption of Nitrogen. Chem. Mater. 12 (2000) 3020-3031.

[13] A. Jayaraman, R. T. Yang, Adsorption of Nitrogen, Oxygen and Argon on Na-CeX Zeolites. Adsorption. 8 (2002) 271-278.

[14] N. D. Hutson, R. T. Yang, Structural effects on the adsorption of atmospheric gases in mixed Li,Ag–X-Zeolite. AIChE Journal. 46 (2000) 2305-2317.

[15] R. L. Chiang, R. D. Whitley, J. E. Ostroski, D. P. Dee, Argon/Oxygen Selective X-Zeolite. US Patent. (2002) 6,432,170.

[16] R. T. Yang, N. D. Hutson, Lithium-Based Zeolites Containing Silver and Copper and Use Thereof for Selective Adsorption. (2004) 6,780,806.

[17] H. W. Habgood, Adsorptive and Gas Chromatographic Properties of Various Cationic Forms of Zeolite X. Canadian Journal of Chemistry. 42 (1964) 2340-2350.

[18] Y. Y. Huang, Adsorption in AgX and AgY zeolites by carbon monoxide and other simple molecules. Journal of Catalysis. 32 (1974) 482-491.

[19] S. J. Weigel, J. E. MacDougall, C. G. Coe, Y. L. Xiong, J. A. Martens, P. A. Jacobs, P. A. Webley, Gas Separation with Lithium-Containing ZSM-2 Metallosilicates. US Patent. (1998) 5,779,766.

[20] N. D. Hutson, S. C. Zajic, R. T. Yang, Influence of residual water on the adsorption of atmospheric gases in Li-X zeolite: experiment and simulation. Ind. Eng. Chem. Res. 39 (2000) 1775-1780.

[21] T. Frising, P. Leflaive, Extraframework cation distributions in X and Y faujasite zeolites: A review. Micro. and Meso. Mat. 114 (2008) 27-63.

[22] D. H. Olson, H. S. Sherry, An X-Ray Study of Strontium-Sodium Ion Exchange in Linde X. An Example of a Two-Phase Zeolite System. J. Phys. Chem. 72 (1968) 4095-4104.

[23] C. Pichon, H. Palancher, J. Lynch, J. L. Hodeau, J. F. Berar, Cationic distribution of Ca^{2+} and Sr^{2+} cations in hydrated and dehydrated zeolite SrX, CaX and CaSrX. An in situ anomalous X-ray diffraction study. Studies in Surface Science and Catalysis. 158 (2005) 789-796.

[24] H. Palancher, C. Pichon, B. Rebours, J. L. Hodeau, J. Lynch, J. F. Berar, S. Prevot, G. Conan, C. Bouchard, A cell for in situ dynamic X-ray diffraction studies: application to the dehydration of zeolite SrX. J. Appl. Cryst. 38 (2005) 370-373.

[25] F. E. Epiepang, J. Li, Y. Liu, R. T. Yang, Low-pressure performance evaluation of CO_2, H_2O, and CH_4 on Li-LSX as a superior adsorbent for air prepurification. Chem. Eng. Sci., 147 (2016) 100-108.

[26] B. J. Marine, P. A. Webley, A new simplified pressure/vacuum swing adsorption model for rapid adsorbent screening for CO_2 capture applications. Intern. J. Greenhouse Gas Contr, 15 (2013) 16-31.

[27] F. E. Epiepang, X. Yang, J. Li, Y. Liu, R. T. Yang, Mixed-Cation LiCa-LSX Zeolite with Minimum Lithium for Air Separation, AIChE Journal, 64 (2017) 406-415.

[28] S. U. Rege, R. T. Yang, Limits for air separation by adsorption with LiX zeolite. Ind. Eng. Chem. Res. 36 (1997) 5358-5365.

[29] V. P. Mulgundmath, F. H. Tezel, F. Hou, T. C. Golden, Binary Adsorption Behavior of Methane and Nitrogen gases. J. Porous Mater. 19 (2012) 455-464.

Appendix A – Supplementary Material for Chapter 2

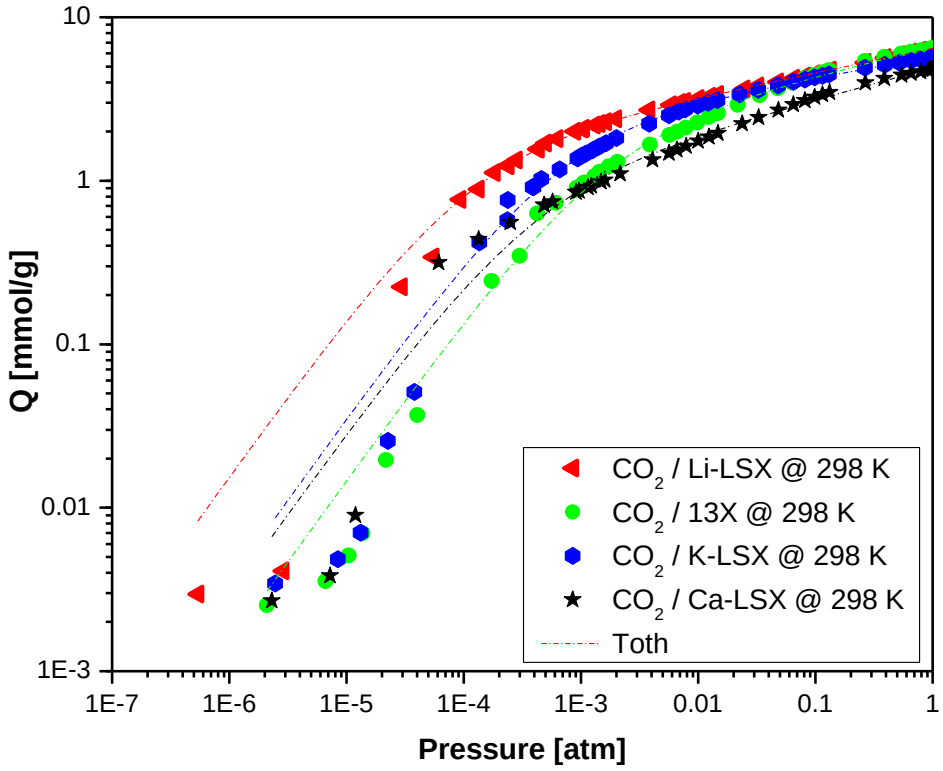

Figure S2.1a Tòth fit model to experimental adsorption Isotherms of CO_2 at 298 K on representative adsorbents.

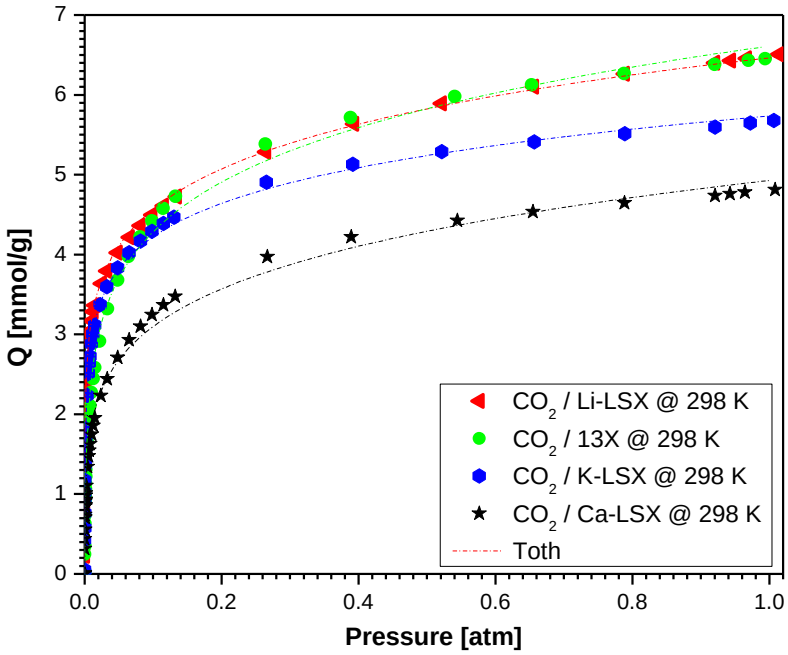

Figure S2.1b Tòth fit model to experimental adsorption Isotherms of CO_2 at 298 K on representative adsorbents.

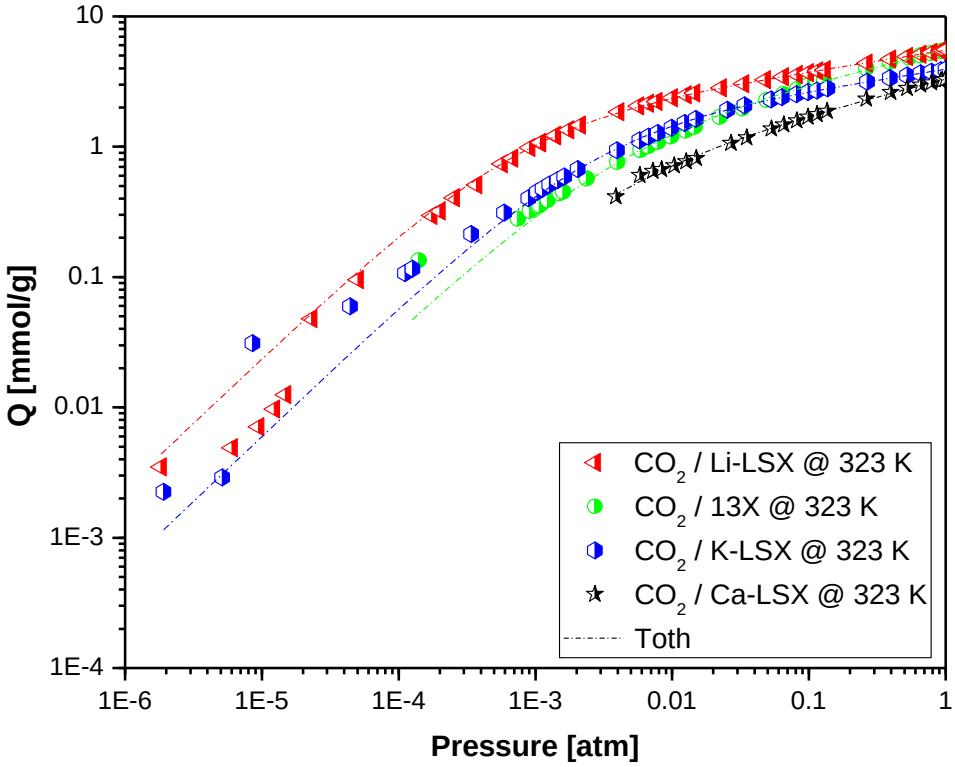

Figure S2.2a Tòth fit model to experimental adsorption Isotherms of CO_2 at 323 K on representative adsorbents.

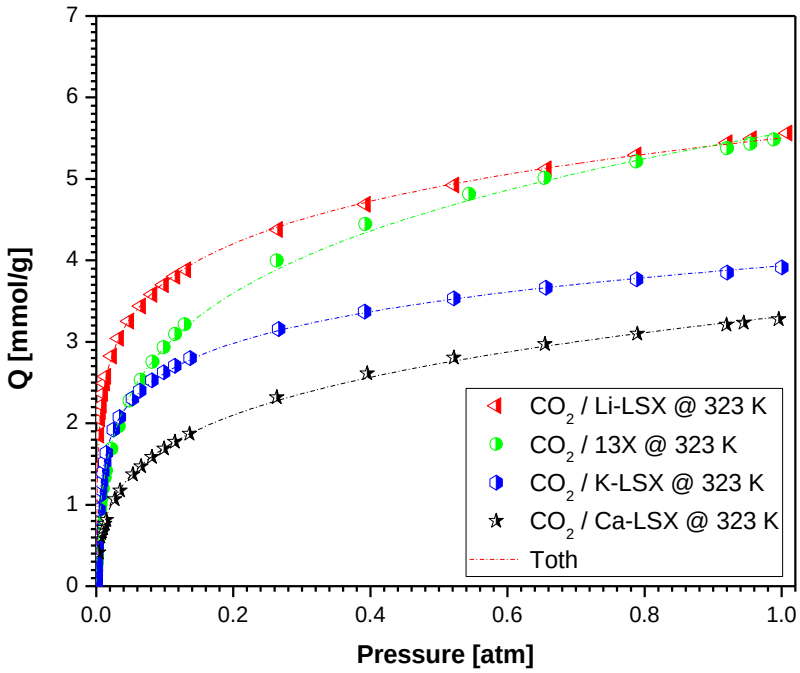

Figure S2.2b Tòth fit model to experimental adsorption Isotherms of CO_2 at 323 K on representative adsorbents.

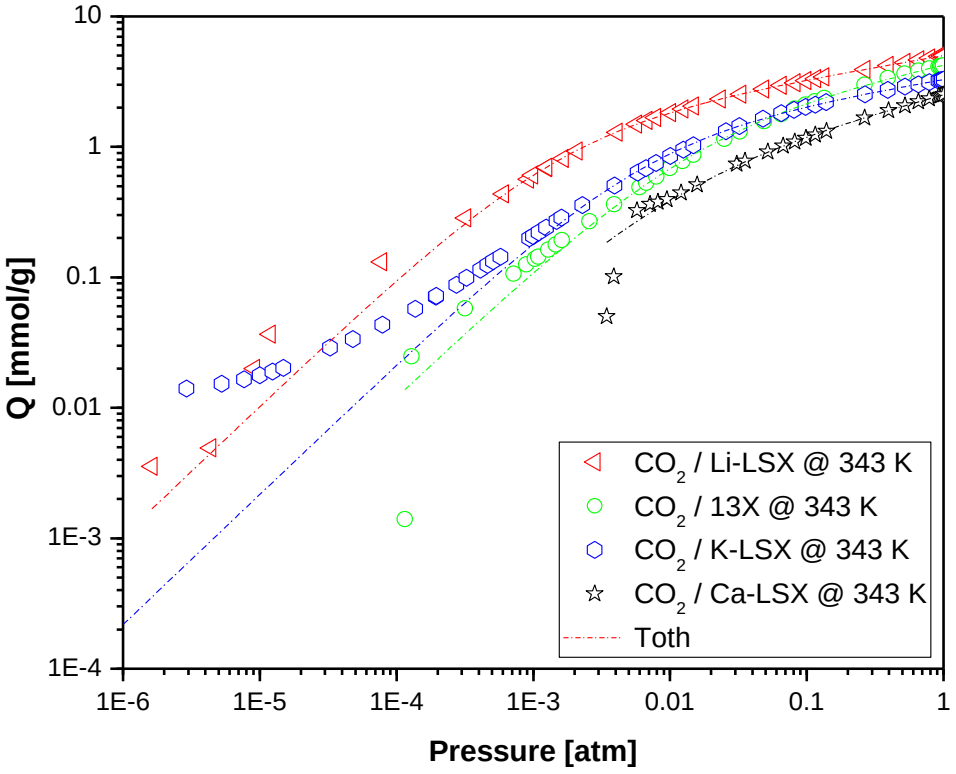

Figure S2.3a Tòth fit model to experimental adsorption Isotherms of CO_2 at 343 K on representative adsorbents.

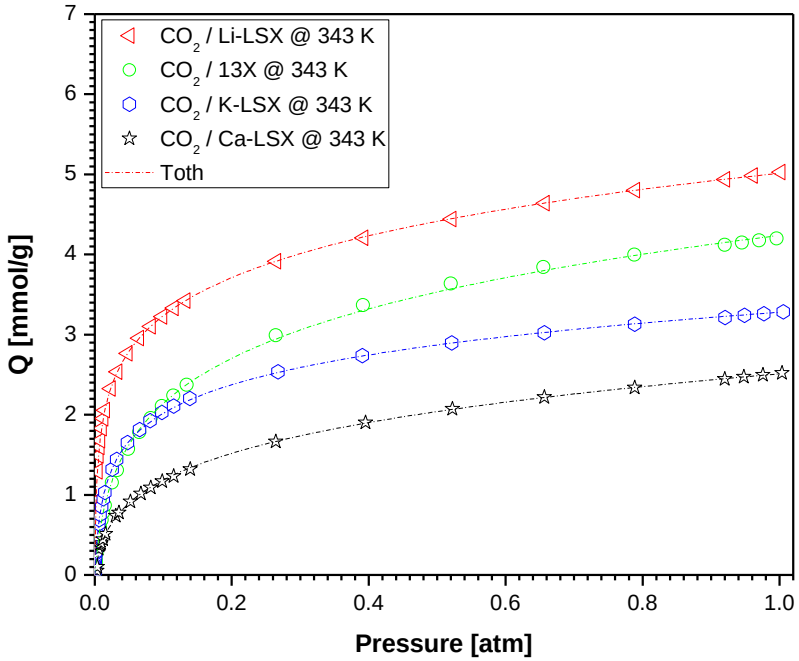

Figure S2.3b Tòth fit model to experimental adsorption Isotherms of CO_2 at 343 K on representative adsorbents.

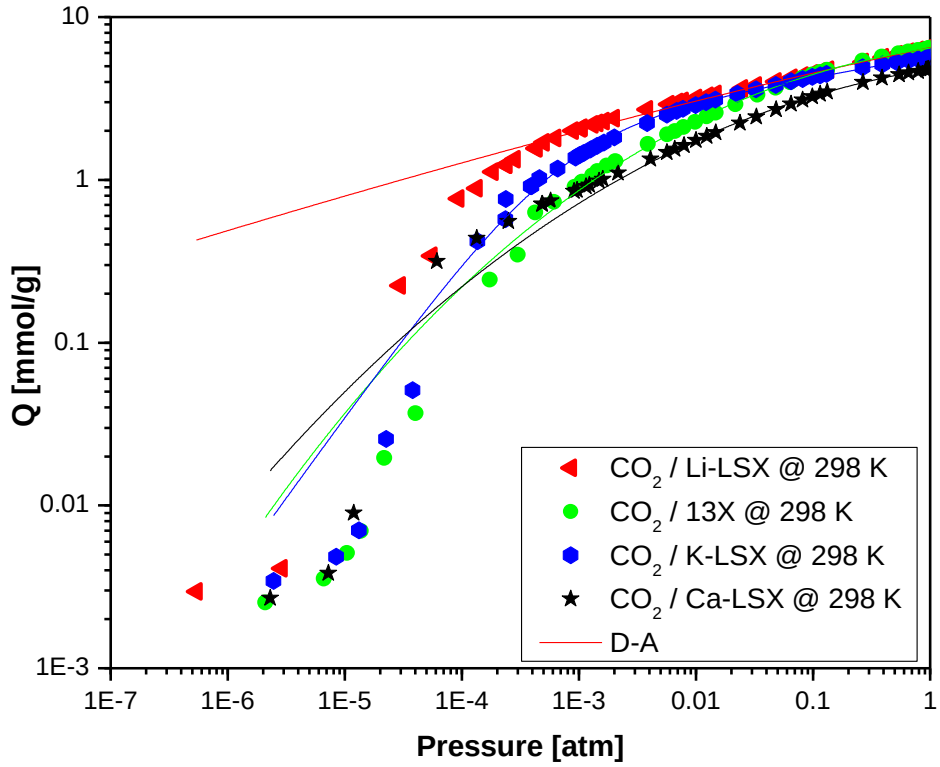

Figure S2.4a D-A fit model to experimental adsorption Isotherms of CO_2 at 298 K on representative adsorbents.

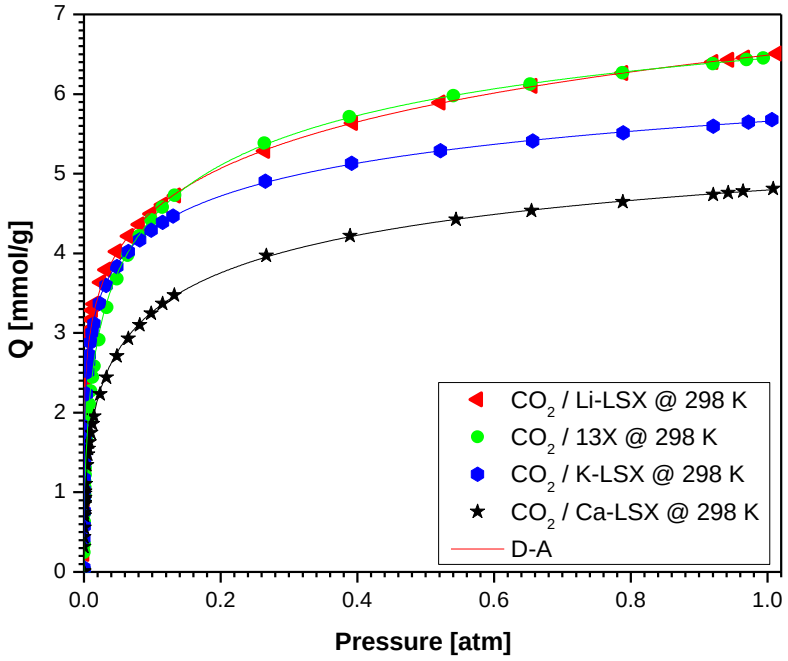

Figure S2.4b D-A fit model to experimental adsorption Isotherms of CO_2 at 298 K on representative adsorbents.

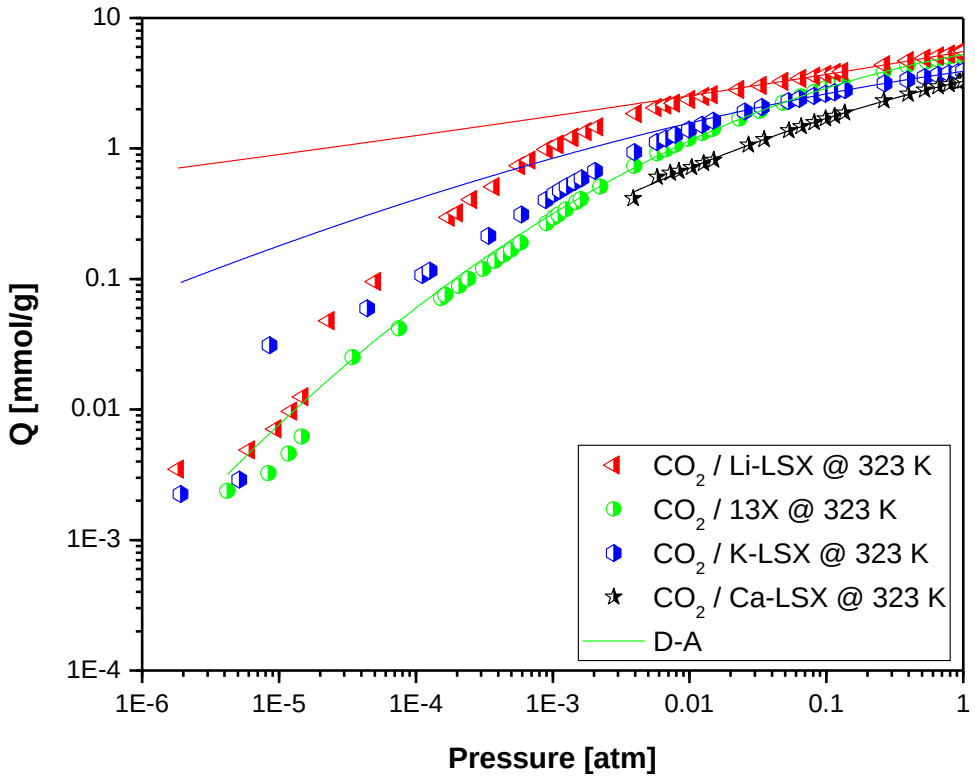

Figure S2.5a D-A fit model to experimental adsorption Isotherms of CO_2 at 323 K on representative adsorbents.

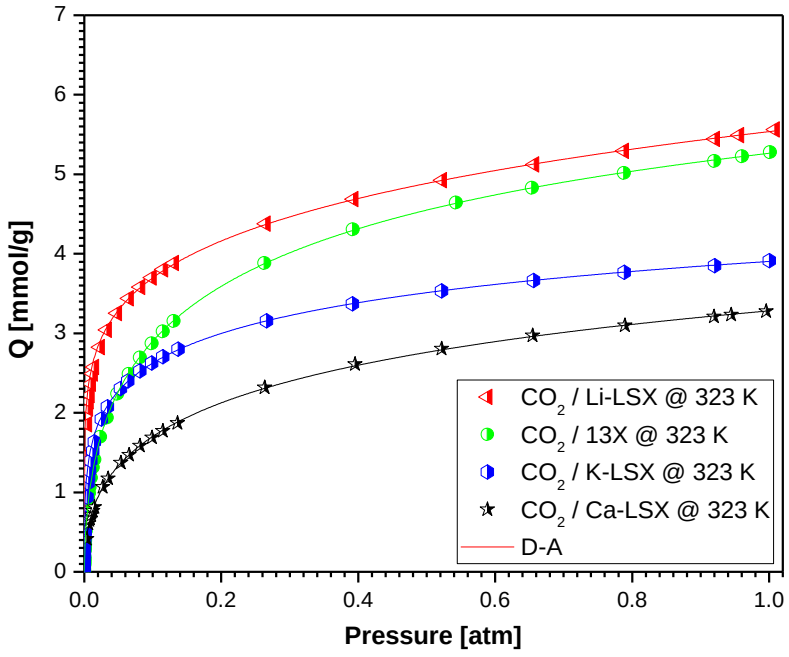

Figure S2.5b D-A fit model to experimental adsorption Isotherms of CO_2 at 323 K on representative adsorbents.

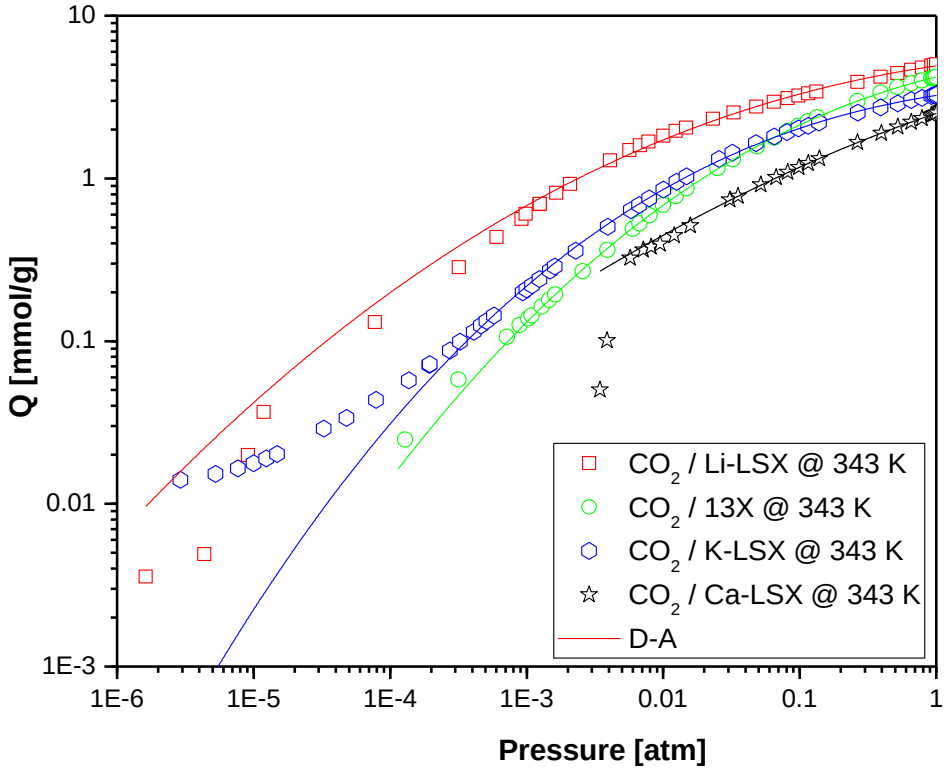

Figure S2.6a D-A fit model to experimental adsorption Isotherms of CO_2 at 343 K on representative adsorbents.

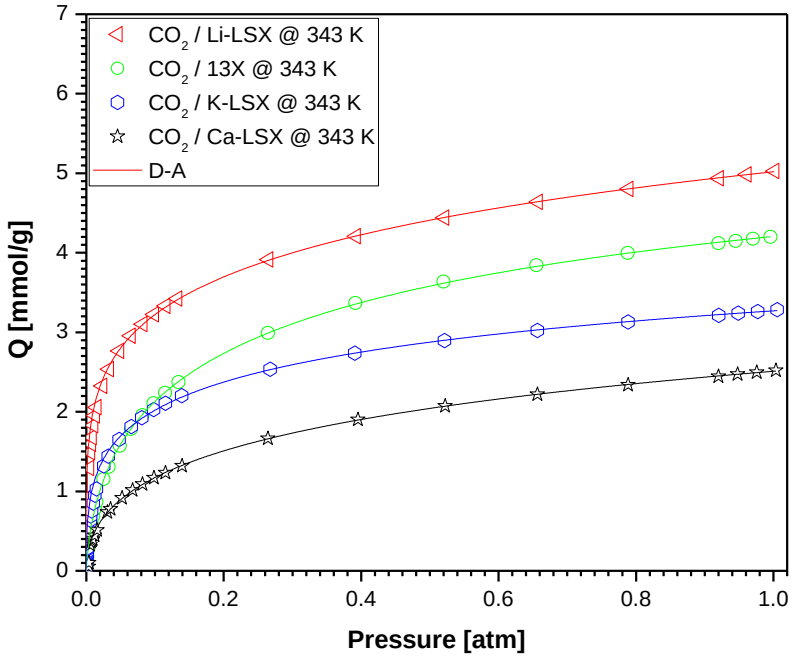

Figure S2.6a D-A fit model to experimental adsorption Isotherms of CO_2 at 343 K on representative adsorbents.

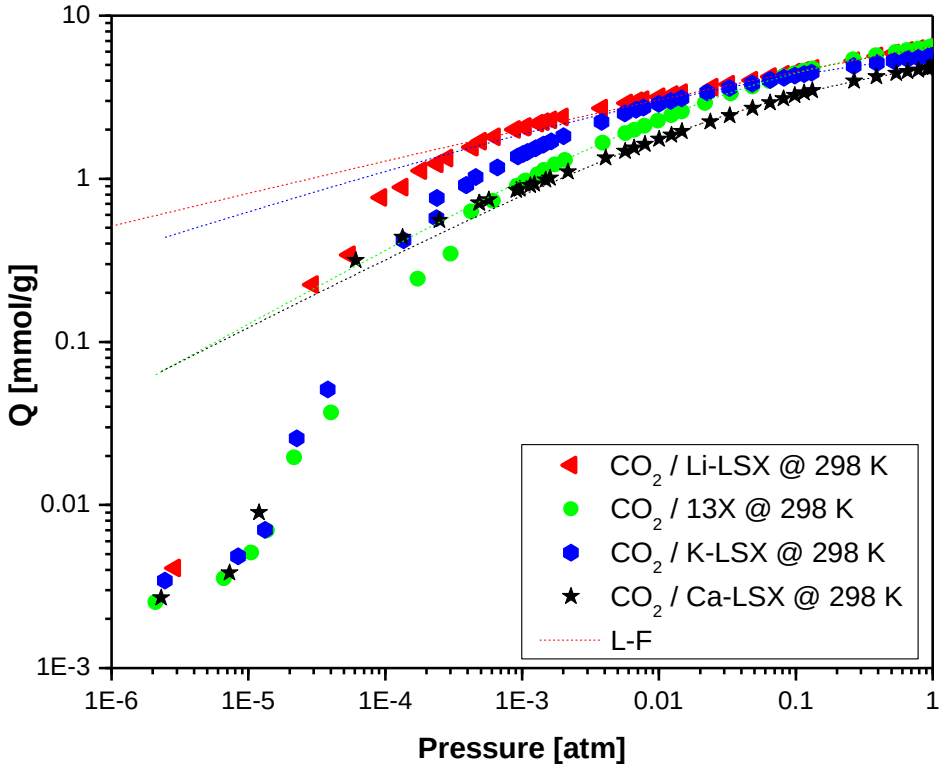

Figure S2.7a L-F fit model to experimental adsorption Isotherms of CO_2 at 298 K on representative adsorbents.

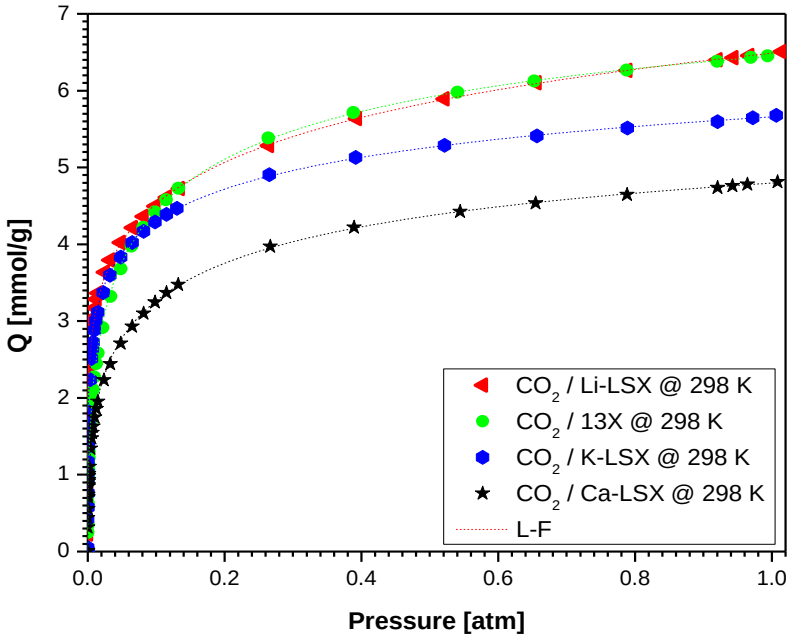

Figure S2.7b L-F fit model to experimental adsorption Isotherms of CO_2 at 298 K on representative adsorbents.

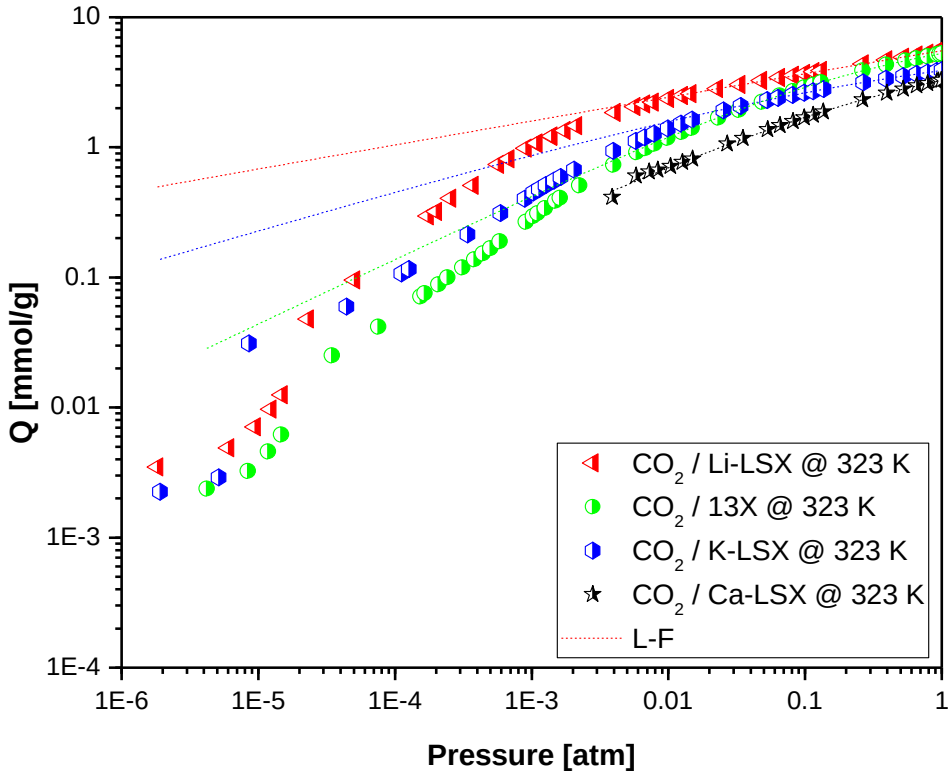

Figure S2.8a L-F fit model to experimental adsorption Isotherms of CO_2 at 323 K on representative adsorbents.

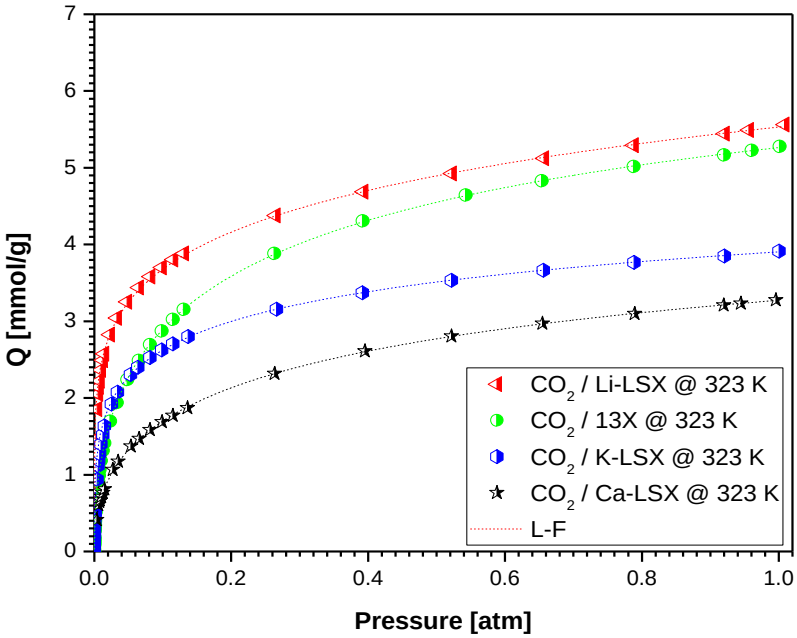

Figure S2.8b L-F fit model to experimental adsorption Isotherms of CO_2 at 323 K on representative adsorbents.

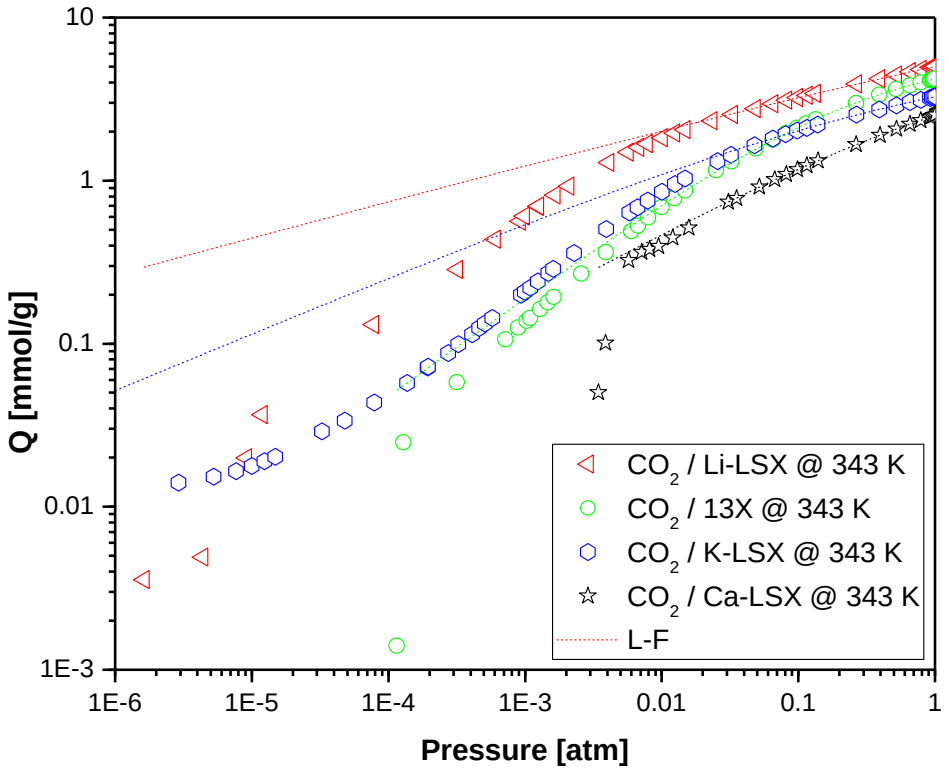

Figure S2.9a L-F fit model to experimental adsorption Isotherms of CO_2 at 343 K on representative adsorbents.

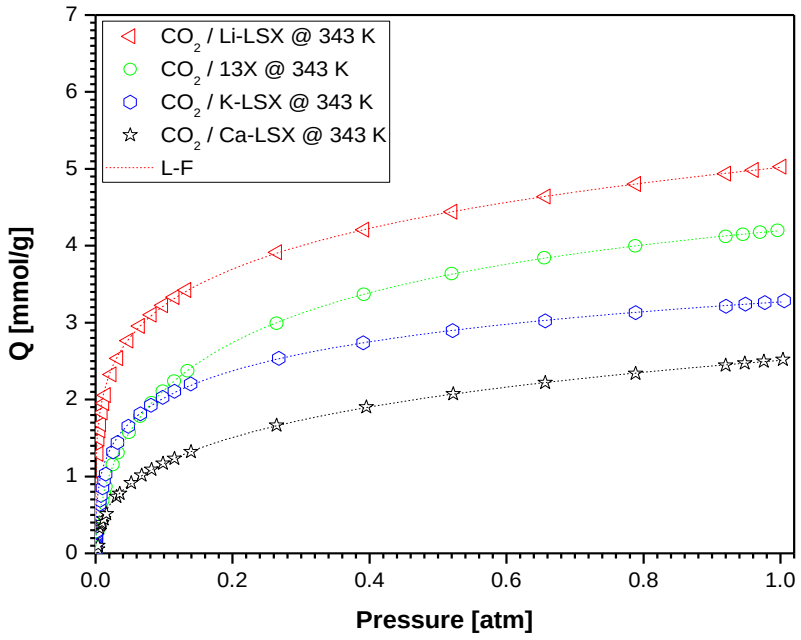

Figure S2.9b L-F fit model to experimental adsorption Isotherms of CO_2 at 343 K on representative adsorbents.

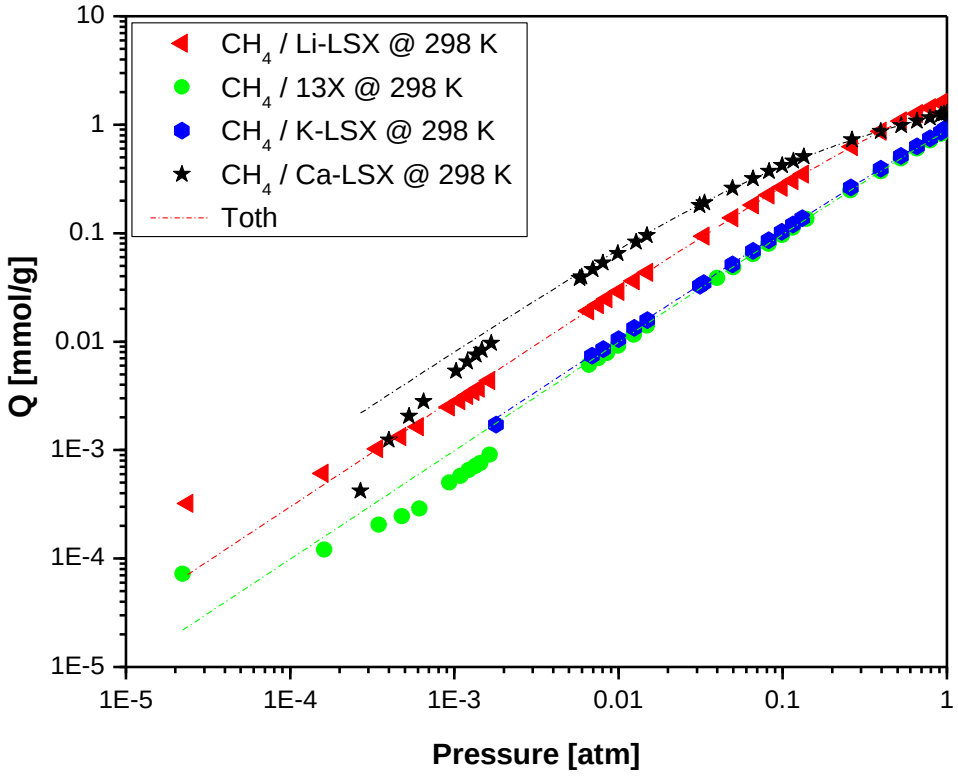

Figure S2.10a Tòth fit model to experimental adsorption Isotherms of CH_4 at 298 K on representative adsorbents.

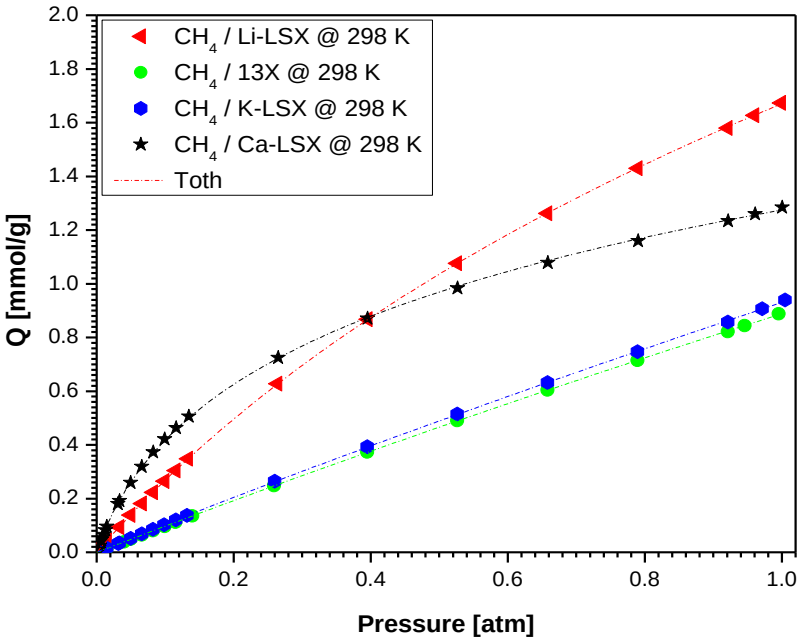

Figure S2.10b Tòth fit model to experimental adsorption Isotherms of CH_4 at 298 K on representative adsorbents.

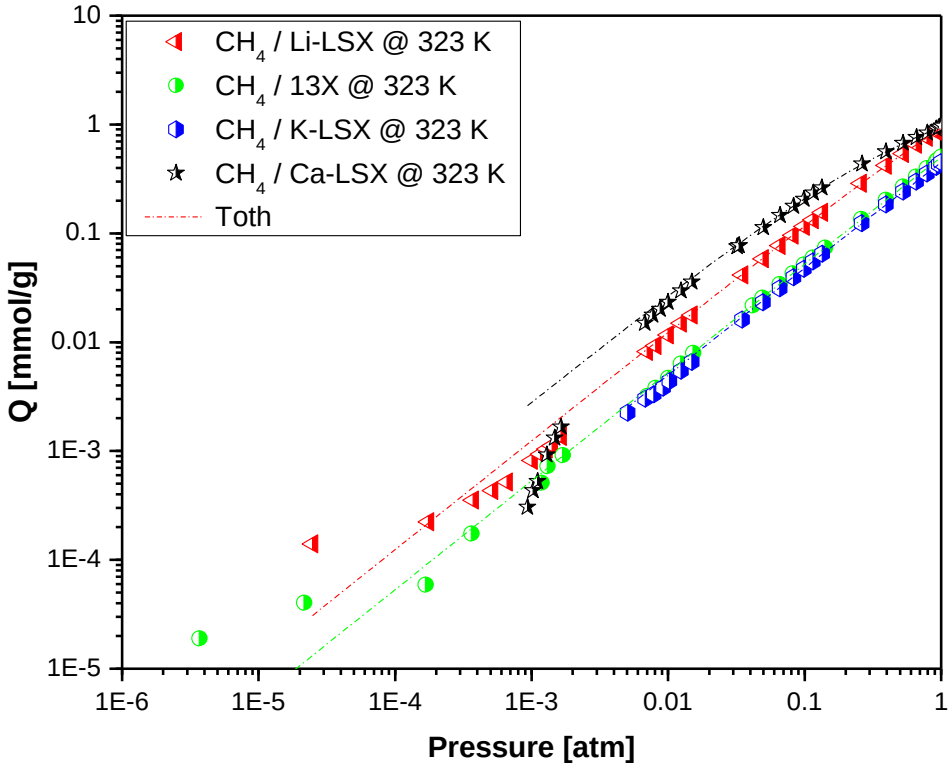

Figure S2.11a Tòth fit model to experimental adsorption Isotherms of CH_4 at 323 K on representative adsorbents.

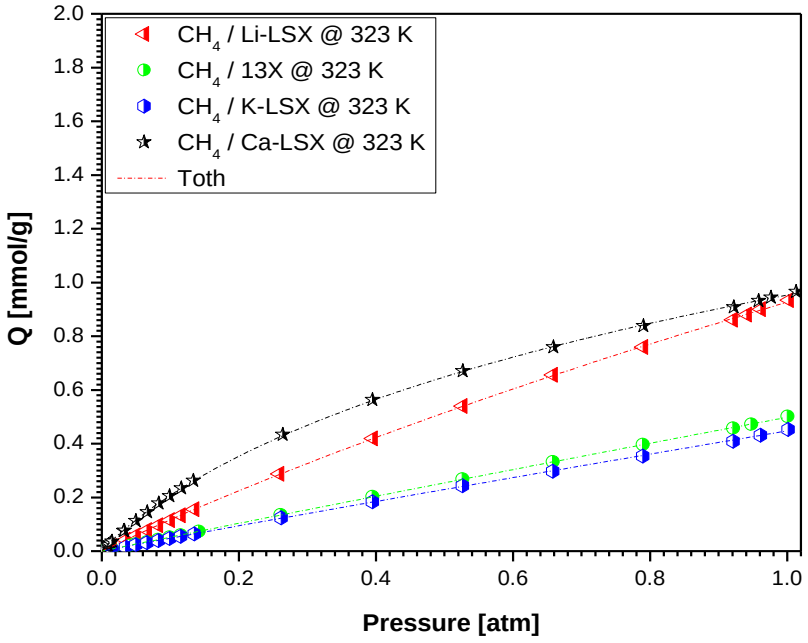

Figure S2.11b Tòth fit model to experimental adsorption Isotherms of CH_4 at 323 K on representative adsorbents.

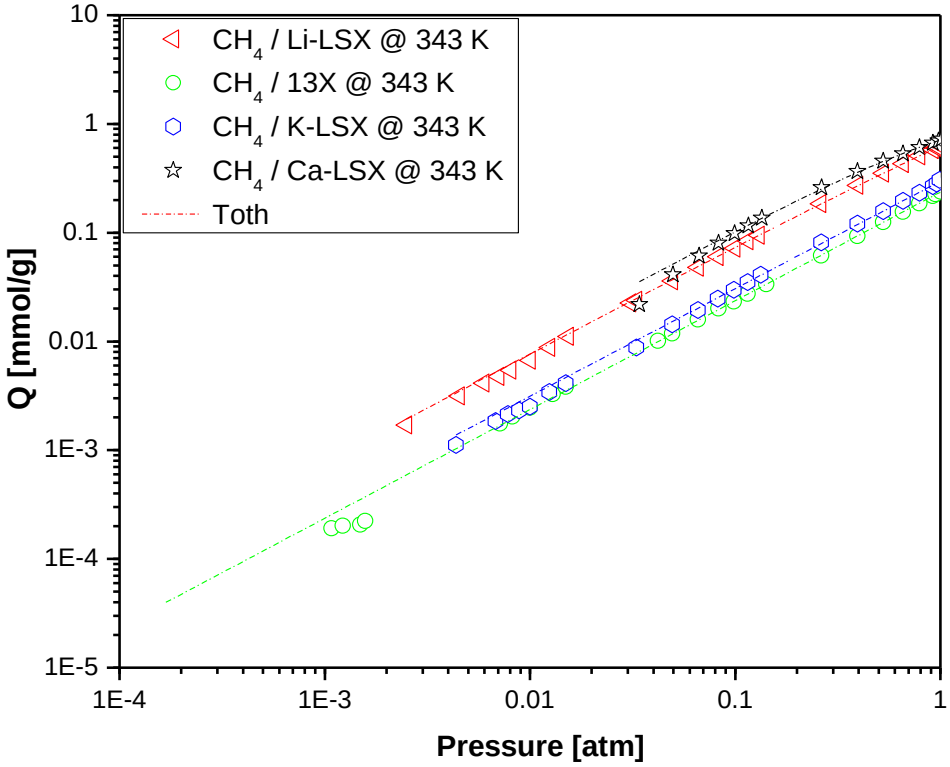

Figure S2.12a Tòth fit model to experimental adsorption Isotherms of CH_4 at 343 K on representative adsorbents.

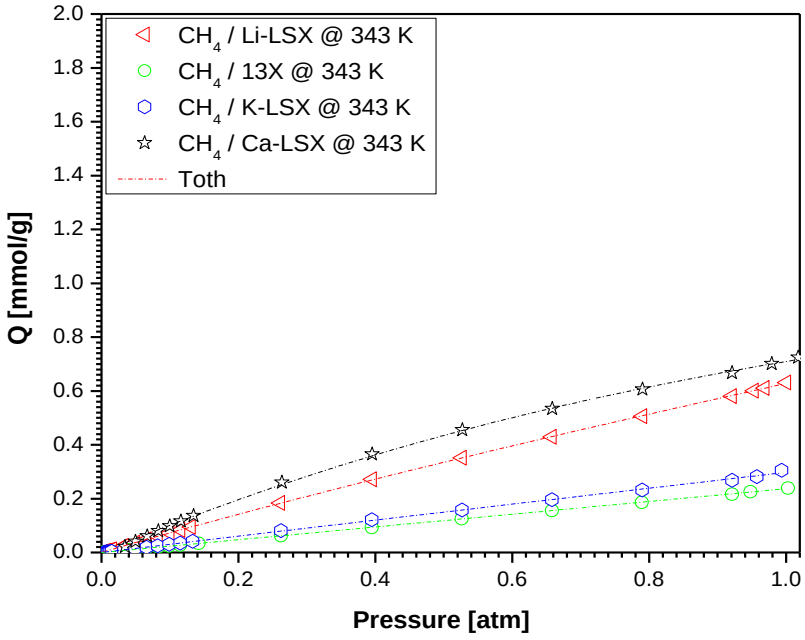

Figure S2.12a Tòth fit model to experimental adsorption Isotherms of CH_4 at 343 K on representative adsorbents.

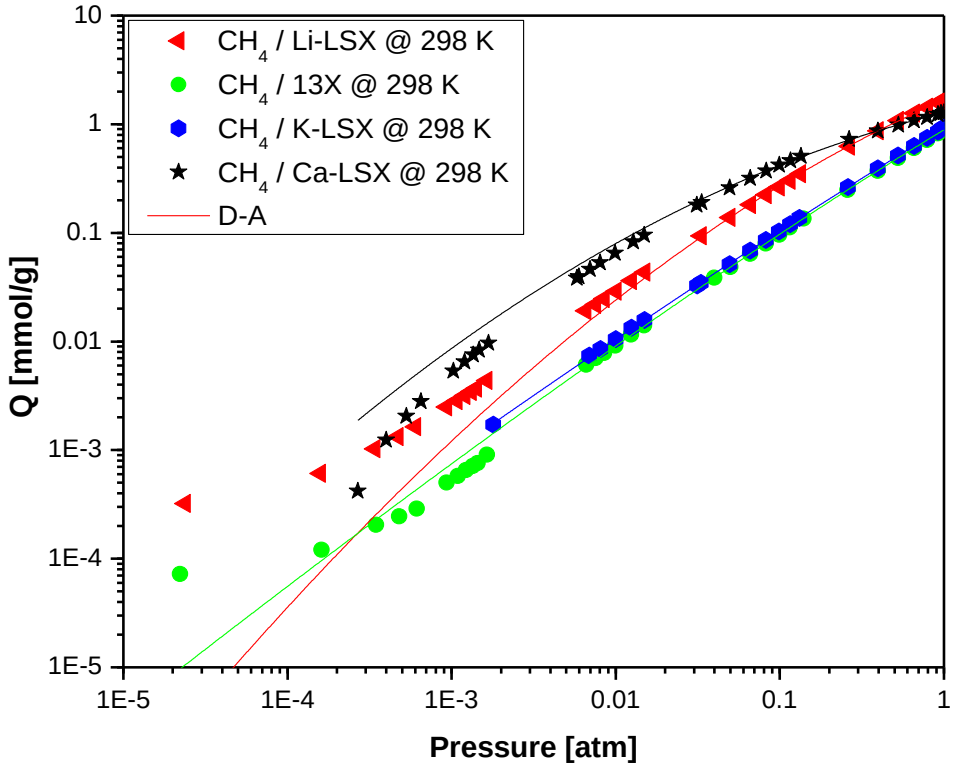

Figure S2.13a D-A fit model to experimental adsorption Isotherms of CH_4 at 298 K on representative adsorbents.

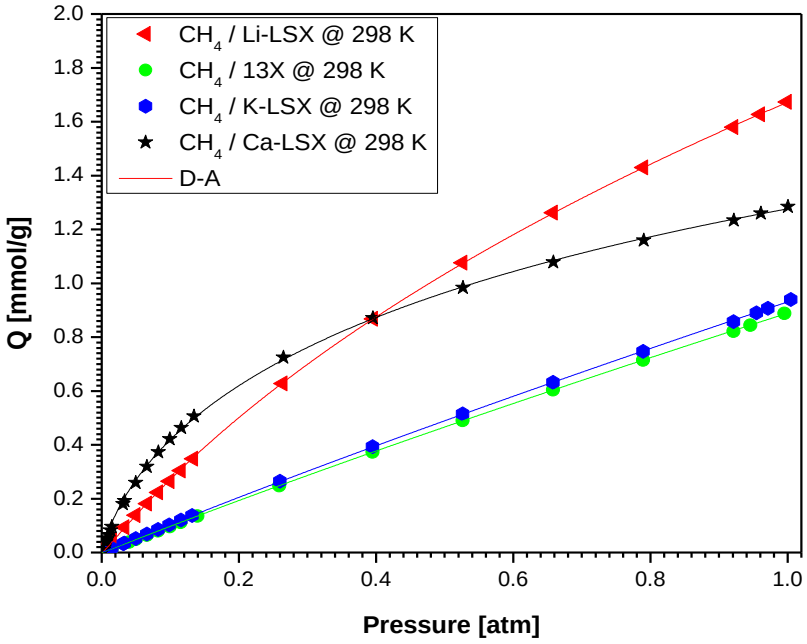

Figure S2.13b D-A fit model to experimental adsorption Isotherms of CH_4 at 298 K on representative adsorbents.

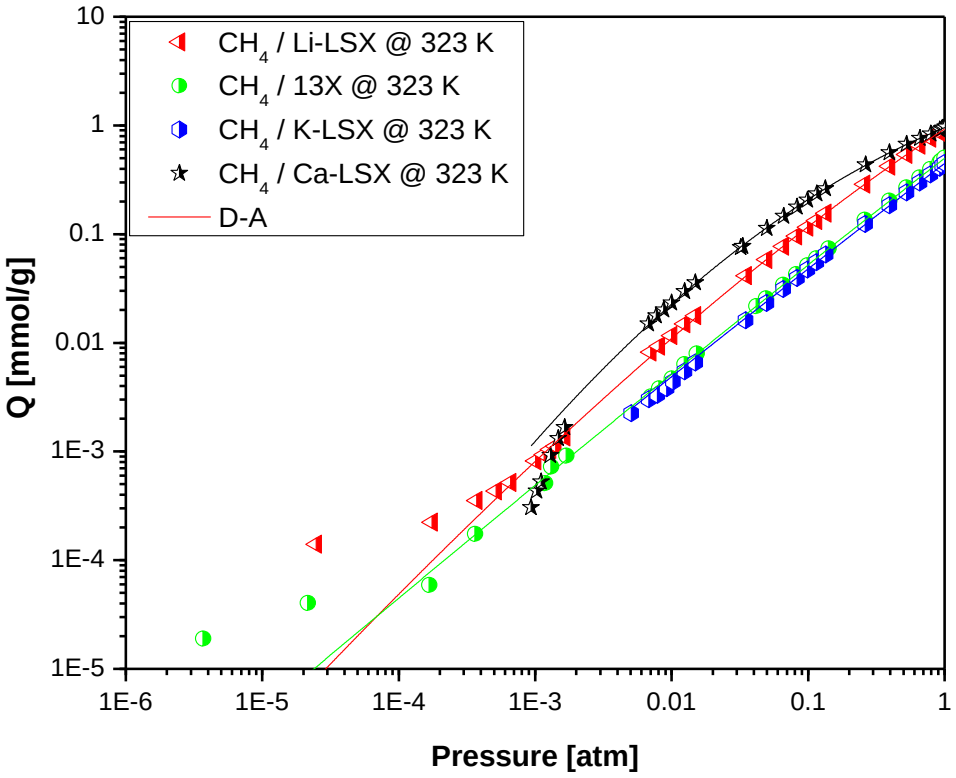

Figure S2.14a D-A fit model to experimental adsorption Isotherms of CH_4 at 323 K on representative adsorbents.

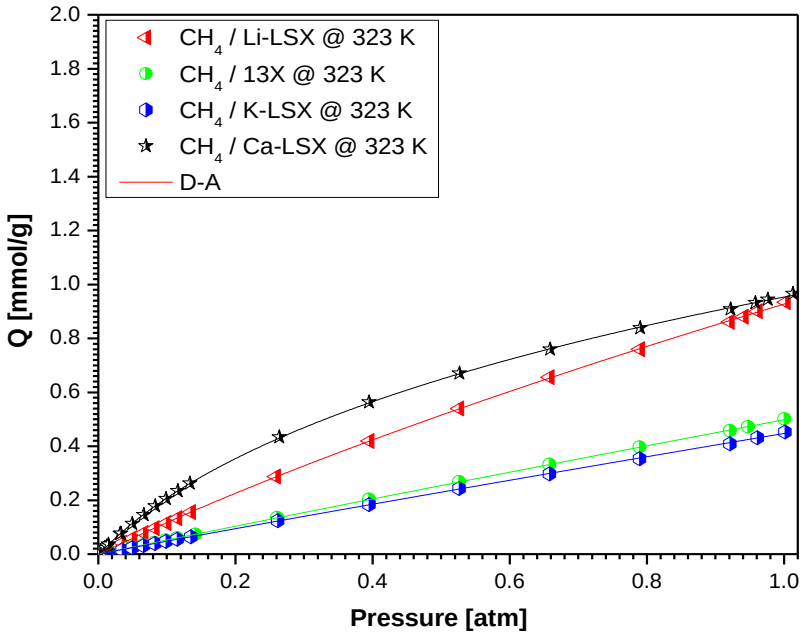

Figure S2.14b D-A fit model to experimental adsorption Isotherms of CH_4 at 323 K on representative adsorbents.

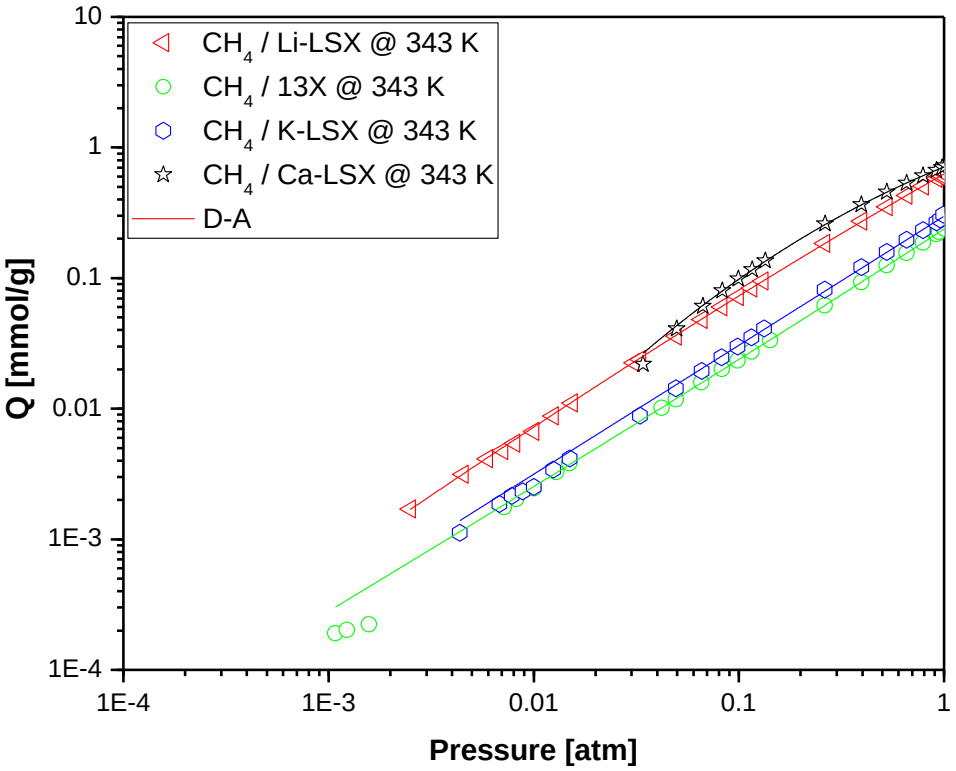

Figure S2.15a D-A fit model to experimental adsorption Isotherms of CH_4 at 343 K on representative adsorbents.

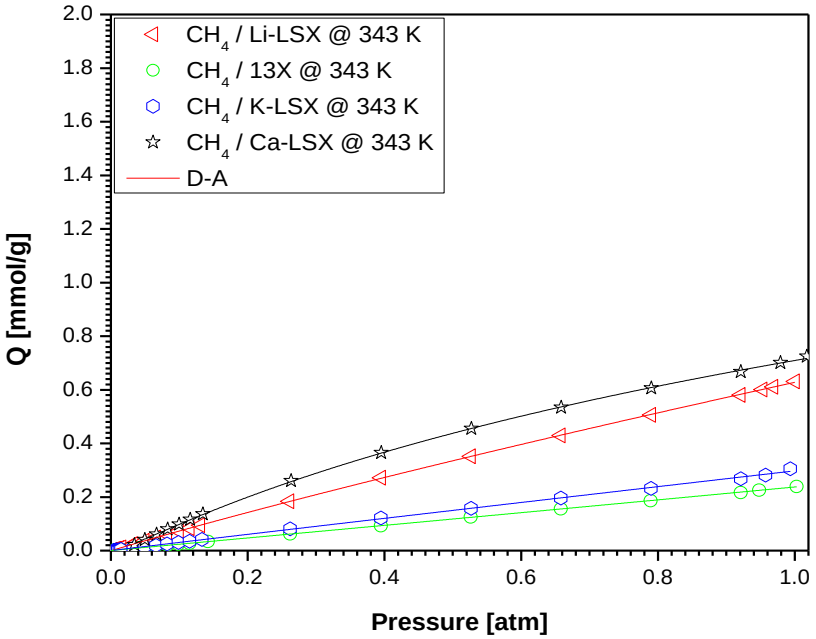

Figure S2.15b D-A fit model to experimental adsorption Isotherms of CH_4 at 343 K on representative adsorbents.

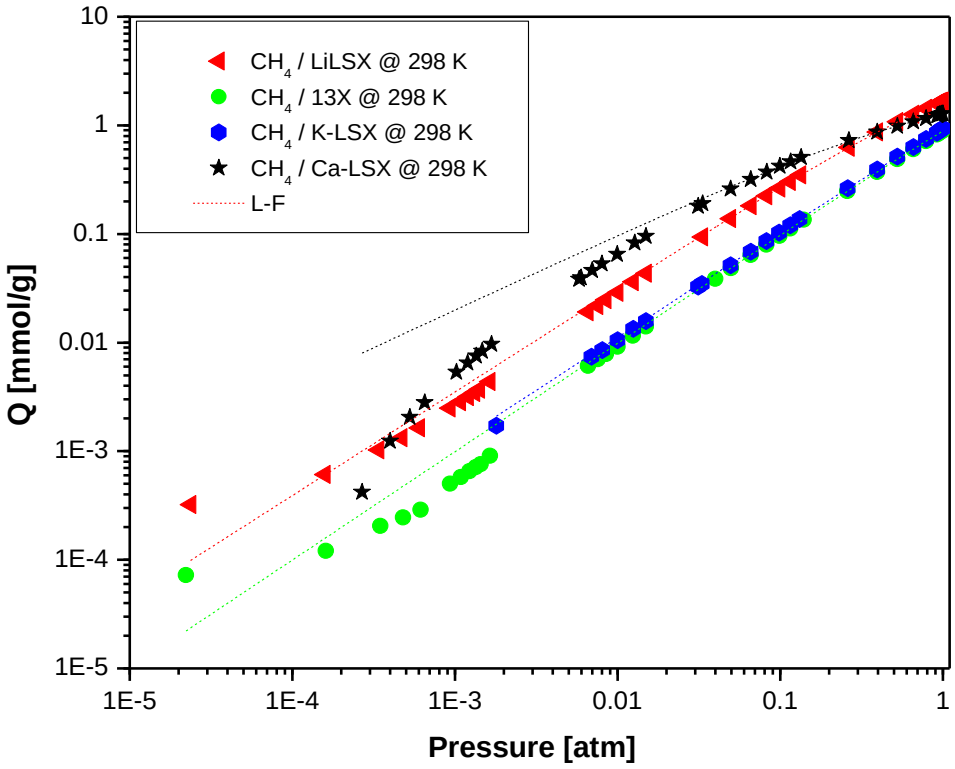

Figure S2.16a L-F fit model to experimental adsorption Isotherms of CH_4 at 298 K on representative adsorbents.

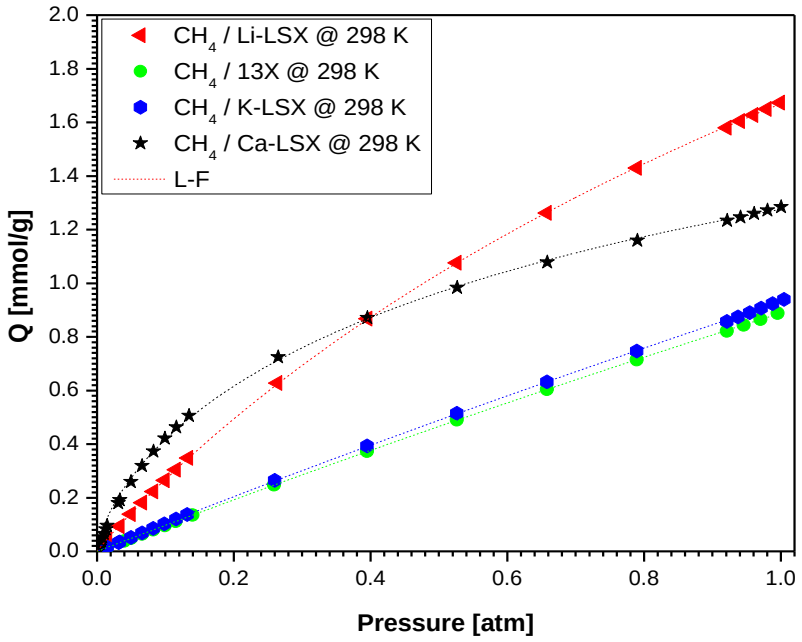

Figure S2.16b L-F fit model to experimental adsorption Isotherms of CH_4 at 298 K on representative adsorbents.

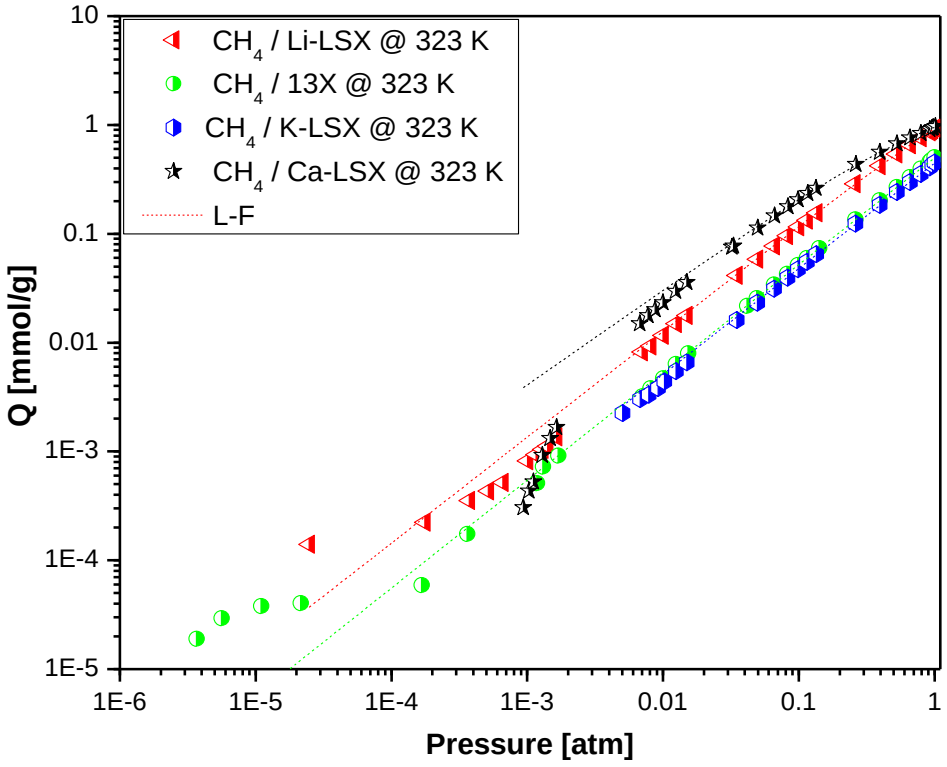

Figure S2.17a L-F fit model to experimental adsorption Isotherms of CH_4 at 323 K on representative adsorbents.

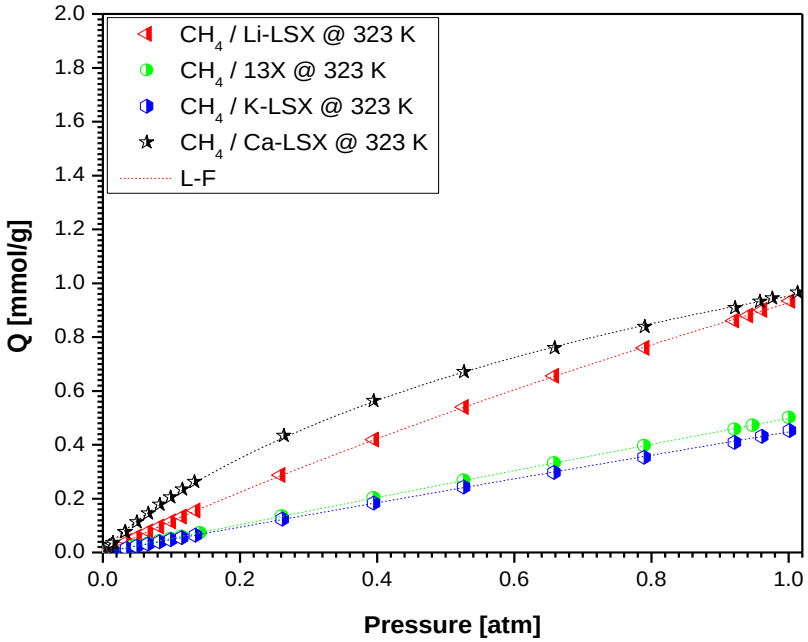

Figure S2.17b L-F fit model to experimental adsorption Isotherms of CH_4 at 323 K on representative adsorbents.

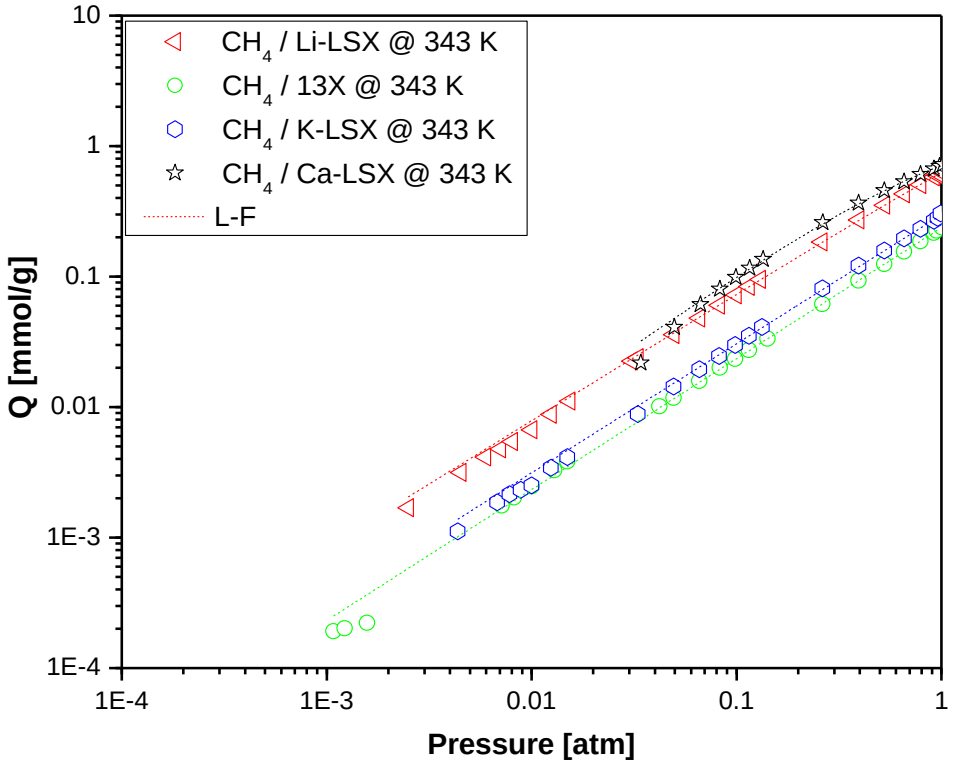

Figure S2.18a L-F fit model to experimental adsorption Isotherms of CH_4 at 343 K on representative adsorbents.

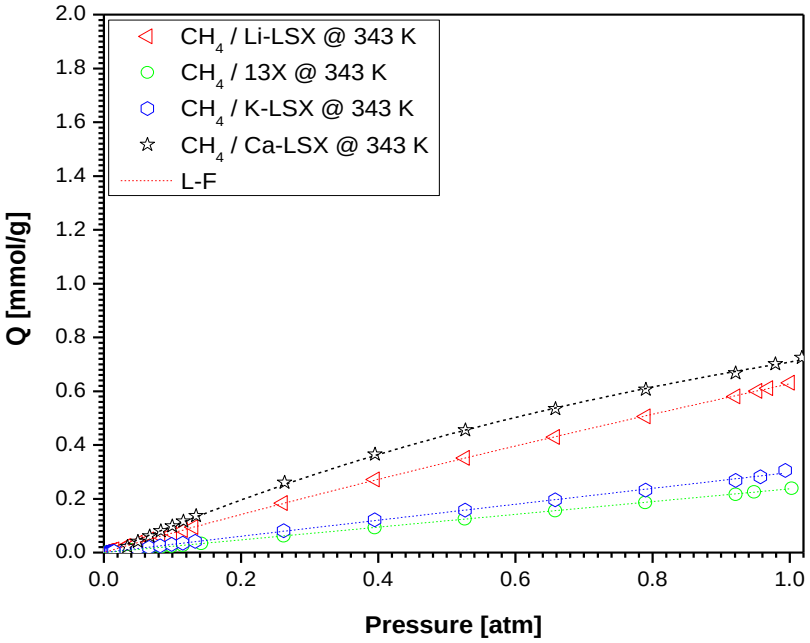

Figure S2.18b L-F fit model to experimental adsorption Isotherms of CH_4 at 343 K on representative adsorbents.

Table S2.1 Representative values of model parameters fit to experimental adsorption data at 323 K.

	Tòth			Dubinin-Astakhov			Langmuir-Freundlich		
	a [mmol/g]	d [atm^k]	k	n_o [mmol/g]	C	m	Q_{sat} [mmol/g]	K [atm^{-n}]	n
CO_2 / Li-LSX	4.62	0.0023	0.84	13.80	0.22	0.81	89.34	0.07	0.19
CO_2 / 13X	4.13	0.015	0.76	7.45	0.15	2.22	8.47	1.64	0.5
CO_2 / K-LSX	3.32	0.007	0.884	5.49	0.13	1.71	7.31	1.15	0.31
CO_2 / Ca-LSX	3.06	0.001	0.75	6.49	0.16	1.67	8.66	0.86	0.37
CH_4 / Li-LSX	2.64	2.93	0.73	10.76	0.48	1.36	5.41	0.21	0.97
CH_4 / 13X	4.05	14.51	0.52	19.53	0.84	1.07	17.97	0.03	0.99
CH_4 / K-LSX	0.94	6.28	0.29	17.68	0.85	1.06	35.61	0.013	0.97
CH_4 / Ca-LSX	1.06	0.51	0.74	2.65	0.25	2.02	2.16	0.79	0.87

Table S2.2 Representative values of model parameters fit to experimental adsorption data at 343 K.

	Tòth			Dubinin-Astakhov			Langmuir-Freundlich		
	a [mmol/g]	d [atm^k]	k	n_o [mmol/g]	C	m	Q_{sat} [mmol/g]	K [atm^{-n}]	n
CO_2 / Li-LSX	4.14	0.005	0.82	6.09	0.13	2.34	26.28	0.24	0.23
CO_2 / 13X	3.58	0.032	0.73	7.43	0.17	2.14	9.28	1.03	0.51
CO_2 / K-LSX	2.75	0.015	0.82	3.94	0.14	2.71	6.52	1.00	0.35
CO_2 / Ca-LSX	2.06	0.003	0.73	6.07	0.20	1.31	11.37	0.325	0.33
CH_4 / Li-LSX	1.86	4.17	0.57	12.82	0.62	1.20	6.88	0.10	0.97
CH_4 / 13X	5.3E-6	1.74	8.2E-6	20.05	1.23	0.93	7975	2.97E-5	1.00
CH_4 / K-LSX	0.03	1.96	0.04	16.51	0.99	0.99	2441	1.22E-4	0.99
CH_4 / Ca-LSX	2.71	2.1	1.23	2.21	0.26	2.24	1.59	0.81	1.09

Appendix B – Supplementary Material for Chapter 3

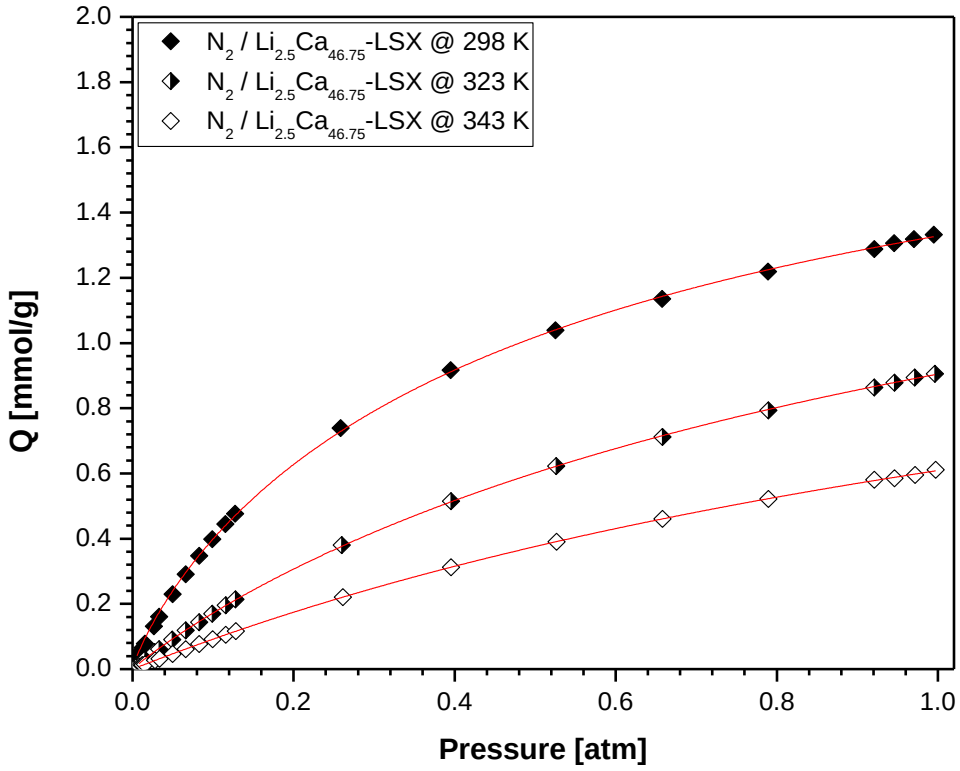

Figure S3.1 Experimental adsorption isotherms of N_2 on $Li_{2.5}Ca_{46.75}$-LSX at various temperatures and at 101 kPa.

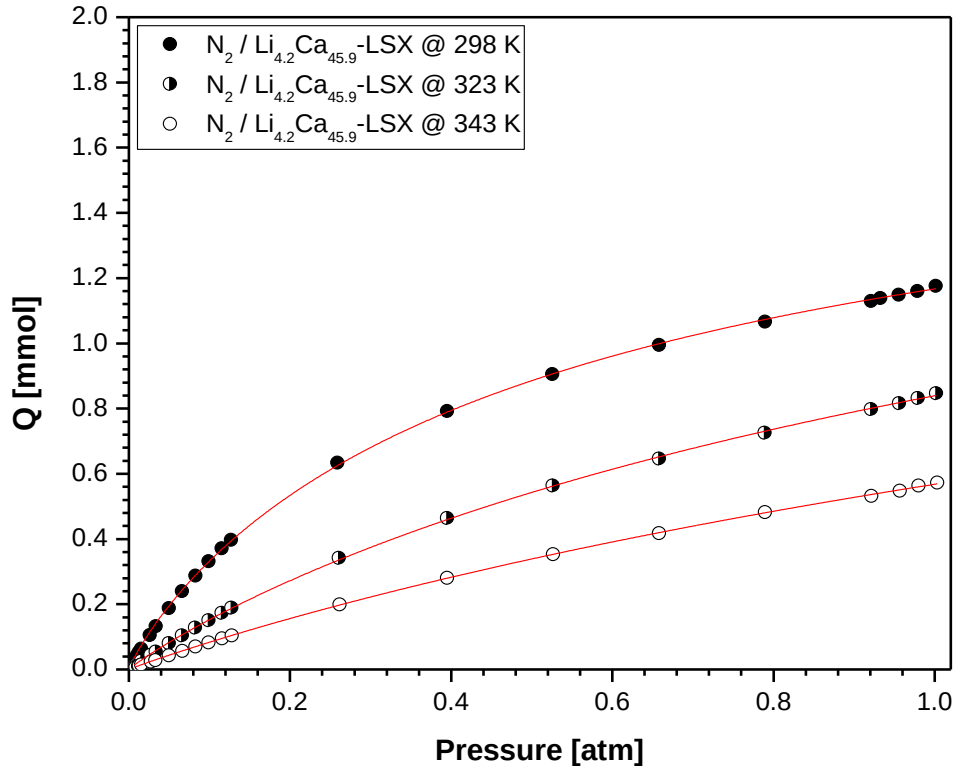

Figure S3.2 Experimental adsorption isotherms of N_2 on $Li_{4.2}Ca_{45.9}$-LSX at various temperatures and at 101 kPa.

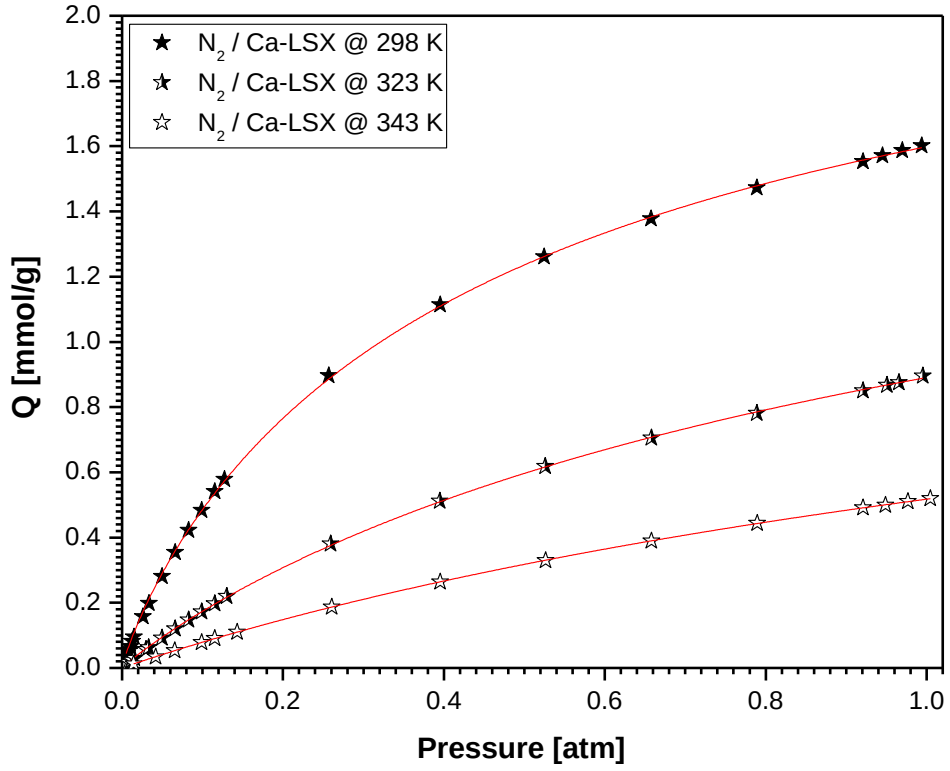

Figure S3.3 Experimental adsorption isotherms of N_2 on Ca-LSX at various temperatures and at 101 kPa.

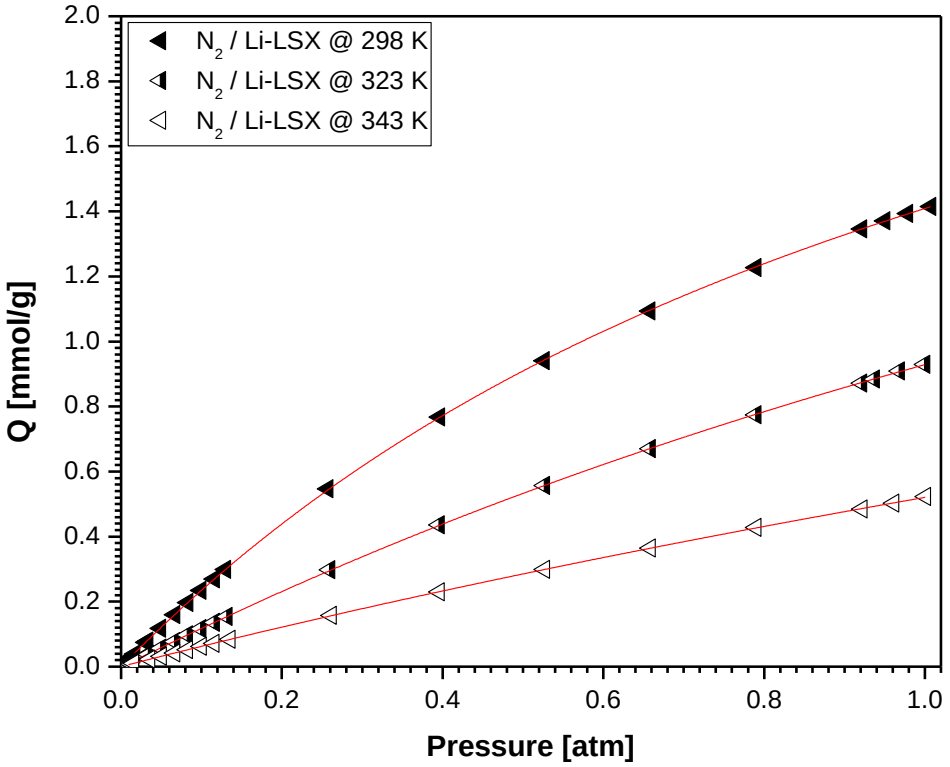

Figure S3.4 Experimental adsorption isotherms of N_2 on Li-LSX at various temperatures and at 101 kPa.

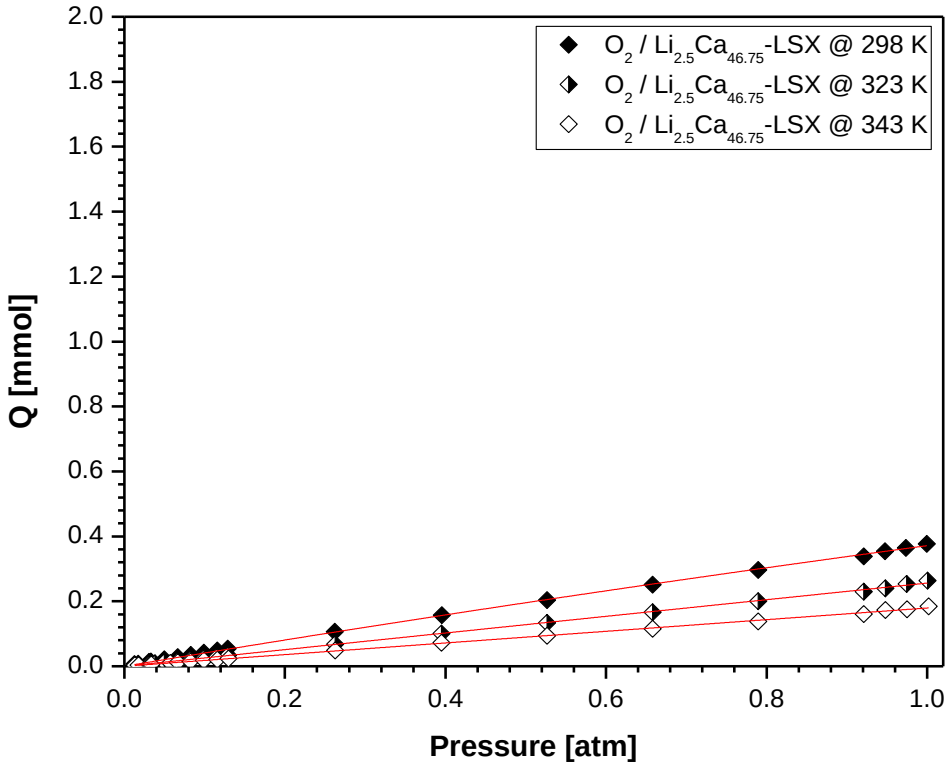

Figure S3.5 Experimental adsorption isotherms of O_2 on $Li_{2.5}Ca_{46.75}$-LSX at various temperatures and at 101 kPa.

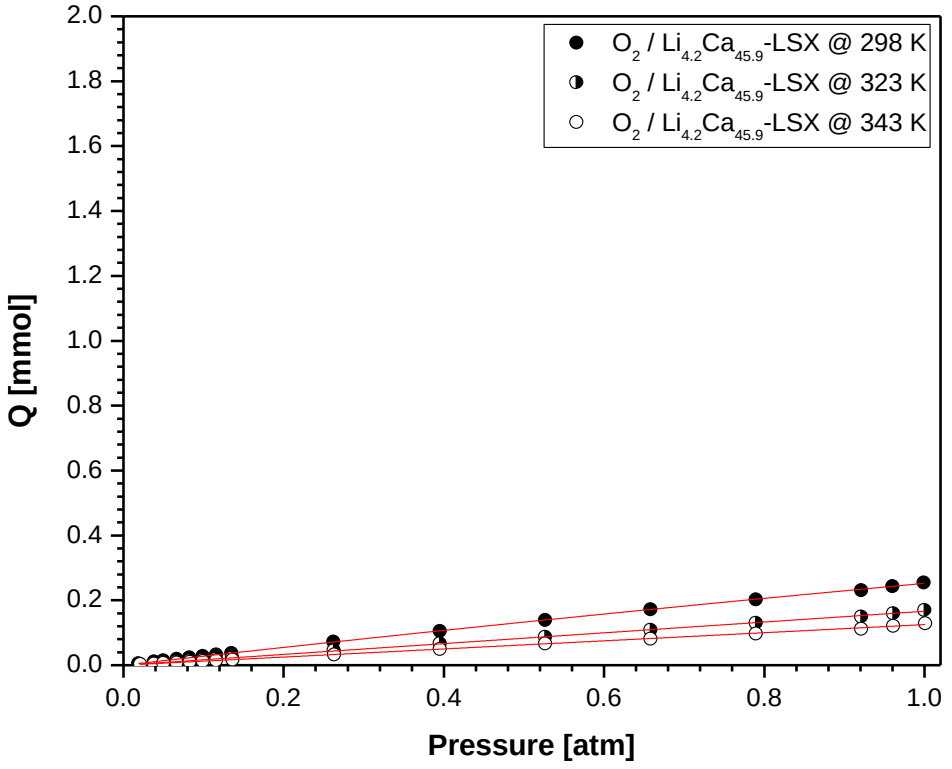

Figure S3.6 Experimental adsorption isotherms of O_2 on $Li_{4.2}Ca_{45.9}$-LSX at various temperatures and at 101 kPa.

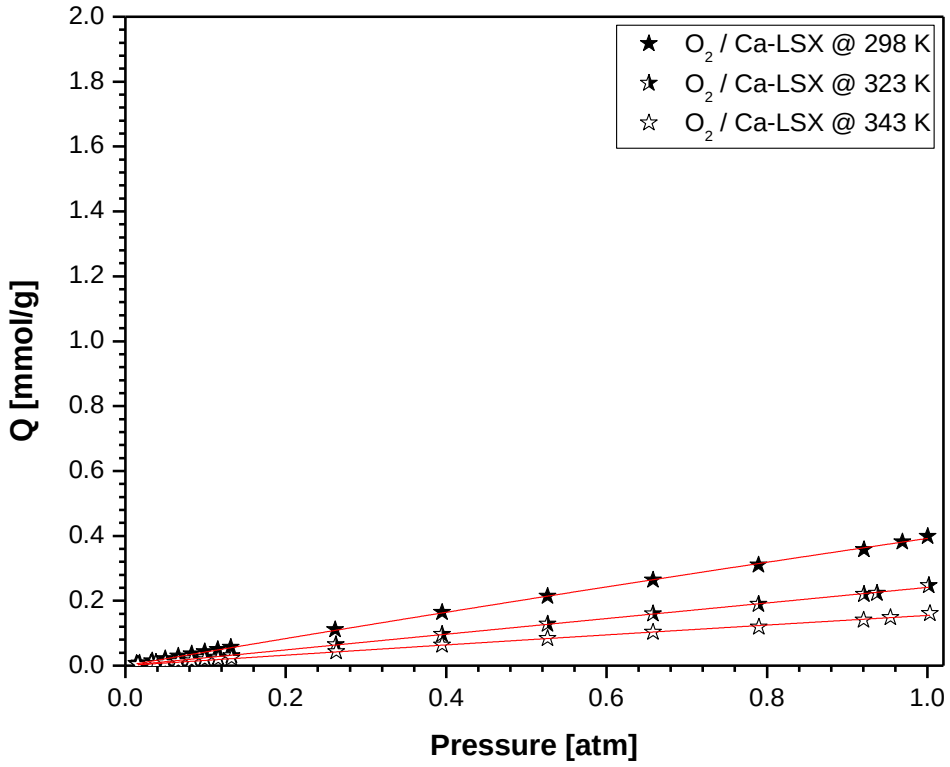

Figure S3.7 Experimental adsorption isotherms of O_2 on Ca-LSX at various temperatures and at 101 kPa.

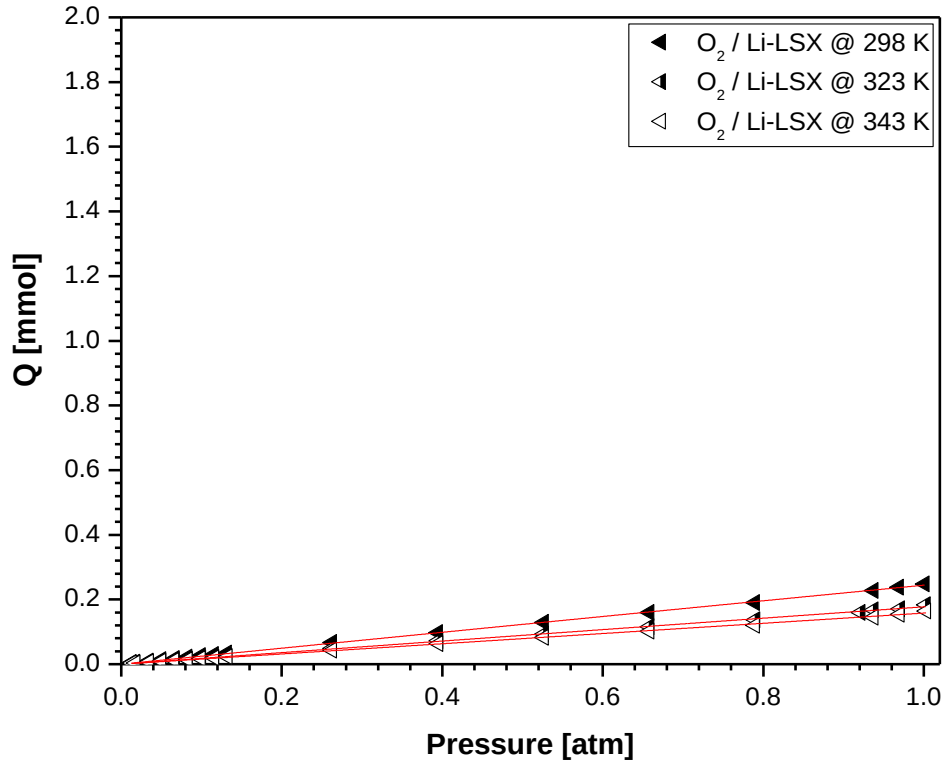

Figure S3.8 Experimental adsorption isotherms of O_2 on Li-LSX at various temperatures and at 101 kPa.

Table S3.1 VPSA Simulation Operating Conditions and Results.

Sorbent	P_H [kPa]	P_{CD} [kPa]	P_L [kPa]	U_H [m/s]	U_L [m/s]	O_2 Product purity [%]	O_2 Product recovery [%]	Product productivity [$tO_2/h/t$]
Ca-LSX	120	80	25	0.79	1.82	95.254	51.582	0.062
Ca-LSX	120	80	33	0.68	1.28	95.123	51.653	0.053
Ca-LSX	120	85	40	0.625	0.961	95.177	51.572	0.06
Ca-LSX	120	90	50	0.5	0.63	95.33	52.101	0.037
$Li_{2.5}Ca_{46.75}$-LSX	120	90	50	0.82	0.99	95.101	51.834	0.05
$Li_{2.5}Ca_{46.75}$-LSX	120	85	40	0.9	1.34	94.923	52.665	0.06
$Li_{2.5}Ca_{46.75}$-LSX	120	85	33	0.981	1.7	95.467	52.336	0.067
$Li_{2.5}Ca_{46.75}$-LSX	120	80	25	1.05	2.39	95.326	51.794	0.074
$Li_{4.2}Ca_{45.9}$-LSX	120	90	50	1.05	1.03	95.169	51.796	0.054
$Li_{4.2}Ca_{45.9}$-LSX	120	85	40	1.16	1.42	95.604	52.474	0.064
$Li_{4.2}Ca_{45.9}$-LSX	120	80	33	1.24	1.87	95.417	52.154	0.070
$Li_{4.2}Ca_{45.9}$-LSX	120	80	25	1.395	2.67	95.465	52.59	0.082
Li-LSX	120	80	25	1.58	3.12	95.084	52.4	0.102
Li-LSX	120	80	33	1.5	2.34	95.441	52.021	0.093
Li-LSX	120	85	40	1.385	1.695	95.02	52.698	0.081
Li-LSX	120	90	50	1.3	1.26	95.471	52.137	0.071
Ca-LSX	150	110	60	1.07	1.15	95.394	52.093	0.077
Ca-LSX	150	110	60	0.312	0.494	95.126	51.573	0.035
Ca-LSX	150	105	50	0.4	0.707	95.118	52.391	0.044
Ca-LSX	150	100	40	0.455	0.982	95.403	52.168	0.051
Ca-LSX	150	95	33	0.488	1.284	95.21	51.725	0.056
Ca-LSX	150	95	25	0.574	1.81	94.811	52.219	0.066
$Li_{2.5}Ca_{46.75}$-LSX	150	110	60	0.61	0.85	94.943	52.309	0.051
$Li_{2.5}Ca_{46.75}$-LSX	150	105	50	0.66	1.1	95.575	52.183	0.058
$Li_{2.5}Ca_{46.75}$-LSX	150	100	40	0.71	1.46	95.267	52.334	0.067
$Li_{2.5}Ca_{46.75}$-LSX	150	95	33	0.735	1.85	95.062	52.167	0.073
$Li_{2.5}Ca_{46.75}$-LSX	150	95	25	0.801	2.5	95.248	52.443	0.082

$Li_{4.2}Ca_{45.9}$-LSX	150	110	60	0.79	0.88	95.334	52.471	0.055
$Li_{4.2}Ca_{45.9}$-LSX	150	105	50	0.87	1.16	95.164	52.111	0.063
$Li_{4.2}Ca_{45.9}$-LSX	150	100	40	0.95	1.58	95.245	51.848	0.071
$Li_{4.2}Ca_{45.9}$-LSX	150	95	33	1	2.02	94.98	52.114	0.078
$Li_{4.2}Ca_{45.9}$-LSX	150	95	25	1.105	2.85	95.206	52.086	0.089
Li-LSX	150	105	50	1.12	1.45	94.826	52.215	0.084
Li-LSX	150	100	40	1.134	1.86	94.911	52.335	0.091
Li-LSX	150	95	33	1.173	2.41	95.623	52.293	0.100
Li-LSX	150	95	26	1.278	3.26	95.53	52.252	0.113

Appendix C – Supplementary Material for Chapter 4

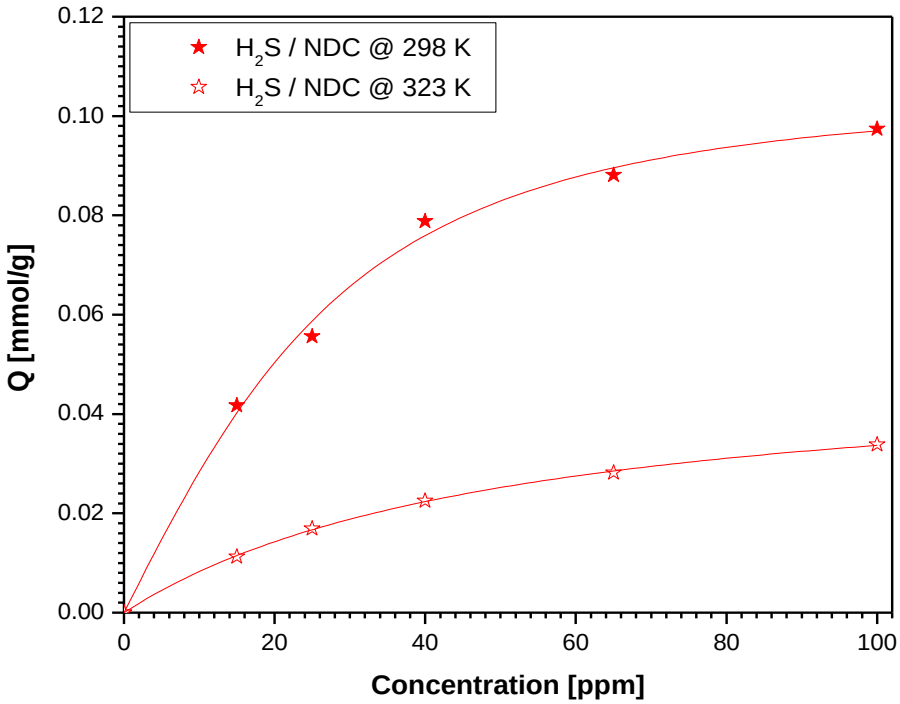

Figure S4.1 Experimental adsorption isotherms of H_2S on NDC at various temperatures and at 101 kPa.

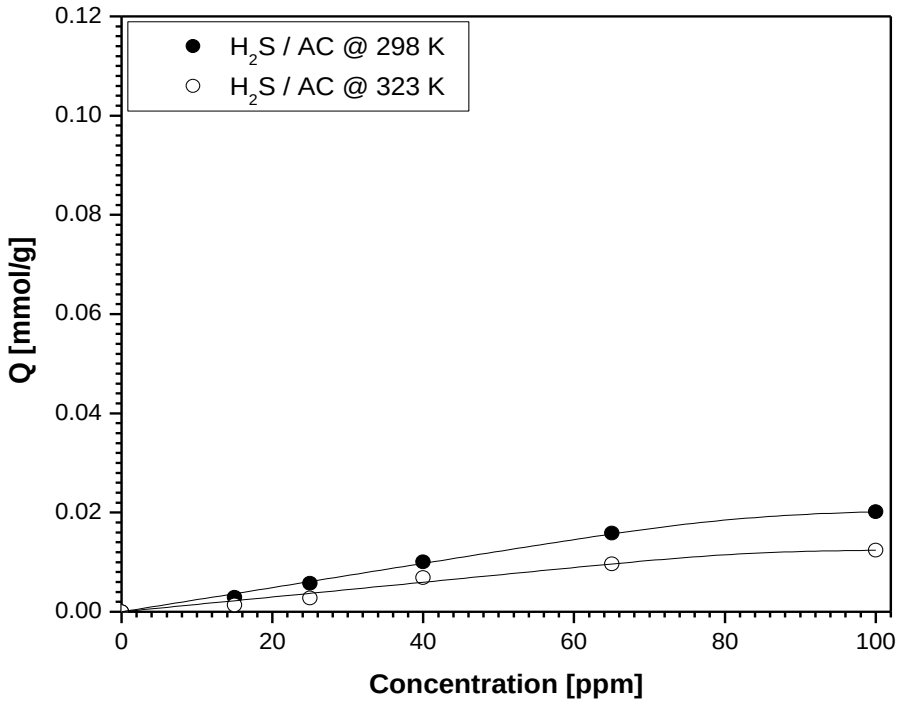

Figure S4.2 Experimental adsorption isotherms of H_2S on AC at various temperatures and at 101 kPa.

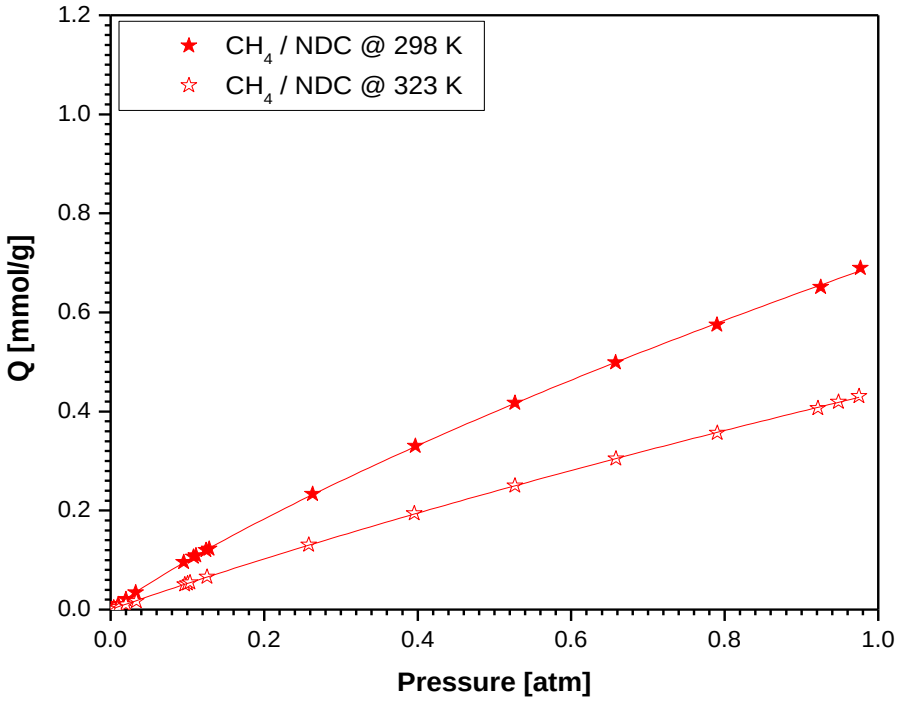

Figure S4.3 Experimental adsorption isotherms of CH_4 on NDC at various temperatures and at 101 kPa.

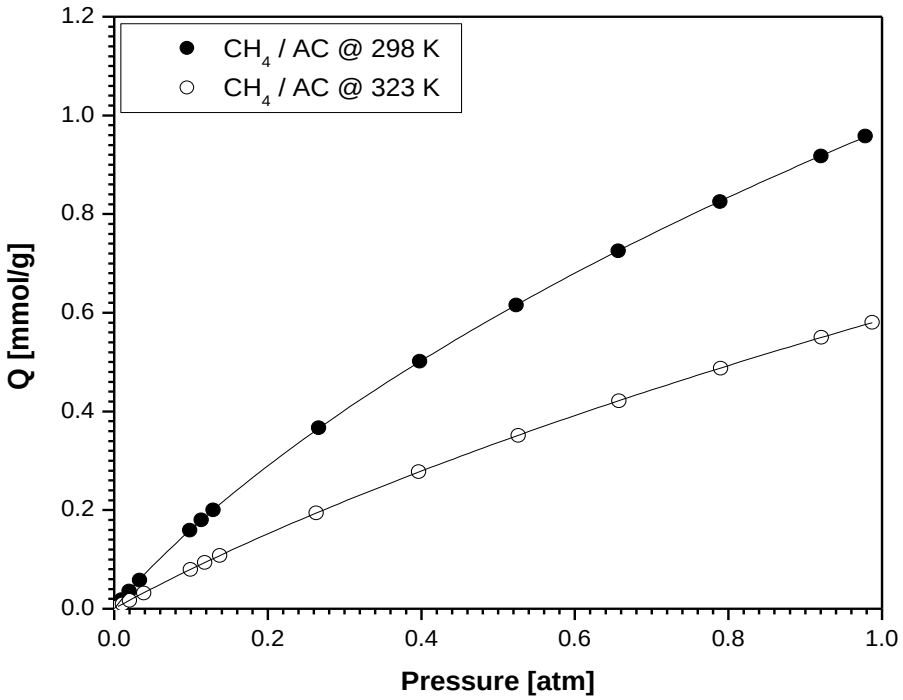

Figure S4.4 Experimental adsorption isotherms of CH_4 on AC at various temperatures and at 101 kPa.

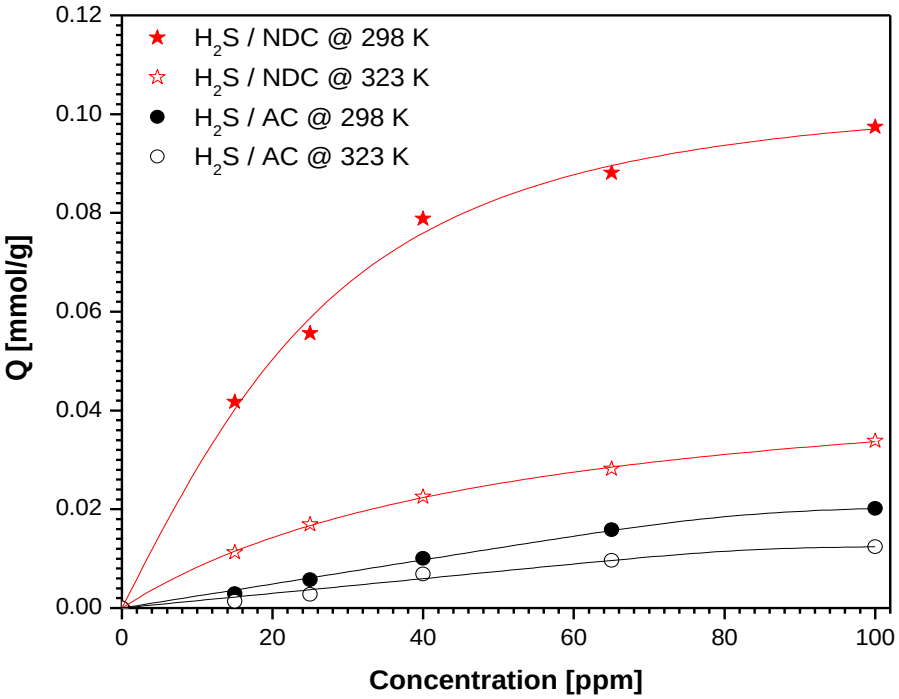

Figure S4.5 Experimental adsorption isotherms of H_2S on NDC and AC at various temperatures and at 101 kPa.

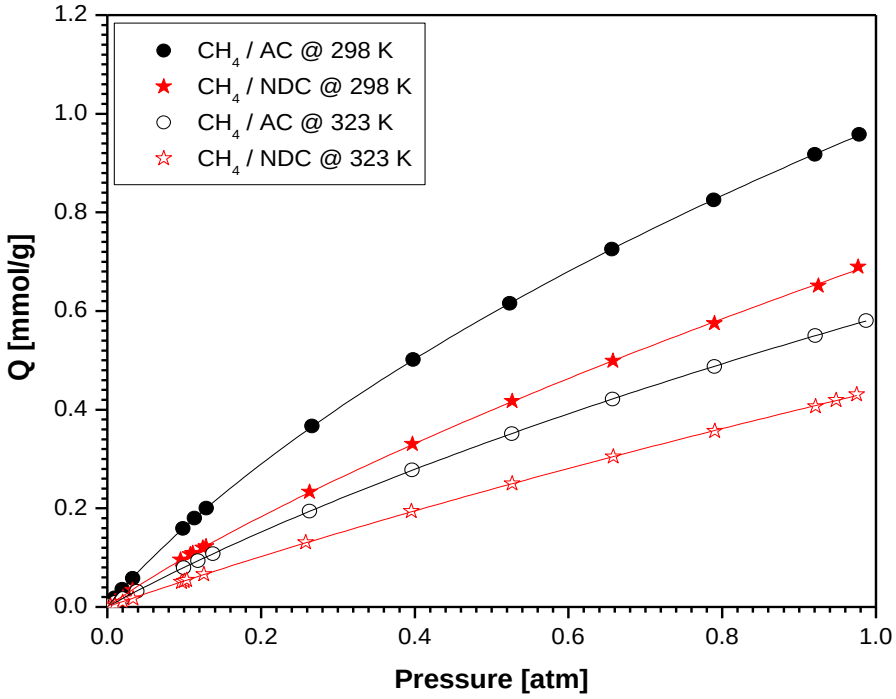

Figure S4.6 Experimental adsorption isotherms of CH_4 on NDC and AC at various temperatures and at 101 kPa.

Table S4.1 Representative values of model parameters fit to experimental adsorption data at 298 and 323K.

Sorbent	Tóth at 298 K			Tóth at 323 K		
	a [mmol/g]	d [atm^k]	k	a [mmol/g]	d [atm^k]	k
H_2S / NDC	0.11	591.90	1.79	0.05	57.24	1.03
H_2S / AC	0.02	8.28E16	8.78	0.01	2.75E23	12.18
CH_4 / NDC	30.06	3.59	0.40	6.61	5.62	0.70
CH_4 / AC	7.73	2.00	0.53	4.92	3.14	0.67

Appendix D – Supplementary Material for Chapter 5

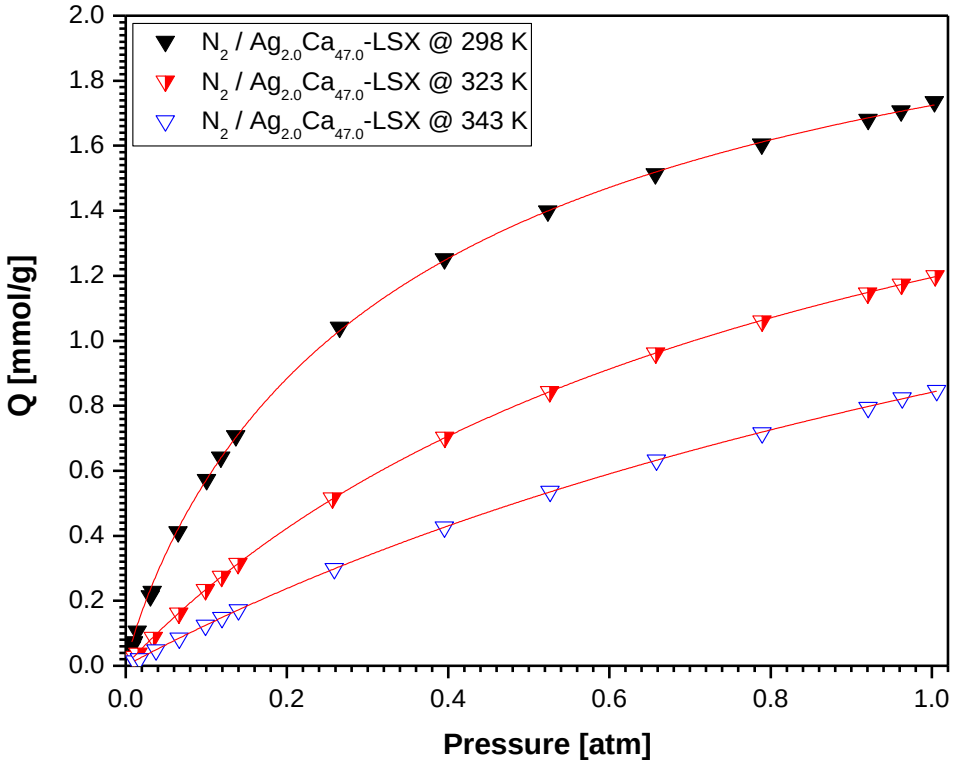

Figure S5.1 N_2 Experimental adsorption Isotherms on $Ag_{2.0}Ca_{47.0}$-LSX at various temperatures and 101 kPa.

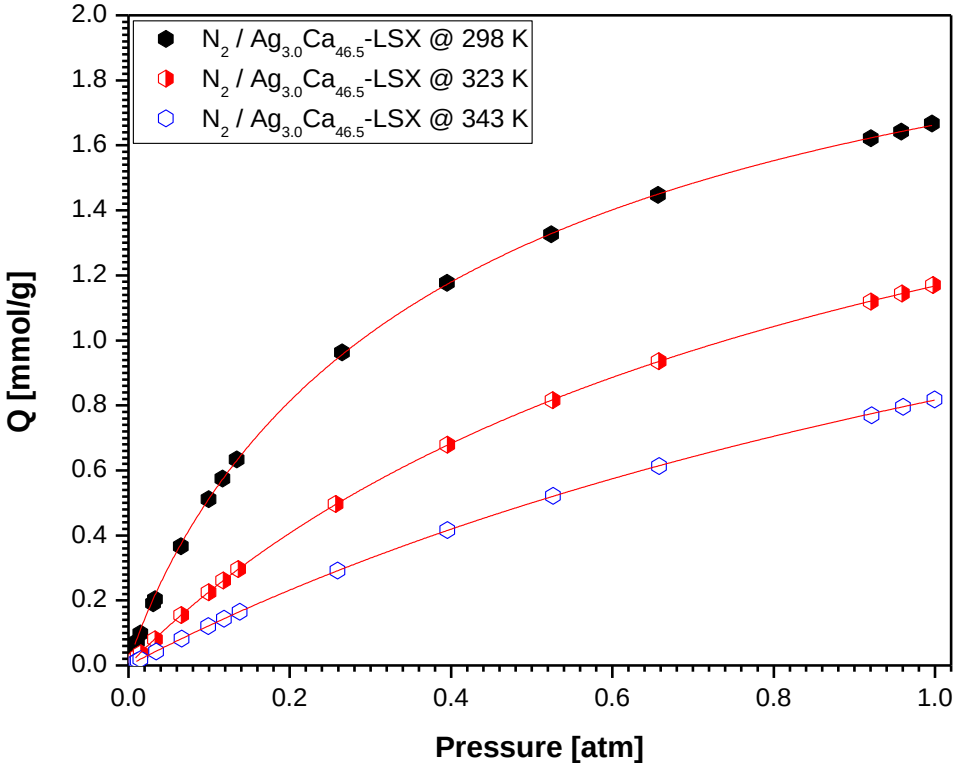

Figure S5.2 N_2 Experimental adsorption Isotherms on $Ag_{3.0}Ca_{46.5}$-LSX at various temperatures and 101 kPa.

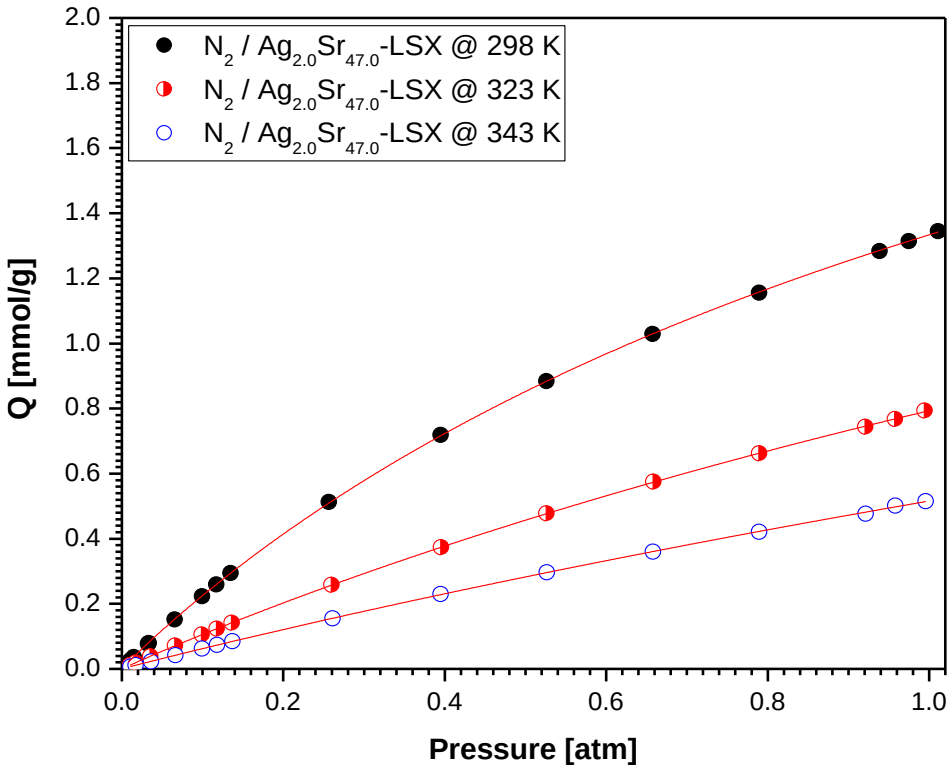

Figure S5.3 N_2 Experimental adsorption Isotherms on $Ag_{2.0}Sr_{47.0}$-LSX at various temperatures and 101 kPa.

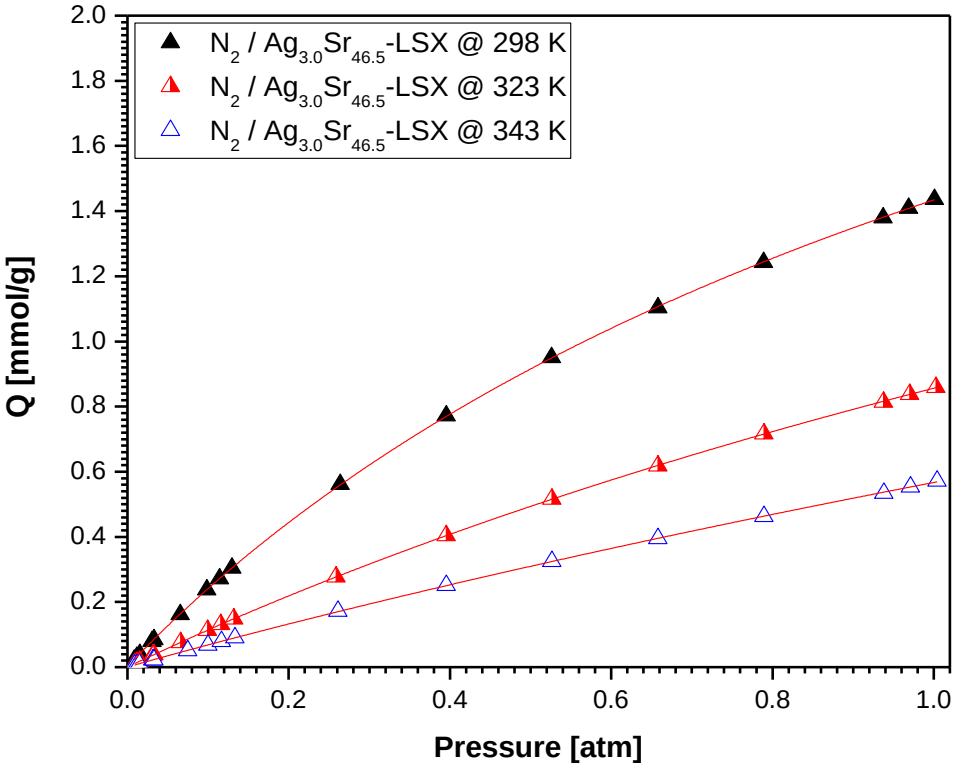

Figure S5.4 N_2 Experimental adsorption Isotherms on $Ag_{3.0}Sr_{46.5}$-LSX at various temperatures and 101 kPa.

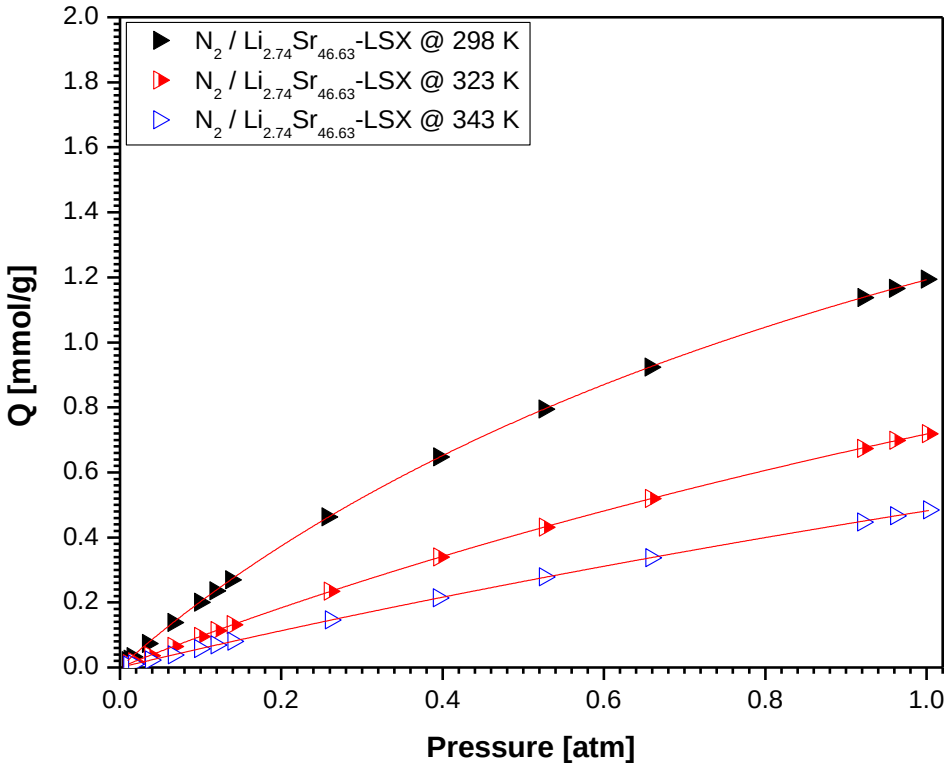

Figure S5.5 N_2 Experimental adsorption Isotherms on $Li_{2.74}Sr_{46-63}$-LSX at various temperatures and 101 kPa.

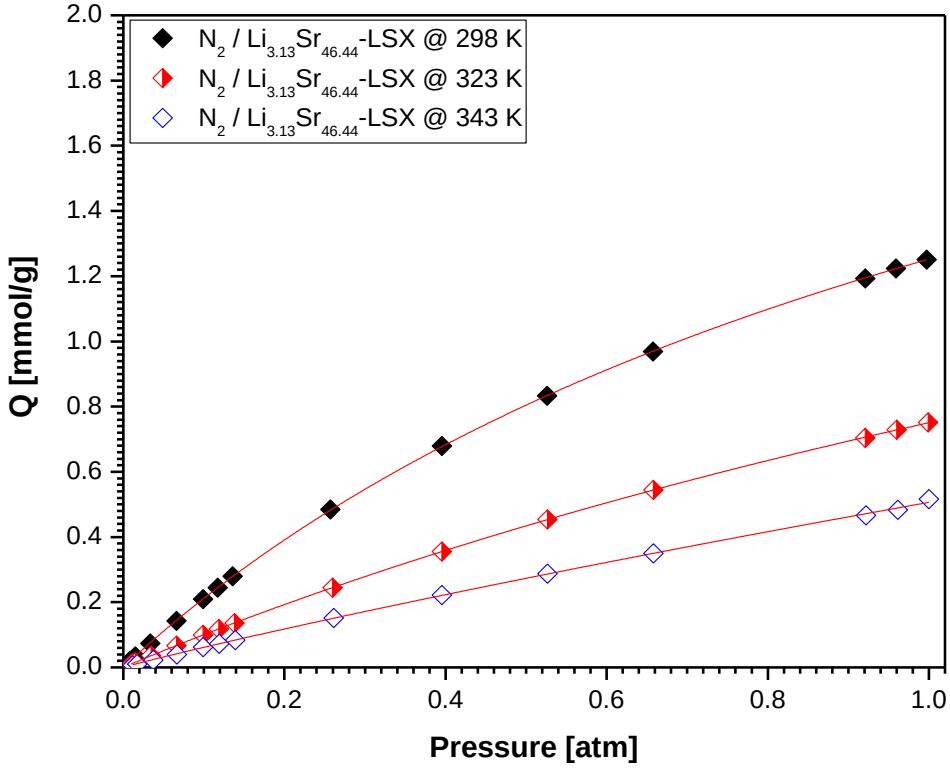

Figure S5.6 N_2 Experimental adsorption Isotherms on $Li_{3.13}Sr_{46-44}$-LSX at various temperatures and 101 kPa.

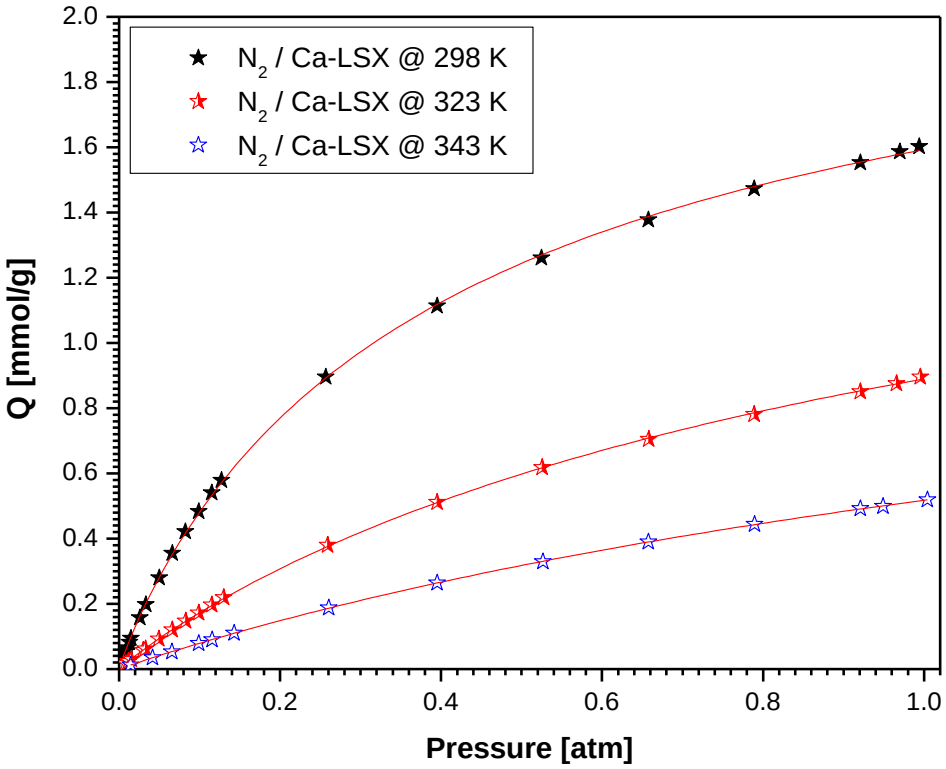

Figure S5.7 N_2 Experimental adsorption Isotherms on Ca-LSX at various temperatures and 101 kPa.

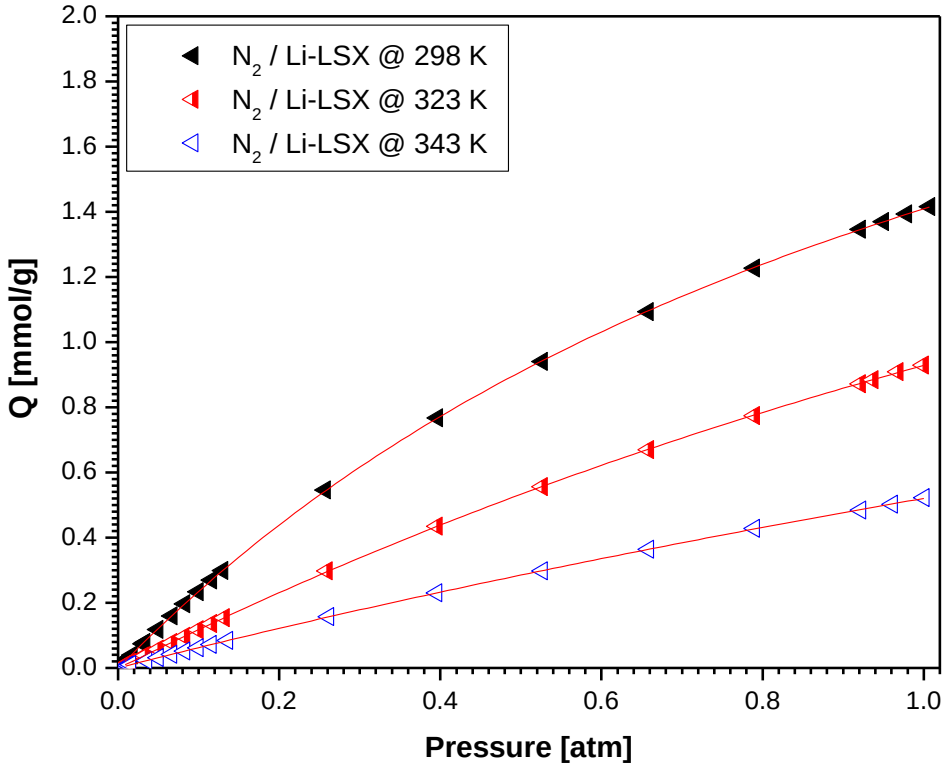

Figure S5.8 N_2 Experimental adsorption Isotherms on Li-LSX at various temperatures and 101 kPa.

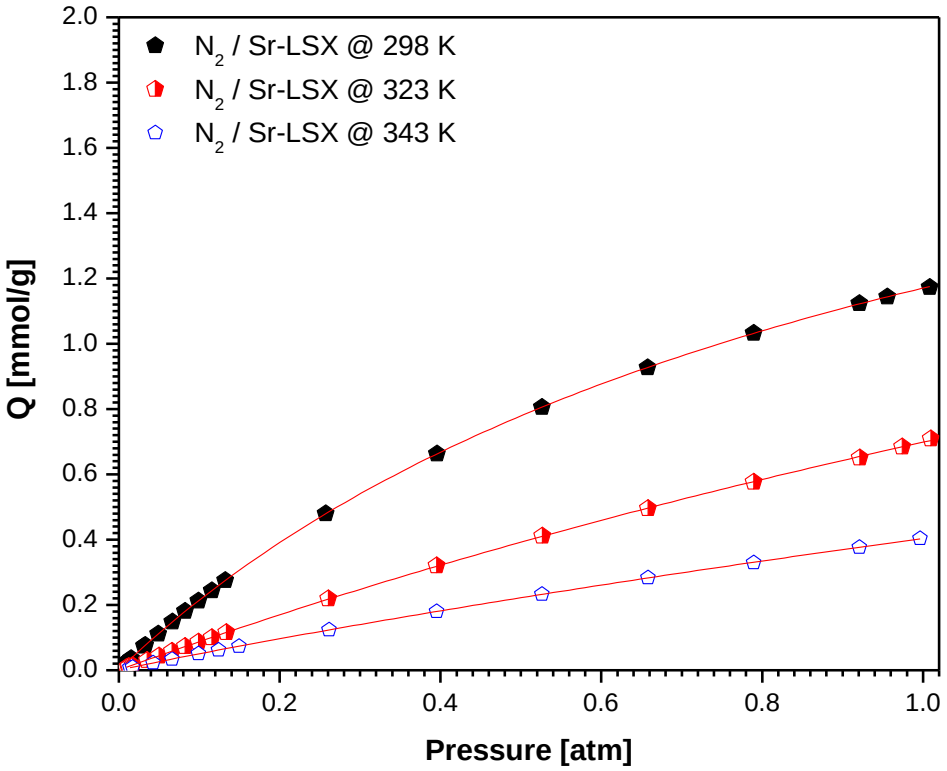

Figure S5.9 N_2 Experimental adsorption Isotherms on Sr-LSX at various temperatures and 101 kPa.

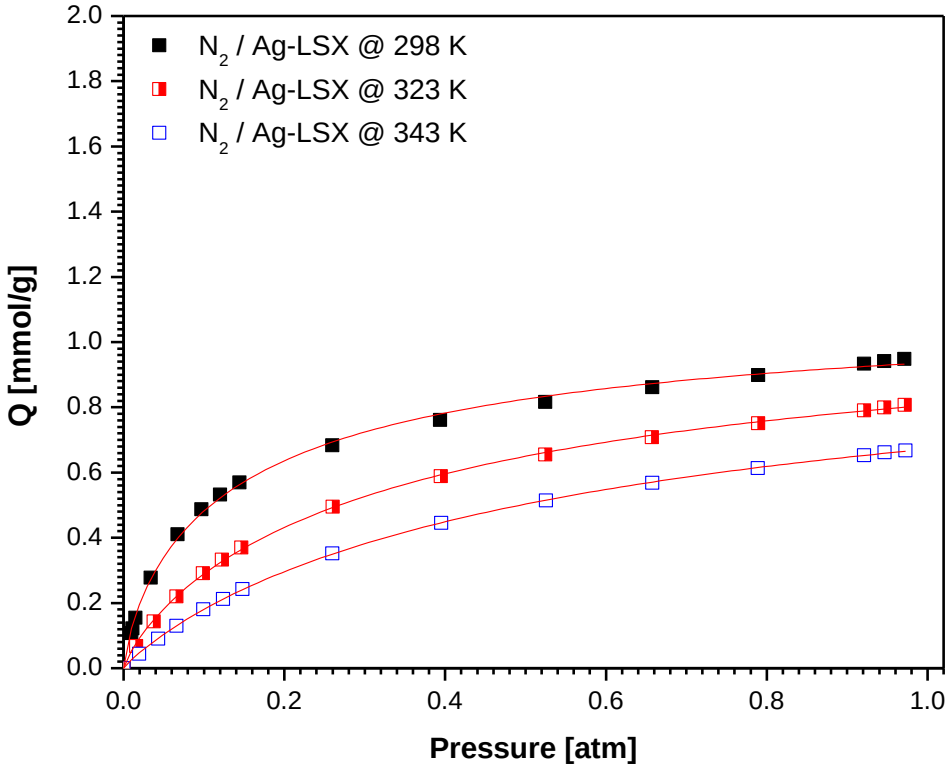

Figure S5.10 N_2 Experimental adsorption Isotherms on Ag-LSX at various temperatures and 101 kPa.

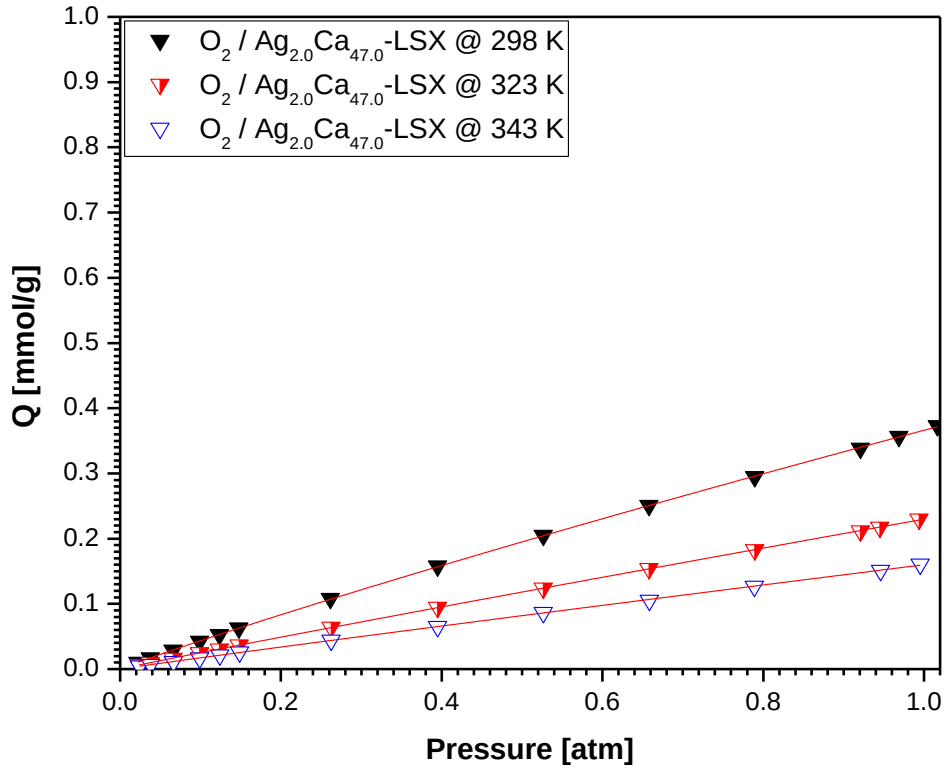

Figure S5.11 O_2 Experimental adsorption Isotherms on $Ag_{2.0}Ca_{47.0}$-LSX at various temperatures and 101 kPa.

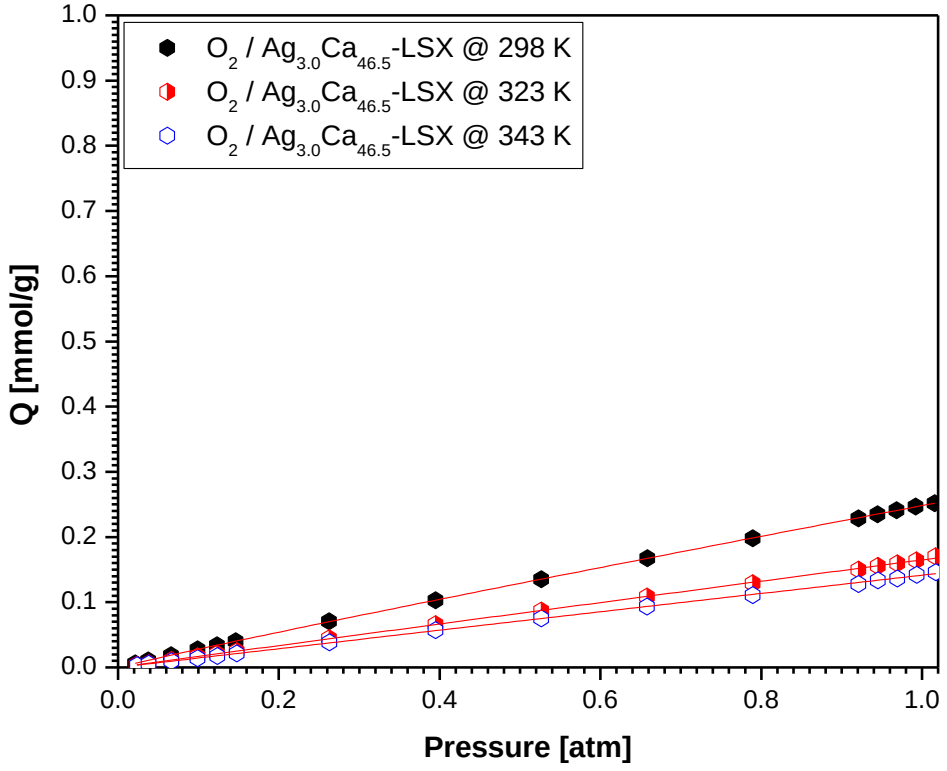

Figure S5.12 O_2 Experimental adsorption Isotherms on $Ag_{3.0}Ca_{46.5}$-LSX at various temperatures and 101 kPa.

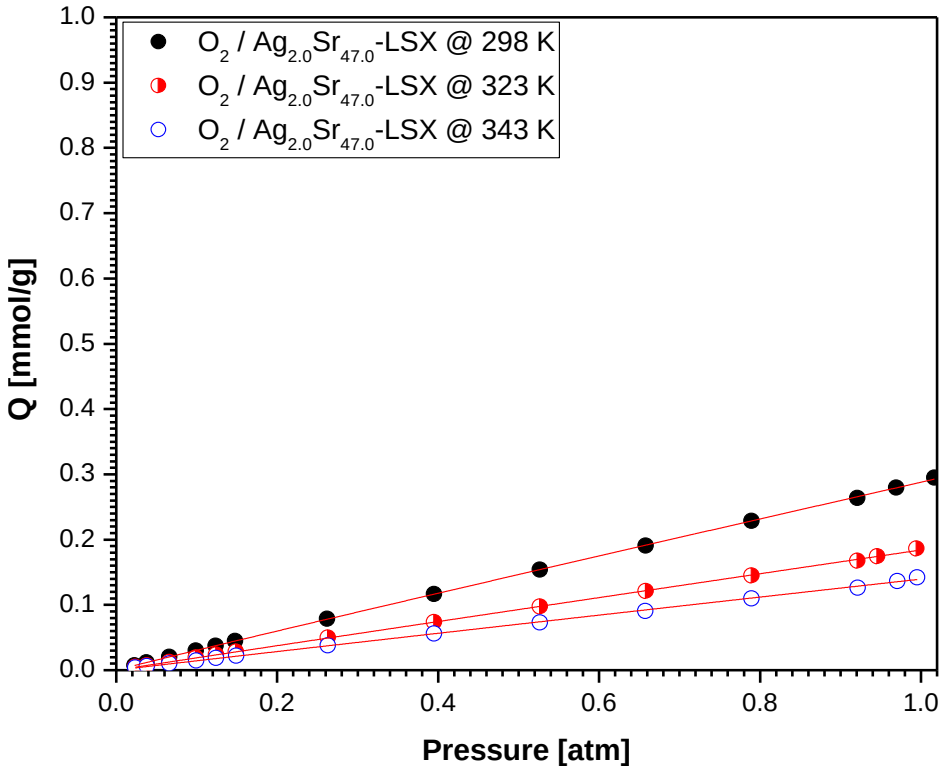

Figure S5.13 O_2 Experimental adsorption Isotherms on $Ag_{2.0}Sr_{47.0}$-LSX at various temperatures and 101 kPa.

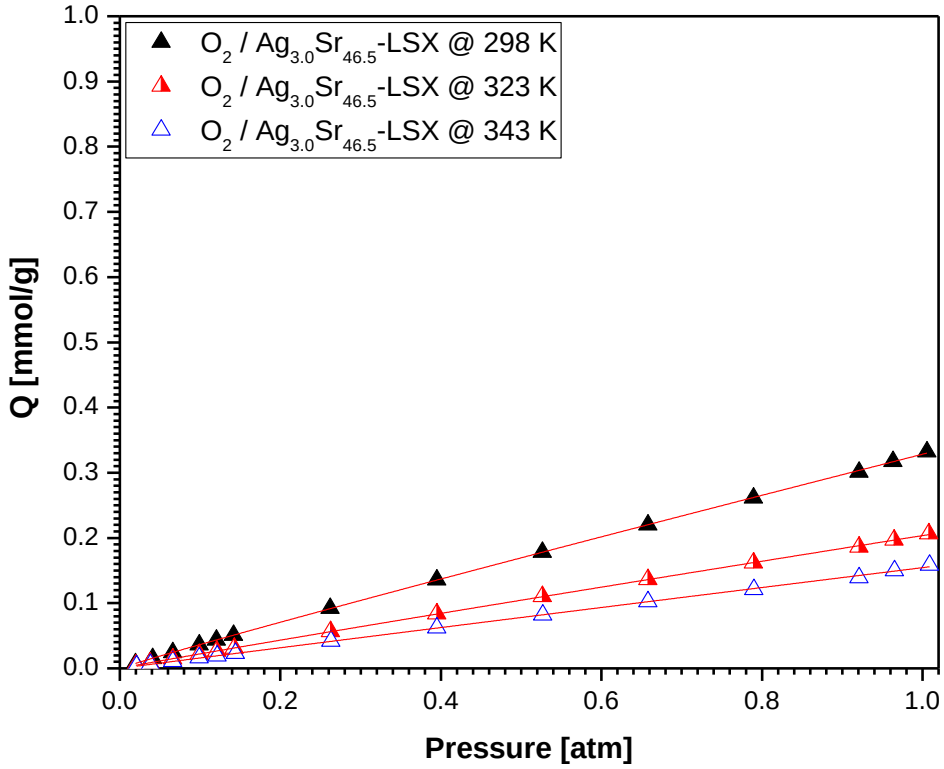

Figure S5.14 O_2 Experimental adsorption Isotherms on $Ag_{3.0}Sr_{46.5}$-LSX at various temperatures and 101 kPa.

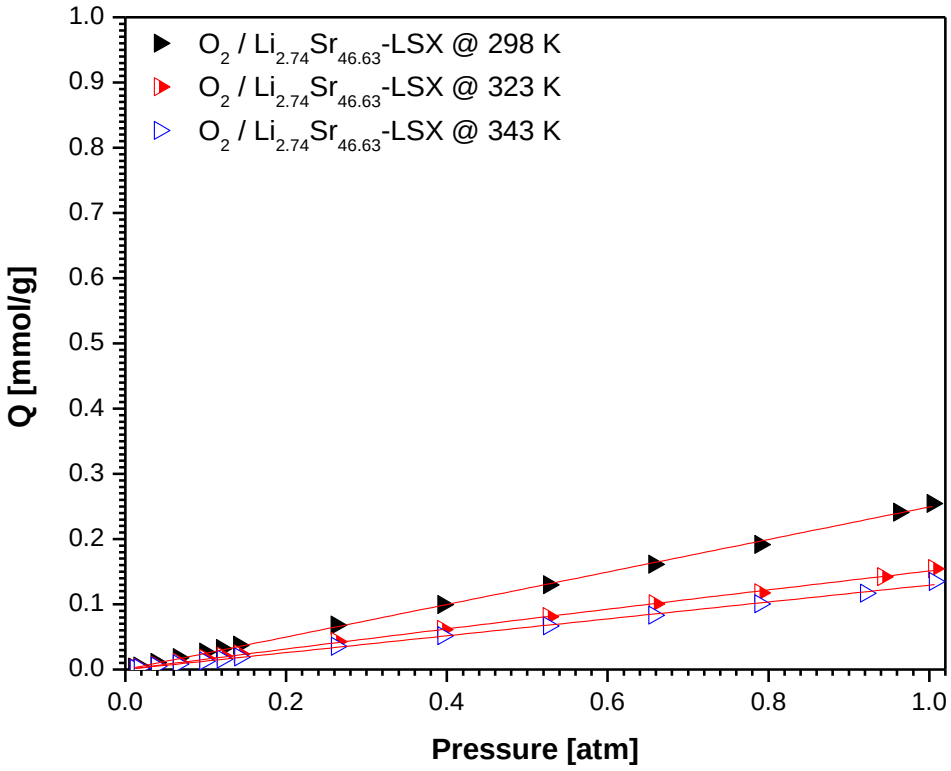

Figure S5.15 O_2 Experimental adsorption Isotherms on $Li_{2.74}Sr_{46-63}$-LSX at various temperatures and 101 kPa.

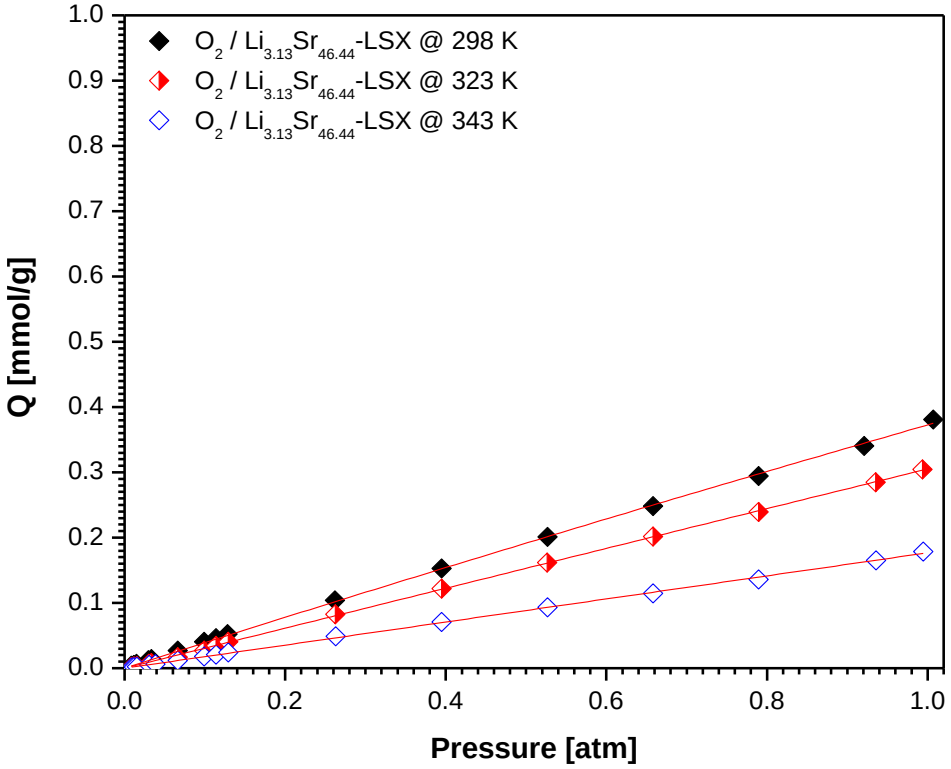

Figure S5.16 O_2 Experimental adsorption Isotherms on $Li_{3.13}Sr_{46-44}$-LSX at various temperatures and 101 kPa.

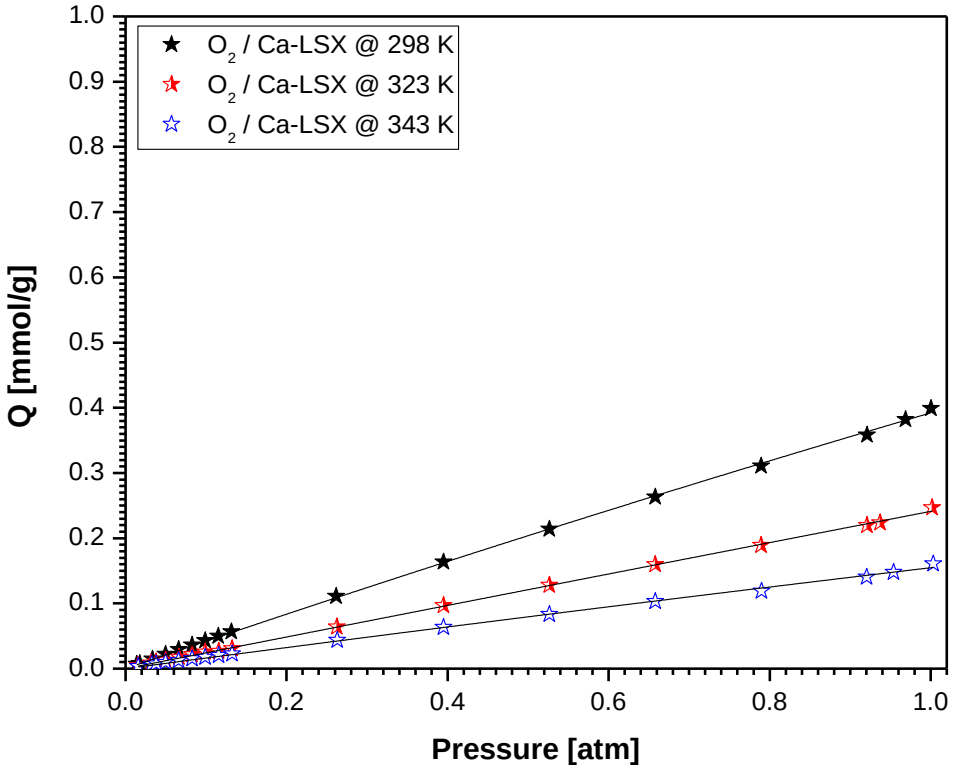

Figure S5.17 O_2 Experimental adsorption Isotherms on Ca-LSX at various temperatures and 101 kPa.

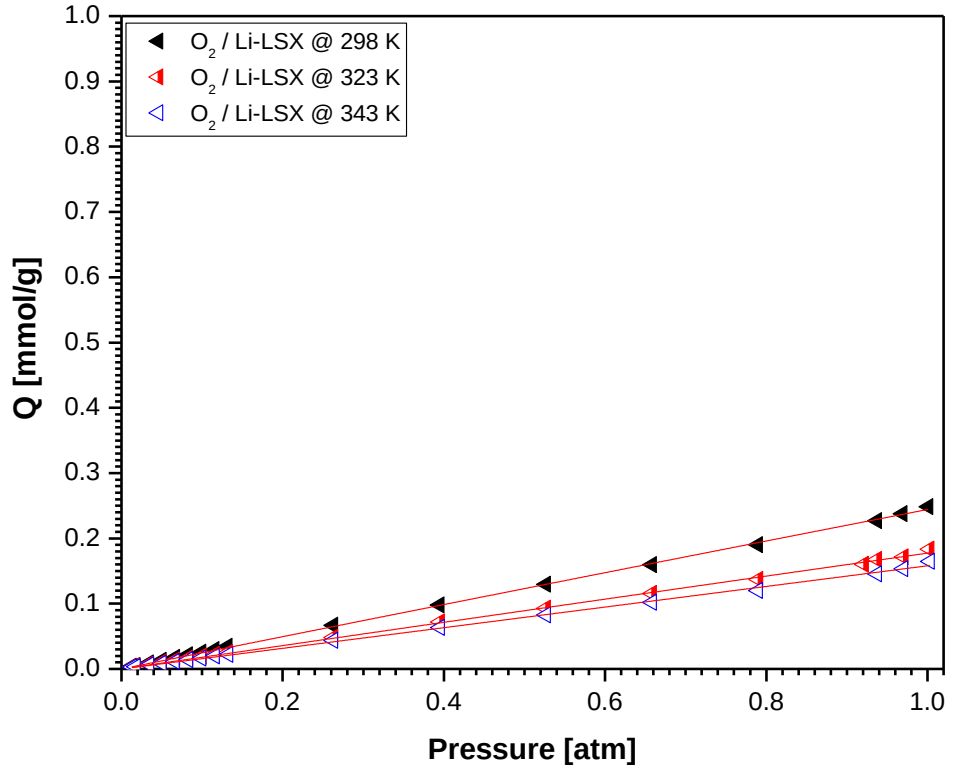

Figure S5.18 O_2 Experimental adsorption Isotherms on Li-LSX at various temperatures and 101 kPa.

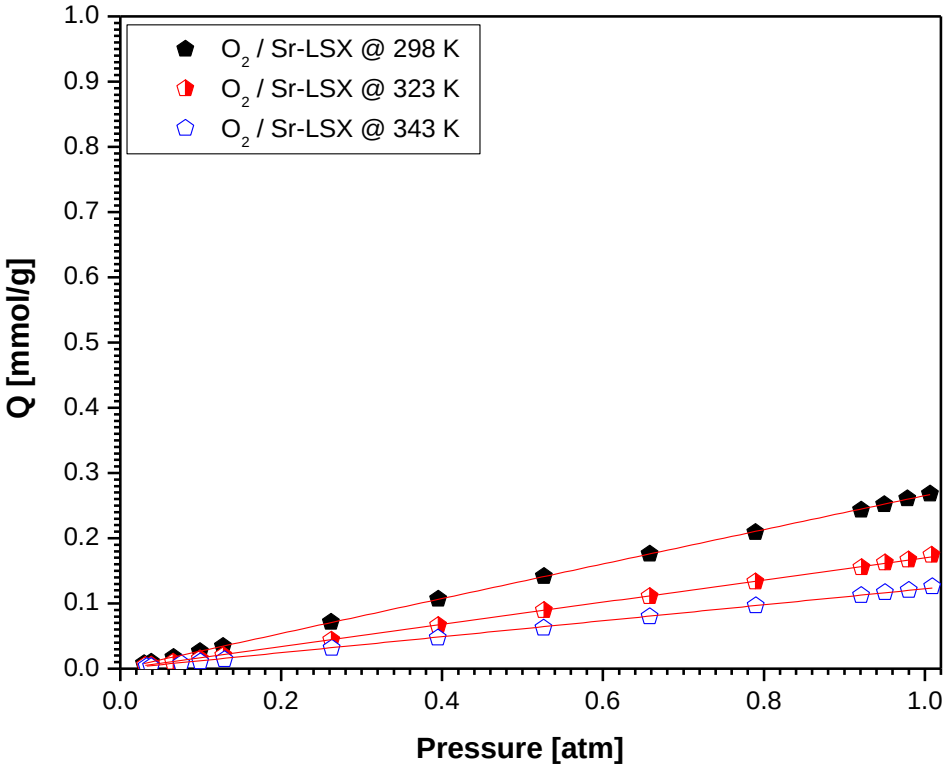

Figure S5.19. O_2 Experimental adsorption Isotherms on Sr-LSX at various temperatures and 101 kPa.

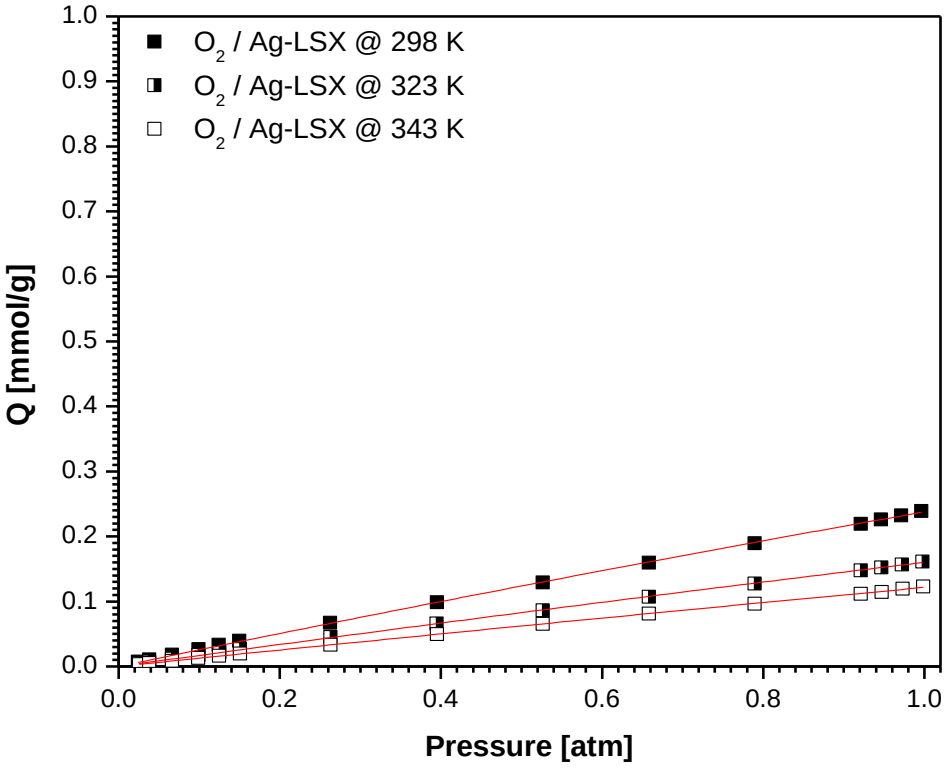

Figure S5.20 O_2 Experimental adsorption Isotherms on Ag-LSX at various temperatures and 101 kPa.

Table S5.1 Representative parameters of Langmuir-Freundlich Isotherm of N_2 and O_2 at 298 K.

Sorbent	Langmuir-Freundlich		
	Q_{sat} [mmol/g]	K [atm^{-n}]	n
N_2 / Ca-LSX	2.32	2.18	0.92
N_2 / Li-LSX	3.08	0.84	1.01
N_2 / Sr-LSX	2.40	0.96	0.99
N_2 / Ag-LSX	1.17	4.08	0.77
N_2 / $Ag_{2.0}Ca_{47.0}$-LSX	2.33	2.83	0.95
N_2 / $Ag_{3.0}Ca_{46.5}$-LSX	2.34	2.43	0.94
N_2 / $Ag_{2.0}Sr_{47.0}$-LSX	3.18	0.72	0.98
N_2 / $Ag_{3.0}Sr_{46.5}$-LSX	3.43	0.72	0.98
N_2 / $Li_{2.74}Sr_{46.63}$-LSX	2.75	0.77	0.98
N_2 / $Li_{3.13}Sr_{46.44}$-LSX	2.88	0.77	0.99
O_2 / Ca-LSX	10298.03	3.82E-5	0.95
O_2 / Li-LSX	32951.23	7.40E-6	0.98
O_2 / Sr-LSX	20.93	0.01	0.99
O_2 / Ag-LSX	169790.65	1.40E-6	0.95
O_2 / $Ag_{2.0}Ca_{47.0}$-LSX	6.81	0.06	0.95
O_2 / $Ag_{3.0}Ca_{46.5}$-LSX	20.07	0.01	0.95
O_2 / $Ag_{2.0}Sr_{47.0}$-LSX	140540.48	2.05E-6	0.97
O_2 / $Ag_{3.0}Sr_{46.5}$-LSX	3208.26	1.02E-4	0.95
O_2 / $Li_{2.74}Sr_{46.63}$-LSX	60553.11	4.11E-6	0.99
O_2 / $Li_{3.13}Sr_{46.44}$-LSX	27268.78	1.37E-5	0.96

Table S5.2 Representative parameters of Langmuir-Freundlich Isotherm of N_2 and O_2 at 323 K and 343 K.

Sorbent	Langmuir-Freundlich at 323 K			Langmuir-Freundlich at 343 K		
	Q_{sat} [mmol/g]	K [atm^{-n}]	n	Q_{sat} [mmol/g]	K [atm^{-n}]	n
N_2 / Ca-LSX	1.87	0.91	0.95	1.45	0.55	0.98
N_2 / Li-LSX	3.24	0.40	1.03	3.23	0.19	0.99
N_2 / Sr-LSX	3.26	0.27	0.99	2.94	0.23	1.00
N_2 / Ag-LSX	1.18	2.17	0.83	1.09	1.61	0.91
N_2 / $Ag_{2.0}Ca_{47.0}$-LSX	2.25	1.13	0.99	2.34	0.56	0.99
N_2 / $Ag_{3.0}Ca_{46.5}$-LSX	2.28	1.05	0.98	2.22	0.58	0.99
N_2 / $Ag_{2.0}Sr_{47.0}$-LSX	3.20	0.33	0.98	3.32	0.18	0.98
N_2 / $Ag_{3.0}Sr_{46.5}$-LSX	3.39	0.34	0.99	3.92	0.17	0.98
N_2 / $Li_{2.74}Sr_{46.63}$-LSX	2.91	0.33	0.98	2.88	0.20	0.99
N_2 / $Li_{3.13}Sr_{46.44}$-LSX	2.88	0.35	0.99	5.83	0.10	0.95
O_2 / Ca-LSX	13613.24	1.77E-5	0.99	35110.71	4.40E-6	0.96
O_2 / Li-LSX	34082.95	5.19E-6	0.98	1381.44	1.14E-4	0.99
O_2 / Sr-LSX	107.05	0.002	1.03	714.95	1.73E-4	1.05
O_2 / Ag-LSX	127652.83	1.26E-6	0.96	4617.63	2.63E-5	0.97
O_2 / $Ag_{2.0}Ca_{47.0}$-LSX	216.76	0.001	0.96	8460.21	1.89E-5	0.97
O_2 / $Ag_{3.0}Ca_{46.5}$-LSX	9241.74	1.78E-5	0.99	4997.82	2.83E-5	0.99
O_2 / $Ag_{2.0}Sr_{47.0}$-LSX	14875.73	1.24E-5	0.99	21475.44	6.50E-6	0.99
O_2 / $Ag_{3.0}Sr_{46.5}$-LSX	113.16	0.002	0.96	12290.97	1.26E-5	0.99
O_2 / $Li_{2.74}Sr_{46.63}$-LSX	17948.23	8.41E-6	0.96	28968.68	4.48E-6	1.01
O_2 / $Li_{3.13}Sr_{46.44}$-LSX	3.51	0.09	1.05	23947.65	7.37E-6	0.99

Table S5.3 Simulation result for $Ag_{2.0}Ca_{47.0}$-LSX

P_H [atm]	P_{CD} [atm]	P_L [atm]	V_{in} [m/s]	V_{purge} [m/s]	O_2 Purity [%]	O_2 Recovery [%]	Productivity [$tO_2/h/t$]
1.5	1.1	0.6	0.85	1	94.962	52.125	0.0595
1.5	1.05	0.5	0.915	1.28	95.421	52.503	0.0681
1.5	1	0.4	0.995	1.72	95.093	52.503	0.0777
1.5	0.95	0.33	1.04	2.2	95.446	52.25	0.0845
1.5	0.95	0.25	1.135	3.05	95.269	52.414	0.0961
1.2	0.9	0.5	1.1	1.1	1.14	95.263	52.503
1.2	0.85	0.4	1.23	1.23	1.59	95.093	52.353
1.2	0.85	0.33	1.35	1.35	2.06	95.504	52.003
1.2	0.8	0.25	1.45	1.45	2.93	95.277	52.313
1.2	0.75	0.2	1.49	1.49	3.85	95.52	52.307

Table S5.4 Simulation results for $Ag_{3.0}Ca_{46.5}$-LSX

P_H [atm]	P_{CD} [atm]	P_L [atm]	V_{in} [m/s]	V_{purge} [m/s]	O_2 Purity [%]	O_2 Recovery [%]	Productivity [$tO_2/h/t$]
1.5	1.1	0.6	1.055	1.04	95.042	52.207	0.0671
1.5	1.05	0.5	1.15	1.37	95.448	52.218	0.0769
1.5	1	0.4	1.26	1.87	95.439	52.192	0.0881
1.5	0.95	0.33	1.326	2.4	95.059	52.161	0.0962
1.5	0.95	0.25	1.42	3.28	95.543	52.853	0.1090
1.2	0.9	0.5	1.38	1.2	95.046	52.347	0.0663
1.2	0.85	0.4	1.56	1.7	94.989	52.289	0.0785
1.2	0.85	0.33	1.7	2.2	95.214	52.068	0.0877
1.2	0.8	0.25	1.812	3.1	95.005	52.58	0.0996
1.2	0.75	0.2	1.86	4.05	95.066	52.358	0.1070

Table S5.5 Simulation result for $Ag_{2.0}Sr_{47.0}$-LSX

P_H [atm]	P_{CD} [atm]	P_L [atm]	V_{in} [m/s]	V_{purge} [m/s]	O_2 Purity [%]	O_2 Recovery [%]	Productivity [$tO_2/h/t$]
1.5	1.1	0.6	0.848	1.04	94.824	52.128	0.0693
1.5	1.05	0.5	0.85	1.32	95.385	51.902	0.0715
1.5	1	0.4	0.849	1.66	94.782	52.052	0.0810
1.5	0.95	0.33	0.845	2.1	94.705	52.196	0.0881
1.5	0.95	0.25	0.847	2.75	95.446	52.279	0.0940
1.2	0.9	0.5	1.02	1.12	94.984	51.819	0.0619
1.2	0.85	0.4	1.02	1.45	94.913	51.915	0.0673
1.2	0.85	0.33	1.04	1.73	95.566	52.601	0.0728
1.2	0.8	0.25	1.04	2.4	94.877	51.826	0.0783
1.2	0.75	0.2	1.005	3.12	95.428	51.879	0.0840

Table S5.6 Simulation result for $Ag_{3.0}Sr_{46.5}$-LSX

P_H [atm]	P_{CD} [atm]	P_L [atm]	V_{in} [m/s]	V_{purge} [m/s]	O_2 Purity [%]	O_2 Recovery [%]	Productivity [$tO_2/h/t$]
1.5	1.1	0.6	0.916	1.12	95.178	52.506	0.0741
1.5	1.05	0.5	0.925	1.38	95.194	51.861	0.0775
1.5	1	0.4	0.903	1.72	94.909	51.977	0.0820
1.5	0.95	0.33	0.856	2.095	94.915	52.379	0.0859
1.5	0.95	0.25	0.872	2.73	95.669	52.285	0.0935
1.2	0.9	0.5	1.087	1.2	95.522	52.189	0.0660
1.2	0.85	0.4	1.11	1.56	94.928	52.444	0.0725
1.2	0.85	0.33	1.14	1.86	95.128	52.67	0.0772
1.2	0.8	0.25	1.09	2.48	95.136	51.992	0.0809
1.2	0.75	0.2	1.05	3.17	95.106	51.964	0.0867

Table S5.7 Simulation result for $Li_{2.74}Sr_{46.63}$-LSX

P_H [atm]	P_{CD} [atm]	P_L [atm]	V_{in} [m/s]	V_{purge} [m/s]	O_2 Purity [%]	O_2 Recovery [%]	Productivity [$tO_2/h/t$]
1.5	1.1	0.6	0.95	1.05	94.974	51.999	0.0700
1.5	1.05	0.5	0.93	1.28	94.494	52.232	0.0738
1.5	1	0.4	0.91	1.63	95.425	95.031	0.0788
1.5	0.95	0.33	0.92	2.1	95.514	52.293	0.0868
1.5	0.95	0.25	0.92	2.7	95.187	52.053	0.0913
1.2	0.9	0.5	1.1	1.11	95.083	52.533	0.0627
1.2	0.85	0.4	1.09	1.44	95.098	51.949	0.0665
1.2	0.85	0.33	1.13	1.75	95.258	52.639	0.0728
1.2	0.8	0.25	1.15	2.2	95.523	52.002	0.0773
1.2	0.75	0.2	1.13	2.98	95.203	52.255	0.0830

Table S5.8 Simulation result for Li-LSX

P_H [atm]	P_{CD} [atm]	P_L [atm]	V_{in} [m/s]	V_{purge} [m/s]	O_2 Purity [%]	O_2 Recovery [%]	Productivity [$tO_2/h/t$]
1	0.8	0.5	1.4	1.06	95.056	52.156	0.0596
1	0.65	0.33	1.7	2.5	95.506	51.926	0.0828
1	0.65	0.25	1.79	3	95.232	51.758	0.0888
1.2	0.8	0.25	1.58	3.12	95.084	52.4	0.102
1.2	0.8	0.33	1.5	2.34	95.441	52.021	0.0926
1.2	0.85	0.4	1.385	1.695	95.02	52.698	0.0812
1.2	0.9	0.5	1.3	1.26	95.471	52.137	0.0712
1.5	1.1	0.6	1.07	1.15	95.394	52.093	0.077
1.5	1.05	0.5	1.12	1.45	94.826	52.215	0.084
1.5	1	0.4	1.134	1.86	94.911	52.335	0.091
1.5	0.95	0.33	1.173	2.41	95.623	52.293	0.100
1.5	0.95	0.26	1.278	3.26	95.53	52.252	0.113

Appendix E – Supplementary Material for Chapter 6

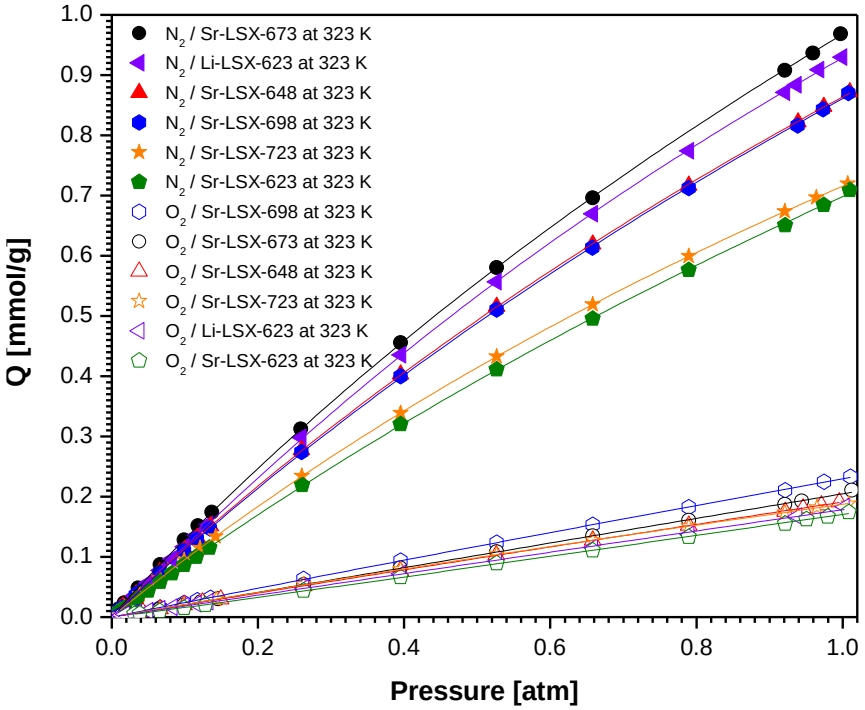

Figure S6.1 Combined N_2 and O_2 adsorption isotherms at 323 K and 101 kPa on sorbents dehydrated at various temperatures.

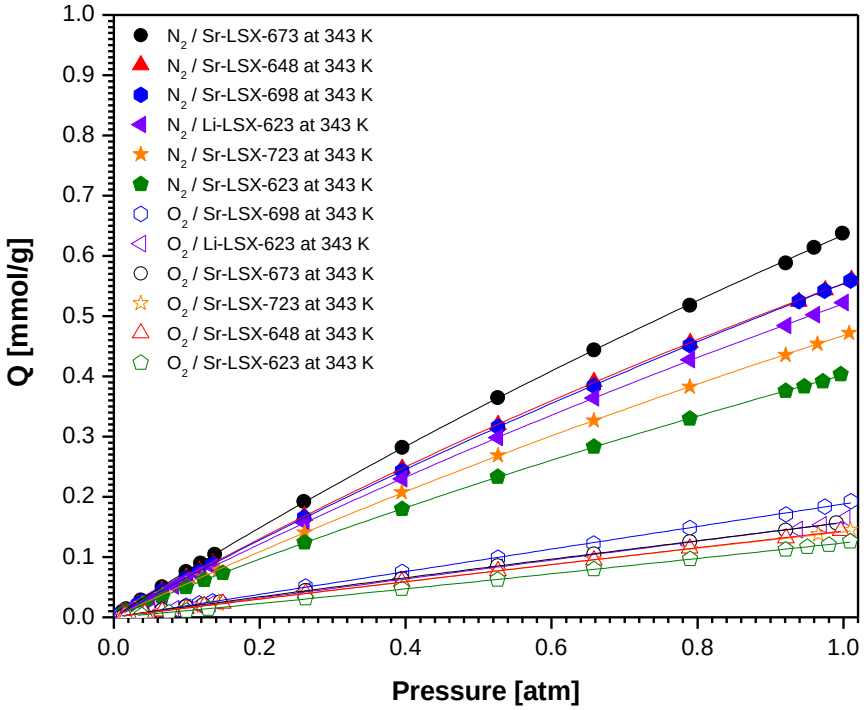

Figure S6.2 Combined N_2 and O_2 adsorption isotherms at 343 K and 101 kPa on sorbents dehydrated at various temperatures.

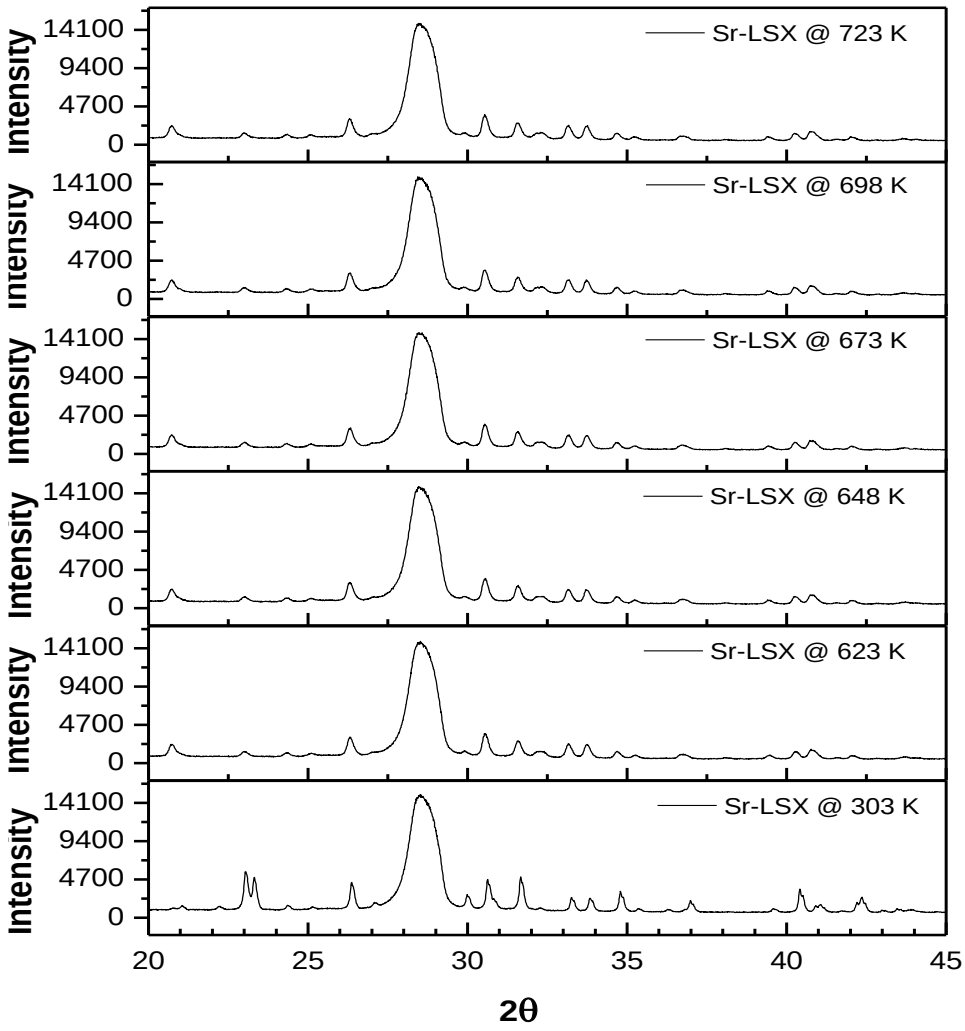

Figure S6.3 Powder XRD pattern for Sr-LSX. The patterns were collected at 303 K with no thermal treatment. The higher temperature patterns (623 – 723 K) were collected by heating to the pictured temperatures *in vacuo*.

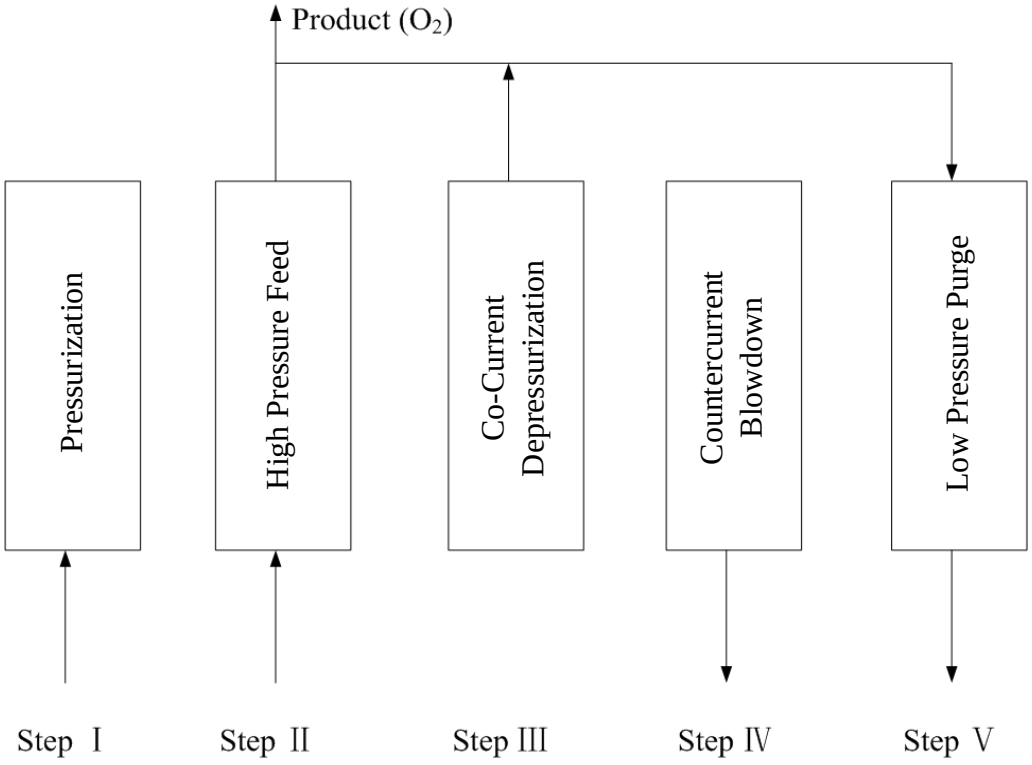

Figure S6.4 Five-Step PSA cycle configuration.

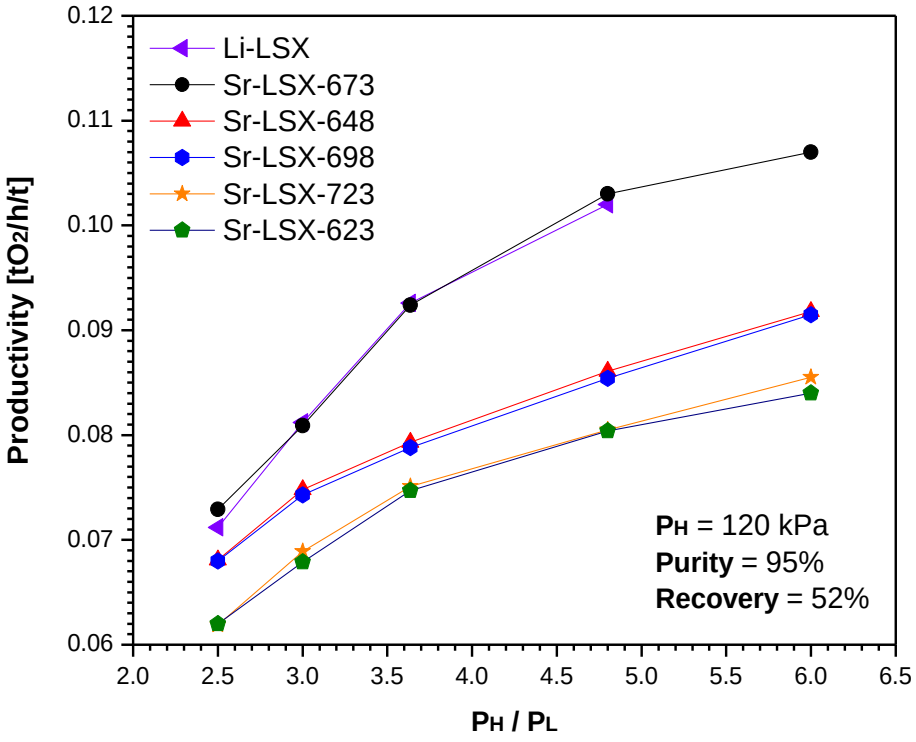

Figure S6.5 Comparison of O_2 productivity at 120 kPa pressure on various sorbents.

Table S6.1 Adsorption Bed Characteristics and Operating Conditions for PSA Simulations

Bed length	2.5 m
Diameter of sorbent	1.0 m
Bed external porosity	0.4
Bed density	720 kg/m^3
Heat capacity of gases	28.72 J/mol/K
Heat capacity of sorbent	1.17 kJ/kg/K
Ambient temperature	298 K
Feed gas temperature	298 K
Feed gas composition	78% N_2, 22% O_2
Axial dispersion coefficient (Dax)	5×10^{-5} m^2/s
Effective heat conductive	0.2 w/m/K

Table S6.2 Temperature-Dependent parameters for Langmuir-Freundlich Isotherm of N_2 and O_2.

Sorbent	**Sorbate**	**k_1** (mmol/g)	**k_2** (K)	**k_3** (atm^{-1})	**k_4** (K)	**n**	**ΔH** (kcal/mol)
Sr-LSX-623	O_2	2.61952	37.274	2.19E-04	1819.73228	1.04983	3.336
Sr-LSX-623	N_2	0.13797	849.94655	2.65E-03	1754.75503	1.01946	5.8063
Sr-LSX-648	O_2	0.15133	1292.06258	0.00865	325.92443	0.9845	3.624
Sr-LSX-648	N_2	1.11372	324.1435	9.11E-05	2702.4184	1.00054	6.071
Sr-LSX-673	O_2	26.78802	1583.05276	4.64E-05	70.26803	0.97131	3.642
Sr-LSX-673	N_2	1.46797	264.59369	8.80E-05	2725.16958	0.99864	6.0814
Sr-LSX-698	O_2	5.05846	1330.62087	2.72E-04	337.83683	0.96168	3.649
Sr-LSX-698	N_2	2.42687	40.2314	3.21E-05	3092.04537	1.03223	5.8458
Sr-LSX-723	O_2	2.20101	1488.64192	2.70E-04	380.59954	0.95633	3.522
Sr-LSX-723	N_2	0.932	322.28712	7.54E-05	2766.67657	0.99484	5.922

Table S6.3 Simulation results for Sr-LSX-623

P_H [kPa]	**P_{CD}** [kPa]	**P_L** [kPa]	**V_{in}** [m/s]	**V_{purge}** [m/s]	**O_2 Purity** [%]	**O_2 Recovery** [%]	**Productivity** [$tO_2/h/t$]
150	110	60	0.91	1.04	95.028	52.31	0.0659
150	105	50	0.945	1.31	95.214	52.299	0.0722
150	100	40	0.967	1.7	95.442	52.149	0.0784
150	95	33	1	2.18	95.281	52.498	0.0870
150	95	25	1.042	2.9	95.042	52.123	0.0929
120	90	50	1.1	1.1	1.14	95.263	0.0620
120	85	40	1.23	1.23	1.59	95.093	0.0679
120	85	33	1.35	1.35	2.06	95.504	0.0747
120	80	25	1.45	1.45	2.93	95.277	0.0804
120	75	20	1.49	1.49	3.85	95.52	0.0840

Table S6.4 Simulation results for Sr-LSX-648

P_H [kPa]	**P_{CD}** [kPa]	**P_L** [kPa]	**V_{in}** [m/s]	**V_{purge}** [m/s]	**O_2 Purity** [%]	**O_2 Recovery** [%]	**Productivity** [$tO_2/h/t$]
150	110	60	1.02	1.145	94.913	52.529	0.0738
150	105	50	1.05	1.44	95.168	52.263	0.0798
150	100	40	1.08	1.87	94.829	52.257	0.0869
150	95	33	1.11	2.4	95.331	51.788	0.0935
150	95	25	1.17	3.22	95.341	51.893	0.1020
120	90	50	1.25	1.25	95.123	52.431	0.0681
120	85	40	1.29	1.65	95.444	52.398	0.0748
120	85	33	1.33	2.01	95.303	52.31	0.0793
120	80	25	1.35	2.75	95.261	52.484	0.0861
120	75	20	1.374	3.63	95.33	52.201	0.0918

Table S6.5 Simulation results for Sr-LSX-673

P_H [kPa]	**P_{CD}** [kPa]	**P_L** [kPa]	**V_{in}** [m/s]	**V_{purge}** [m/s]	**O_2 Purity** [%]	**O_2 Recovery** [%]	**Productivity** [$tO_2/h/t$]
150	110	60	1.12	1.255	95.266	52.25	0.0792
150	105	50	1.14	1.555	95.106	51.974	0.0844
150	100	40	1.152	1.98	94.659	52.156	0.0908
150	95	33	1.205	2.57	95.134	52.25	0.1010
150	95	25	1.29	3.5	94.915	52.28	0.1110
120	90	50	1.25	1.37	1.37	95.563	52.028
120	85	40	1.29	1.44	1.82	94.567	52.08
120	85	33	1.33	1.59	2.38	95.377	52.111
120	80	25	1.35	1.65	3.33	95.445	52.342
120	75	20	1.374	1.63	4.25	95.127	52.262

Table S6.6 Simulation results for Sr-LSX-698

P_H [kPa]	**P_{CD}** [kPa]	**P_L** [kPa]	**V_{in}** [m/s]	**V_{purge}** [m/s]	**O_2 Purity** [%]	**O_2 Recovery** [%]	**Productivity** [$tO_2/h/t$]
150	110	60	0.958	1.23	94.909	52.115	0.0738
150	105	50	0.962	1.51	95.424	52.189	0.0795
150	100	40	0.967	1.92	94.856	52.106	0.0857
150	95	33	0.96	2.4	95.568	51.866	0.0914
150	95	25	0.97	3.05	94.997	52.478	0.0980
120	90	50	1.175	1.34	95.351	51.948	0.0680
120	85	40	1.19	1.73	95.189	52.059	0.0743
120	85	33	1.21	2.07	95.25	52.087	0.0788
120	80	25	1.217	2.835	95.267	51.743	0.0854
120	75	20	1.22	3.68	95.504	51.753	0.0915

Table S6.7 Simulation results for Sr-LSX-723

P_H [kPa]	**P_{CD}** [kPa]	**P_L** [kPa]	**V_{in}** [m/s]	**V_{purge}** [m/s]	**O_2 Purity** [%]	**O_2 Recovery** [%]	**Productivity** [$tO_2/h/t$]
150	110	60	0.865	1.11	94.98	51.955	0.0666
150	105	50	0.88	1.37	94.963	51.971	0.0721
150	100	40	0.89	1.755	94.932	52.176	0.0790
150	95	33	0.91	2.25	95.138	52.642	0.0885
150	95	25	0.94	2.95	95.203	52.293	0.0944
120	90	50	1.06	1.2	95.112	52.302	0.0619
120	85	40	1.09	1.575	95.563	52.427	0.0689
120	85	33	1.17	1.99	95.309	51.685	0.0751
120	80	25	1.15	2.65	95.331	51.93	0.0805
120	75	20	1.13	3.4	95.216	52.025	0.0855

Table S6.8 Simulation results for Li-LSX-623

P_H [kPa]	**P_{CD}** [kPa]	**P_L** [kPa]	**V_{in}** [m/s]	**V_{purge}** [m/s]	**O_2 Purity** [%]	**O_2 Recovery** [%]	**Productivity** [$tO_2/h/t$]
100	80	50	1.4	1.06	95.056	52.156	0.0596
100	65	33	1.7	2.5	95.506	51.926	0.0828
100	65	25	1.79	3	95.232	51.758	0.0888
120	80	25	1.58	3.12	95.084	52.4	0.102
120	80	33	1.5	2.34	95.441	52.021	0.0926
120	85	40	1.385	1.695	95.02	52.698	0.0812
120	90	50	1.3	1.26	95.471	52.137	0.0712
150	110	60	1.07	1.15	95.394	52.093	0.077
150	105	50	1.12	1.45	94.826	52.215	0.084
150	100	40	1.134	1.86	94.911	52.335	0.091
150	95	33	1.173	2.41	95.623	52.293	0.100
150	95	26	1.278	3.26	95.53	52.252	0.113